Model-based analysis of myocardial strains for the evaluation of cardiovascular function

Kimi Piedad Owashi Vallejo

To cite this version:

Kimi Piedad Owashi Vallejo. Model-based analysis of myocardial strains for the evaluation of cardiovascular function. Other. Université de Rennes, 2021. English. NNT : 2021REN1S043 . tel-03456920

HAL Id: tel-03456920
https://theses.hal.science/tel-03456920v1

Submitted on 30 Nov 2021

THÈSE DE DOCTORAT DE

L'UNIVERSITÉ DE RENNES 1

ÉCOLE DOCTORALE N° 601
Mathématiques et Sciences et Technologies
de l'Information et de la Communication
Spécialité : *Signal, Image, Vision*

Par

Kimi Piedad OWASHI VALLEJO

«Model-based analysis of myocardial strains for the evaluation of cardiovascular function»

Thèse présentée et soutenue à Rennes, le 17 Juin 2021
Unité de recherche : LTSI - INSERM 1099

Rapporteurs avant soutenance :
Luca Mainardi, Professeur, Politecnico di Milano.
Frida Sandberg, Maître de conférences, Lund University.

Composition du Jury :

Rapporteurs :	Luca Mainardi, Professeur, Politecnico di Milano.
	Frida Sandberg, Maître de conférences, Lund University.
Dir. de thèse :	Virginie Le Rolle, Maître de conférences, Université de Rennes 1.
Co-dir. de thèse :	Alfredo Hernández, Directeur de Recherche INSERM, Université de Rennes 1.
Examinateurs :	Catherine Marque, Professeure, Université de Technologie de Compiègne.
	Elena Galli, Praticien hospitalier, CHU de Rennes.

RÉSUMÉ EN FRANÇAIS

L'échocardiographie est une technique d'imagerie médicale, employant les ultrasons, couramment utilisées pour le diagnostic, la prise en charge et le suivi de patients insuffisants cardiaques. Le *«speckle-tracking echocardiography»* (STE) permet la quantification de l'asynchronisme ventriculaire en produisant des signaux de 'strain' associés à la déformation. Cependant, la majorité des méthodes existantes d'analyse du 'strain' est basée sur l'étude des valeurs optimales et des instants associés à celles-ci. Ces méthodes négligent notamment la morphologie des signaux même si des valeurs identiques des pics de 'strain' peuvent être associées à des dynamiques très différentes. De nouvelles méthodes sont donc nécessaires pour analyser conjointement la morphologie des signaux de 'strain' acquis simultanément dans différentes régions du myocarde. Cette tâche est particulièrement difficile à cause de la multi-dimensionnalité du problème et des nombreux processus impliqués dans la génération de la contraction ventriculaire (interactions mécano-hydrauliques, activation et propagation électrique, etc.), qui doivent être considérées conjointement.

L'objectif du travail de thèse est de proposer **une approche à base de modèles afin d'améliorer l'analyse des signaux de 'strain' issus de l'échocardiographie**. Cette approche semble particulièrement adaptée car cela permet d'intégrer des connaissances physiologiques dans le traitement des données et d'analyser les mécanismes sous-jacents qui sont difficiles ou impossibles à observer en clinique avec des méthodes non-invasives (propriétés passives du myocarde, activation électromécanique, ...). L'approche proposée dans la thèse nécessite donc la définition de modèles cardiaques dont la résolution spatio-temporelle doit être adaptée à l'échocardiographie. Par ailleurs, il est nécessaire d'intégrer une description des activités électriques, mécaniques et hydrauliques cardiaques afin de prendre en compte les différents processus qui mènent à la contraction du myocarde. L'approche globale repose sur le couplage entre les modèles et des méthodes appropriées d'analyse de sensibilité et d'identification. Le développement des modèles, proposés dans la thèse, pourront notamment bénéficier de l'environnement de **modélisation et de simulation multiformalisme (M2SL)**, précédemment développé par l'équipe SEPIA du LTSI. Deux applications cliniques sont visées par nos travaux : la **sténose aortique** et la **thérapie de resynchronisation cardiaque**.

La sténose aortique (SA) est un rétrécissement de l'ouverture de la valve aortique qui bloque le flux sanguin du ventricule gauche (VG) vers l'aorte, en provoquant une surcharge de la pression du VG. Même si la sévérité de la stenose aortiques est principalement basée sur des indices échocardiographiques liés à la valve, les décisions thérapeutiques reposent également sur l'évaluation de la fonction ventriculaire et la présence de symptômes. Dans ce contexte, il est essentiel de proposer des méthodes robustes et indépendantes des conditions de charge afin d'estimer l'atteinte du myocarde. Récemment, des indices de travail myocardique ont été proposés afin d'évaluer la fonction cardiaque à partir des signaux de strain et de pression ventriculaire. Les indices de travail cardiaque ont pu être validés dans diverses application, notamment liées aux désynchronisations ventriculaires. Cependant, leur évaluation chez les patients SA est difficile car la mesure par cathétérisme de la pression VG est contre-indiquée et l'estimation à partir des méthodes non invasives, actuellement proposées dans la littérature, n'est pas possible à cause du gradient de pression transaortique. Une première application de cette thèse consiste à proposer une **nouvelle approche à base de modèle pour 1) estimer la courbe de pression ventriculaire de manière non-invasive et 2) évaluer les indices de travail cardiaque à partir des signaux de strain obtenus par échocardiographie**. Le modèle proposé est composé de : *i)* l'activité électrique cardiaque, *ii)* une représentation de l'activité mécanique basée sur des élastances, *iii)* les circulations systémique et pulmonaire et *iv)* les valves cardiaques. Une stratégie d'identification utilisant une technique de *cross-validation* en 2 étapes a d'abord été appliquée sur une première base de données de 12 patients SA, puis la stratégie d'identification a été appliquée de manière prospective sur une seconde base de données de 23 patients SA. Les résultats montrent globalement un bon accord entre les indices de travail cardiaque obtenus à partir des simulations spécifiques au patient et des mesures expérimentales. À notre connaissance, ce projet présent la première méthode d'estimation du travail cardiaque, basée sur un modèle physiologique. L'évaluation du travail cardiaque est prometteuse car elle pourrait être une alternative simple et physiologique à des investigations plus complexes et coûteuses (IRM cardiaque, ...) pour l'évaluation de la fonction myocardique.

La thérapie de resynchronisation cardiaque (CRT) est une option thérapeutique chez les patients atteints d'insuffisance cardiaque (IC) avec un bloc de branche gauche (BBG). Le BBG est un trouble du système électrique cardiaque dans lequel les impulsions électriques sont bloquées au niveau de la branche gauche du faisceau de His avant d'arriver au ventricule gauche. La propagation et distribution des impulsions électriques sur le VG génère une contraction du myocarde inefficace et asynchrone. La CRT est une technique de stimulation électrique générée par un dispositif implantable permettant d'améliorer la coordination ventriculaire. Néanmoins, jusqu'à 30% des patients sélectionnés en fonction des recommandations utilisées en Europe et aux Etats-Unis, ne s'améliorent pas cliniquement après l'implantation du dispositif de CRT. Une relation entre les morphologies des signaux de *strain* et les réponses au CRT a été montré. Cependant, l'analyse des morphologies des *strain* associées au BBG est particulièrement difficile car les déformations du myocarde sont associées à la fois aux retards de conduction électrique et aux activités cardiaques mécaniques. La seconde application de cette thèse consiste à **proposer une nouvelle approche à base de modèles afin d'améliorer l'analyse des signaux de *strain***. Le modèle proposé intègre quatre sous-modèles principaux : *i)* le système électrique cardiaque, *ii)* les activités mécaniques de l'oreillette droite et gauche, *iii)* une representation multi-segment des activités mécaniques ventriculaires gauche et droite *iv)* les circulations systémiques et pulmonaires. Après une étape d'analyse de sensibilité, les paramètres du modèle ont été identifiés spécifiquement pour chaque patient. Ce modèle est capable de fournir des simulations des principales variables hémodynamiques (pression et débit ventriculaires...) et des signaux de *strain* caractéristiques. L'approche a été appliquée sur une base de données constituée de 10 sujets sains et 10 patients BBG, intégrant 5 patients avec une ischémie myocardique diagnostiquée et 5 patients sans ischémie. Les paramètres patient-spécifiques, déduits des modèles, ont été analysés afin de mettre en évidence les niveaux de retard électrique et de contractilité dans les différentes régions du ventricule gauche. Ainsi, l'approche à base des modèles permet d'analyser et d'interpréter la morphologie des signaux de strain en apportant des informations supplémentaires sur la fonction électrique et mécanique régionale du VG. Les résultats proposés mettent en évidence la complexité intrinsèque de la mécanique VG chez les candidats à la CRT, et présentent un pas en avant dans le développement de la modélisation VG personnalisée dans le domaine de la CRT.

L'une des principales contributions de cette thèse concerne l'intégration des méthodes **d'analyse de sensibilité et d'identification de paramètres** pour la création des modèles **spécifiques au patient** et la proposition d'indices physiologiques pour l'interprétation des mécanismes liés à la fonction cardiaque. L'évaluation des paramètres cliniques, spécifiquement pour chaque patient, a l'avantage de prendre en compte les caractéristiques associées au sujet et à la pathologie. La proposition des modèles computationnels, l'intégration de connaissances dans l'analyse de données, l'application d'intelligence artificielle à la santé, sont les différents aspects abordés dans ma thèse de doctorat qui est fortement soutenue par le caractère multidisciplinaire des chercheurs impliqués dans le projet.

Le premier chapitre de ce manuscrit présente le contexte physiologique et clinique dans lequel s'inscrit cette thèse. Après une brève revue de la physiologie et de l'anatomie cardiovasculaire, une description générale de la sténose aortique et du bloc de branche gauche est présentée. Enfin, l'échocardiographie, en tant qu'outil important pour le diagnostic, la prise en charge et le suivi en cardiologie ; ainsi que les paramètres basés sur l'écho pour l'évaluation de la fonction cardiaque sont également présentés.

Le chapitre 2 se concentre sur les stratégies et outils mis en œuvre pour la modélisation et la simulation des systèmes. L'environnement de modélisation et de simulation multiformalisme (M2SL) et les stratégies d'analyse des paramètres du modèle sont décrites. Nous présentons des méthodes d'analyse de sensibilité des paramètres qui peuvent être utiles pour simplifier le temps de calcul lors de la simulation. Nous présentons également les algorithmes évolutionnaires et la bibliothèque d'optimisation parallèle (PAGMO) utilisés pour l'identification des paramètres afin de proposer des simulations spécifiques au patient.

Dans le chapitre 3, une estimation à base des modèles de la pression VG est développée dans le cas de la SA afin de proposer un nouvel outil pour estimer des indices de travail myocardiques fiables pour cette population. Par un modèle multiformalisme du système cardiovasculaire et une stratégie d'identification des paramètres, les courbes de pression VG spécifiques au patient et les indices de travail myocardique ont été estimés par des procédures non invasives. L'approche à base des modèles proposée est une première étape essentielle pour l'estimation du travail cardiaque chez les patients SA.

Le dernier chapitre propose une approche à base de modèles permettant l'analyse de la morphologie des courbes de *strain* myocardique de manière spécifique-patient, afin d'améliorer l'interprétabilité des paramètres issus de l'échocardiographie. Un modèle multi-segment du système cardiovasculaire, intégrant des interactions électriques, mécaniques et hydrauliques, et une méthode d'identification des paramètres utilisant des algorithmes évolutionnaires ont été mis en œuvre afin d'obtenir des indices de contractilité et des délais d'activation électrique chez les patients BBG ischémiques et non ischémiques et chez les sujets sains.

ACKNOWLEDGEMENTS

First, I would like to express my deepest and sincere gratitude to my thesis advisors, *Virginie Le Rolle* and *Alfredo Hernández*. I will always be eternally grateful for accepting me to be part of a fascinating project, in an admirable team, in such a respectable laboratory. Thanks for the huge professional and personal opportunity gave to me and for the trust placed in me from the first moment. *Virginie* has not only been an exemplary and visionary mentor to me, but also a lovely, patient and inspiring role model. I cannot thank her enough for her mentorship, guidance and support over these years, and for being such an integral part of my career. *Alfredo* has been an inspiration, a leader, a mentor. I treasure everything he have taught me and I appreciate all his guidance and words of encouragement. I would also like to extend my special gratitude to *Elena Galli* for supporting and guiding me in the cardiology area. She was not only a competent and excellent cardiologist but also a really kind human being.

My deepest sense of gratitude to all the members of the LTSI for making me feel part of the team and supporting me at every moment. To all the professors (*Oscar, Guy, Jean-Louis, Fabienne, Fabrice Tudoret, Lotfi …*) that I had the opportunity to share and work with for being so generous and kind. I also want to thanks the members of the GEII department at the IUT of Rennes for accepting me as ATER, for being so welcoming since day one, for their patience and generosity. Special thanks to *Hervé Gauvrit*, his passion for teaching is inspiring and it has made me consider it as a career path in the future.

I also want to thank all the doctoral students, postdocs and trainees who are or were part of the LTSI and with whom I had the pleasure to spend time with. Just to name few and I will surely miss many, thanks to *Pablo, Henry, Elena, Karim, Alban, Yannick, Marouan, Angelica, Diana, Mireia, Carlos…* for all the good moments, the nice conversations, the laughs and the support inside and outside the Lab. Special thanks to the RU team, to *Remo* for being the kindest and coolest, it was a pleasure to share our birthdays; to *Cristhyne* for all the conversations enjoying a coffee and some sweet guilty pleasure; to *Gustavo* for all the help since before arriving the Lab, for the contagious joy, for the salsa lessons, for the support, for cooking me, for the thousands of laughs, for all the serious, funny and weird questioning of life.

I want to seize this moment to thank all my Colombian friends living in France for the great moments and for reminding me home. To all my friends in Colombia that despite the distance we support each other with the same friendship as always. To *Alejo* for being my partner, my accomplice and my greatest support in good and bad moments, for believing in me when I cannot, for loving me and for spoiling me.

Y finalmente quiero agradecer a las personas más importantes en mi vida, a mi familia. Sin ellos nunca hubiera sido esto posible, no tengo manera de agradecerles todo el apoyo que me han brindado. Gracias por permitirme vivir una experiencia tan increíble y enriquecedora, gracias por animarme en los momentos difíciles, gracias por creer en mí y por estar siempre presentes a pesar de la distancia física que nos separa. Gracias *mami* y *papi*, por su educación, por su amor, por sus valiosas lecciones, por su madurez, por ser el mejor ejemplo y los mejores papás del mundo. Gracias a mi hermanito, *Ken*, por todos sus consejos y por siempre buscar nuestro bienestar, porque a pesar de ser el menor es claramente el más centrado, el más sabio, y el que siempre ha estado para protegernos y guiarnos. Gracias a mi hermanita, *Emi*, por ser el contraste perfecto, por ser la alegría, el arte, la locura, la sensibilidad, gracias por alegrarnos con tus ocurrencias, por complementarnos, por apoyarnos. Estoy muy orgullosa de ustedes y me siento muy afortunada de tenerlos como mi familia.

TABLE OF CONTENTS

LIST OF ACRONYMS

AHA	American Heart Association
ARP	Absolute refractory period
AS	Aortic stenosis
AV	Atrio ventricular
AVA	Aortic valve area
AVC	aortic valve closure
AVO	aortic valve opening
AVN	Atrioventricular node
B	Bernoulli resistance
BA	Bland-Altman
CRT	Cardiac resynchronization therapy
CVS	Cardiovascular system
E	Elastance
EA	Evolutionary algorithms
ECG	Electrocardiogram
EE	Elementary effect
EF	Ejection fraction
EMDF	Electro-mechanical driving function
FEM	Finite element method
GA	Genetic algorithms
GCW	Global constructive work
GWE	Global work efficiency
GWW	Global wasted work
HF	Heart failure
HR	Heart rate
IVR	Isovolumic relaxation
L	Inertia
LA	Left Atrium
LBB	Left bundle branch
LBBB	Left bundle branch block
LGE	Late gadolinium enhancement
LHC	Left heart catheterization
LV	Left Ventricle
LVEF	Left ventricle ejection fraction
M2SL	Multi-formalism Modeling and Simulation Library

MRI	Magnetic resonance imaging
MVC	Mitral valve closure
MVO	Mitral valve opening
P	Pressure
Q	Flow
R	Resistance
RA	Right Atrium
RBB	Right bundle branch
RMSE	Root-mean-square error
RRP	Relative refractory period
RV	Right Ventricle
S	Systole
SA	Sinoatrial
SAN	Sinoatrial node
SAVR	surgical aortic valve replacement
SDD	Slow diastolic depolarization
STE	Speckle-tracking echocardiography
TAVI	Transcatheter aortic valve implantation
TDI	Tissue Doppler imaging
TTE	Trans-Thoracic echocardiography
UH	Upper bundle of His
UDP	Upstroke depolarization period
V	Volume
VHD	Valvular heart disease
W	Work

INTRODUCTION

According to the World Health Organization, cardiovascular diseases are the leading cause of death in the world, representing around 17.9 million death each year [1]. Heart failure (HF) is a pathological state characterized by the inability for the heart to provide a sufficient pump action to maintain the blood flow necessary for the needs of the body. About 1 to 2% of the general adult population in developed countries suffers from heart failure, which corresponds in Europe to about 10 million people [2]. The HF prognosis remains poor when clinical signs appear. An estimated 32 000 annual deaths are associated with heart failure in France. Although non-invasive imaging techniques such as cardiac CT, cardiac MRI and PET (Positron emission tomography) are developing rapidly and are emerging as major diagnostic tools, echocardiography remains the initial examination tool for studying the morphology and function of the heart because of its versatility, mobility, high spatiotemporal resolution and low cost.

Strain imaging method using speckle-tracking echocardiography (STE) has been introduced as a complementary tool for the assessment of myocardial function [3, 4, 5]. STE is used to acquire regional strain traces representing regional tissue deformation and is mathematically defined as the change in the myocardial fiber length relative to its original length presented at end-diastole. Although, previous studies [6, 7, 8, 9] have suggested that the analysis of strain traces obtained by STE might be an alternative for quantifying cardiac function compared to other measures such as left ventricle ejection fraction (LVEF), guidelines still neglect the value of these methods for different medical conditions. In fact, most of the analysis methods proposed in the literature are based on peak timings and values of strain signals. These methods neglect the dynamics of strain signals, since the same values of strain peaks or timings can be observed with different strain curve morphologies. As a consequence, new methods are needed to jointly analyze the morphology of strain signals acquired concurrently at different regions of the myocardium. However, this is a very difficult task, partly due to the multidimensionality of the problem and the fact that many different processes are involved in the generation of ventricular contraction (mechano-hydraulic interactions, electrical activation and propagation, etc.), which should be jointly considered for an appropriate interpretation.

In this context, a model-based approach seems particularly promising because: i) it allows the integration of physiological knowledge on data processing tasks, ii) it permits the analysis of underlying mechanisms that are difficult or impossible to observe, iii) it could help to improve the therapy planning by evaluating hypothesis or configuration scenarios of the system. Although modelling of cardiac activity is increasingly used in research field and the state-of-art is wide and very active [10, 11], only few patient-specific cardiovascular system (CVS) models have been proposed for the assessment of cardiac function. Most of the proposed personalized human heart models are based on the Finite Element method (FEM) [12, 13, 14, 15] and consist in multi-scale models that consider different features of the heart such as anatomy, electrical activation, myocardial conductivity, afterload, active contraction, circulatory systems, etc. As technology advances and more data becomes available, these approaches tend to increase the level of detail and complexity of the models, requiring high computational resources which impose an important challenge for personalizing therapy. Particularly, several FEM based approaches [16, 12, 17, 18, 19] have proposed customized and validated computational models to assess the response to cardiac resynchronization therapy. Nevertheless, the findings were generated in a small number of patients due to the high quality and detailed experimental measurements required that might even be difficult to obtain in a clinical setting, which limited the development of a greater number of personalized models.

In 2008, our team proposed the first model-based approach used to analyze echocardiography imaging [20]. This model is recognized in the literature as the first patient-specific model that could help the interpretation of Tissue Doppler Imaging (TDI) and provides physiological markers of electromechanical activation of the myocardium [21, 22]. This ventricular model has also been used to reproduce and interpret left ventricular pressure waveforms by taking into account electro-mechanical desynchronizations of one part of the myocardium [23]. Since the publication of this paper, the modelling methodology proposed by our team was improved in several ways. A multiformalism modeling and simulation environment (M2SL) was proposed in order to ease the integration of models representing different biological or physiological functions, at different resolutions, spanning through different scales [24]. A formalization of the model integration problem was further proposed and new coupling methods were presented in [25]. Sensitivity analysis methods were implemented to study input/output relationship [26, 27] and define a rank of importance in model parameters [28]. Identification methods have also been improved by using evolutionary algorithms [29], multi-objective optimization [28], and recursive identification [30]. Based on this methodological framework, a number of integrated models have been proposed in the cardiovascular field [29, 31], including neuromodulation applications [32] and for the analysis of the respiratory system [33, 34]. In parallel to these model-based analysis contributions, our team proposed the first data processing methods to take into account the dynamics of strain signals acquired from HF patients, by characterizing the integrals of regional strain traces [35] and recent works integrate these different approaches into complete data-processing and machine learning chains for the evaluation of HF patients [36, 37, 38].

Other teams have worked, more recently, on the development of such model-based methods, applied to HF [39, 40, 41], based on the CircAdapt closed-loop cardiovascular system model. Although Walmsley et al. [39] were able to simulate cardiac deformation patterns with generally correct magnitudes, efforts are still required to reproduce myocardial strain curves specifically to each patient. New methodological contributions are therefore needed in order to bring model-based approaches to the clinical field and provide patient-specific interpretation of strain curves.

The main objective of this thesis is **to propose a new model-based method for the analysis of cardiac regional strain data, obtained from cardiac echocardiography**. This includes a first phase of proposal and integration of a set of sub-models of the CVS, presenting low computational costs and adapted for model analysis and parameter identification. A second phase of this work targets two clinical applications of the proposed model-based method. This thesis is in direct continuity with the previous contributions of our team. All the methodological developments mentioned above were essential to the proposal of a new, integrated CVS model that could be used to analyze STE strain curves. Moreover, the sensitivity analysis and identification methods, proposed in our laboratory, were highly important to create a patient-specific model and to produce accurate physiological markers to the interpretation of cardiac strain. The results and tools developed in this thesis were performed within the framework of French ANR MAESTRo project (ANR-16-CE19-0008-01), which aims to provide novel tools for the analysis of echocardiography strains.

The first application of this thesis consists of the **proposal of a non-invasive model-based estimation of the LV pressure curve in the case of aortic stenosis (AS) to obtain reliable myocardial work indices.** AS is characterized by a narrowing of the aortic valve opening, which induces a LV pressure overload. Although AS severity evaluation is primarily based on echocardiographic characteristics of the valve, treatment decisions are also based on assessment of ventricular function and the presence of symptoms. In this context, it is essential to propose robust methods independent of the loading conditions in order to evaluate the impairment of myocardial diastolic and systolic functions. Myocardial work assessment was recently introduced [42, 43] as an interesting afterload-independent alternative to evaluate accurate cardiac function using strain signals and LV pressure curve. Because of the transaortic pressure gradient, non-invasive LVP estimation, proposed by [42], cannot be used. Moreover, the invasive measurement, by catheterization, is not recommended in AS patients. The first challenge was to propose a model-based estimation of LV pressure using non-invasive parameters, and the second challenge was to propose a novel tool to estimate myocardial work in AS.

The second application of the thesis concerns **a novel model-based approach for the analysis of myocardial strains in patients presenting a left bundle branch block (LBBB).** Cardiac resynchronization therapy (CRT) usually causes reverse LV remodeling and has shown a major favorable impact on the care of heart failure patients with LBBB. Despite the great success of randomized clinical trials, 25% to 35% of patients undergoing CRT are non-responders to treatment and can even be harmed by biventricular stimulation [44]. Observational studies of patients with LBBB have shown a relation between strain curve morphologies and responses to CRT [8, 45, 46]. However, the assessment of desynchrony patterns in LBBB appears as particularly complex because strains morphologies reflect dynamics associated with both electrical conduction delays and mechanical cardiac activities. A model-based approaches could help to improve the interpretation of myocardial deformations observed in LBBB, before CRT implantation. The main challenge was to propose a CVS model that integrates the mechanisms involved in the generation of ventricular contraction (mechano-hydraulic interactions, electrical activation and propagation, etc.) and the multidimensionality of the problem. We intend to propose a model-based approach that could bring additional information on regional LV electrical and mechanical function, as well as help to disclose the intrinsic complexity of LV mechanics in CRT candidates.

This thesis is organized as follows:

Chapter 1 provides the clinical context in which this thesis is framed. After a brief review about cardiovascular physiology and anatomy, a general overview of AS and LBBB is presented. Finally, the echocardiography, as an important tool for diagnosis, management and follow up in cardiology; as well as echo-based parameters for cardiac function assessment are also presented.

The chapter 2 focuses on the strategies and tools implemented for computer modeling and simulation. The Multi-Formalism Modeling and Simulation Library (M2SL) and the strategies for model parameter analysis are described.

In chapter 3, a model-based estimation of the LV pressure is developed in the case of AS in order to propose a novel tool to estimate reliable myocardial work indices for this population. By a multiformalism model of the cardiovascular system and a parameter identification strategy, patient-specific LV pressure waveforms and myocardial work indices were estimated by non-invasive procedures. The proposed approach is a first essential step for the proposition of work estimation based on computational modeling that could improve the prognostic significance in AS population.

The chapter 4 proposes innovative tools, including both data analysis methods and model-based approaches, in order to assist the analysis of myocardial strain curves and improve the interpretability of echo-based parameters. A multi-segment model of the cardiovascular system, integrating electrical, mechanical and hydraulic interactions, and a parameter identification method using evolutionary algorithms were implemented in order to obtain patient-specific regional myocardial strain and echo-based parameters in ischemic and non-ischemic LBBB patients and in healthy patients.

Bibliography

[1] A. Timmis, N. Townsend, C. P. Gale, A. Torbica, M. Lettino, S. E. Petersen, E. A. Mossialos, A. P. Maggioni, D. Kazakiewicz, *et al.*, "European Society of Cardiology: Cardiovascular Disease Statistics 2019," *European Heart Journal*, vol. 41, pp. 12–85, Jan. 2020. Publisher: Oxford Academic.

[2] Virani Salim S., Alonso Alvaro, Benjamin Emelia J., Bittencourt Marcio S., Callaway Clifton W., Carson April P., Chamberlain Alanna M., Chang Alexander R., Cheng Susan, Delling Francesca N., Djousse Luc, Elkind Mitchell S.V., *et al.*, "Heart Disease and Stroke Statistics—2020 Update: A Report From the American Heart Association," *Circulation*, vol. 141, pp. e139–e596, Mar. 2020. Publisher: American Heart Association.

[3] O. A. Smiseth, H. Torp, A. Opdahl, K. H. Haugaa, and S. Urheim, "Myocardial strain imaging: how useful is it in clinical decision making?," *European Heart Journal*, vol. 37, pp. 1196–1207, Apr. 2016. Publisher: Oxford Academic.

[4] E. Potter and T. H. Marwick, "Assessment of Left Ventricular Function by Echocardiography: The Case for Routinely Adding Global Longitudinal Strain to Ejection Fraction," *JACC. Cardiovascular imaging*, vol. 11, pp. 260–274, Feb. 2018.

[5] L. G. Klaeboe and T. Edvardsen, "Echocardiographic assessment of left ventricular systolic function," *Journal of Echocardiography*, vol. 17, pp. 10–16, Mar. 2019.

[6] J. Magne, B. Cosyns, B. A. Popescu, H. G. Carstensen, J. Dahl, M. Y. Desai, L. Kearney, P. Lancellotti, T. H. Marwick, K. Sato, M. Takeuchi, C. Zito, A.-C. Casalta, D. Mohty, L. Piérard, G. Habib, and E. Donal, "Distribution and Prognostic Significance of Left Ventricular Global Longitudinal Strain in Asymptomatic Significant Aortic Stenosis: An Individual Participant Data Meta-Analysis," *JACC. Cardiovascular imaging*, vol. 12, pp. 84–92, Jan. 2019.

[7] W. M. van Everdingen, J. Walmsley, M. J. Cramer, I. van Hagen, B. W. L. De Boeck, M. Meine, T. Delhaas, P. A. Doevendans, F. W. Prinzen, J. Lumens, and G. E. Leenders, "Echocardiographic Prediction of Cardiac Resynchronization Therapy Response Requires Analysis of Both Mechanical Dyssynchrony and Right Ventricular Function: A Combined Analysis of Patient Data and Computer Simulations," *Journal of the American Society of Echocardiography: Official Publication of the American Society of Echocardiography*, vol. 30, pp. 1012–1020.e2, Oct. 2017.

[8] N. Risum, B. Tayal, T. F. Hansen, N. E. Bruun, M. T. Jensen, T. K. Lauridsen, S. Saba, J. Kisslo, J. Gorcsan, and P. Sogaard, "Identification of Typical Left Bundle Branch Block Contraction by Strain Echocardiography Is Additive to Electrocardiography in Prediction of Long-Term Outcome After Cardiac Resynchronization Therapy," *Journal of the American College of Cardiology*, vol. 66, pp. 631–641, Aug. 2015.

[9] J. M. Aalen, E. W. Remme, C. K. Larsen, O. S. Andersen, M. Krogh, J. Duchenne, E. Hopp, S. Ross, A. S. Beela, E. Kongsgaard, J. Bergsland, H. H. Odland, H. Skulstad, A. Opdahl, J.-U. Voigt, and O. A. Smiseth, "Mechanism of Abnormal Septal Motion in Left Bundle Branch Block: Role of Left Ventricular Wall Interactions and Myocardial Scar," *JACC. Cardiovascular imaging*, vol. 12, pp. 2402–2413, Dec. 2019.

[10] S. A. Niederer, J. Lumens, and N. A. Trayanova, "Computational models in cardiology," *Nature Reviews. Cardiology*, vol. 16, pp. 100–111, Feb. 2019.

[11] M. Peirlinck, F. S. Costabal, J. Yao, J. M. Guccione, S. Tripathy, Y. Wang, D. Ozturk, P. Segars, T. M. Morrison, S. Levine, and E. Kuhl, "Precision medicine in human heart modeling," *Biomechanics and Modeling in Mechanobiology*, Feb. 2021.

[12] J.-i. Okada, T. Washio, M. Nakagawa, M. Watanabe, Y. Kadooka, T. Kariya, H. Yamashita, Y. Yamada, S.-i. Momomura, R. Nagai, T. Hisada, and S. Sugiura, "Multiscale, tailor-made heart simulation can predict the effect of cardiac resynchronization therapy," *Journal of Molecular and Cellular Cardiology*, vol. 108, pp. 17–23, July 2017.

[13] T. Mansi, I. Voigt, B. Georgescu, X. Zheng, E. A. Mengue, M. Hackl, R. I. Ionasec, T. Noack, J. Seeburger, and D. Comaniciu, "An integrated framework for finite-element modeling of mitral valve biomechanics from medical images: application to MitralClip intervention planning," *Medical Image Analysis*, vol. 16, pp. 1330–1346, Oct. 2012.

[14] F. Scardulla, V. Agnese, G. Romano, G. Di Gesaro, S. Sciacca, D. Bellavia, F. Clemenza, M. Pilato, and S. Pasta, "Modeling Right Ventricle Failure After Continuous Flow Left Ventricular Assist Device: A Biventricular Finite-Element and Lumped-Parameter Analysis," *Cardiovascular Engineering and Technology*, vol. 9, pp. 427–437, Sept. 2018.

[15] F. Cosentino, F. Scardulla, L. D'Acquisto, V. Agnese, G. Gentile, G. Raffa, D. Bellavia, M. Pilato, and S. Pasta, "Computational modeling of bicuspid aortopathy: Towards personalized risk strategies," *Journal of Molecular and Cellular Cardiology*, vol. 131, pp. 122–131, June 2019.

[16] A. Crozier, B. Blazevic, P. Lamata, G. Plank, M. Ginks, S. Duckett, M. Sohal, A. Shetty, C. A. Rinaldi, R. Razavi, N. P. Smith, and S. A. Niederer, "The relative role of patient physiology and device optimisation in cardiac resynchronisation therapy: A computational modelling study," *Journal of Molecular and Cellular Cardiology*, vol. 96, pp. 93–100, July 2016.

[17] M. Sermesant, R. Chabiniok, P. Chinchapatnam, T. Mansi, F. Billet, P. Moireau, J. M. Peyrat, K. Wong, J. Relan, K. Rhode, M. Ginks, P. Lambiase, H. Delingette, M. Sorine, C. A. Rinaldi, D. Chapelle, R. Razavi, and N. Ayache, "Patient-specific electromechanical models of the heart for the prediction of pacing acute effects in

CRT: A preliminary clinical validation," *Medical Image Analysis*, vol. 16, pp. 201–215, Jan. 2012.

[18] S. A. Niederer, G. Plank, P. Chinchapatnam, M. Ginks, P. Lamata, K. S. Rhode, C. A. Rinaldi, R. Razavi, and N. P. Smith, "Length-dependent tension in the failing heart and the efficacy of cardiac resynchronization therapy," *Cardiovascular Research*, vol. 89, pp. 336–343, Feb. 2011.

[19] A. Krishnamurthy, C. T. Villongco, J. Chuang, L. R. Frank, V. Nigam, E. Belezzuoli, P. Stark, D. E. Krummen, S. Narayan, J. H. Omens, A. D. McCulloch, and R. C. P. Kerckhoffs, "Patient-specific models of cardiac biomechanics," *Journal of Computational Physics*, vol. 244, pp. 4–21, July 2013.

[20] V. Le Rolle, A. I. Hernández, P.-Y. Richard, E. Donal, and G. Carrault, "Model-based analysis of myocardial strain data acquired by tissue Doppler imaging," *Artificial Intelligence in Medicine*, vol. 44, pp. 201–219, Nov. 2008.

[21] M. L. Neal and R. Kerckhoffs, "Current progress in patient-specific modeling," *Briefings in Bioinformatics*, vol. 11, pp. 111–126, Jan. 2010.

[22] A. I. Hassaballah, M. A. Hassan, A. N. Mardi, and M. Hamdi, "An Inverse Finite Element Method for Determining the Tissue Compressibility of Human Left Ventricular Wall during the Cardiac Cycle," *PLOS ONE*, vol. 8, p. e82703, Dec. 2013. Publisher: Public Library of Science.

[23] V. Le Rolle, G. Carrault, P.-Y. Richard, P. Pibarot, L.-G. Durand, and A. I. Hernández, "A Tissue-Level Electromechanical Model of the Left Ventricle: Application to the Analysis of Intraventricular Pressure," *Acta Biotheoretica*, vol. 57, p. 457, Oct. 2009.

[24] A. I. Hernández, V. Le Rolle, A. Defontaine, and G. Carrault, "A multiformalism and multiresolution modelling environment: application to the cardiovascular system and its regulation," *Philosophical Transactions of the Royal Society A: Mathematical, Physical and Engineering Sciences*, vol. 367, pp. 4923–4940, Dec. 2009. Publisher: Royal Society.

[25] A. I. Hernández, V. Le Rolle, D. Ojeda, P. Baconnier, J. Fontecave-Jallon, F. Guillaud, T. Grosse, R. G. Moss, P. Hannaert, and S. R. Thomas, "Integration of detailed modules in a core model of body fluid homeostasis and blood pressure regulation," *Progress in Biophysics and Molecular Biology*, vol. 107, pp. 169–182, Oct. 2011.

[26] V. Le Rolle, D. Ojeda, and A. I. Hernández, "Embedding a cardiac pulsatile model into an integrated model of the cardiovascular regulation for heart failure followup," *IEEE transactions on bio-medical engineering*, vol. 58, pp. 2982–2986, Oct. 2011.

[27] D. Ojeda, V. L. Rolle, H. M. Romero-Ugalde, C. Gallet, J.-L. Bonnet, C. Henry, A. Bel, P. Mabo, G. Carrault, and A. I. Hernández, "Sensitivity Analysis

of Vagus Nerve Stimulation Parameters on Acute Cardiac Autonomic Responses: Chronotropic, Inotropic and Dromotropic Effects," *PLOS ONE*, vol. 11, p. e0163734, Sept. 2016. Publisher: Public Library of Science.

[28] D. Ojeda, V. Le Rolle, M. Harmouche, A. Drochon, H. Corbineau, J.-P. Verhoye, and A. I. Hernández, "Sensitivity analysis and parameter estimation of a coronary circulation model for triple-vessel disease," *IEEE transactions on bio-medical engineering*, vol. 61, pp. 1208–1219, Apr. 2014.

[29] M. Calvo, V. Le Rolle, D. Romero, N. Béhar, P. Gomis, P. Mabo, and A. I. Hernández, "Model-based analysis of the autonomic response to head-up tilt testing in Brugada syndrome," *Computers in Biology and Medicine*, vol. 103, pp. 82–92, Dec. 2018.

[30] V. Le Rolle, A. Beuchee, J.-P. Praud, N. Samson, P. Pladys, and A. I. Hernández, "Recursive identification of an arterial baroreflex model for the evaluation of cardiovascular autonomic modulation," *Computers in Biology and Medicine*, vol. 66, pp. 287–294, Nov. 2015.

[31] M. Calvo, V. Le Rolle, D. Romero, N. Béhar, P. Gomis, P. Mabo, and A. I. Hernández, "Recursive model identification for the analysis of the autonomic response to exercise testing in Brugada syndrome," *Artificial Intelligence in Medicine*, vol. 97, pp. 98–104, June 2019.

[32] H. M. R. Ugalde, D. Ojeda, V. Le Rolle, D. Andreu, D. Guiraud, J.-L. Bonnet, C. Henry, N. Karam, A. Hagege, P. Mabo, G. Carrault, and A. I. Hernandez, "Model-Based Design and Experimental Validation of Control Modules for Neuromodulation Devices," *IEEE transactions on bio-medical engineering*, vol. 63, pp. 1551–1558, July 2016.

[33] V. Le Rolle, N. Samson, J.-P. Praud, and A. I. Hernández, "Mathematical modeling of respiratory system mechanics in the newborn lamb," *Acta Biotheoretica*, vol. 61, pp. 91–107, Mar. 2013.

[34] S. Al-Omar, V. Le Rolle, P. Pladys, N. Samson, A. Hernandez, G. Carrault, and J.-P. Praud, "Influence of nasal CPAP on cardiorespiratory control in healthy neonate," *Journal of Applied Physiology (Bethesda, Md.: 1985)*, vol. 127, pp. 1370–1385, Nov. 2019.

[35] A. Bernard, E. Donal, C. Leclercq, F. Schnell, M. Fournet, A. Reynaud, C. Thebault, P. Mabo, J. C. Daubert, and A. Hernandez, "Impact of Cardiac Resynchronization Therapy on Left Ventricular Mechanics: Understanding the Response through a New Quantitative Approach Based on Longitudinal Strain Integrals," *Journal of the American Society of Echocardiography*, vol. 28, pp. 700–708, June 2015.

[36] A. Hubert, A. Gallard, V. L. Rolle, O. A. Smiseth, C. Leclercq, J.-U. Voigt, E. Galli, V. Galand, A. Hernandez, and E. Donal, "Left ventricular strain for predicting the

response to cardiac resynchronization therapy: two methods for one question," *European Heart Journal - Cardiovascular Imaging*, Jan. 2021.

[37] A. Gallard, A. Bidaut, A. Hubert, E. Sade, S. Marechaux, M. Sitges, J. Separovic-Hanzevacki, V. Le Rolle, E. Galli, A. Hernandez, and E. Donal, "Characterization of Responder Profiles for Cardiac Resynchronization Therapy through Unsupervised Clustering of Clinical and Strain Data," *Journal of the American Society of Echocardiography*, Jan. 2021.

[38] A. Gallard, A. Hubert, O. Smiseth, J.-U. Voigt, V. Le Rolle, C. Leclercq, A. Bidaut, E. Galli, E. Donal, and A. I. Hernandez, "Prediction of response to cardiac resynchronization therapy using a multi-feature learning method," *The International Journal of Cardiovascular Imaging*, vol. 37, pp. 989–998, Mar. 2021.

[39] J. Walmsley, T. Arts, N. Derval, P. Bordachar, H. Cochet, S. Ploux, F. W. Prinzen, T. Delhaas, and J. Lumens, "Fast Simulation of Mechanical Heterogeneity in the Electrically Asynchronous Heart Using the MultiPatch Module," *PLoS computational biology*, vol. 11, p. e1004284, July 2015.

[40] B. Kirn, J. Walmsley, and J. Lumens, "Uniqueness of local myocardial strain patterns with respect to activation time and contractility of the failing heart: a computational study," *Biomedical Engineering Online*, vol. 17, p. 182, Dec. 2018.

[41] L. J. Dupuis, T. Arts, F. W. Prinzen, T. Delhaas, and J. Lumens, "Linking cross-bridge cycling kinetics to response to cardiac resynchronization therapy: a multiscale modelling study," *EP Europace*, vol. 20, pp. iii87–iii93, Nov. 2018.

[42] K. Russell, M. Eriksen, L. Aaberge, N. Wilhelmsen, H. Skulstad, O. Gjesdal, T. Edvardsen, and O. A. Smiseth, "Assessment of wasted myocardial work: a novel method to quantify energy loss due to uncoordinated left ventricular contractions," *American Journal of Physiology. Heart and Circulatory Physiology*, vol. 305, pp. H996–1003, Oct. 2013.

[43] K. Russell, M. Eriksen, L. Aaberge, N. Wilhelmsen, H. Skulstad, E. W. Remme, K. H. Haugaa, A. Opdahl, J. G. Fjeld, O. Gjesdal, T. Edvardsen, and O. A. Smiseth, "A novel clinical method for quantification of regional left ventricular pressure-strain loop area: a non-invasive index of myocardial work," *European Heart Journal*, vol. 33, pp. 724–733, Mar. 2012.

[44] C. Daubert, S. Cazeau, P. Ritter, and C. Leclercq, "Past, present and future of cardiac resynchronization," *Archives of Cardiovascular Diseases*, vol. 105, pp. 291–299, May 2012.

[45] B. W. L. De Boeck, A. J. Teske, M. Meine, G. E. Leenders, M. J. Cramer, F. W. Prinzen, and P. A. Doevendans, "Septal rebound stretch reflects the functional substrate to cardiac resynchronization therapy and predicts volumetric and neurohormonal response," *European Journal of Heart Failure*, vol. 11, pp. 863–871, Sept. 2009.

[46] I. Stankovic, C. Prinz, A. Ciarka, A. M. Daraban, M. Kotrc, M. Aarones, M. Szulik, S. Winter, A. Belmans, A. N. Neskovic, T. Kukulski, S. Aakhus, R. Willems, W. Fehske, M. Penicka, L. Faber, and J.-U. Voigt, "Relationship of visually assessed apical rocking and septal flash to response and long-term survival following cardiac resynchronization therapy (PREDICT-CRT)," *European Heart Journal Cardiovascular Imaging*, vol. 17, pp. 262–269, Mar. 2016.

1

EVALUATION OF THE CARDIAC FUNCTION

The evaluation of the cardiac function is crucial to estimate the heart's ability to satisfy all the metabolic requirements that an organism demands. The volume of blood entering the heart, the volume of blood ejected by the heart, the vascular resistance, and the myocardial contractility are some of the factors that affect the cardiac function. Pathologies as restrictive cardiomyopathies and valvular insufficiency could affect the aforementioned factors, producing a deficient cardiac function.

Understanding the physiology of the cardiovascular system, as well as the different intertwined mechanisms involved to meet the demands of the body, is of utmost importance to perform an adequate evaluation of cardiac function. Therefore, in this chapter, a brief and general description of the physiology and anatomy of the cardiovascular system will be presented, highlighting the electrical, mechanical and hydraulic mechanisms underlying the cardiovascular function. In addition, the physiology of two particular conditions, the left bundle branch block and the aortic stenosis, will be detailed. These cardiac pathologies significantly affect cardiac function, hence our interest to study and understand their underlying physiology. Finally, echocardiography, a tool providing reliable and accurate solutions for cardiac function evaluation, will be briefly presented, showing the advantages that this technology proposes.

1.1 The cardiovascular system

The cardiovascular system (CVS), also called circulatory system or vascular system is a transportation, protection and regulation system of the body. This system *i)* protect the body from diseases, *ii)* maintain a stable temperature and pH, and *iii)* transport oxygen, nutrients, hormones and cellular waste products throughout the body [1].

The CVS consists of three major components: the blood, the blood vessels and the heart.

1.1.1 Circulatory physiology

There are two primary circulatory loops in the human body (Fig. 1.1), which work together in a closed circulatory system: *i)* the pulmonary circulation loop and *ii)* the systemic circulation loop. In pulmonary circulation, the pulmonary artery transports deoxygenated blood from the right side of the heart to the lungs, where the blood is oxygenated. Then, pulmonary veins brings this oxygen-rich blood back to the heart by the left side. In systemic circulation, the aorta receives the oxygenated blood from the left side of the heart and transport it throughout the body. Systemic veins remove wastes from all the tissues of the body and bring oxygen-poor blood back to the heart by the right side. As previously mentioned, the circulatory loops form a closed system where the blood never leaves the blood vessels networks.

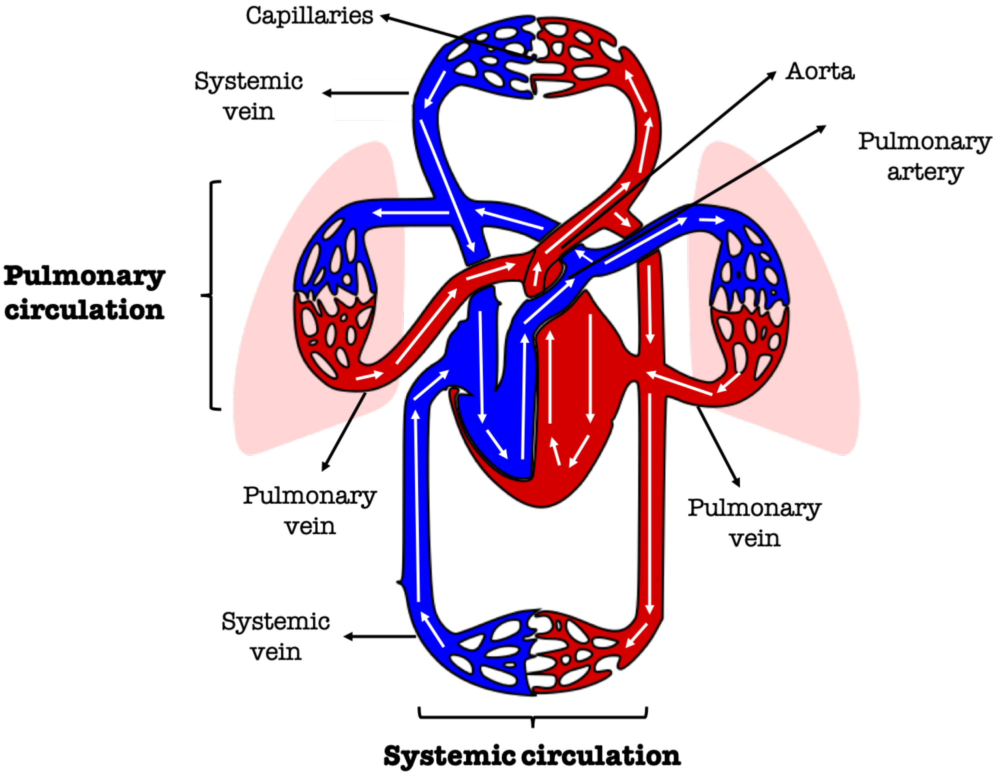

Figure 1.1: Circulatory system. The heart, the pulmonary circulation loop and the systemic circulation loop work together in a closed circulatory system. *"Blood flow from the heart" by OpenStax is licensed under CC BY 4.0.*

Blood is a connective tissue composed of: *i)* plasma, a liquid that carries cells and proteins; *ii)* red blood cells that transport oxygen to the body tissues; *iii)* white blood cells that protect the body from external threats; and *iv)* platelets that produce a blood clot as a response for bleeding. Blood is responsible for the transport of substances, immunological functions, heat distribution, and maintenance of homeostasis in the human body. Blood is transported trough the hole body by the blood vessels, starting in the heart, with the arterial vessels [2].

Arteries are subdivided into arterioles, which further connect with the smallest blood vessel in the body: the capillaries. As the arteries divide their elasticity decrease, increasing their compliance. Arterial walls contract or expand to regulate the flow of blood, affecting the blood pressure. At the capillaries, gas exchange occurs, the oxygen and nutrients are delivered to the cells and carbon dioxide with other wastes are collected by the venules (small venous blood vessels). Blood flows back from the body to the heart through the veins. Due to the low blood pressures that veins and venules are subjected, venous blood vessels walls are much thinner, less elastic, and less muscular than arterial blood vessels walls.

1.1.2 Anatomy of the heart

The heart is a muscular organ whose function is to pumps out the blood to the whole body in order to move nutrients and remove the metabolic wastes.

The heart (Fig.1.2) has four hollow chambers: two upper chambers known as left and right atrium and two lower chambers known as left and right ventricle. The right atrium (RA) and right ventricle (RV) support the pulmonary circulation loop. Likewise, the left atrium (LA) and left ventricle (LV) assist the systemic circulation loop. The atria receive the blood that returns to the heart and then blood flows to the ventricles to be pumped out of the heart. A wall known as septum separates the left and right sides of the heart.

Blood flows unidirectionally through the heart chambers due to the cardiac valves [2]. The heart has 4 valves: *i)* the mitral valve, located between the LA and the LV; *ii)* the tricuspid valve, located between the RA and the RV; *iii)* the aortic valve, located between the LV and the aorta; and *iv)* the pulmonary valve, located between the RV and the pulmonary artery [3]. Valves situated between atria and ventricles are known as atrioventricular valves and those located between the ventricles and the arteries are known as semilunar valves. Each valve has flaps (cusps or leaflets) that open and close (causing the sound of a heartbeat) to allow blood to flow in one direction. Opening and closing depends on the differential blood pressure on each side of the cardiac valve. Cardiac valve opens to minimize any obstruction and allows blood to flow freely in the right direction. In addition, the valve closes completely to not allowing the backward flow of blood.

The heart is made up of three layers of tissue: *i)* the innermost layer called the endocardium, that consists in a thin membrane located inside of the heart chambers and forms the surfaces of the valves; *ii)* the myocardium, the middle layer, is the muscular wall of the heart; and *iii)* the pericardium that consists in a tough and fibrous double layer that covers the whole heart [3].

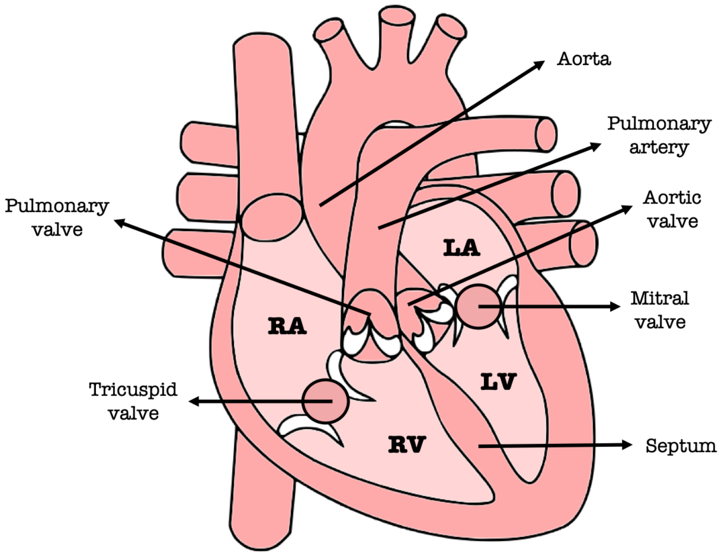

Figure 1.2: Heart anatomy: heart chambers and cardiac valves. LA: left atria. RA: right atria. LV: left ventricle. RV: right ventricle. *"Diagram of the human heart (cropped)" by Wikipedia is licensed under CC BY-SA: Attribution-ShareAlike.*

1.1.3 Cardiac electrical system

The heart, as a muscular organ, must contract to ensure the flow of blood through the blood vessels. The heart has its own independent electrical conduction system that provides the energy necessary for cardiac contraction. Contrary to the skeletal muscle, the cardiac muscle does not require nervous stimulation to cause depolarization of muscle fibers, the heart itself is able to send electrical signals to contract the myocardium [1].

The heart is composed of two kinds of cells: the cardiomyocytes (specialized muscle cells) and the cardiac pacemaker cells. The cardiac myocytes form the atria and the ventricles, and the pacemaker cells have the ability to stimulate the heart.

The automaticity of the heart's electrical system is due to the three clumps of cardiac pacemaker cells: *i)* the sinoatrial (SA) or sinus node; *ii)* the atrioventricular (AV) node; and *iii)* the bundle of His and Purkinje fibers.

The contraction of the cardiac cells is initiated by electrical impulses known as action potentials, which exhibit different forms depending on the type of cell. A type of cell junction, known as GAP junctions, connect adjacent cells ensuring electrical coupling and ions transmission between them. Thus, an action potential in a cell triggers another action potential in its neighbor. Thanks to these cellular bridges all the cardiac cells are able to act in synchrony as a single coordinated unit.

1.1.3.1 Action potential in cardiomyocytes

As long as the cells of the body are not subjected to any type of stimulation, they maintain a resting membrane potential that is characterized by a negative charge inside the cell relative to the outside [4]. The unequal distribution of charges generated in the intra and extracellular space is due to the selective permeability of the cell membrane that allows positively charged inorganic ions diffusion to the extracellular space and leaves negatively charged molecules trapped inside the cell.

The resting potential is measured by the difference in the voltage between the inside and outside of the cell. In a cardiac cell, the resting membrane potential is about -90 mV (the sign indicates the charge of the inner surface of the cell).

The entrance of positive charges into the cell by an appropriate stimulus is called depolarization. The cardiac cell usually reaches values of +50 mV during depolarization. The recovery to the resting membrane potential is called repolarization. The flow of charged ions through the cell membrane produces a current and, consequently, an alteration of the cell membrane potential. This change in membrane potential is known as action potential. The cardiac action potential constitutes the electrical impulse that allow the pumping of the heart.

One of the differences between the action potential of a skeletal muscle cell and a cardiac myocyte is the duration. The cardiac action potential lasts approximately 200 milliseconds, which is up to 15 times longer than the duration of the skeletal muscle action potential. This is due to the different types of ion channels that skeletal and cardiac cells possess.

The action potential in cardiomyocytes consists of 5 phases (Fig. 1.3):

- **Phase 4:** The cardiomyocyte is in the resting membrane potential (-90 mV) until a stimulus is generated.
- **Phase 0** or depolarization: Occurs only when cardiac cells are stimulated. The membrane potential goes from -90 mV to +50 mV. The membrane voltage must reaches a minimal value (threshold) of -70 mV to produce an action potential. The fast sodium (Na^+) channels open creating a rapid Na^+ influx and a sharp rise in voltage.
- **Phase 1:** L-type or slow. The calcium (Ca^{2+}) channels open causing a slow but steady influx of Ca^{2+}. The Na^+ channels close quickly and the potassium (K^+) channels open causing a little efflux of K^+. This result in a small decrease in membrane potential known as early repolarization phase.
- **Phase 2:** The calcium channels remain open and the K^+ efflux is eventually balanced by the Ca^{2+} influx. The output and input of positive charges from the intracellular compartment result in a net charge flow approaching to zero. This

keeps the membrane potential relatively stable for about 200 milliseconds resulting in the plateau phase, characteristic of cardiac action potentials. This phase ends when the calcium channels are closed.

- **Phase 3** or repolarization: K^+ efflux predominates and causes the membrane potential to rapidly returns to its resting value.

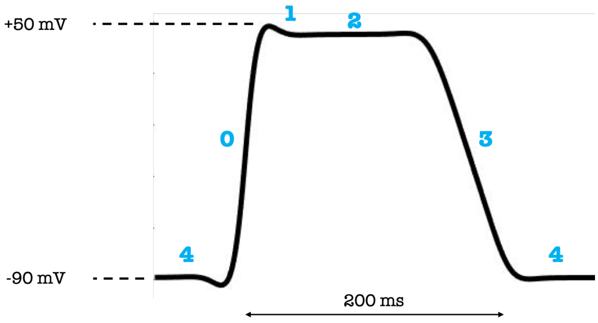

Figure 1.3: Action potential phases in cardiac myocytes. Phase 0: depolarization. Phase 1: early repolarization phase. Phase 2: plateau phase. Phase 3: repolarization. Phase 4: resting membrane potential. *"The action potential of a ventricular myocyte" by Wikipedia is licensed under CC BY-SA: Attribution-ShareAlike.*

The absolute refractory period, which is the period that regardless of the power of the stimulus no new action potential will occur, is much longer in cardiac muscle. It ranges from phase 0 to mid-phase 3. This is essential in preventing summation and tetanus. The relative refractory period comprises the last half of phase 3. During this period, in which the cell has not yet been completely repolarized, a stronger stimulus than normal can lead to an action potential.

1.1.3.2 Action potential in pacemaker cells

The action potential in pacemaker cells consists of 3 phases (Fig. 1.4):

- **Pacemaker potential phase (Phase 4):** Funny channels, which are only present in pacemaker cells, open when membrane potential becomes lower than -40mV and allow slow influx of Na^+. The voltage of the cell starts at about -60mV and spontaneously moves upward until it reaches the threshold of -40mV.
- **Rising phase (Phase 0):** At the threshold the calcium channels are enable to open creating a rapid influx of Ca^{2+}.
- **Falling phase (Phase 3):** At the peak of depolarization (around +10mV), K^+ channels open and Ca^{2+} channels close. Potassium ions leave the cell and the voltage returns to -60mV. At this point, K^+ channels close and the original ionic gradient is restored to starts again the cycle.

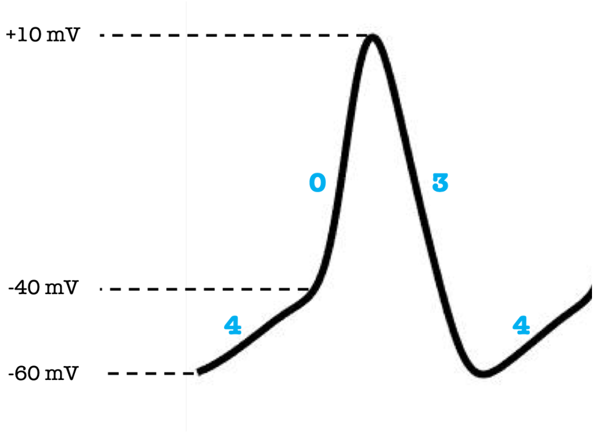

Figure 1.4: Action potential phases in pacemaker cells. Phase 0: rising phase. Phase 3: falling phase. Phase 4: Pacemaker potential phase. *"Pacemaker potential" by Wikipedia is licensed under CC BY-SA: Attribution-ShareAlike.*

It is important to remark that although the phases of the two different types of cardiac cells are intended to be matched, pacemaker cells do not have a really resting membrane potential [4]. There is not a phase when this type of cells are precisely resting, the action potential is always rising or falling.

1.1.3.3 Electrical conduction system

The heart's electrical conduction system consists of a sequence of electrical signals transmission that causes myocardial contraction (Fig. 1.5).

The SA node, which is located in the right atrium of the heart, starts the sequence by generating an action potential. This first electrical stimulus contracts the two upper chambers of the heart (atria) passing blood to the ventricles. Then, the electrical impulse travels from the SA node to the AV node, which is located on the back wall of the heart between the right atria and the right ventricle. Thanks to the AV node, the electrical signal reaches the ventricles, the major pumping chambers of the heart. The electrical impulse continues to the Bundle of His, which is located in the heart's septum. The Bundle of His is divided into right and left conduction pathways in order to provide electrical stimulation to both ventricles. The electrical impulse then travels to the Purkinje fibers that send out the signal to contract the ventricles muscles allowing blood to pump into the arteries.

Normally, the heart contracts about 60 to 100 times in a minute. Each contraction represents one heartbeat.

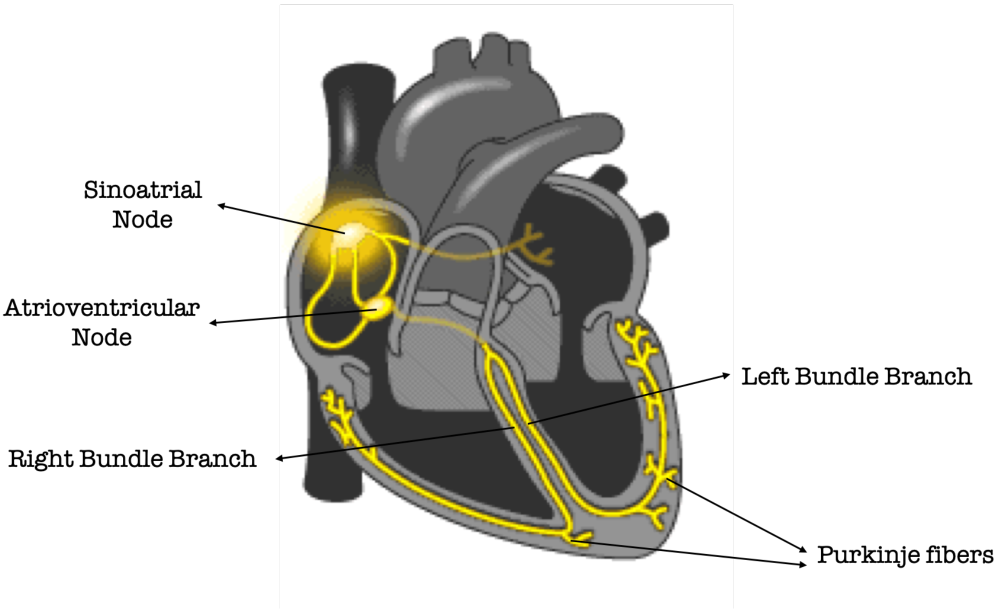

Figure 1.5: Electrical conduction system of the heart. A sequence of electrical signals transmission, starting at the sinoatrial node and finishing in the Purkinje fibers. *This Photo by Unknown Author is licensed under CC BY-NC.*

1.1.3.4 Electrocardiogram

Changes in the electrical activity of the heart can be measured using surface electrodes on the thorax. These measurements can be represented by a voltage versus time graph, known as electrocardiogram (ECG). The ECG is generally used to detect irregularities or any cardiac problem.

To perform a standard 12-lead ECG, 10 electrodes divided into two groups are placed: the peripheral electrodes and the precordial electrodes [1]. There are four peripheral electrodes and they are placed on the patient's extremities. The other six electrodes are placed in the precordial region as follows (Fig. 1.6):

- **V1:** Fourth intercostal space, at the right border of the sternum.
- **V2:** Fourth intercostal space, at the left border of the sternum.
- **V3:** Midway between V2 and V4.
- **V4:** Fifth intercostal space, at the mid-clavicular line.
- **V5:** The same horizontal line as V4, but at the anterior axillary line.
- **V6:** The same horizontal line as V4 and V5, but at the mid-axillary line.

The heart's electrical conduction system is translated by the ECG through a sequence of waves superimposed on a zero potential line, called the isoelectric line [5].

There are three main waves in an ECG (Fig. 1.7):

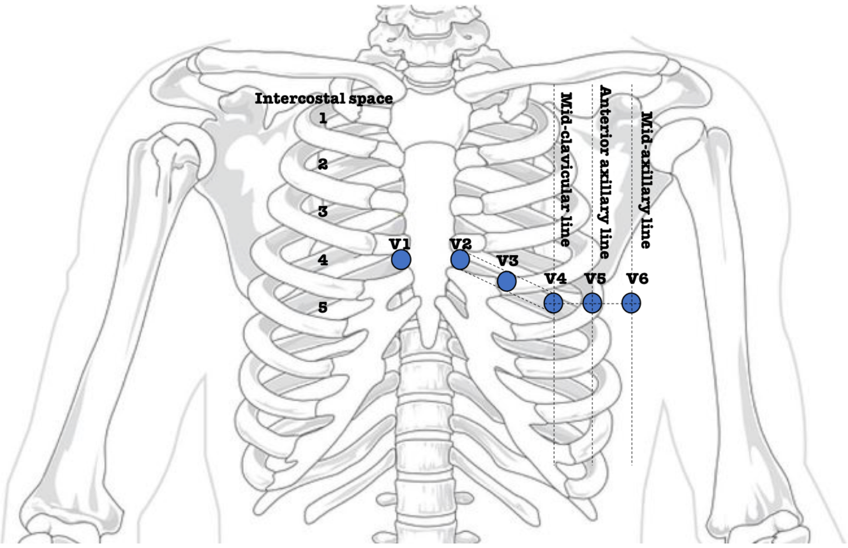

Figure 1.6: Precordial electrodes placement on the thorax to perform a standard 12-lead ECG. *This Photo by Unknown Author is licensed under CC BY-NC.*

- The **P-wave**, which is associated with the atria depolarization. The atria repolarization is usually not visible in the ECG because of its low amplitude.
- The **QRS complex**, which represents the depolarization of the ventricles. The amplitude of the QRS complex is significantly larger than the amplitude of the P-wave since the ventricles have more depolarizing cells compared with the atria. Not every QRS complex will contain Q, R, and S waves.
- The **T-wave**, which represents the ventricles repolarization.

Sometimes is possible to observe a small wave between T-wave and P-wave, called U-wave, but the biological explanation for a U wave is unknown.

In addition, the following intervals can also be measured in the ECG (Fig. 1.7):

- **RR interval:** separates the vertices of two consecutive R waves which define the instantaneous heart rate (HR).
- **PR interval:** is measured between the start of the P-wave and the beginning of the QRS complex. This interval represents the time that the electrical impulse takes to travel from the SA node through the AV node.
- **QT interval:** represents the time between the start of the QRS complex and the end of the T-wave. It is an indicator of the length of the ventricular depolarization and repolarization phases.

1.1.4 Mechanical properties of the heart

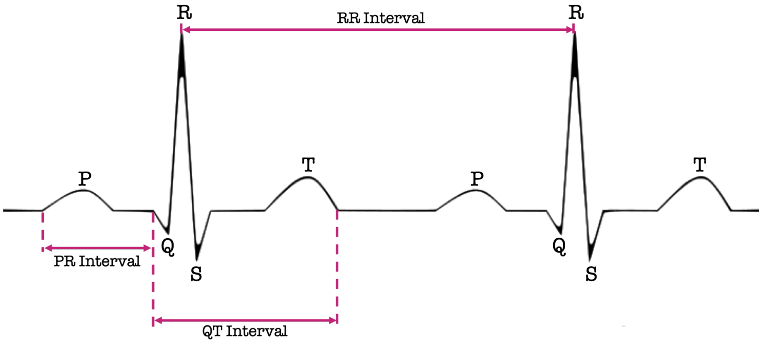

Figure 1.7: Main intervals and waves measured in a normal ECG waveform. *"ECG of a heart in normal sinus rhythm" by Wikipedia is licensed under CC BY-SA: Attribution-ShareAlike.*

1.1.4.1 Cardiac muscle anatomy

Cardiac muscle or myocardium is made up of striated uninucleated cells. Cardiac muscle cells or cardiomyocytes are composed of one nucleus, a cytoplasm called sarcoplasm and a plasma membrane called sarcolemma (Fig. 1.8).

The cardiomyocytes are composed of cylindrically shaped structures called myofibrils that contains several sarcomeres connected one to another. The sarcomeres are contractile units that consist of alternating thick (myosin) and thin (actin) protein filaments. Each sarcomere is composed of dark bands (A), where myosin is found, and light bands (I), where actin is found. Z disk delimits the ends of each sarcomere and the middle area of the sarcomere is known as the M line. The thin actin bands are attached to the Z-disks, and the thick myosin bands are located at the middle of the sarcomere.

Inside the cell, surrounding the myofibrils, there is also the sarcoplasmic reticulum (SR) that contains a high concentration of calcium needed for the proper muscle contraction. Relatively large mitochondria are also presented in the cell to provide the energy used for force generation.

In the sarcolemma, we can find deep invaginations called T-tubules that begin in the plasma membrane and extend throughout the cell. They are basically responsible for allowing the action potential to propagate quickly and uniformly throughout the entire cardiac muscle cell.

Cardiomyocytes are connected by intercalated discs, which contains two types of junction (Fig. 1.9):

- **GAP junction:** ensure a rapid communication between adjacent cardiac muscle cells, allowing a uniform propagation of the action potential and the movement of ions between them.
- **Desmosomes:** intracellular junction that holds two adjacent cardiac muscle cells

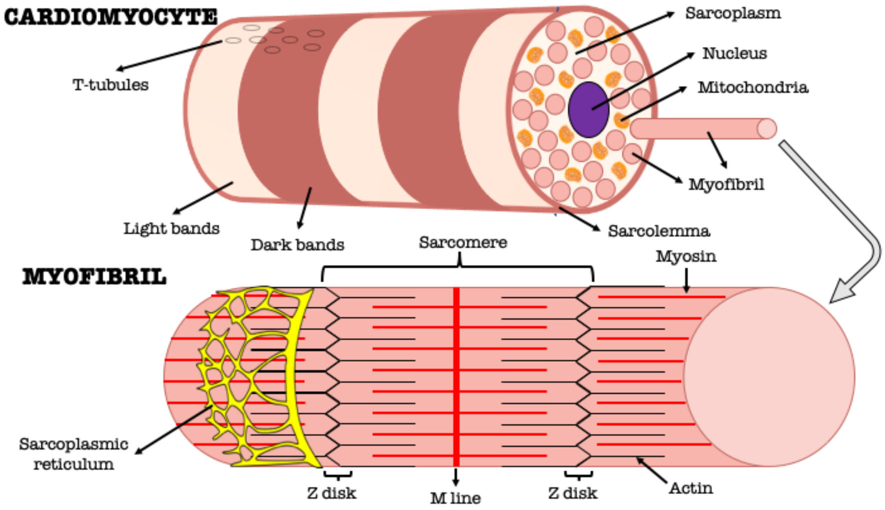

Figure 1.8: Composition of cardiac muscle cells or cardiomyocytes *(top)*. Myofibrils composition *(bottom)*

and allows them to stay together during a contraction.

1.1.4.2 Cardiac contraction

The action potential is responsible for triggering a cardiac contraction that extends through the cell and passes to the sarcolemma surface by a GAP junction. There, the action potential produce voltage-gated calcium channels activation, allowing extracellular calcium to pass inside the cardiac cell. The free calcium present intracellularly then activates the voltage-gated calcium channels of the sarcoplasmic reticulum, in a process known as “calcium-induced calcium release", diffusing calcium from SR into the sarcoplasm. The resulting free calcium in the sarcoplasm is led to the sarcomeres (Fig. 1.10).

When a contraction occurs, the myosin head attaches to a binding site on the actin, forming a cross-bridge and exerting a force to move the actin along the myosin [6]. This action is known as the sliding filament mechanism of muscle contraction. It is important to highlight that the actin is associated with regulatory proteins called troponin and tropomyosin, and that in the base configuration tropomyosin blocks the cross-bridge binding sites on actin. However, troponin, which is attached to tropomyosin, contains binding sites for calcium. Therefore, the free calcium present in sarcomeres interacts with troponin and causes tropomyosin to move, exposing the actin binding sites and allowing the muscle contraction.

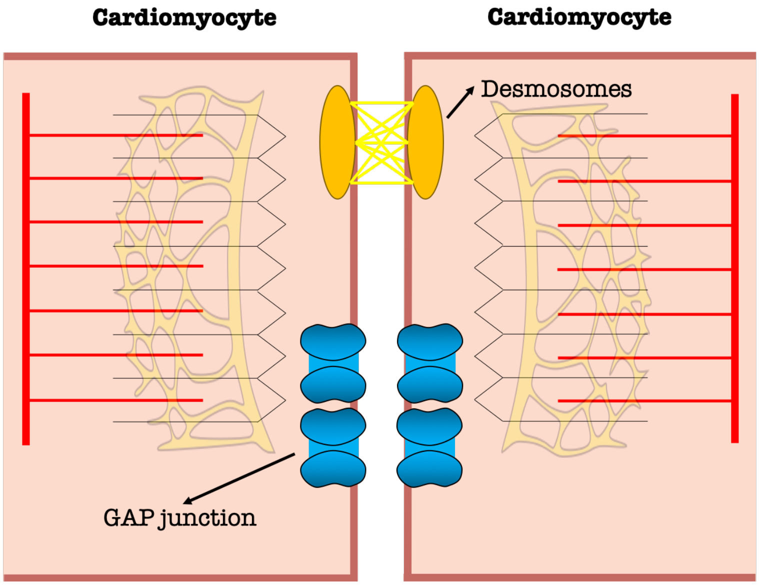

Figure 1.9: The junctions connect the cells and enable electrical coupling and ions transmission between adjacent cardiomyocytes. Thanks to these cellular bridges all the cardiac cells are able to act in synchrony as a single coordinated unit.

1.1.5 Cardiac cycle

The cardiac cycle refers to the sequence of events (electrics, mechanics, hydraulics, . . .) that occurs in repeat with each heartbeat. The cardiac cycle is divided in five phases (Fig. 1.11):

1. Active ventricular filling (atrial systole)
2. Isovolumic contraction
3. Ejection
4. Isovolumic relaxation
5. Passive ventricular filling

The isovolumic contraction and ejection phases correspond to the systole or contraction of ventricles and the other three phases to the diastole or relaxation of ventricles.

At the beginning of the cardiac cycle, all the heart cavities are relaxed, the AV valves are open and the semilunar valves are closed. The cycle is initiated in the atrial systole phase with the firing of the SA node that stimulates and produce atria depolarization. As mentioned before, the atrial depolarization is represented by the P-wave in the ECG. Atrial contraction starts shortly after the P-wave begins and causes an increase in the atria pressure ejecting the blood into the ventricles [7].

When atrial contraction is completed, atrial pressure becomes lower than ventricular pressure, reversing the pressure gradient across the AV valves and closing them.

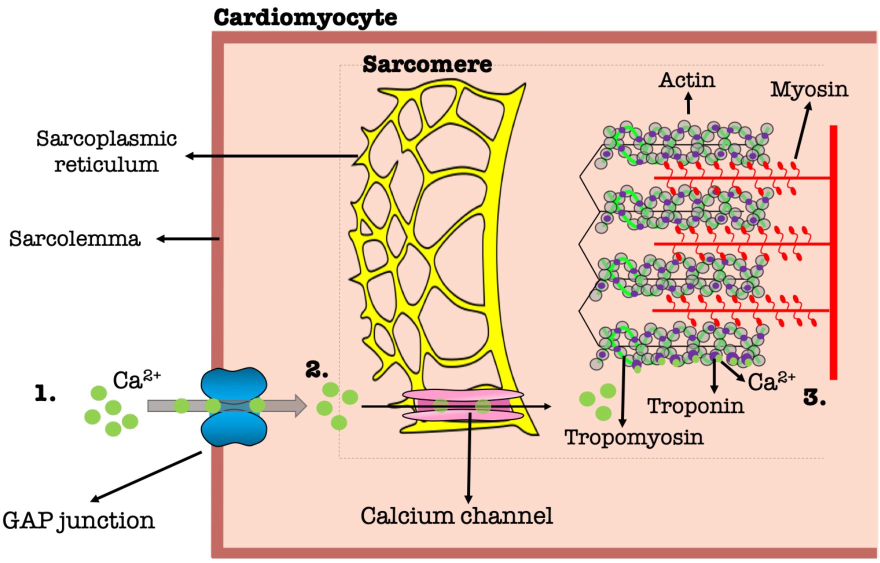

Figure 1.10: Cardiac contraction process: *1)* extracellular Ca^{+2} pass inside the cardiac cell; *2)* the free Ca^{+2} present intracellularly activates the Ca^{+2} channels of the sarcoplasmic reticulum; *3)* the resulting free Ca^{+2} in the sarcoplasm is led to the sarcomeres allowing a muscle contraction.

AV valves closing produces the first heart sound, S1, and indicates the beginning of systole.

The cycle continues with the isovolumic contraction phase. The wave of depolarization reaches the ventricles, represented by the QRS complex in the ECG. In the halfway of the QRS complex, the ventricles begin to contract, causing an increase in ventricular pressure. This phase is referred as isovolumetric contraction since all the heart valves are closed and no blood is ejected from the ventricles, leaving the ventricular volume unchanged.

Then the ejection phase is presented in the cardiac cycle. Ventricular pressure exceeds the pressure within the aorta and the pulmonary artery, causing the opening of the semilunar valves. Consequently, blood is rapidly ejected from the ventricles, and the ventricular pressure begins to decrease while the blood vessels pressure increases. This ends up equalizing both pressures, which causes that part of the blood does not pass by pressure gradient towards the aorta and pulmonary trunk. The volume of blood that is retained in the heart at the end of the ejection is called residual volume, end-systolic volume or final stroke volume; while the volume of blood ejected is called the stroke volume or beat volume.

Subsequently, the ventricles begin to repolarize, reflected by the T-wave in the ECG. Ventricular pressure starts to decrease until it becomes lower than aortic and pulmonary pressures. This causes the semilunar valves closure, marking the end of systole and the beginning of diastole. Semilunar valves closure produces the second

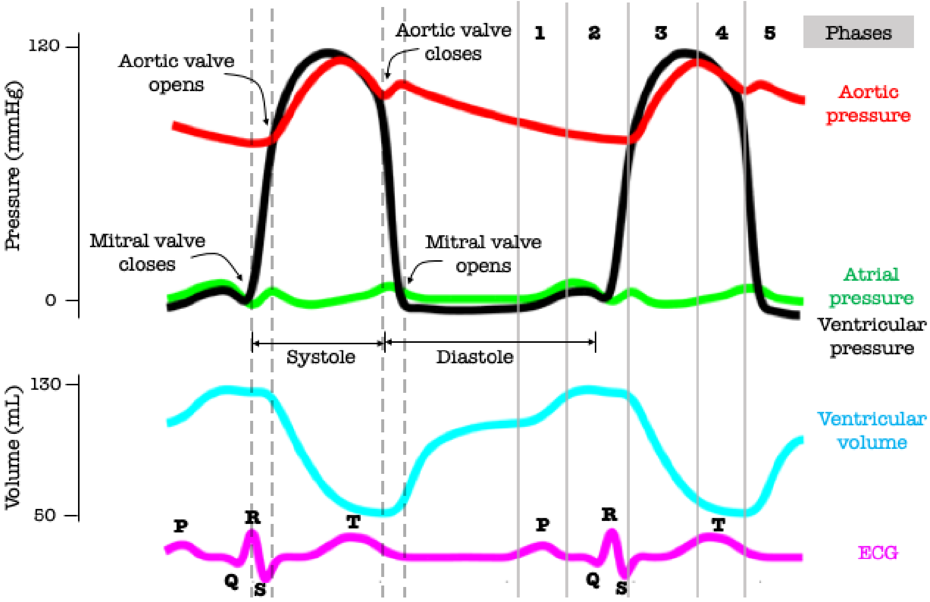

Figure 1.11: Cardiac cycle representation indicating the five phases and the heart valves closing and opening. The main pressure signals of the left side of the heart, the left ventricular volume curve and the ECG waveform in a normal case are illustrated: aortic pressure *(red)*, LV pressure *(black)*, LA pressure *(green)*, LV volume *(blue)* and ECG *(magenta)*. *"A Wiggers diagram" by Wikipedia is licensed under CC BY-SA: Attribution-ShareAlike.*

heart sound, S2.

Diastole begins with the isovolumic relaxation phase, where all valves are closed. Ventricular pressure drops rapidly but the volume remain unchanged. Meanwhile, the atria are being filled with blood and the atrial pressure is slowly starting to rise.

Finally, the atrial pressure becomes higher than ventricular pressure, causing the opening of AV valves and the beginning of the passive ventricular filling phase. A new atrial contraction originated in the SA node will end this phase and initiate the atrial systole of the next cycle.

1.2 Pathological states

1.2.1 Left bundle branch block

Left bundle branch block (LBBB) is a disorder of the heart's electrical system in which electrical impulses are partially or completely blocked in the left branch of the His bundle before reaching the left ventricle (Fig. 1.12). The electrical signal should spread from the right bundle branch through the heart muscle and slowly activate the LV. When this happens, the heartbeat (contraction) is slower than normal and the left ventricle contracts later than the right ventricle. As a result, a dyssynchronous myocardial contraction is generated and the ventricles may eject blood less efficiently [8].

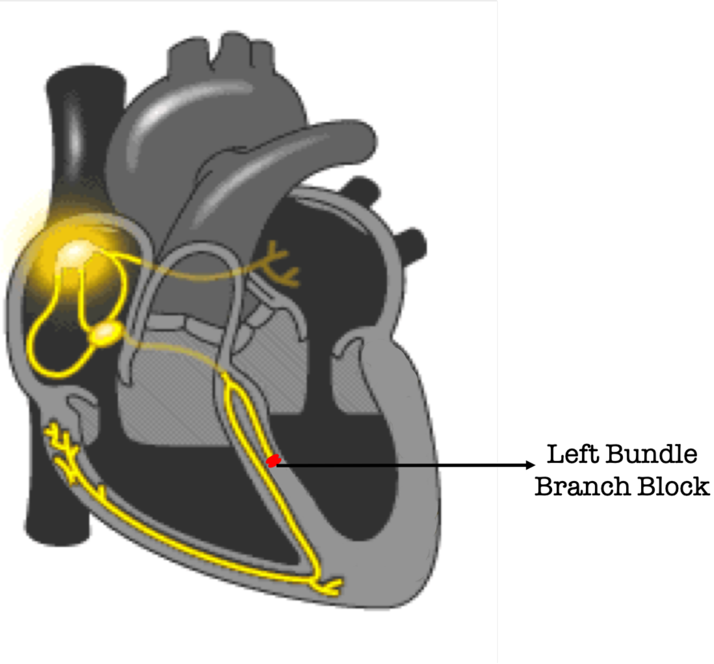

Figure 1.12: Left Bundle Branch Block (LBBB). Electrical impulses are blocked in the left branch of the His bundle before reaching the LV. *This Photo by Unknown Author is licensed under CC BY-NC.*

The main causes of LBBB can include [9, 10, 11]:

- Heart attacks (myocardial infarction).
- Thickened, stiffened or weakened heart muscle (cardiomyopathy).
- A viral or bacterial infection of the heart muscle (myocarditis).
- High blood pressure (hypertension)
- Heart valve disease.

Usually, LBBB by itself does not cause symptoms [12]. However, LBBB can be of great consequence and importance, especially in patients with acute chest pain, syncope and in those suffering from heart failure with reduced ejection fraction. Approximately 25% of patients with heart failure present LBBB [13, 14].

LBBB is often detected on the ECG waveform (Fig. 1.13). The following ECG criteria are commonly used to diagnose LBBB [15]:

- QRS duration greater than 120 ms.
- Lead V1 should have either a QS or a small R-wave with large S-wave. It should present positive T-wave.
- Lead V6 should have a notched R-wave and no Q-wave. It should present T-wave inversions.

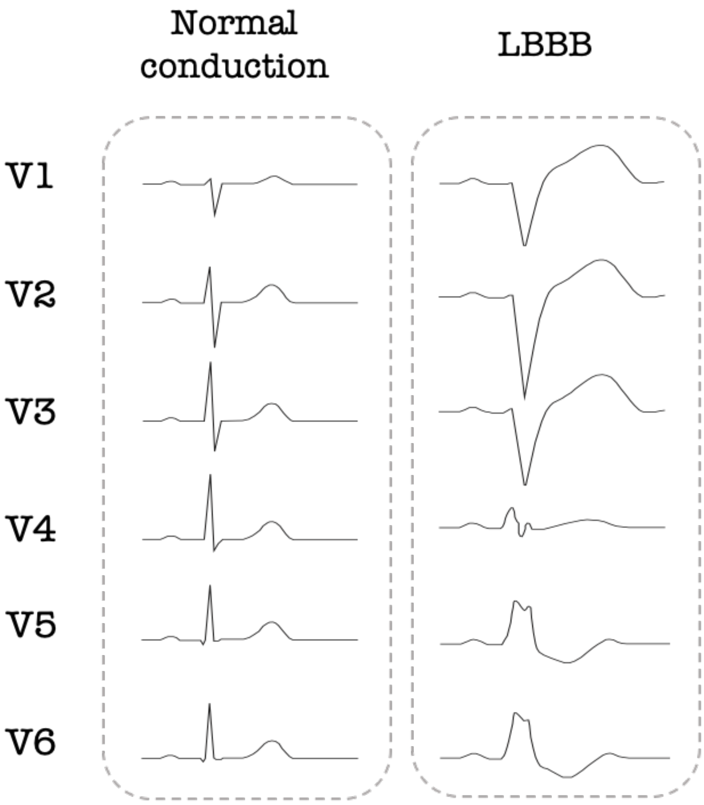

Figure 1.13: ECG waveform of leads V1 to V6 for a normal conduction and a typical LBBB case. *"Figure 1, Section 4, Chapter 8" by ECGWaves is licensed under CC BY 4.0.*

LBBB itself appears to have little effect and has no specific treatment. However, patients who also present heart failure may have an increased risk of death.

The cardiac resynchronization therapy is used as a treatment of choice in patients with systolic heart failure and LBBB with wide QRS (>120 ms), who remain symptomatic despite optimized medical therapy.

1.2.1.1 Heart failure

Heart failure (HF) is a chronic and degenerative disease of the heart characterized by a low capacity to pump blood and, therefore, to carry enough oxygen and nutrients to the rest of the body organs. It usually occurs because the heart has become too weak or stiff due to certain conditions. Heart failure is a long-term condition that tends to get gradually worse over time [16].

The main signs and symptoms of HF may include:

- Breathlessness after activity or at rest.
- Fatigue and weakness.

- Swelling (edema) in legs, ankles and feet.
- Reduced ability to exercise

According to the form of manifestation, HF is classified as: chronic, when the disease gradually manifests; and acute, when the symptoms appear suddenly and are serious from the beginning.

The ejection fraction (EF) is an important measurement of how well the heart pumps blood, and is used to help classify heart failure and guide treatment. Patients with heart failure may have a low ventricular ejection fraction (systolic dysfunction) or normal ejection fraction (diastolic dysfunction, when heart muscle becomes stiff for conditions such as high blood pressure).

HF can involve one or both ventricles of the heart. Generally, heart failure begins with the left ventricle, the heart's main pumping chamber.

Coronary artery disease and heart attack, high blood pressure (hypertension), faulty heart valves, damage to the heart muscle (cardiomyopathy), myocarditis, congenital heart defects, and abnormal heart rhythms are some of the most common conditions that can damage or weaken the heart causing HF.

1.2.1.2 Cardiac resynchronization therapy

Cardiac resynchronization therapy (CRT), also known as biventricular pacing, is a device-based intervention that tries to promote ventricular synchrony by pacing the ventricles from two different sites (Fig. 1.14). The device emits small painless electrical signals that serve to stabilize the electromechanical system [17, 18]. This treatement is adressed to symptomatic patients who have systolic heart failure, with severely reduced LV ejection fraction (below 35% versus a normal value above 55%) and significant intraventricular conduction delay, defined by a QRS duration >120 msec [19].

The CRT has been shown to improve HF symptoms in adults, such as shortness of breath, and may decrease both mortality and hospitalization rates. However, a significant (approximately 30%) patients selected according to the recommendations used in Europe and the United States do not improve clinically after implantation of the CRT device [20].

1.2.2 Aortic stenosis

Healthy heart valves allow blood flows in the one-way correct direction through the heart, avoiding a backward leakage. In heart valve disease, one or more of the valves does not work properly, causing disruption in the blood flow.

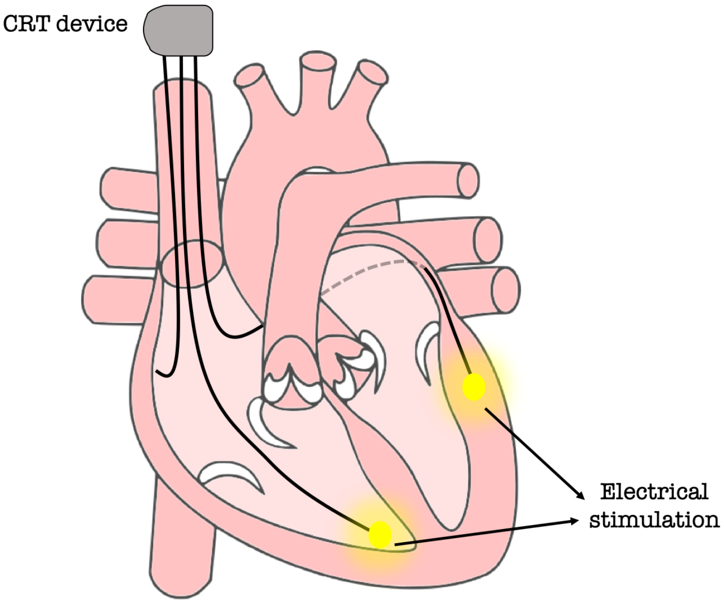

Figure 1.14: Cardiac resynchronization therapy (CRT). The CRT device emits small painless electrical signals to stimulate the ventricles from different sites, promoting the stabilization of the cardiac electromechanical system. *"Diagram of the human heart (cropped)" by Wikipedia is licensed under CC BY-SA: Attribution-ShareAlike.*

There are two different type of valve disease: valvular regurgitation where the valve does not close completely; and valvular stenosis where the valve opening is smaller than normal. When cardiac valves fail to open and close properly, the implications for the heart can be serious, possibly hampering the heart's ability to pump blood adequately through the body.

Aortic stenosis (AS) is the most common valvular heart disease (VHD) in Western countries, with a prevalence that increases progressively with age up to 9.8% in octogenarians [21]. AS is characterized by a reduction of the size of the aortic valve orifice (Fig. 1.15) which reduces the blood flow from the left ventricle to the aorta. This reduction in aortic valve area induces the development of a pressure gradient across the valve and the development of chronic LV pressure overload.

A heart suffering AS needs extra work to pump sufficient amount of blood, and eventually, this weakens the heart muscle, and it can ultimately lead to heart failure [22]. Some people suffering AS not experience symptoms until the narrowing of the valve is severe.

From a clinical point of view, a distinctive systolic heart murmur is usually the first clue that leads a doctor to suspect aortic valve stenosis. Then, the key tool to confirm diagnosis is transthoracic echocardiography, which allows the quantification of aortic valve area and trans-aortic gradient as far as the assesement of LV morphology

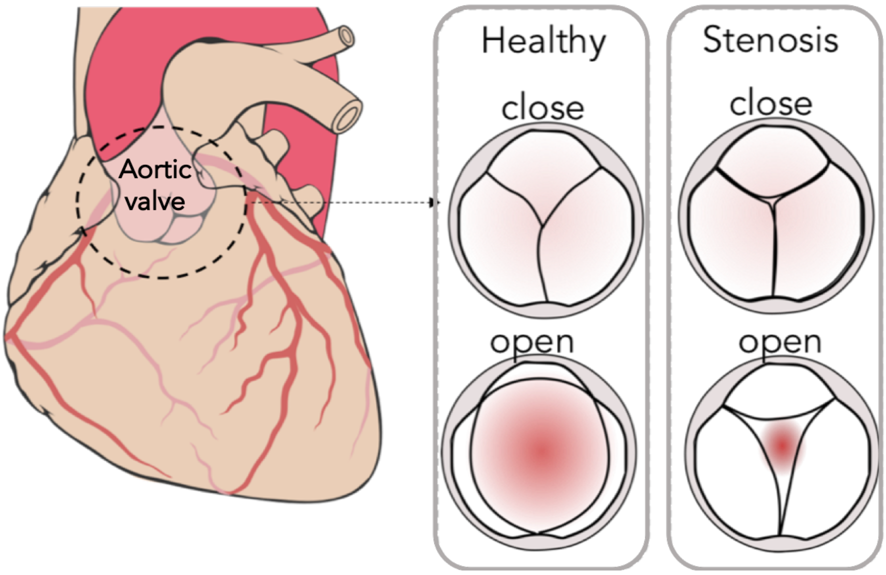

Figure 1.15: Aortic stenosis (AS). The aortic valve, located between the LV and the aorta, does not open completely. In the case of AS, the aortic valve opening is smaller than in the healthy case.

and function [23].

Treatment for AS depends on the severity of the condition, the signs and symptoms, and the condition of the heart and lungs. Early treatment can help to reverse or slow down the progress of this disease. Possible treatments may include surgical aortic valve replacement (SAVR), using mechanical or biological prostheses, by heart-open surgery or transcatheter aortic valve implantation (TAVI).

1.3 Echocardiography

An echocardiography is a test that uses ultrasound (high frequency sound waves) to produce a moving image of the heart. Sound waves are transmitted through the body by a transducer. The sound waves bounce off the heart and return to the transducer in the form of echoes. The echoes become electrical signals that produce images of the heart that can be observed on a screen.

Echocardiograms provide information about the shape, size, function, and strength of the heart. The movement and thickness of the walls and the cardiac valves function are also evaluated.

The echocardiogram images can be obtained in these main ways:

- **M or one-dimensional mode:** a narrow portion of the heart is detected.

- **2D mode:** offers an image of the anatomy of the heart, allowing to see the different structures during the movement (Fig. 1.16).
- **Color Doppler:** allows to see and measure the flow of blood in the heart and arteries.
- **3D mode:** the images that are achieved are in 3 dimensions. A 3D image is created from multiple images in 2 dimensions.

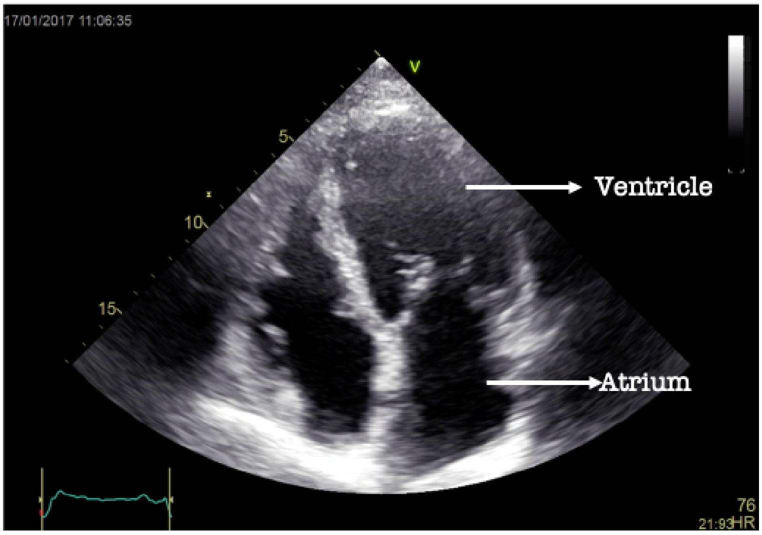

Figure 1.16: Example of a 2D echocardiography image obtained from a healthy subject.

The echocardiography is one of the most widely used techniques for the diagnosis of heart diseases since it provides images of excellent quality and is non-invasive, harmless, relatively cheap and widely available.

All patients with heart failure should undergo an echocardiogram at least once in order to be able to make the diagnosis. It not only allows to confirm the diagnosis, but also to establish what type of HF the patient has. Similarly, the echocardiogram can also detect the stenosis and/or the insufficiency of the cardiac valves.

1.3.1 Myocardial strain

Traditionally, the global systolic function is assessed by the left ventricle ejection fraction (LVEF), which indicates the percentage of blood that leaves the LV in each contraction. Echocardiography is widely used to measure LVEF, however, analysis is qualitative, subjective and dependent on the available image quality. In addition, the results are very susceptible to change depending on the loading conditions, heart rate, etc. Another important limitation is that LVEF is not sensitive enough to detect subtle changes in the contractile function, which would help to detect early myocardial damage. Even if contractility is reduced, compensatory mechanisms as ventricular dilatation, geometry changes, etc., can still assure that LV function remains normal.

Tissue Doppler imaging (TDI) is an echocardiographic technique that measures the velocity of the myocardial tissues, therefore, it indicates the rate at which a particular point in the heart moves relative to the echocardiogram transducer. TDI is designed to characterize the lower-velocity, higher-amplitude signals of myocardial tissue motion. Although TDI measurements are useful to quantify global and regional systolic and diastolic myocardial function, a dependence on the angle of Doppler movement relative to myocardial motion is presented. In addition, TDI measures are not able to discriminate translational motions from fiber shortening or lengthening motions. Consequently it has been found that TDI assessment do not present good reproducibility.

Strain imaging method using speckle-tracking echocardiography (STE) has been introduced as an alternative to quantify regional systolic function and promises to overcome many of the limitations of LVEF [24, 25]. STE is used to acquire regional strain curves that represent tissue deformation in 3 spatial directions: longitudinal, radial, and circumferential. The strain is expressed as a percentage and is mathematically defined as the change in the myocardial fiber length relative to its original length presented at end-diastole. Thus, negative longitudinal strain indicates fiber shortening or contraction and positive longitudinal strain represents fiber elongation or relaxation (Fig. 1.17).

STE technique uses several speckle artifacts in the echocardiography image produced by the reflections, refractions, and scattering of the ultrasound beam. The STE software identifies these speckles and then tracks them frame-by-frame during the whole cardiac cycle. Spatial movement of these speckles allows strain calculation [26].

Myocardial strain obtained by 2D STE has demonstrated to be an accurate tool for assessing ventricular function in early myocardial diseases. For example, reduced LV global longitudinal strain can be observed in asymptomatic patients with AS, showing a higher risk for developing symptoms and requiring aortic intervention [27]. Strain assessment has also contributed to improved understanding of left ventricular dyssynchrony in order to predict cardiac resynchronization therapy response [28, 29, 30]. Nevertheless, in spite of the different methods proposed to evaluate LV dyssynchrony, there is still a lack of reliability in these methods. The routine use of LV mechanical delay as an adjunct to the electrocardiographic criteria for the selection of CRT candidates has not gained clinical acceptance and has been shown to even be detrimental in patients with normal QRS. The main limitation is that they neglect the dynamics of strain signals, since the same values of strain peaks or timings can be observed with different strain curve morphologies. As a consequence, new methods are needed to jointly analyze the morphology of strain signals acquired concurrently at different regions of the myocardium.

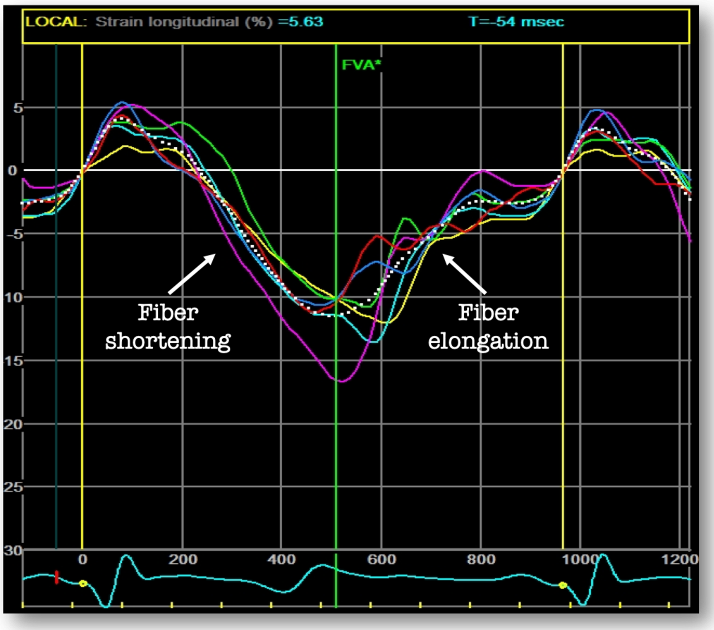

Figure 1.17: Example of myocardial strain signals obtained by speckle-tracking echocardiography (STE) in a healthy subject. Each curve represents different regions of the myocardium. Negative longitudinal strain indicates fiber shortening or contraction and positive longitudinal strain represents fiber elongation or relaxation.

1.3.2 Indices deduced from strain signals

Integral-derived longitudinal strain and myocardial work are two promising indices deduced from strain signals to quantify cardiac function.

1.3.2.1 Calculation of strains integrals

Researchers from the team proposed a new approach based on the automatic quantification of the integrals of regional longitudinal strain signals [31, 32], which takes into account the accumulated strain during different parts of the cardiac cycle to evaluate LV mechanics. By quantifying the areas under the segmental strain curves, the variation in myocardial contractility could be evaluated.

The area under each curve (integrals) is calculated over two time intervals: *i)* from the start of the QRS complex to the minimum value of the strain curve and *ii)* from the start of the QRS complex to the closure of the aortic valve. Measurement of these indices and other derived indices such as the standard deviation, the mean and the difference can provide important and complementary information for LV mechanical dyssynchrony assessment.

Strain integrals calculation could be fully automatically computed and therefore, suitable to machine-learning approaches. In a recent study [33], integral-derived longitudinal strain in a multiparametric application, such as what could be done in a machine-learning approach, has shown promising results and a good performance for the prediction of the CRT-response.

1.3.2.2 Myocardial work

Myocardial work, in turn, is an extension of the concept of strain integrals evaluated from mitral valve closure until mitral valve opening in which estimation of LV pressure is required.

The assessment of the myocardial work was recently introduced as an interesting alternative to evaluate accurate LV function [34, 35, 36] since it considers load conditions that methods such as strain imaging and LVEF do not take into account. As proposed by Russell et al. [37], based on the LV pressure dynamic and the strain curves we are able to calculate myocardial work indices as the Constructive Work (CW), which represents the productive work, and the Wasted Work (WW), that quantifies the energy loss, and likewise, the Work Efficiency (WE) index.

In addition, the LV pressure–strain loop area reflects myocardial or stroke work. In particular, Russell et al [34] have shown that regional differences in myocardial work have a strong correlation with regional myocardial glucose metabolism, evaluated using PET imaging. The LV pressure-strain loop area showed a pattern of regional work distribution, which was very similar to the distribution of glucose uptake.

Results from preliminary studies [34, 35, 37, 38, 39] concluded that the evaluation of the distribution and related indices of myocardial work could give additional information to assess patients with different cardiac pathologies.

1.4 Conclusion

The early diagnosis of diseases, the correct classification of pathological conditions, the prediction of treatments, are some of the challenges that are currently intended to be overcome in the bio-engineering field. Particularly, for cardiovascular pathologies, such as AS or LBBB with HF, knowledge of anatomy and physiological processes for the proper functioning of the cardiovascular system are essential and are the first step for understanding the different mechanisms (electrical, mechanical, hydraulic,...) involved in cardiac function.

Information acquired by echocardiography, such as strain signals and different echo-based parameters, are innovative tools that help to interpret cardiac mechanisms and LV function. Although, previous studies have suggested that the analysis of strain traces obtained by STE might be an alternative for quantifying LV function, guidelines still neglect, for example, the value of the assessment of LV mechanical dyssynchrony for the prediction of CRT-response. As a consequence, new methods are needed to analyze LV function and novel approaches for the prognosis, diagnosis and treatment of various cardiovascular pathologies still need to be proposed.

Bibliography

[1] J. E. Hall, *Guyton and Hall Textbook of Medical Physiology E-Book*. Elsevier Health Sciences, July 2010.

[2] A. Noordergraaf, *Circulatory System Dynamics*. Elsevier, Dec. 2012.

[3] F. H. Netter, *Atlas of Human Anatomy*. Elsevier Health Sciences, May 2010.

[4] R. Rhoades and D. R. Bell, *Medical Physiology: Principles for Clinical Medicine*. Lippincott Williams & Wilkins, 2009.

[5] A. Sohaib, *Decoding Cardiac Electrophysiology: Understanding the Techniques and Defining the Jargon*. Springer Nature, Nov. 2019.

[6] D. K. Moser and B. Riegel, *Cardiac Nursing: A Companion to Braunwald's Heart Disease*. Elsevier Health Sciences, Aug. 2007.

[7] W. R. Milnor, *Cardiovascular Physiology*. Oxford University Press, 1990.

[8] U. C. Nguyên, N. J. Verzaal, F. A. van Nieuwenhoven, K. Vernooy, and F. W. Prinzen, "Pathobiology of cardiac dyssynchrony and resynchronization therapy," *Europace: European Pacing, Arrhythmias, and Cardiac Electrophysiology: Journal of the Working Groups on Cardiac Pacing, Arrhythmias, and Cardiac Cellular Electrophysiology of the European Society of Cardiology*, vol. 20, no. 12, pp. 1898–1909, 2018.

[9] P. Francia, C. Balla, F. Paneni, and M. Volpe, "Left bundle-branch block—pathophysiology, prognosis, and clinical management," *Clinical Cardiology*, vol. 30, pp. 110–115, Mar. 2007.

[10] R. Imanishi, S. Seto, S. Ichimaru, E. Nakashima, K. Yano, and M. Akahoshi, "Prognostic significance of incident complete left bundle branch block observed over a 40-year period," *The American Journal of Cardiology*, vol. 98, pp. 644–648, Sept. 2006.

[11] V. Kumar, R. Venkataraman, W. Aljaroudi, J. Osorio, J. Heo, A. E. Iskandrian, and F. G. Hage, "Implications of Left Bundle Branch Block in Patient Treatment," *American Journal of Cardiology*, vol. 111, pp. 291–300, Jan. 2013. Publisher: Elsevier.

[12] E. Surkova, L. P. Badano, R. Bellu, P. Aruta, F. Sambugaro, G. Romeo, F. Migliore, and D. Muraru, "Left bundle branch block: from cardiac mechanics to clinical and

diagnostic challenges," *Europace: European Pacing, Arrhythmias, and Cardiac Electrophysiology: Journal of the Working Groups on Cardiac Pacing, Arrhythmias, and Cardiac Cellular Electrophysiology of the European Society of Cardiology*, vol. 19, pp. 1251–1271, Aug. 2017.

[13] S. Baldasseroni, C. Opasich, M. Gorini, D. Lucci, N. Marchionni, M. Marini, C. Campana, G. Perini, A. Deorsola, G. Masotti, L. Tavazzi, and A. P. Maggioni, "Left bundle-branch block is associated with increased 1-year sudden and total mortality rate in 5517 outpatients with congestive heart failure: A report from the Italian network on congestive heart failure," *American Heart Journal*, vol. 143, pp. 398–405, Mar. 2002.

[14] F. Zannad, E. Huvelle, K. Dickstein, D. J. v. Veldhuisen, C. Stellbrink, L. Køber, S. Cazeau, P. Ritter, A. P. Maggioni, R. Ferrari, and P. Lechat, "Left bundle branch block as a risk factor for progression to heart failure," *European Journal of Heart Failure*, vol. 9, no. 1, pp. 7–14, 2007. _eprint: https://onlinelibrary.wiley.com/doi/pdf/10.1016/j.ejheart.2006.04.011.

[15] B. Surawicz, R. Childers, B. J. Deal, L. S. Gettes, J. J. Bailey, A. Gorgels, E. W. Hancock, M. Josephson, P. Kligfield, J. A. Kors, P. Macfarlane, J. W. Mason, D. M. Mirvis, P. Okin, O. Pahlm, P. M. Rautaharju, G. van Herpen, G. S. Wagner, H. Wellens, American Heart Association Electrocardiography and Arrhythmias Committee, Council on Clinical Cardiology, American College of Cardiology Foundation, and Heart Rhythm Society, "AHA/ACCF/HRS recommendations for the standardization and interpretation of the electrocardiogram: part III: intraventricular conduction disturbances: a scientific statement from the American Heart Association Electrocardiography and Arrhythmias Committee, Council on Clinical Cardiology; the American College of Cardiology Foundation; and the Heart Rhythm Society. Endorsed by the International Society for Computerized Electrocardiology," *Journal of the American College of Cardiology*, vol. 53, pp. 976–981, Mar. 2009.

[16] A. Mosterd and A. W. Hoes, "Clinical epidemiology of heart failure," *Heart*, vol. 93, no. 9, pp. 1137–1146, 2007. Publisher: BMJ Publishing Group Ltd _eprint: https://heart.bmj.com/content/93/9/1137.full.pdf.

[17] C. Linde, K. Ellenbogen, and F. A. McAlister, "Cardiac resynchronization therapy (CRT): Clinical trials, guidelines, and target populations," *Heart Rhythm*, vol. 9, pp. S3–S13, Aug. 2012.

[18] B. Cannon and P. Wackel, "Chapter 45 - Electrophysiologic Devices in Heart Failure," in *Heart Failure in the Child and Young Adult* (J. L. Jefferies, A. C. Chang, J. W. Rossano, R. E. Shaddy, and J. A. Towbin, eds.), pp. 575–581, Boston: Academic Press, Jan. 2018.

[19] European Society of Cardiology (ESC), European Heart Rhythm Association (EHRA), M. Brignole, A. Auricchio, G. Baron-Esquivias, P. Bordachar, G. Boriani,

O.-A. Breithardt, J. Cleland, J.-C. Deharo, V. Delgado, P. M. Elliott, B. Gorenek, C. W. Israel, C. Leclercq, C. Linde, L. Mont, L. Padeletti, R. Sutton, and P. E. Vardas, "2013 ESC guidelines on cardiac pacing and cardiac resynchronization therapy: the task force on cardiac pacing and resynchronization therapy of the European Society of Cardiology (ESC). Developed in collaboration with the European Heart Rhythm Association (EHRA)," *Europace: European Pacing, Arrhythmias, and Cardiac Electrophysiology: Journal of the Working Groups on Cardiac Pacing, Arrhythmias, and Cardiac Cellular Electrophysiology of the European Society of Cardiology*, vol. 15, pp. 1070–1118, Aug. 2013.

[20] M. R. Bristow, L. A. Saxon, J. Boehmer, S. Krueger, D. A. Kass, T. De Marco, P. Carson, L. DiCarlo, D. DeMets, B. G. White, D. W. DeVries, and A. M. Feldman, "Cardiac-Resynchronization Therapy with or without an Implantable Defibrillator in Advanced Chronic Heart Failure," *New England Journal of Medicine*, vol. 350, pp. 2140–2150, May 2004. Publisher: Massachusetts Medical Society _eprint: https://doi.org/10.1056/NEJMoa032423.

[21] C. M. Otto and B. Prendergast, "Aortic-valve stenosis from patients at risk to severe valve obstruction," *The New England Journal of Medicine*, vol. 371, pp. 744–756, Aug. 2014.

[22] B. A. Carabello and W. J. Paulus, "Aortic stenosis," *The Lancet*, vol. 373, pp. 956–966, Mar. 2009.

[23] H. Baumgartner, V. Falk, J. J. Bax, M. De Bonis, C. Hamm, P. J. Holm, B. Iung, P. Lancellotti, E. Lansac, D. Rodriguez Muñoz, R. Rosenhek, J. Sjögren, P. Tornos Mas, A. Vahanian, T. Walther, O. Wendler, S. Windecker, J. L. Zamorano, and ESC Scientific Document Group, "2017 ESC/EACTS Guidelines for the management of valvular heart disease," *European Heart Journal*, vol. 38, no. 36, pp. 2739–2791, 2017.

[24] C. M. N. Haddour, G. Dufaitre, S. Janower, E. Berthelot-Garcias, F. Douna, S. Ederhy, F. Boccara, and A. Cohen, "Qu'est-ce que l'échographie 2D strain ?," *Réalités Cardiologiques*, Mar. 2011. Library Catalog: www.realites-cardiologiques.com.

[25] O. A. Smiseth, H. Torp, A. Opdahl, K. H. Haugaa, and S. Urheim, "Myocardial strain imaging: how useful is it in clinical decision making?," *European Heart Journal*, vol. 37, pp. 1196–1207, Apr. 2016.

[26] M. Bansal and R. R. Kasliwal, "How do I do it? Speckle-tracking echocardiography," *Indian Heart Journal*, vol. 65, pp. 117–123, Jan. 2013.

[27] J. Magne, B. Cosyns, B. A. Popescu, H. G. Carstensen, J. Dahl, M. Y. Desai, L. Kearney, P. Lancellotti, T. H. Marwick, K. Sato, M. Takeuchi, C. Zito, A.-C. Casalta, D. Mohty, L. Piérard, G. Habib, and E. Donal, "Distribution and Prognostic Significance of Left Ventricular Global Longitudinal Strain in Asymptomatic Significant

Aortic Stenosis: An Individual Participant Data Meta-Analysis," *JACC. Cardiovascular imaging*, vol. 12, no. 1, pp. 84–92, 2019.

[28] W. M. van Everdingen, J. Walmsley, M. J. Cramer, I. van Hagen, B. W. L. De Boeck, M. Meine, T. Delhaas, P. A. Doevendans, F. W. Prinzen, J. Lumens, and G. E. Leenders, "Echocardiographic Prediction of Cardiac Resynchronization Therapy Response Requires Analysis of Both Mechanical Dyssynchrony and Right Ventricular Function: A Combined Analysis of Patient Data and Computer Simulations," *Journal of the American Society of Echocardiography: Official Publication of the American Society of Echocardiography*, vol. 30, pp. 1012–1020.e2, Oct. 2017.

[29] N. Risum, B. Tayal, T. F. Hansen, N. E. Bruun, M. T. Jensen, T. K. Lauridsen, S. Saba, J. Kisslo, J. Gorcsan, and P. Sogaard, "Identification of Typical Left Bundle Branch Block Contraction by Strain Echocardiography Is Additive to Electrocardiography in Prediction of Long-Term Outcome After Cardiac Resynchronization Therapy," *Journal of the American College of Cardiology*, vol. 66, pp. 631–641, Aug. 2015.

[30] J. M. Aalen, E. W. Remme, C. K. Larsen, O. S. Andersen, M. Krogh, J. Duchenne, E. Hopp, S. Ross, A. S. Beela, E. Kongsgaard, J. Bergsland, H. H. Odland, H. Skulstad, A. Opdahl, J.-U. Voigt, and O. A. Smiseth, "Mechanism of Abnormal Septal Motion in Left Bundle Branch Block: Role of Left Ventricular Wall Interactions and Myocardial Scar," *JACC. Cardiovascular imaging*, vol. 12, no. 12, pp. 2402–2413, 2019.

[31] A. Bernard, *Prédiction de la réponse à la resynchronisation biventriculaire : au delà des asynchronismes*. These de doctorat, Rennes 1, Dec. 2014.

[32] A. Bernard, E. Donal, C. Leclercq, F. Schnell, M. Fournet, A. Reynaud, C. Thebault, P. Mabo, J. C. Daubert, and A. Hernandez, "Impact of Cardiac Resynchronization Therapy on Left Ventricular Mechanics: Understanding the Response through a New Quantitative Approach Based on Longitudinal Strain Integrals," *Journal of the American Society of Echocardiography*, vol. 28, pp. 700–708, June 2015.

[33] A. Hubert, A. Gallard, V. L. Rolle, O. A. Smiseth, C. Leclercq, J.-U. Voigt, E. Galli, V. Galand, A. Hernandez, and E. Donal, "Left ventricular strain for predicting the response to cardiac resynchronization therapy: two methods for one question," *European Heart Journal - Cardiovascular Imaging*, Jan. 2021.

[34] K. Russell, M. Eriksen, L. Aaberge, N. Wilhelmsen, H. Skulstad, E. W. Remme, K. H. Haugaa, A. Opdahl, J. G. Fjeld, O. Gjesdal, T. Edvardsen, and O. A. Smiseth, "A novel clinical method for quantification of regional left ventricular pressure-strain loop area: a non-invasive index of myocardial work," *European Heart Journal*, vol. 33, pp. 724–733, Mar. 2012.

[35] J. Vecera, M. Penicka, M. Eriksen, K. Russell, J. Bartunek, M. Vanderheyden, and O. A. Smiseth, "Wasted septal work in left ventricular dyssynchrony: a novel prin-

ciple to predict response to cardiac resynchronization therapy," *European Heart Journal Cardiovascular Imaging*, vol. 17, pp. 624–632, June 2016.

[36] A. Hubert, V. Le Rolle, C. Leclercq, E. Galli, E. Samset, C. Casset, P. Mabo, A. Hernandez, and E. Donal, "Estimation of myocardial work from pressure-strain loops analysis: an experimental evaluation," *European Heart Journal Cardiovascular Imaging*, vol. 19, no. 12, pp. 1372–1379, 2018.

[37] K. Russell, M. Eriksen, L. Aaberge, N. Wilhelmsen, H. Skulstad, O. Gjesdal, T. Edvardsen, and O. A. Smiseth, "Assessment of wasted myocardial work: a novel method to quantify energy loss due to uncoordinated left ventricular contractions," *American Journal of Physiology. Heart and Circulatory Physiology*, vol. 305, pp. H996–1003, Oct. 2013.

[38] E. Galli, C. Leclercq, A. Hubert, A. Bernard, O. A. Smiseth, P. Mabo, E. Samset, A. Hernandez, and E. Donal, "Role of myocardial constructive work in the identification of responders to CRT," *European Heart Journal Cardiovascular Imaging*, vol. 19, no. 9, pp. 1010–1018, 2018.

[39] J. Chan, N. F. A. Edwards, B. K. Khandheria, K. Shiino, S. Sabapathy, B. Anderson, R. Chamberlain, and G. M. Scalia, "A new approach to assess myocardial work by non-invasive left ventricular pressure-strain relations in hypertension and dilated cardiomyopathy," *European Heart Journal Cardiovascular Imaging*, vol. 20, no. 1, pp. 31–39, 2019.

MODEL SIMULATION AND ANALYSIS

2

This chapter presents state-of-the-art of modeling and simulation methods and tools required to develop, evaluate and analyze patient-specific model-based applications in clinical contexts. For this thesis, we proposed multiformalism and multiscale computational models of the cardiovascular system (CVS) for the study of specific cardiovascular pathologies. Hence, different processes involved in the genesis of the cardiac function and different anatomical levels of detail were considered. The Multi-Formalism Modeling and Simulation Library (M2SL), is the framework used to create and simulate such models. M2SL is briefly presented in the first section of this chapter. Model parameter analysis is a fundamental step to better understand the characteristics and behaviors of both the model and the system under study. Therefore, the next section will focus on the methods applied for evaluating parameters sensitivity and the strategies implemented for parameter identification, detailing the evolutionary algorithms and the parallel optimization library (PAGMO) used in order to propose specific-patient simulations.

2.1 Modeling and simulation framework

Computer simulations are useful for reproducing, interpreting and predicting the behavior of real-world processes or systems in response to various assigned conditions. Modeling consists in the simplified representation of the functioning of a real system, which permits to describe such system as a structure that receives an input and generates a corresponding output.

There are several goals that can be achieved using modeling and simulation, such as interpretation, explanation or understanding of experimental observations, formal representation and description of current knowledge, prediction of unobserved behaviors, evaluation of hypothesis or configuration scenarios of the system, design of controllers, or just provide a simplified approach to a problem whose analytical solution is too complex.

Briefly, a model M could be defined as a tuple denoted $M\left(F, \mathbf{I}, \mathbf{O}, \mathbf{E}, \mathbf{P}\right)$ where $\mathbf{I}$, $\mathbf{O}$ and $\mathbf{E}$ denote the input, output and state **variable sets**, $\mathbf{P}$ denotes the **parameter set** of the model, and F is the formalism in which the model is described [2].

2.1.1 Modeling and simulation concepts

- An **input** is a variable that triggers and influences the behavior of the model or system. Inputs have a defined range from which they can take a value.
- Correspondingly, an **output** is the exit variable of a model or system. Outputs are also defined within a range.
- A **state variable** is a value intrinsic to the system, which is not necessarily observable since it is not a part of the system. Yet, it represents some knowledge of an internal mechanism of the system. Indeed, the set of state variables of a system is a sufficient description of the status of the system to determine its current and future behavior. Output variables are usually calculated as a function of state variables, parameters and input variables. In the case of a model based on ordinary differential equations, the system is typically described through the variations (time derivatives) of the state variables.
- A **parameter** is a special kind of input variable that characterizes, defines or sets the conditions of a particular element of a system. As with input, output and state variables, parameters are defined in a range, but they are often used as a constant value for a given simulation. The behavior of a system can be drastically different according to the value of its parameters. Moreover, slight modifications of some parameters may evoke significant modifications on the state and output variables, while significant modifications of some parameters may have negligible effect on these variables. Hence, the exploration and analysis of the parameters of a model, as well as their relative importance on their effect on state and output variables (parameter sensitivity) is very important to the modeling and simulation process.
- A **formalism** is the group of rules, structures and tools that permits to define a model: they express how the input and outputs are related and how the internal states change with respect to the inputs, parameters, etc.

2.1.2 Model-based design process

The creation of a model and its simulation must be done in an organized manner and following certain steps, described in [3], that will lead to the successful fulfillment of the stated objectives:

1. The first step is to define precisely the system that is going to be modeled and the reasons why it is going to be modeled. It is important to characterize the elements of the system and define the available knowledge about it in order to identify the inputs and outputs, recognize which elements must be manipulated and which

elements must be measured, define the conditions that should be assumed and, consequently, the possible limitations of the system.

2. Once the system has been specified, the next step consists in selecting a range of mathematical tools that help to describe the system. The objective of the description of the system is to create a model M that represents the system dynamics under a certain formalism F. The type of formalism chosen to create a model will depend on what was stipulated in the previous step: the system definition and the goals of the modeling application.

3. The third step consists in simulating the complete model created in the previous step. In general, a simulation is the process that interprets the model definition to generate its output. Simulation process controls the trajectories of the input variables, the values of each parameter, the initial values of internal states, and the specific definitions of each function according to the model formalism. The simulation process tackles two distinct problems: *i)* the interpretation of the model specification under its formalism F, and *ii)* the simultaneous simulation of all the sub-systems defined within the model.

4. The model can be parametrized, it means that is possible to control the output response by changing the input and parameters of the model. The next step is to implement a parameter analysis in order to better understand the characteristics and behavior of the model. The analysis of parameters deserves a detailed description, which will be presented in section 2.3.

5. Finally, the last stage in the modeling and simulation framework is the validation analysis. Vangheluwe et al. [4] present four different validation schemes: behavioral validation, structural validation, conceptual validation, and simulation verification. *i)* Behavioral validation is the evaluation of the simulated model behavior with respect to the system observations. The experimental data and model output must agree within an acceptable tolerance. *ii)* Structural validation is the evaluation of the structure of the model with respect to the structure observed in the system. *iii)* Conceptual validation is the relation between the system and the model in a conceptual level; it evaluates the realism of the model description with respect to the system and the experimental frame. *iv)* Verification refers to the consistency between the model description and the interpretation provided by the simulator. It ensures that the simulation correctly generates the model outputs and that the model implementation is correct and does not contain errors.

2.2 Simulation tool: Multi-formalism Modeling and Simulation Library (M2SL)

All the computational models proposed in this thesis were simulated in the Multi-formalism Modeling and Simulation Library (M2SL). This library has been designed, adapted and progressively improved due to different studies developed by LTSI laboratory researchers [2, 3, 5, 6].

2.2.1 Model representation

A model in M2SL is a set of interconnected components; a combination of two types of model objects: atomic models (M^a) and coupled models (M^{coup}). An atomic model M^a is a model with a specific component of a system using one particular formalism. A coupled model $M^c\left(F, \mathbf{I}, \mathbf{O}, \mathbf{E}, \mathbf{P}, \{M_i\}\right)$ is a model composed of a set of components ($\{M_i\}$), i.e. sub-models, which can be either atomic or coupled as well. Coupled models may be defined under different formalisms and the connections between them. A graphical representation of atomic and coupled models, including their organization, is presented as the model hierarchy in the left part of Figure 2.1.

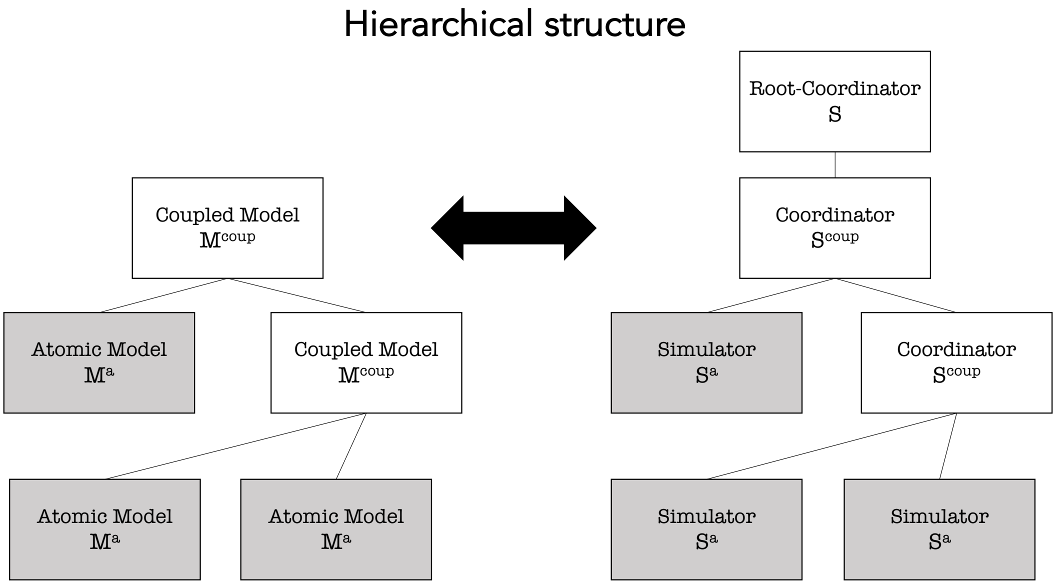

Figure 2.1: Hierarchical structure of models and their corresponding simulators. Schema based on [7], adpated from [3].

When a computational model is defined in M2SL, a global simulator S, called the *root coordinator*, is first created. This object analyses the model hierarchy and creates a *simulator* S_i^a for each atomic model M_i^a. The choice of the appropriate simulator type is automatically handled by the library. In this way, a model with formalism F_i is associated with a simulator designed for the same formalism F_i. For each coupled model M_i^{coup}, a *coordinator* S_i^{coup} is created. Coordinators are a special kind of simulator that handle the connection of the internal components of a complex model and computes model outputs at the coupled level (Fig. 2.1, right side).

Using an object-oriented methodology, models in M2SL are represented with different abstract classes, which define the structural elements of a model and its behaviors. The development of a model in M2SL consists in choosing a base abstract class, defining its data structures and then the programming of its behavior. The available data structures and behaviors of a model depends on the formalism of the model. However, it always follows the definition introduced previously: a model is represented as a tuple $M\ (F, \mathbf{I{,}O{,}E{,}P})$. The relation between each element of this tuple and the structures of M2SL is explained below:

Variables I,O,E,P: The variables of a model are organized in four different groups according to their semantic definition: `inputs`, `outputs`, `states`, and `parameters`. Each single variable or parameter can be represented by any data structure provided by the `C++` language.

Components: As explained before, in M2SL, models can be either atomic or complex. To permit the creation of complex models, the `submodels` container is also included in the definition of a model, which accommodates a list of references to other models.

Behaviors: The behavioral definition of a model comprises four different procedures:

- Initialization: the calculation or simple assignment of initial values to all variables of the model.
- Variable synchronization: the update or modification of the internal state of the model due to a change in the input variables.
- Output calculation: the computation of the output variables from the current internal state and the input variables.
- Termination: the final procedure executed when the simulation ends.

Formalism F: The formalism of a model is defined by the abstract class chosen as base class for its implementation. In other words, for each formalism, M2SL provides an abstract class. The available formalisms are summarized in Table 2.1. Following an object-oriented paradigm, a model in M2SL must inherit from one of these classes. Moreover, each formalism requires the implementation of particular behaviors, represented by the methods of each class.

Table 2.1: Formalisms supported in M2SL and their corresponding class. Adapted from [3].

Formalism F	**Class**
Algebraic equations	`GenericModel`
Ordinary differential equations	`OdeModel`
Algebraic equations with discrete time	`DiscreteTimeModel`

2.2.2 The simulation loop

All the objects, procedures and relations defined by M2SL are brought together in the simulation loop. A simulation in M2SL is conducted by a root coordinator, represented by the `RootCoordinator` class. This crucial element defines and updates the global time of the simulation, while coordinating the underlying simulators and their local simulation time. It consists of three procedures executed in a sequential fashion: initialization, simulation loop and finalization (Fig. 2.2, left side).

First, the initialization step prepares all models and simulators for the simulation, which includes the following activities:

1. Creation of a simulator for each model, according to its formalism.
2. Association and linking of all simulators in a hierarchical structure that follows the model hierarchy, as illustrated before in Fig. 2.1.
3. Initialization of all simulators and models.
4. Override of variable values, if the user has manually set values to some model variables.
5. Initialization of the global time to its initial value, usually 0.

After the initialization step, the simulation loop repeats the following steps, illustrated in Fig. 2.2 (right side):

1. Synchronization of models: at this point, all models have updated values for each of their output variables, calculated from the initialization phase or from a previous iteration of the simulation loop. This step performs the transformation of these output values to new input values. Once the input variables have been assigned with new values, all internal values of the model that depend on the inputs should be updated as well.
2. Simulation of models: it calculates the internal transitions of the model in order to advance the local simulation time of one or several time steps, depending on the temporal synchronization procedure. For instance, the adaptive strategies can iterate in this step several times until a target time is achieved, as shown in Fig. 2.2.

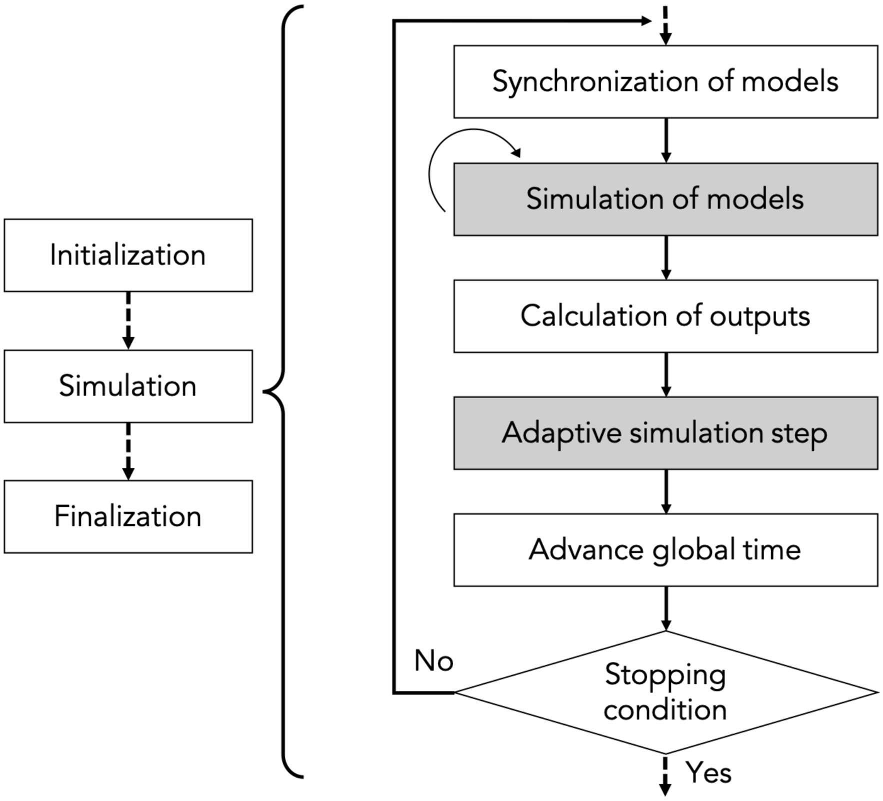

Figure 2.2: General execution flow of a simulation in M2SL *(left)* and its detailed simulation loop with adaptive simulation steps *(right)*. Gray boxes denote the steps that are different from the general simulation loop. Adapted from [3].

3. Calculation of outputs: since the previous step modifies the state variables of the model to a new point in time, this step calculates new values of the output variables for all models.

4. Advance global time: this step increments the global simulation time according to the results of the current iteration. Depending on the temporal synchronization procedure, this step can be as simple as an addition, but it may calculate an optimal time step for the next iteration.

5. Stopping condition: at the end of each iteration, the target simulation time is evaluated to determine if the simulation should stop. Other elements may be taken into account as well, such as stopping conditions introduced by an external tool like the user interface.

Lastly, when the simulation loop meets the stopping condition, the finalization step releases all resources acquired during the simulation.

2.3 Parameter analysis

The analysis of parameters is highly important to better understand the characteristics and behavior of the model; to acquire knowledge on the relation between the parameters and the outputs of the model. Parameter analysis encompasses two different activities: *i)* the characterization of the effect of a parameter on the model dynamics, particularly its outputs, and *ii)* the identification or estimation of meaningful parameter values to the model. These two activities are conceptually independent but related since they can benefit from the information obtained from each other.

2.3.1 Sensitivity Analysis

Model parameters represent an element of the real system, or rather, a simplification of such element. These parameters can sometimes be measured directly from the system, estimated from the observable data, or even guessed from prior knowledge. In any case, it is highly likely that the parameter value contains an intrinsic error or a level of uncertainty. Then, some questions arise regarding these parameters: What is the effect of this incertitude on the model outputs? Is it possible to measure quantitatively or qualitatively the effect of changes in parameter values on the outputs? The field of sensitivity analysis, along with the highly related area of uncertainty analysis, provides a set of tools that can answer this questions.

In the context of the modeling applications presented in this manuscript, sensitivity analysis is defined as the measurement of the effect of changes in input values and model parameters on the outputs of a system. In other words, sensitivity analysis methods are applied to determine how much the parameters involved in a model affect one or more outputs.

Sensitivity analysis can provide important information for modeling and simulation applications. The objectives include:

- Factor prioritization: it can determine which inputs or parameters are more important, which can help guide the parameter estimation or motivate further attention in the observation of certain inputs.
- Model simplification: it can identify which elements of the model have little effect and can be replaced with a simpler definition.
- Parameter regions identification: it can pinpoint critical or interesting ranges in the parameter or input spaces.
- Parameter interaction: not only it can measure the effect of changes of one parameter, it can also measure the effect of the interaction of parameters, i.e. the outcome of changes in two or more parameters.

This information is highly useful since it facilitates the analysis of the cardiovascular system models used in this thesis, which are complex multi-scale models. Based on this information, the number of parameters to analyze for a specific phenomenon can be minimized, reducing computational costs. Factor prioritization is particularly important for patient-specific simulations, which is also interesting for the thesis objective.

The approach followed by most sensitivity analysis methods is summarized in Fig. 2.3. It consists in:

1. The definition of the distribution for each source of uncertainty, each input or parameter X_i, or the definition of the relevant parameter space $\mathbb{P}$. For simplicity it will be assumed that there are k parameters denoted $[X_1, X_2, \ldots, X_k]$.
2. The creation of an *experimental design*, which will be denoted D, consisting of n sets of input values:

$$D = \begin{bmatrix} x_1^{(1)} & x_2^{(1)} & \ldots & x_k^{(1)} \\ x_1^{(2)} & x_2^{(2)} & \ldots & x_k^{(2)} \\ \vdots & \vdots & \ddots & \vdots \\ x_1^{(n)} & x_2^{(n)} & \ldots & x_k^{(n)} \end{bmatrix}, \tag{2.1}$$

   where a row represents the values for each parameter.
3. The evaluation of each row of the experimental design D, which yields a vector of outputs

$$Y = \left[y^{(1)}, y^{(2)}, \ldots, y^{(n)}\right]^T. \tag{2.2}$$

4. The analysis of the outputs Y, identifying and associating the source of the variations in the outputs, with respect to the variations in the parameters.

The variety of the existing methods in sensitivity analysis lies on the diverse schemes to produce an experimental design and to analyze the variability of the evaluated outputs. However, the choice of the sensitivity analysis depends on several factors, such as the assumptions on the parameters of $f(X)$ (linearity, independence or interaction) and the available computational resources for the evaluation of this function. Existing methods can be divided into three groups: local sensitivity methods, global sensitivity methods and screening methods. This categorization is not strict, considering that some methods can be considered as part of more than one of these groups.

2.3.1.1 Local sensitivity analysis

Local methods represent the most simple form of sensitivity analysis. The term *local* emphasizes the fact that the sensitivity of the parameters are studied in a small

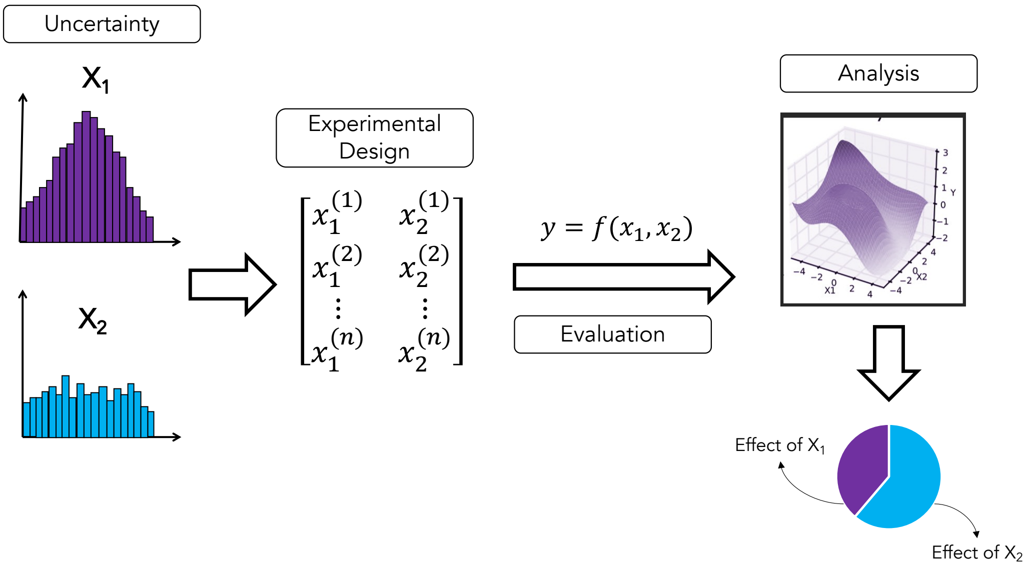

Figure 2.3: Simplified diagram of the process of uncertainty and sensitivity analysis, based on [8], adapted from [3].

region of the parameter space $\mathbb{P}$. A natural approach consists in the selection of a working point $X^{(0)} = [x_0^{(0)}, x_1^{(0)}, \dots, x_k^{(0)}]$, followed by the evaluation of the function $f(X^{(0)})$ and at other points close to $X^{(0)}$. When the variations are introduced only in one parameter X_i at a time, the approach is termed a one-at-time (OAT) analysis. For example, a typical OAT experimental design for X_i would be:

$$D_i = \begin{bmatrix} x_0^{(0)} & \dots & x_i^{(0)} & \dots & x_k^{(0)} \\ x_0^{(0)} & \dots & x_i^{(0)} + \delta & \dots & x_k^{(0)} \\ x_0^{(0)} & \dots & x_i^{(0)} + 2\delta & \dots & x_k^{(0)} \\ \vdots & & \vdots & & \vdots \\ x_0^{(0)} & \dots & x_i^{(0)} + (n-1)\delta & \dots & x_k^{(0)} \end{bmatrix}, \tag{2.3}$$

where δ is a predefined perturbation of parameter X_i. In this example, only the variations in $[x_i^0, x_i^0 + (n-1)\delta]$ are explored, but this range can be defined as evenly spaced variations from the minimum and maximum values of parameter X_i, or as an arbitrary variation of δ.

Once Y is obtained from the evaluation of matrix D_i (Eq. 2.3), the results can be analyzed in several ways. On one hand, the partial derivatives $\partial Y / \partial X_i$ can be estimated or averaged, which can be normalized and compared to the partial derivatives of other parameters $\partial Y / \partial X_j$. On the other hand, the results of the evaluation can be plotted with respect to the different values of the varying parameter, as shown in Fig. 2.4. In this case, the effect of the parameter variation can be identified visually, or directly quantified using a linear regression and its coefficient of determination R^2.

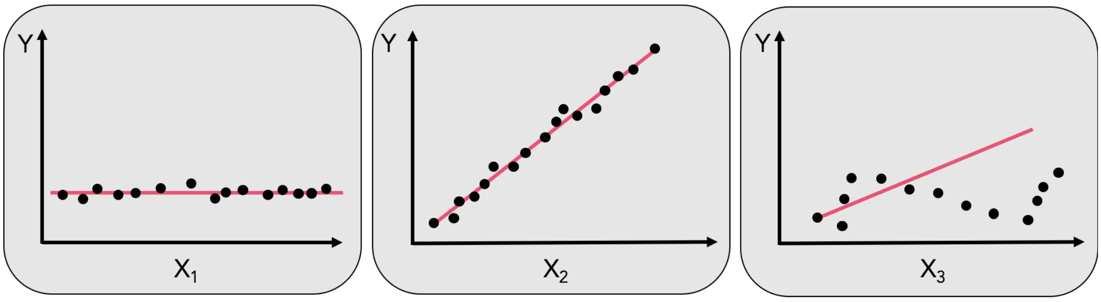

Figure 2.4: An example of one-at-time sensitivity analysis for three parameters X_1, X_2 and X_3 over an output $Y = f(X)$. The left plot shows little effect of X_1 over the output, the middle plot shows a linear effect of X_2, and the right plot shows a non-linear effect of X_3. Adapted from [3].

Local sensitivity analyses are practical for their simplicity and reduced number of evaluations. However, as their name imply, the parameter space is not fully explored, since it does not consider simultaneous variations of parameters. Consequently, local OAT approaches cannot detect interactions between parameters. Moreover, the linear regression analysis mentioned above supposes a linearity of the relation between the parameters and the outputs, which will fail to identify nonlinear relationships as illustrated in Fig.2.4.

2.3.1.2 Global sensitivity analysis

In contrast with local methods, global sensitivity analysis focuses on the study of the effect of the parameters but it does not constrain their values to the small region around a working point. Instead, it permits the parameters to take any value in a large region of interest.

The most popular family of global sensitivity analysis methods is the variance-based approach. This approach tries to identify what part of the variability of Y can be attributed to the variability of each parameter X_i (or groups of parameters) [9, 10, 11]. All the input factors are varied simultaneously and the sensitivity is measured across the whole input space.

In most of the global sensitivity analysis methods, the amount of evaluations, or model simulations, necessary to calculate the sensitivity indices is very high, which limits the application of global sensitivity analysis to models where the number of parameter is reduced and when one counts with a significant computational budget. This is the main reason that drives another type of global sensitivity analysis that permits to cheaply identify and exclude unimportant parameters: screening methods.

2.3.1.3 Screening methods

In contrast to previous global sensitivity methods, screening methods do not quantify the sensitivity of a parameter. Instead, they permit to identify qualitatively which parameters of a function are relatively influent on the function's output and which parameters can be ignored. This information can help to reduce the dimensionality of future analysis or estimation phases.

The most common screening method is the Morris elementary effects method [12]. This method is well suited in large dimension models, where the mathematical model is computationally cost. The Morris method uses the one-step-at-a-time (OAT) technique, which means that in each execution only one input parameter changes its value to measure the variation in the model's output.

Morris methodology starts with a first execution of the algorithm using the established initial values of the input parameters X. Then, the value of a single parameter x_i is changed and the resulting change in the model output Y compared with the previous execution is calculated by the elementary effect (Eq. 2.4). The same process continues until all parameters values are changed. Before applying Morris method, the ranges of values must be defined for the k input parameters.

The algorithm is repeated r times (where r is usually taken between 5 and 15), each time with a different set of initial values. In conclusion, the method is based on calculating for each input parameter a number of incremental ratios, called elementary effects $EE_{i,j}$ $(i = 1, ..., r.j = 1, ..., k)$.

$$EE_{i,j} = \frac{Y(x_1, x_2, ..., x_i + \Delta_i, ..., x_k) - Y(x_1, x_2, ..., x_i, ..., x_k)}{\Delta_i}, \tag{2.4}$$

where Δ is a predefined multiple of $1/k-1$, and $(x_1, x_2, \ldots, x_k)$ is a randomly selected point, such that each x_i takes a value in $\{0, 1/(k-1), 2/(k-1), \ldots, 1 - \Delta\}$.

Finally, basic statistics are computed to derive sensitivity information. Two sensitivity measures for each input parameter is calculated:

- **The standard deviation,** σ **:** estimates the non-linear effects and the interactions with other parameters.

$$\sigma_j = \sqrt{\frac{1}{r}\sum_{i=1}^{r}\left(EE_{i,j} - \frac{1}{r}\sum_{i=1}^{r}(EE_{i,j})\right)^2}, \tag{2.5}$$

- **The mean of the absolute values,** μ*** :** assesses the overall influence of the parameter on the output. This measure is an improvement of Morris method developed by [13]. The use of μ* solves the problem of the effects of opposite signs that occur when the model is non-monotonic canceling each other output.

$$\mu_j* = \frac{1}{r}\sum_{i=1}^{r}|EE_{i,j}|, \tag{2.6}$$

The results of Morris methodology implemented in the model are represented by the μ* vs. σ plane, illustrated in Fig. 2.5, which provides the following information:

- Parameters with low μ* and σ have negligible effect on the output.
- Parameters with large μ* but low σ reveal a significant and linear effects on the output.
- Parameters with large μ* and σ are considered to have significant and nonlinear effects on the output, or important interactions with other parameters.

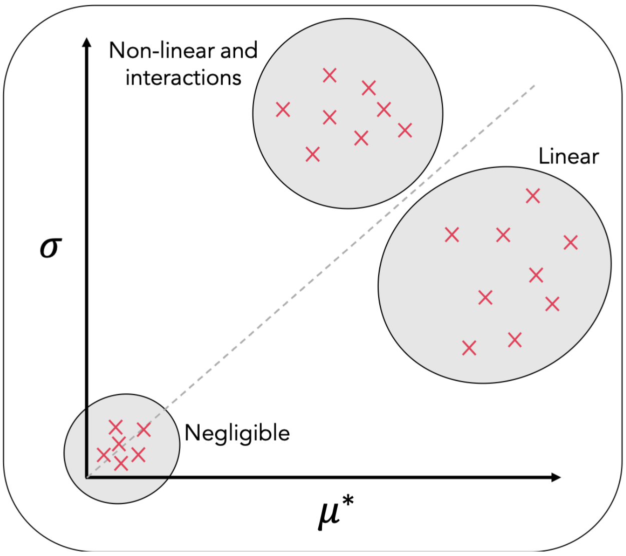

Figure 2.5: Example of the results of the Morris elementary effects method. The elementary effects of all parameters are analyzed in the $\mu^* - \sigma$ plane, identifying negligible effects, parameters with a linear effects and parameters that have a non-linear or interaction-related effect. Adapted from [3].

The Morris elementary method is an advantageous tool to examine and identify important parameters of a function or model. Due to its relative low computational requirements, it can be used prior to any heavy sensitivity analysis or extensive parameter exploration such as during a parameter estimation method. This method can quickly point out linear relations between parameters and outputs. On the other hand, the elementary effect method presents two specific disadvantages: it does not quantify the effect of a parameter, and it cannot discern between nonlinear relations and parameter interactions.

In order to complement the qualitative identification of the nature of the param-

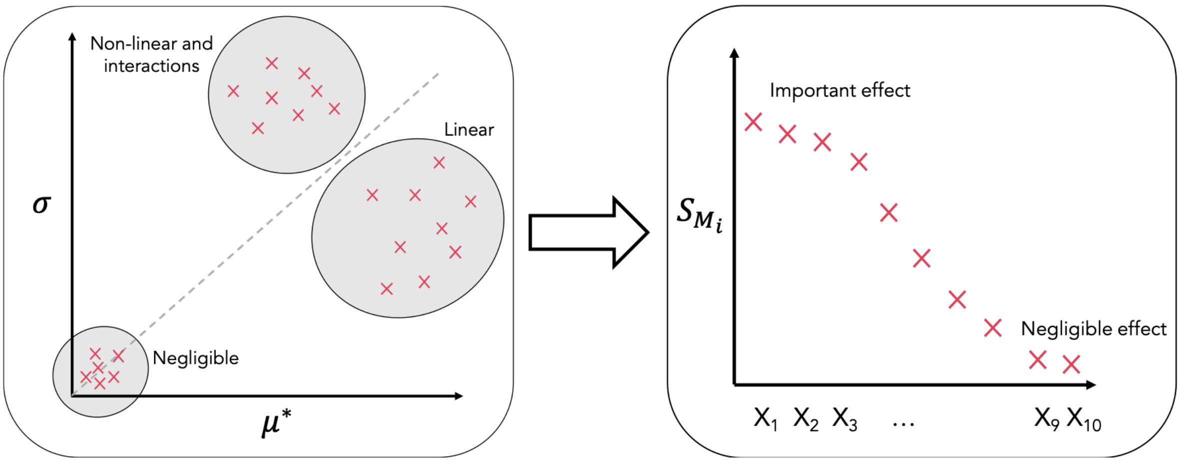

Figure 2.6: Identification of important and negligible parameters from the elementary effects. The right plot shows the same results of a Morris analysis, but ranked according to the S_{Mi} index (Eq. 2.7). Adapted from [3].

eter effects provided by Morris' method, the following sensitivity index was used:

$$S_{Mi} = \sqrt{(\mu_i^*)^2 + (\sigma_i)^2}\,, \tag{2.7}$$

applied to all parameters X_i. Then, parameters are sorted according to their S_{Mi}, as illustrated in Fig. 2.6. This index, which has been used in other modeling applications [14, 15] provides a rank of the parameter effects; parameters with a high sensitivity or strong interactions will have a high S_{Mi}, while unimportant ones are associated with a low S_{Mi}.

2.3.2 Parameter Identification

The parameter identification or optimization is a process that consists in the selection of the best estimation of the parameters' values $\mathbf{P}_{\text{opt}}$, from some set of available boundaries, that minimize a specific cost function g_ϵ in order to obtain an output $O_{\text{sim}}(\mathbf{P})$ that well agrees with the clinical data O_{obs}:

$$\mathbf{P}_{\text{opt}} = \underset{\mathbf{P}\in\mathbb{P}}{\arg\min}\; g_\epsilon(O_{\text{sim}}(\mathbf{P}), O_{\text{obs}}) \tag{2.8}$$

The field of mathematical optimization offers a vast choice of methods and algorithms that solve this kind of problems: analytic approaches, iterative methods, gradient-based methods, deterministic and stochastic approaches, among others [16]. However, not all of these methods are appropriate for the problem of parameter identification because: *i)* for the clinical applications of this manuscript, the dimensionality of the problem is high enough to forbid the employment of methods whose computational complexity is exponential with respect to the number of parameters, *ii)* the nature of the underlying equations are either non-linear, discontinuous or not well understood, and *iii)* the objective functions and constraints are the result of complex model equations which complicate the calculation of their derivatives or partial derivatives.

These limitations quickly discard classical optimization methods, such as Newton's method, or Lagrange multipliers; linear programming approaches, such as the simplex algorithm [17]; and exhaustive exploration approaches, such as branch-and-bound methods [18]. The remaining methods include approaches that approximate numerically the derivatives of the objective function, methods that use an heuristic to select interesting points in the parameter space, and methods based on a stochastic process.

2.3.2.1 Deterministic approaches

In this categorization of optimization techniques, deterministic approaches are defined to provide a contrast to stochastic approaches: these methods find the optimal or a sub-optimal solution to Eq. 2.8 with a process that does not rely on a random behavior. Algorithms that calculate or approximate derivatives and gradients fall into this category, as the gradient descent method. The hill-climbing algorithm [19] and the Nelder-Mead algorithm [20] are also popular methods that use deterministic approaches.

In general, deterministic methods are interesting because they eventually converge to a solution and do not need much information regarding the objective functions. However, the main disadvantages of these methods are: *i)* the gradient estimations and the heuristics used require several evaluations of the objective function, which becomes problematic when the dimensionality of the parameter space is considerable, and *ii)* the convergence of these methods is not guaranteed: it depends on the initial point, which yields a convergence towards a local minimum, where the algorithm remains stuck.

2.3.2.2 Stochastic approaches

Stochastic search approaches are interesting when the parameter space and objective function are not well understood, or when the parameter exploration requires random perturbations in order to avoid local minima.

A notable and popular stochastic approach is the particle swarm optimization [21]: an iterative procedure where a list of solutions is maintained and each candidate solution *wanders* the parameter space with a behavior that mixes exploration and attraction to good solutions. The converge of approaches that constantly evolve a list of candidate solutions is not guaranteed either; it mostly depends on a good choice of the algorithm parameters, principally the size of the candidate solution list and the number of iterations. However, stochastic approaches are praised for their ability to constantly explore the parameter space and avoid local minima.

2.3.2.3 Evolutionary algorithms

Within the stochastic approaches, evolutionary algorithms stand out for their original foundations. Evolutionary algorithms (EA) follow the approach of maintaining a set of candidate solutions, termed *population*, and repeatedly evolving this population with processes inspired by biological evolution: selection of the fittest, reproduction, recombination and mutation.

Evolutionary algorithms (EA) are methods of optimization and search for solutions based on the postulates of biological evolution established by Darwin in 1859. They are mainly used in problems with extensive and non-linear search spaces (domain of the function to be optimized), where other methods are not able to find solutions in a reasonable time. These algorithms are modeled computationally simulating the natural selection and cross-linking of species through genetic recombination and mutation [22].

Among the wide range of algorithms classified as EA, the most popular group used in optimization is the genetic algorithms (GA), initially conceived in [23] and thoroughly formalized in [24].

These algorithms are characterized by the existence of *individuals* or chromosomes in a *population*. These individuals represent the candidate solutions to the optimization problem in the form of genetic information, or *alleles*.

The *fitness* function determines the quality of the solutions or in other words the degree of adaptation of an individual to its environment. Based on this fitness, some of the better candidates are chosen to seed the next generation by applying recombination and/or mutation to them.

The *recombination* is an operator that mixes the information of two or more selected candidates generating one or more new candidates. And the *mutation* consists of a random change applied to a candidate to generate a new one. Executing recombination and mutation leads to a set of new candidates that compete with the old ones for a place in the next generation. Given that individuals who represent the most appropriate solutions (best fitness) to the problem are more likely to survive, the population gradually improves.

The population evolves as a result of the following procedure, illustrated in Fig. 2.7:

1. An initial population with N individuals is initialized, where each individual contains a random value for each one of its alleles. This generates a first generation of possible solutions.
2. Each individual of the population is assigned with a value that measures its *fitness*, a quantification of how good the individual is. The fitness value of an individual directly affects its chances to survive and reproduce. The calculation of the fitness requires the evaluation of the target function g_ϵ, but it can also be affected by other variables.
3. An internal variable that counts the number of generation is incremented. This variable can be useful for the stopping criteria.
4. According to their fitness and a stochastic process, a selection of individuals is performed. This phase designates pairs of individuals that will reproduce.
5. For each pair of selected individuals a reproduction operation generates two new individuals whose alleles are a combination of the two progenitors. This reproductive process occurs with a predefined probability p_c for each pair of individuals. Newly generated individuals may go through a mutation process, with another predefined probability p_m, which slightly modifies one or more of its alleles. The probabilities p_c and p_m directly control the exploration of new solutions. At the end of this stage, $2N$ individuals exist: the parent population of size N and a new offspring population of the same size.
6. All new generated individuals are evaluated; their fitness is determined as well.
7. At this point, different strategies are possible: either the new population completely replaces the old population, or a replacement procedure that accounts for each individual fitness selects and discards all individuals to produce the next generation, a population of size N.
8. Finally, if a stopping criteria is met, the algorithm stops or, in the contrary, the algorithm restarts from step 3. Possible stopping criteria include a maximum number of generations (i.e. iterations) or when the individuals of the population have reached a certain fitness value.

As other stochastic approaches, EAs cannot assure convergence toward the optimal solution and their performance depend on a good choice of the EA parameters. Nevertheless, they present an interesting compromise of space exploration, number of evaluations and quality of the solutions found, and they has been successfully used for parameter identification in other application [25].

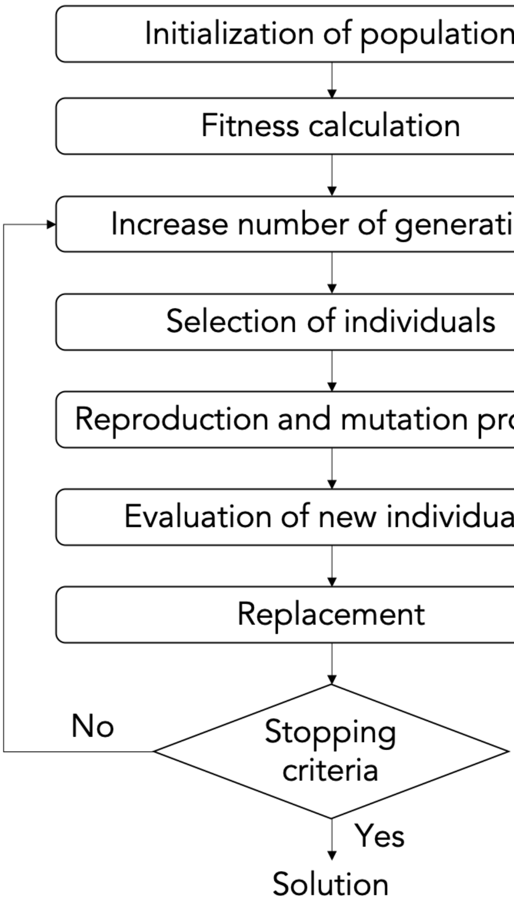

Figure 2.7: General scheme of genetic algorithms. Adapted from [3].

2.3.2.4 Proposed approach

Identification strategies, based on evolutionary algorithms, were implemented in this thesis in order to obtain patient-specific simulations. Based on the results of the sensitivity analysis, a reduced group of parameters are selected for patient-specific model identification, reducing computational cost and calculation time.

The objective function $g_\epsilon(O_{\text{sim}}(\mathbf{P}), O_{\text{obs}})$ used for the parameter identification will be defined in the next two chapters where patient-specific identification is performed for the two clinical applications addressed in this thesis. To implement the parameter identification in an efficient way, parallel optimization library PAGMO was used.

Parallel optimization library PAGMO

PAGMO is a scientific library for massively parallel optimization that can be used in `C++` environments. PAGMO uses efficient implementations of bio-inspired and evolutionary algorithms in order to solve constrained, unconstrained, single objective, multiple objective, continuous and integer optimization problems.

For the implementation of an optimization problem, first, the user must define the parameters $\mathbf{P}$ that wish to be identified in order to minimize a cost function g_ϵ also proposed by the user. The optimization problem is subject to the boundary parameters values fixed by the user $[lb, ub]$.

The optimization problem (Fig. 2.8) is then evaluated in the island I_i. Each island is an instance of the optimization problem and it contains *i)* the type (evolutionary algorithms,...) and properties (number of generations, ...) of the algorithm used to solve the optimization problem and *ii)* a population of N individuals. The population of individuals are considered potential candidates to solve the optimization problem. Each individual is determined by: *i)* a unique ID used to track it across generations and migrations, *ii)* a chromosome, which is the vector that contains the identified parameters, and *iii)* the fitness that determines the quality of the chromosome.

The collection of islands represents an archipelago A, which provides a convenient way to perform multiple optimizations in parallel. The connections between islands are denominated migrations. From each island the individual with the best fitness is chosen to replace the worst individual of the contiguous island. Then the population continuously evolve for generations and migrations until the stopping criteria is met.

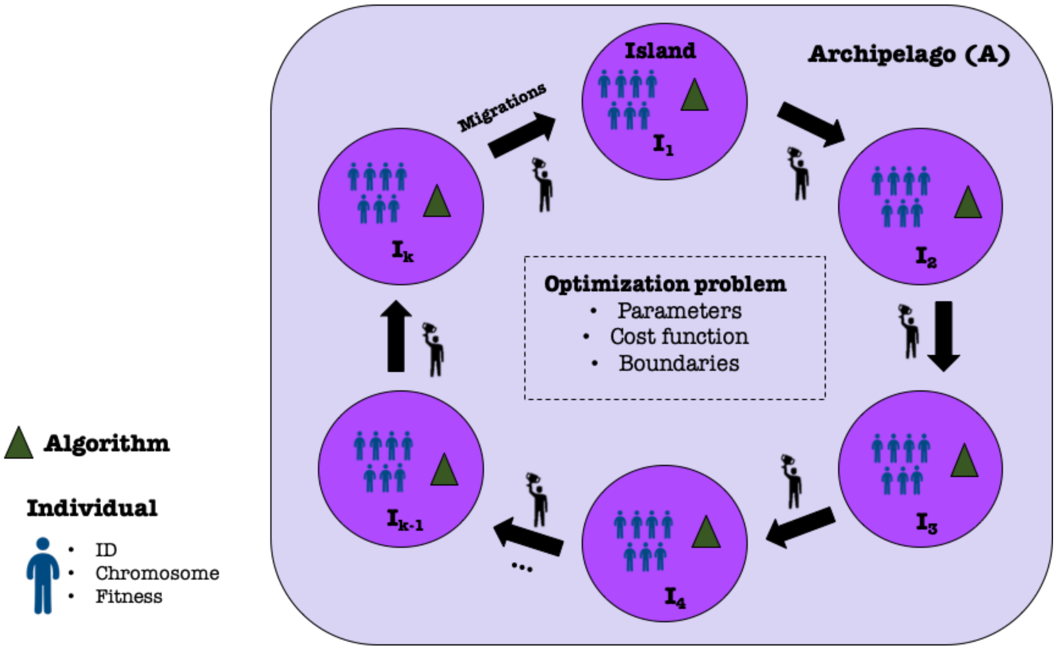

Figure 2.8: General scheme for PAGMO. Each island $I_i, i = 1, ...k$ contains an algorithm and a population of N individuals. In a migration, the individual with the best fitness is chosen to replace the worst individual of the contiguous island.

For this work, M2SL was integrated in the optimization problem class of PAGMO, in order to include the model simulation in the identification algorithm.

2.4 Conclusion

Decisions such as the type of model, the algorithms implemented and the tools used must be studied and chosen according to the specific application and the different processes desired to interpret.

Both the modeling and simulation tools and the analysis of parameters are essential for proposing a computational model capable of reproducing and predicting the mechanisms and functions, in this case, of the cardiovascular system. Sensitivity analysis and parameter identification are complementary and widely used techniques to improve the efficiency and predictions of the computational models. They are also practical for patient-specific simulations, where simulated data seeks to approximate clinical data.

M2SL is a powerful environment that allows submodels coupling, which is particularly interesting in this work since different mechanisms are involved in cardiac function. Moreover, M2SL allows a simple coupling of the model with methods of analysis of the model parameters using PAGMO, which makes it a very useful tool, and therefore, the chosen tool to simulate the CVS and achieve the objectives of this thesis.

Bibliography

[1] M. Calder, C. Craig, D. Culley, R. de Cani, C. A. Donnelly, R. Douglas, B. Edmonds, J. Gascoigne, N. Gilbert, C. Hargrove, D. Hinds, D. C. Lane, D. Mitchell, G. Pavey, D. Robertson, B. Rosewell, S. Sherwin, M. Walport, and A. Wilson, "Computational modelling for decision-making: where, why, what, who and how," *Royal Society Open Science*, vol. 5, no. 6, p. 172096. Publisher: Royal Society.

[2] A. Defontaine, *Modelisation multiresolution et multiformalisme de l'activite electrique cardiaque*. These de doctorat, Rennes 1, feb 2006.

[3] D. Ojeda Avellaneda, *Multi-resolution physiological modeling for the analysis of cardiovascular pathologies*. These de doctorat, Rennes 1, Dec. 2013.

[4] H. Vangheluwe, *Multi-Formalism Modelling and Simulation*. These de doctorat, Universiteit Gent, Jan. 2001.

[5] A. I. Hernández, V. Le Rolle, D. Ojeda, P. Baconnier, J. Fontecave-Jallon, F. Guillaud, T. Grosse, R. G. Moss, P. Hannaert, and S. R. Thomas, "Integration of detailed modules in a core model of body fluid homeostasis and blood pressure regulation," *Progress in Biophysics and Molecular Biology*, vol. 107, pp. 169–182, Oct. 2011.

[6] A. I. Hernández, V. Le Rolle, A. Defontaine, and G. Carrault, “A multiformalism and multiresolution modelling environment: application to the cardiovascular system and its regulation,” *Philosophical Transactions of the Royal Society A: Mathematical, Physical and Engineering Sciences*, vol. 367, pp. 4923–4940, Dec. 2009. Publisher: Royal Society.

[7] B. P. Zeigler, H. Praehofer, and T. Kim, *Theory of Modeling and Simulation*. Academic Press, 2nd edition ed., Jan. 2000.

[8] EPA, “Guidance on the development, evaluation, and application of environmental models,” tech. rep., U.S. Environmental Protection Agency, 2009.

[9] A. Saltelli, M. Ratto, T. Andres, F. Campolongo, J. Cariboni, D. Gatelli, M. Saisana, and S. Tarantola, *Global sensitivity analysis: the primer*. Wiley-Interscience, 2008.

[10] I. M. Sobol, “Global sensitivity indices for nonlinear mathematical models and their monte carlo estimates,” *Mathematics and computers in simulation*, vol. 55, no. 1-3, pp. 271–280, 2001.

[11] I. M. Sobol, “Sensitivity estimates for nonlinear mathematical models,” *Mathematical Modelling and Computational Experiments*, vol. 1, no. 4, pp. 407–414, 1993.

[12] M. D. Morris, “Factorial Sampling Plans for Preliminary Computational Experiments,” *Technometrics*, vol. 33, pp. 161–174, May 1991. Publisher: Taylor & Francis _eprint: https://www.tandfonline.com/doi/pdf/10.1080/00401706.1991.10484804.

[13] F. Campolongo, J. P. C. Kleijnen, and T. Andres, “Screening methods,” *Sensitivity Analysis*, pp. 65–80, 2000. Publisher: John Wiley & Sons.

[14] S. Schreider and R. Braddock, “Application of the morris algorithm for sensitivity analysis if the realm model for the goulburn irrigation system,” *Environmental Modeling and Assessment*, vol. 11, no. 4, pp. 297–313, 2011.

[15] J. Duarte, M. Vélez-Reyes, S. Tarantola, F. Gilbes, and R. Armstrong, “A probabilistic sensitivity analysis of water-leaving radiance to water constituents in coastal shallow waters,” in *Proceedings of SPIE*, vol. 5155, p. 162, 2003.

[16] G. L. Nemhauser, A. R. Kan, and M. Todd, *Optimization, volume 1 of Handbooks in operations research and management science*. North-Holland, Amsterdam, 1989.

[17] G. B. Dantzig, *Linear programming and extensions*. Princeton university press, 1998.

[18] A. H. Land and A. G. Doig, “An automatic method of solving discrete programming problems,” *Econometrica: Journal of the Econometric Society*, pp. 497–520, 1960.

[19] M. Minsky, “Steps toward artificial intelligence,” *Proceedings of the IRE*, vol. 49, no. 1, pp. 8–30, 1961.

[20] J. Nelder and R. Mead, “A simplex method for function minimization,” *The computer journal*, vol. 7, no. 4, p. 308, 1965.

[21] R. Eberhart and J. Kennedy, “A new optimizer using particle swarm theory,” in *Micro Machine and Human Science, 1995. MHS’95., Proceedings of the Sixth International Symposium on*, pp. 39–43, IEEE, 1995.

[22] T. Bäck and H.-P. Schwefel, “An Overview of Evolutionary Algorithms for Parameter Optimization,” *Evolutionary Computation*, vol. 1, pp. 1–23, Mar. 1993. Conference Name: Evolutionary Computation.

[23] J. Holland, *Adaptation in Natural and Artificial Systems*. Michigan Press, 1975.

[24] D. E. Goldberg, *Genetic algorithms in search, optimization, and machine learning*. Addison-Wesley Longman Publishing Co., Inc., 1st ed., 1989.

[25] J. Fleureau, *Intégration de données anatomiques issues d’images MSCT et de modéles électrophysiologique et mécanique du coeur*. PhD thesis, Université de Rennes 1, 2008.

3

MODEL-BASED ESTIMATION OF LEFT VENTRICULAR PRESSURE AND MYOCARDIAL WORK IN AORTIC STENOSIS

Aortic stenosis (AS) is characterised by a narrowing of the aortic valve opening, which induces a left ventricular (LV) pressure overload. The development of LV hypertrophy in AS is accompanied by coronary microcirculatory dysfunction [1] that may gradually affect systolic and diastolic function [2]. LV ejection fraction (LVEF) is used routinely to assess LV systolic function and is an important parameter for prognosis stratification [3]. However, LVEF depends not only upon the contractility of LV, but also on loading conditions. In fact, ejection fraction may appear to be preserved despite underlying reduced contractility.

The characterisation of myocardial dysfunction is of primary importance to identify patients with reduced contractility. Speckle-tracking echocardiography (STE) assessment of myocardial strain usually provides a better quantification of systolic function than global LVEF [4]. Although strain echocardiography can provide prognostic information in patients with AS [5], the shortening indices, calculated from cardiac strains, do not reflect myocardial work or oxygen demand. As opposed to the normal LV, where all segments contract almost synchronously and myocardial energy is used effectively, regional dysfunction, that could be induced by myocardial fibrosis [6], could bring a significant loss of efficient work. For instance, the impairment of myocardial diastolic and systolic function, due to fibrosis [7], have shown to induce significant mechanical dispersion in patients with severe AS [8].

Recently, Russell et al [9, 10] have proposed a non-invasive method for LV work analysis, which is based upon an estimated LV pressure curve. Since strain is largely influenced by LV afterload [11], model-based myocardial work might be a robust complementary tool, taking into account AS severity and arterial pressures values. In previous works of our team, we have shown that the non-invasive estimation of global myocardial work, when using an LV pressure curve estimation as proposed in [9], is correlated with that obtained when using the observed invasive LV pressure curve, in the context of cardiac resynchronization therapy [12]. However, the accuracy of estimated LV pressure has never been evaluated in the case of aortic stenosis, where high pressure gradients could be observed between LV and the aorta [13]. The experimental observation of LV pressure is notably difficult to perform clinically because it requires an invasive, intraventricular measurement. As a consequence, it is necessary to propose novel tools to assess non-invasive LV pressure and to calculate myocardial work in the case of AS.

The first objective of this chapter is to propose a model-based estimation of LV pressure in the case of AS. Previous works [14, 15] have already shown that lumped-parameter models of ventricular-vascular coupling are able to provide a good agreement between the estimated and the measured left ventricular and aortic pressure waveforms. Based on these papers and previous works of our team [16, 17, 18], a model-based approach is proposed here, including a multiformalism model of the cardiovascular system and a parameter identification strategy in order to: 1) estimate the LV pressure waveform from the experimental LV pressure curve as well as systolic and diastolic aortic pressure values, 2) assess LV pressure waveform from only systolic and diastolic aortic pressure values.

The second objective of this chapter is to propose a novel tool to estimate myocardial work in AS. Work indices, as proposed in [9, 10] and validated in [12], were calculated from non-invasive model-based LV pressure and compared with indices evaluated from experimental signals.

3.1 Materials and methods

3.1.1 Experimental data

3.1.1.1 Study population

We included 35 adults (≥18 years old) with severe (aortic valve area (AVA) ≤ 1cm^2, n=33) and moderate (n=2) aortic stenosis who underwent a coronary angiography with left heart catheterization. Table 3.1 summarizes patients' clinical characteristics for the two methods used in this study. We excluded patients with concomitant significant aortic regurgitation and mitral stenosis. The study was carried out in accordance with the principles outlined in the Declaration of Helsinki on research in human subjects and with the procedures of the local Medical Ethics Committee (Person Protection Committee West V—CPP Ouest V, authorization number: 2014-A01331-456). All patients were informed and a written consent was obtained.

Table 3.1: AS patients' clinical characteristics.

	Age *years old*	**Male sex** *n (%)*	**BSA (body surface area)**	**NYHA class I/II/III,** *n*
Database 1 (n=12)	78.16 ± 5.50	7 (58.3%)	1.75 ± 0.10	0/8/4
Database 2 (n=23)	82.7 ± 3.57	10 (43.5%)	1.78 ± 0.18	2/9/12

3.1.1.2 Echocardiography

All patients underwent a standard Trans-Thoracic Echocardiography (TTE) using a Vivid S6, E7 or E9 ultrasound system (General Electric Healthcare, Horten, Norway). Images were recorded on a remote station for off-line analysis by dedicated software (EchoPAC PC, version BT 202, General Electric Healthcare, Horten, Norway). The analysis of aortic and mitral valve events during a complete TTE loop [mitral valve closure (MVC), aortic valve opening (AVO), aortic valve closure (AVC), mitral valve opening (MVO)] was performed in apical long-axis view and individual valvular events were manually segmented. Standard STE analysis was applied in order to extract regional myocardial strain curves. Also aortic stenosis analysis was performed to estimate the AVA (cm^2).

3.1.1.3 Experimental pressure

The left heart catheterization (LHC) was performed via a retrograde access from the radial artery with a 5 French Judkin R4 catheter (ICU Medical, San Clemente, CA, USA) placed at the mid LV cavity using fluoroscopic screening. Before coronary angiography, transducers were calibrated, with a 0-level set at the mid-axillary line. In a second time, the instantaneous systolic and diastolic arterial pressure values were estimated by a brachial artery cuff. The experimental data set includes the invasive measured ventricular pressure P_{LV}^{exp}, and the systolic $P_{ao,sys}^{exp}$ and diastolic $P_{ao,dias}^{exp}$ arterial pressures non-invasively estimated.

3.1.2 Computational model

Four main sub-models were created and coupled: *i)* cardiac electrical system, *ii)* elastance-based cardiac cavities, *iii)* systemic and pulmonary circulations and *iv)* heart valves. The first three submodels are strongly based on our previous works [19, 20, 21, 16, 17, 18]. The model of the heart valves was adapted from [22].

3.1.2.1 Cardiac electrical system

The proposed model of the cardiac electrical activity, is based on a set of coupled automata [19, 20] (Fig. 3.1). Each automaton represents the electrical activation state of a given myocardial tissue, covering the main electrophysiological activation periods: slow diastolic depolarisation (SDD), upstroke depolarization (UDP), absolute refractory (ARP) and relative refractory (RRP). Briefly, the state of the cellular automata cycles through these four stages, sending an output stimulation signal to neighboring cells when a given cell is activated (end of UDP phase).

The whole simplified model consists of nine automata representing: the sinoatrial node (SAN), right and left atria (RA and LA), the atrioventricular node (AVN), upper bundle of His (UH), bundle branches (RBB and LBB), and both ventricles (RV and LV). The electrical activation of the automata is used to synthesize an electrocardiogram (ECG), from which the QRS peak was extracted to synchronize the experimental and simulated signals.

3.1.2.2 Elastance-based cardiac cavities

Although the literature offers a wide range of cardiovascular models, elastance-based models offer a good compromise between complexity and number of parameters [23, 16, 17, 18]. Ventricle pressures are represented by a combination of the end-systolic (es) and end-diastolic (ed) pressure-volume relationships [24]:

$$P_{es,lv}(V,t) = E_{es,lv}(V(t) - V_{d,lv}), \tag{3.1}$$

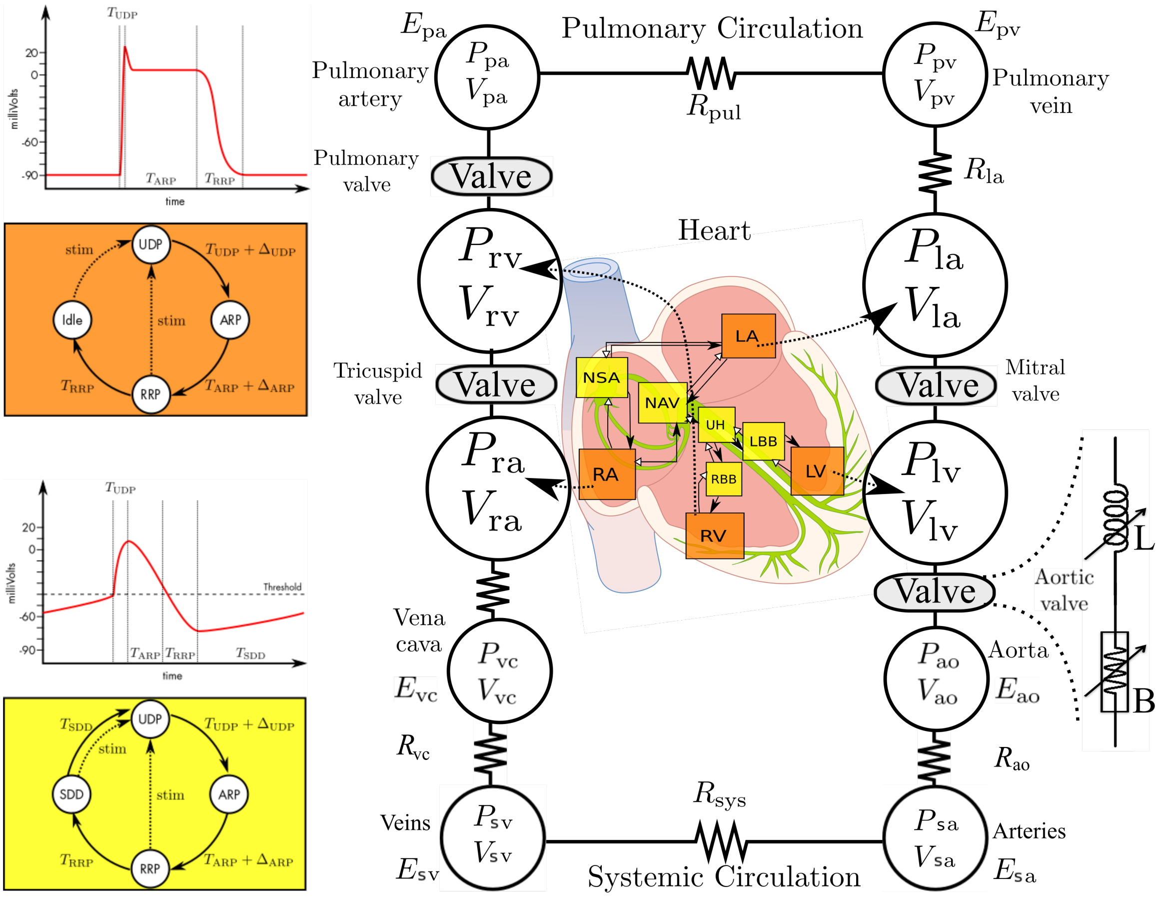

Figure 3.1: *Left panel*: State diagram of the cellular automata that represent nodal cells (yellow, botton) and myocardial cells (orange, top) and diagrams showing the correspondence of the automata's transition parameters with the myocardial action potential dynamics. *Right panel*: Closed-loop model of the cardiovascular system. E: elastance; R: resistance; P: pressure; V: volume; pul: pulmonary; sys: systemic; pv: pulmonary vein; pa: pulmonary artery; ao: aorta; sa: systemic artery; sv: systemic veins; vc: vena cava; LA: left atrium; LV: left ventricle; RA: right atrium; RV: right ventricle. In the middle, a representation of the cardiac electrical system. On the right, a representation of the heart valve model.

$$P_{ed,lv}(V,t) = P_{0,lv}\left(e^{\lambda_{lv}(V(t)-V_{0,l})} - 1\right) \tag{3.2}$$

In Eq. 3.1, systolic pressure $P_{es,lv}$ is defined as a linear relationship with the ventricular volume V, determined by the systolic elastance $E_{es,lv}$ and the volume intercept $V_{d,lv}$. Eq 3.2 also describes the nonlinear diastolic pressure defined by a gradient $P_{0,lv}$, curvature λ_{lv} and volume intercept $V_{0,lv}$.

The instantaneous pressure of the ventricle is then calculated as :

$$P_{lv}(V,t) = e_{lv}(t)P_{es,lv}(V,t) + (1 - e_{lv}(t))P_{ed,lv}(V,t) \tag{3.3}$$

where $e_{lv}(t)$ is the driver function that controls time-variant elastance. In this work we have selected a “double Hill" driver function [25] that best fits our observed data:

$$e_{lv}(t) = k \cdot \left[\frac{\left(\frac{t}{\alpha_1 T}\right)^{n_1}}{1 + \left(\frac{t}{\alpha_1 T}\right)^{n_1}}\right] \cdot \left[\frac{1}{1 + \left(\frac{t}{\alpha_2 T}\right)^{n_2}}\right] \tag{3.4}$$

The first and second terms in Eq. 3.4 represent ventricle contraction and relaxation, respectively. k is a scaling factor that defines the maximal value of elastance, T is the heart period, α_1, α_2 are shape parameters, and n_1,n_2 control the steepness of the curve.

To account for the mechanical function of the atria, the atrial pressure P_{la} is represented as a linear function of its instantaneous volume V_{la}, whose slope E_{la} represents the elastic properties of the atrial wall:

$$P_{la}(V_a,t) = E_{la}(t) \cdot (V_{la}(t) - V_{d,la}), \tag{3.5}$$

$$E_{la}(t) = E_{la,max}\left(e_{la}(t) + \frac{E_{la,min}}{E_{la,max}}\right) \tag{3.6}$$

where $e_{la}(t)$ is a Gaussian driving function that cycles between atrial diastole and systole:

$$e_{la}(t) = \exp\left(-B_{la} \cdot (t - C_{la})^2\right) \tag{3.7}$$

Using B_{la} and C_{la}, it is possible to control the rise and peak of the atrial systole.

3.1.2.3 Systemic and pulmonary circulations

Concerning the circulatory models [21], the volume of each cardiac or vessel chamber is calculated from the net flow: $\Delta V(t) = \int (Q_{in} - Q_{out})\, \mathrm{d}t$. The flows are defined by the pressure gradient across chambers and a resistance: $Q = {}^{\Delta P}/_{R}$. The pressure of arterial and venous vessels are defined as an elastance dependent linear relationship, similar to Eq. 3.1. The circulatory model allows for the simulation of systolic and diastolic aortic pressures ($P^{model}_{ao,sys}$ and $P^{model}_{ao,dias}$).

3.1.2.4 Cardiac Valves

The CVS model was coupled to a detailed representation of the heart valves dynamics (mitral, aortic, tricuspid and pulmonary) according to [22]. The relation between the pressure gradient (ΔP) and the fluid flow (Q) across an open valve is approximated by the Bernoulli equation (Eq. 3.8):

$$\Delta P = BQ|Q| + L\frac{dQ}{dt}, \tag{3.8}$$

$$B = \frac{\rho}{2A^2_{eff}},\ L = \frac{\rho l_{eff}}{A_{eff}} \tag{3.9}$$

where B and L are respectively the Bernoulli resistance and the blood inertance. Parameter ρ stands for the blood density, A_{eff} is the effective cross-sectional area of the valve (eq.3.10) and l_{eff} is the effective length of the valve:

$$A_{eff}(t) = [A_{eff,max}(t) - A_{eff,min}(t)]\,\xi(t) + A_{eff,min}(t) \tag{3.10}$$

$$\frac{d\xi}{dt} = \begin{cases} (1-\xi)K_{vo}\Delta P, & if \Delta P > 0 \\ \xi K_{vc}\Delta P, & if \Delta P \leq 0 \end{cases} \tag{3.11}$$

$A_{eff,max}$ and $A_{eff,min}$ are the maximum and minimum effective areas. The rate of opening $\xi(t)$ describes the dynamic of the valve position (Eq. 3.11), in response to ΔP. K_{vo} and K_{vc} are the rate coefficients for valve opening and closure, respectively.

3.1.3 Estimation of myocardial work

Segmental myocardial work, as proposed by Russell et al [10], could be calculated from 1) the clinical strain signals, deduced from TTE, and 2) the LV pressure obtained invasively by catheterization (P_{LV}^{exp}) or the patient-specific pressure (P_{LV}^{model}) from the model-based approach. The instantaneous power was first obtained by multiplying the strain rate, obtained by differentiating the strain curve, and the instantaneous LV pressure. Then, segmental myocardial work was calculated by integrating the power over time, during the cardiac cycle from mitral valve closure until mitral valve opening.

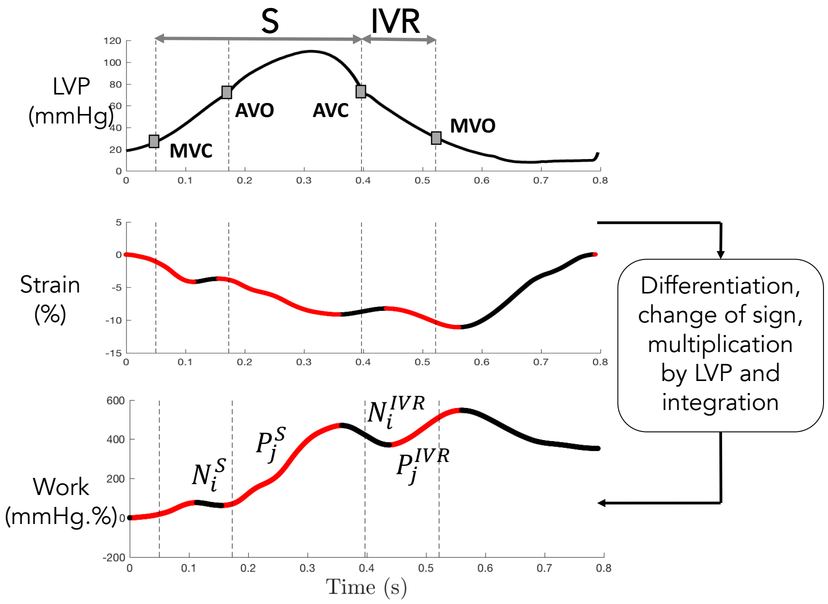

Figure 3.2: Calculation of positive and negative segmental work. Positive (P_j) and negative (N_i) work are marked respectively as red and black. Phase S corresponds to isovolumic contraction and ejection. IVR is the isovolumic relaxation. S phase is defined by the time interval spanning from MVC to AVC, whereas the IVR phase is defined between AVC and MVO.

Positive and negative work [12] were determined as the ascending and descending parts of the curves (Figure 3.2), during isovolumic contraction and ejection (S phase) and isovolumic relaxation (IVR phase). Then, positive segmental work W_p (respectively W_n) is defined as the sum of positive (respectively negative) variations for each segment k and for each phase (S and IVR) :

$$W_{p,k}^{S} = \sum_{i} P_{i,k}^{S},\ W_{n,k}^{S} = \sum_{j} N_{j,k}^{S}, \tag{3.12}$$

$$W_{p,k}^{IVR} = \sum_{i} P_{i,k}^{IVR},\ W_{n,k}^{IVR} = \sum_{j} N_{j,k}^{IVR} \tag{3.13}$$

where P_i (respectively N_j) is the variation associated with each ascending (respectively descending) parts i (respectively j) of the segmental work (Figure 3.2). The indices i (respectively j) are comprised between 1 and the total number of ascending (respectively descending) parts. Finally, global constructive (GCW) and wasted (GWW) work are defined as mean values over all segments:

$$GCW = \frac{1}{k}\sum_{k=1}^{K}(W_{p,k}^{S} + W_{n,k}^{IVR}), \tag{3.14}$$

$$GWW = \frac{1}{k}\sum_{k=1}^{K}(W_{n,k}^{S} + W_{p,k}^{IVR}) \tag{3.15}$$

where K is the total number of segments. GCW represents segmental shortening during the systole, i.e. effective energy for blood ejection, and lengthening during IVR, whereas GWW corresponds to segmental stretching during the systole, i.e. energy loss for blood ejection and shortening during the isovolumic relaxation phase. GWE is defined as the global work efficiency:

$$GWE = \frac{GCW}{GCW + GWW} \tag{3.16}$$

3.1.4 Model-based, patient-specific LV pressure estimation

3.1.4.1 Sensitivity analysis

The objective of the sensitivity analysis is to determine the sets of ventricular $\{\mathbf{X}_{LV}\}$ and circulatory $\{\mathbf{X}_{art}\}$ parameters that have the most important influence on the gradient of pressure ($\Delta P^{model} = max(P_{LV}^{model}) - P_{ao,sys}^{model}$) between LV and aorta. Using the Morris elementary effects method [26], described in section 4.5, the sensitivity of each parameter is estimated by repeated measurements of a simulation output Y with parameters **X**, while changing one parameter X_j at a time. Analysis were performed with $Y = \Delta P^{model}$ and, for each parameter X_j, the range of possible values was defined as ±30% of the initial values.

3.1.4.2 Parameter identification

3.1.4.2.1 Database 1: The parameter identification process is included into a Monte-Carlo cross-validation approach (Fig.3.3). Cross-validation methods consist on statistical techniques, mainly used in predictive models, to improve the estimation of the parameter values. Different cross-validation strategies exist to reduce the variability in the results. We implemented a K-fold cross-validation approach where the dataset is randomly divided into training and test subsets N times. Each time the training and the test sets are distributed in a different way and the validation process is repeated N times for each different pair of training and test subsets. Finally, the average measure across all N trials is computed. These methods avoid overfitting (the model performs well for the training set but poorly on the test set) and underfitting (the model performs poorly in the training and the test set) problems.

Hence, available data from the 12 patients were divided randomly into two sets of 6 patients (training and test sets). This random selection process was applied N times ($n \leqslant N$) and for each realization n a two-step procedure was applied. For all patients, the maximum effective area $A_{eff,max}$ parameter was fixed to the observed AVA, measured from TTE.

The following sections provide more details on the two steps.

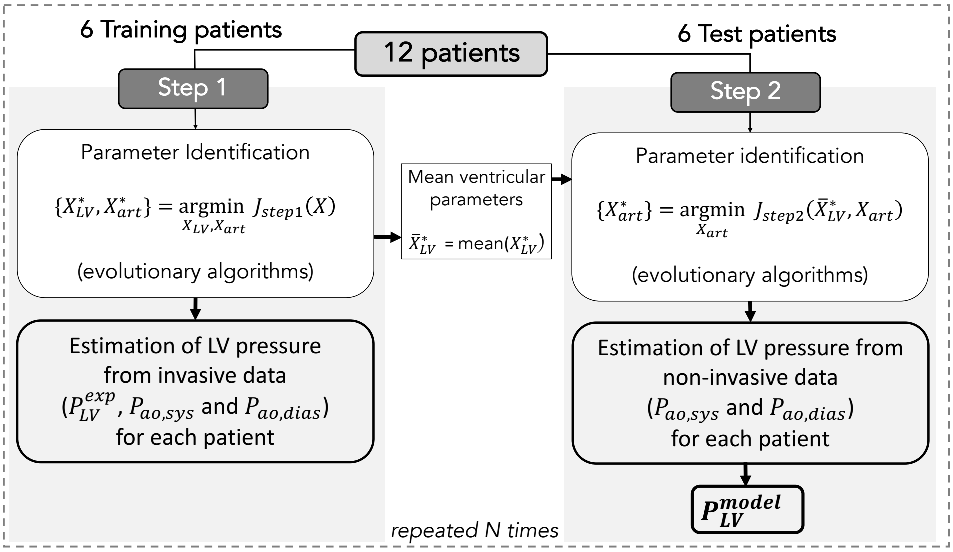

Figure 3.3: Two steps of the identification process. Step 1 consists in the minimization of J_{step1} for the identification of $\{\mathbf{X}_{LV}, \mathbf{X}_{art}\}$ from invasive LV pressure and non-invasive arterial pressure. Step 2 consists in the minimization of J_{step2} for the identification of $\{\mathbf{X}_{art}\}$ from non-invasive arterial pressure. Finally, P^{model}_{LV} is estimated for each patient from $\bar{\mathbf{X}}^*_{LV}$ and $\mathbf{X}^*_{art}$.

Step 1: For each training patient, a parameter identification stage was implemented to find the best set of parameters $\{\mathbf{X}^*_{LV}, \mathbf{X}^*_{art}\}$ that minimises the error function between simulation outputs and experimental signals:

$$J_{step1} = J_{PLV} + J_{Pao,sys} + J_{Pao,dias} \tag{3.17}$$

$J_{Pao,sys}$, $J_{Pao,dias}$ and J_{PLV} could be defined as:

$$J_{Pao,sys} = \mid P^{exp}_{ao,sys} - P^{model}_{ao,sys} \mid, \tag{3.18}$$

$$J_{Pao,dias} = \mid P^{exp}_{ao,dias} - P^{model}_{ao,dias} \mid, \tag{3.19}$$

$$J_{PLV} = \frac{1}{T_c} \sum_{t_e=0}^{T_c-1} \mid P_{LV}^{exp}(t_e) - P_{LV}^{model}(t_e) \mid \tag{3.20}$$

where t_e corresponds to the time elapsed since the onset of the identification period and T_c is the duration of a cardiac cycle. The error function J_{step1} was minimised using evolutionary algorithms (EA). These stochastic search methods are founded on theories of natural evolution, such as selection, crossover and mutation [27]. After this identification step, ventricular parameters were fixed equal to the average values over all the training patients ($\overline{\mathbf{X}}_{LV}^{*}$ = mean($\mathbf{X}_{LV}^{*}$)).

Step 2 : For each test patient, only circulatory parameters $\{\mathbf{X}_{art}\}$ were identified by minimising the error function:

$$J_{step2} = J_{Pao,sys} + J_{Pao,dias} \tag{3.21}$$

From the best set of parameters $\{\mathbf{X}_{art}^{*}\}$, LV pressure $P_{LV}^{model,i}$ was simulated for each test patient and for each iteration i of the 2-step identification algorithm. Then, $GCW^{model,i}$ and $GWW^{model,i}$ were calculated from $P_{LV}^{model,i}$ of each patient. Therefore, at the end of the N iterations, a set of i simulated pressure and work indices was generated for each patient and averaged markers were determined : $GCW^{model} = \overline{GCW^{model,i}}$, $GCW^{model} = \overline{GCW^{model,i}}$ and $GWE^{model} = \overline{GWE^{model,i}}$.

3.1.4.2.2 Database 2: The step 2, implemented on *database 1*, was also applied in the 23 patients (Fig. 3.4). For all patients, the maximum effective area $A_{eff,max}$ parameter was fixed to the observed AVA, measured from TTE. Ventricular parameters were fixed equal to the average values over the 12 patients (considered as training patients) from the *database 1* ($\overline{\mathbf{X}}_{LV}^{*}$ = mean($\mathbf{X}_{LV}^{*}$)). For each patient, circulatory parameters $\{\mathbf{X}_{art}\}$ were identified and from the best set of parameters $\{\mathbf{X}_{art}^{*}\}$, the LV pressure P_{LV}^{model} was simulated. Then, GCW^{model}, GWW^{model} and GWE^{model} were calculated for each patient. This process was applied once.

3.1.5 Comparison between simulations and experimental data

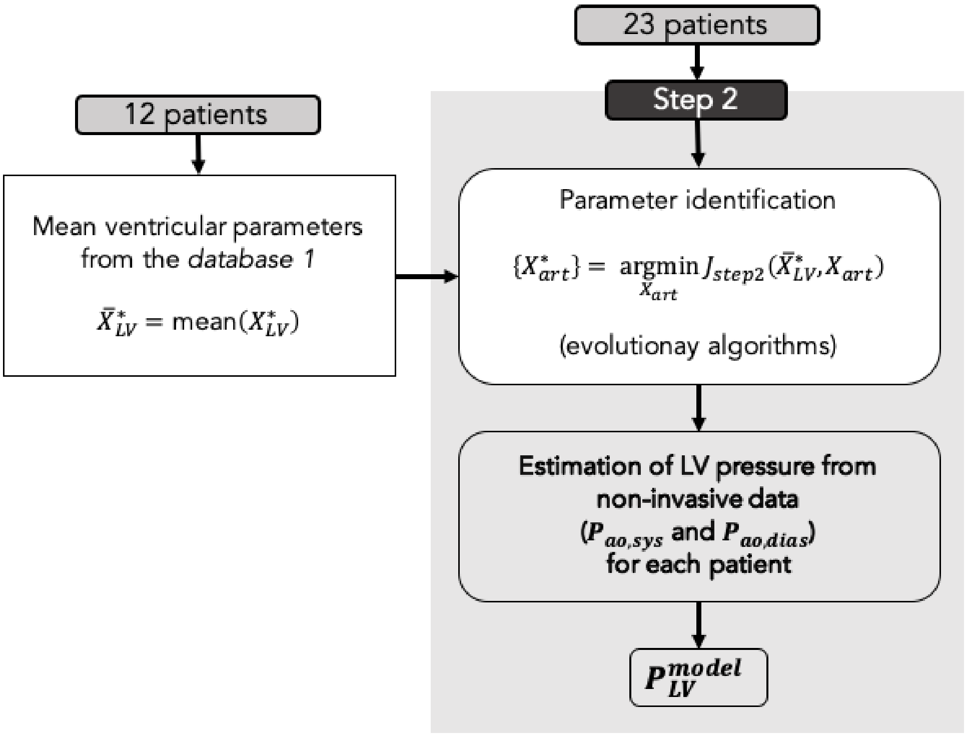

Figure 3.4: The identified mean ventricular parameters were calculated from the *database 1*. Step 2 was applied for the identification of $\{\mathbf{X}_{art}\}$ from non-invasive arterial pressures. Finally, P^{model}_{LV} is estimated for each patient from $\overline{\mathbf{X}}^*_{LV}$ and $\mathbf{X}^*_{art}$.

3.1.5.1 Comparison of estimated and measured pressures:

Inspired form [14], estimated P_{LV}, $P_{ao,sys}$ and $P_{ao,dias}$ were compared with measured pressures by calculating the total relative error defined as:

$$e_{\%} = 50\left(\frac{\|P^{exp}_{LV} - P^{model}_{LV}\|}{\|P^{exp}_{LV}\|}\right) + 50\left(\frac{\mid P^{exp}_{ao,sys} - P^{model}_{ao,sys}\mid}{\mid P^{exp}_{ao,sys}\mid} + \frac{\mid P^{exp}_{ao,dias} - P^{model}_{ao,dias}\mid}{\mid P^{exp}_{ao,dias}\mid}\right) \quad (3.22)$$

where $\|.\|$ stands for the vectorial 1-norm. A linear regression was performed on all the points from experimental and simulated pressure waveforms. The slope (β) and coefficient of determination (R^2) were deduced from a linear regression.

3.1.5.2 Comparison of estimated and measured work indices:

In this study, GCW, GWW, and GWE were calculated in two different manners : 1) GCW^{exp}, GWW^{exp} and GWE^{exp} using the invasive experimental pressure P^{exp}_{LV}, and 2) GCW^{model}, GWW^{model} and GWE^{model} using the proposed patient-specific pressure P^{model}_{LV} from the model-based approach.

The goodness of work estimations was evaluated by performing a linear regression using indices calculated from invasive experimental and the proposed model-based pressures. The shape of the pattern that the data points form on the diagram obtained from the linear regression determines the degree of correlation. The more the data points shape resembles a straight line, the higher is the degree of relationship. The correlation is also represented by a quantitative measure r^2, which varies from -1 to $+1$. The closer the coefficient r^2 is to $+1$, the greater is the strength of the linear relationship. The degree of correlation is high when the points plotted is close to the straight line and is positive when they show a rising tendency from the lower left-hand corner to the upper right-hand corner. The degree of correlation is small when the points are randomly distributed in space with any particular pattern and r^2 tending to 0.

It is important that two methods that are designed to measure the same property have a good correlation. However, a high correlation between the two methods does not necessarily imply that there is good agreement between them.

Therefore, Bland-altman (BA) plots were also presented for the three work indices. Bland Altman analysis assesses and quantifies the agreement between two methods of measurements. A XY graphical plot can represent Bland Altman analysis, where the X-axis express the mean of the two quantities ($(A+B)/2$) and Y-axis the differences between them ($A-B$). After the graph approach is obtained, the mean bias ($mean(A-B)$) is quantified and the limits of agreement are defined using the mean and standard deviation of the differences between the two measurements. The mean difference between the quantities allows identifying the estimated bias, and the standard deviation of the differences measures the random fluctuations around this mean. Finally, mean ± 1.96 standard deviation is used to define a 95% confidence interval. It means that if the data points are located between the 95% limits of agreement, this indicates that the two assay methods are systematically producing similar results. Therefore, Bland-Altman analysis is an appropriate way to evaluate the comparison between two measurements techniques and presents quantified measures to decide whether the new method is acceptable or not [28].

3.2 Results

3.2.1 Hemodynamic simulations

Fig. 3.5 illustrates the hemodynamic simulation results of the proposed computational model; the LV and aortic pressures in healthy and AS subjects. Concerning the healthy subject, systolic LV pressure is equal to 120 mmHg, and the aortic pressure varies between 50 and 120 mmHg. AS was represented as a decrease in the $A_{eff,max}$ parameter (from 2.5 to 0.75 cm^2). In Fig. 3.5, it is observed an important gradient pressure between LV (0-150 mmHg) and aorta (50-110 mmHg), characteristic of an AS, in which the narrowing of the aortic valve opening evokes an LV pressure overload.

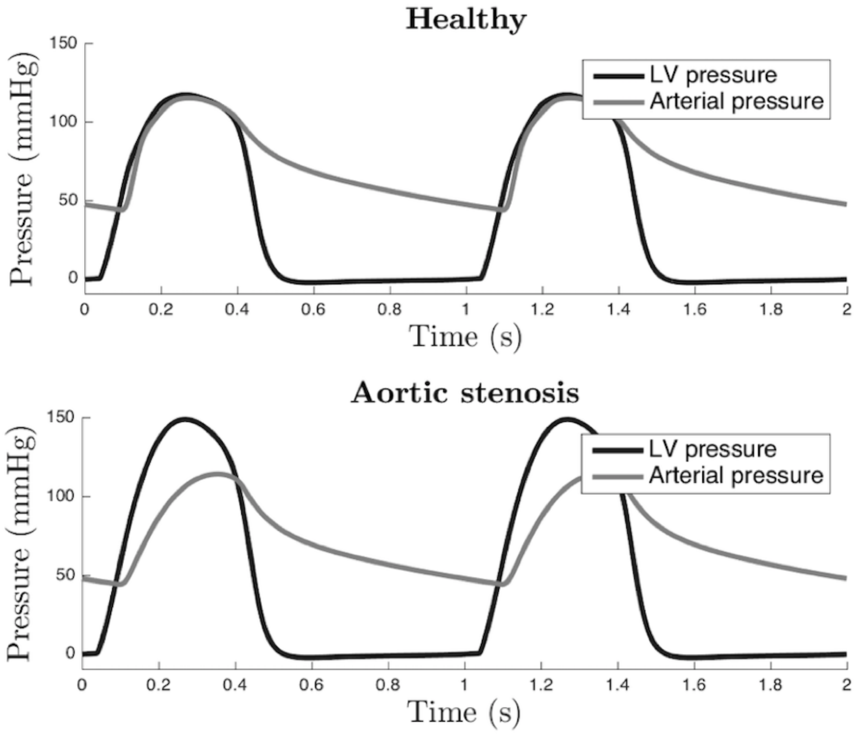

Figure 3.5: Example simulated LV and arterial pressure for a healthy (top) and an aortic stenosis subject (bottom).

3.2.2 Sensitivity analysis

Sensitivity results evaluated on the gradient of systolic pressure between LV and aorta (ΔP^{model}), are presented in Fig. 3.6, only showing those parameters having the highest sensitivities. Fig. 3.6 shows the 25 most relevant parameters based on their D_j index $\left(D_j = \sqrt{(\mu_i^*)^2 + (\sigma_i)^2}\right)$; μ_j* and σ_j are also represented. The most influential parameter corresponds to the effective area of the aortic valve ($A_{eff,max}$). In fact, a decrease of the effective area causes an increase in the ventricular systolic pressure, and consequently, on the gradient of systolic pressure between LV and aorta. Parameters related to the elastance of the LV ($E_{es,lv}$ and α_2) have also a high sensitivity on the gradient of systolic pressures. $E_{es,lv}$ corresponds to the maximum LV elastance and is related to myocardial contractility. α_2 represents the shape parameters related to the LV relaxation phase.

$A_{eff,max}$ presents the highest sensitivity. Fortunately, this parameter can be non-

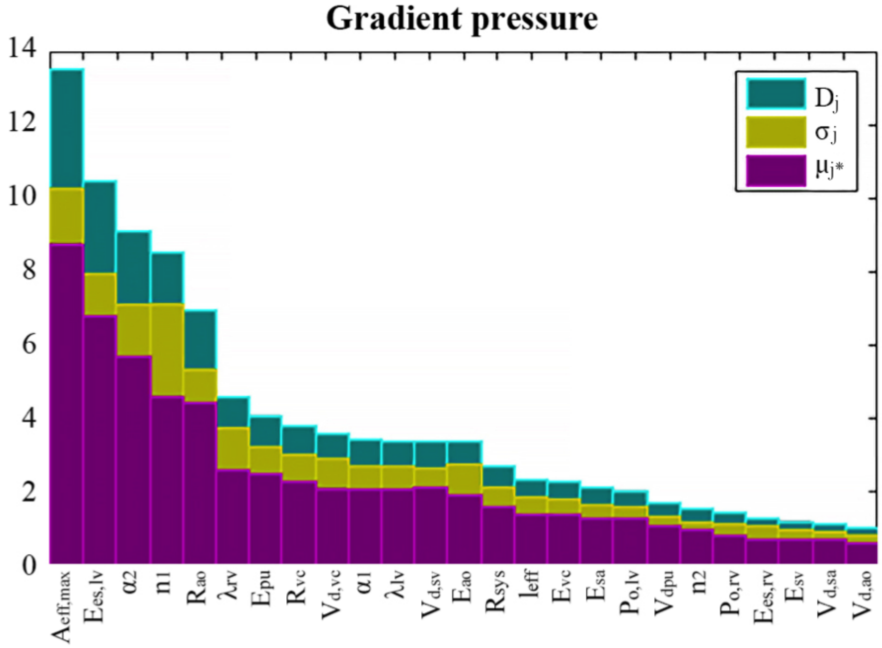

Figure 3.6: Most influential parameters on the gradient of systolic pressure between LV and aorta according to Morris sensitivity results. For each parameter, the distance D_i (green bars), the absolute mean μ_i* (purple bars) and the standard deviation σ_j (yellow bars) of the elementary effects are represented.

invasively observed and has been fixed to the AVA value measured from TTE specifically to each patient. The ventricular and circulatory parameters with the highest sensitivities were selected for ventricular and circulatory parameter estimations:

- $\mathbf{X}_{LV} = \{E_{es,lv}, \lambda_{lv}, P_{0,lv}, \alpha_1, \alpha_2, n_1, n_2\}$
- $\mathbf{X}_{art} = \{E_{ao}, E_{vc}, E_{sa}, E_{sv}, Vd_{ao}, Vd_{vc}, Vd_{sa}, Vd_{sv}, R_{ao}, R_{sys}, R_{vc}\}$.

Except for $\{\mathbf{X}_{LV}, \mathbf{X}_{art}\}$, model parameter values were selected from the publications from which each model was originally based on: ventricular and circulatory parameters were taken from [23, 16, 17, 18], heart valve parameters were adapted from [22], and cardiac electrical conduction system from [19].

3.2.3 Patient-specific model-based pressure

3.2.3.1 Database 1

Step 1: Estimation of LV pressure from invasive data

Concerning step 1 of the parameter identification, there was a good agreement between estimated and measured pressure waveforms (Fig.3.7). Mean R^2 was equal to

0.96 (min: 0.91, max: 0.99). Mean slope and intercept of the regression line between the simulated and the measured pressure data were 1.04 (95% confidence interval: 1.0,1.09) and -8.48 (-8.52,-8.44) mmHg respectively. Mean total relative error was equal to 11.9% and ranged from 6.4% to 17.3%.

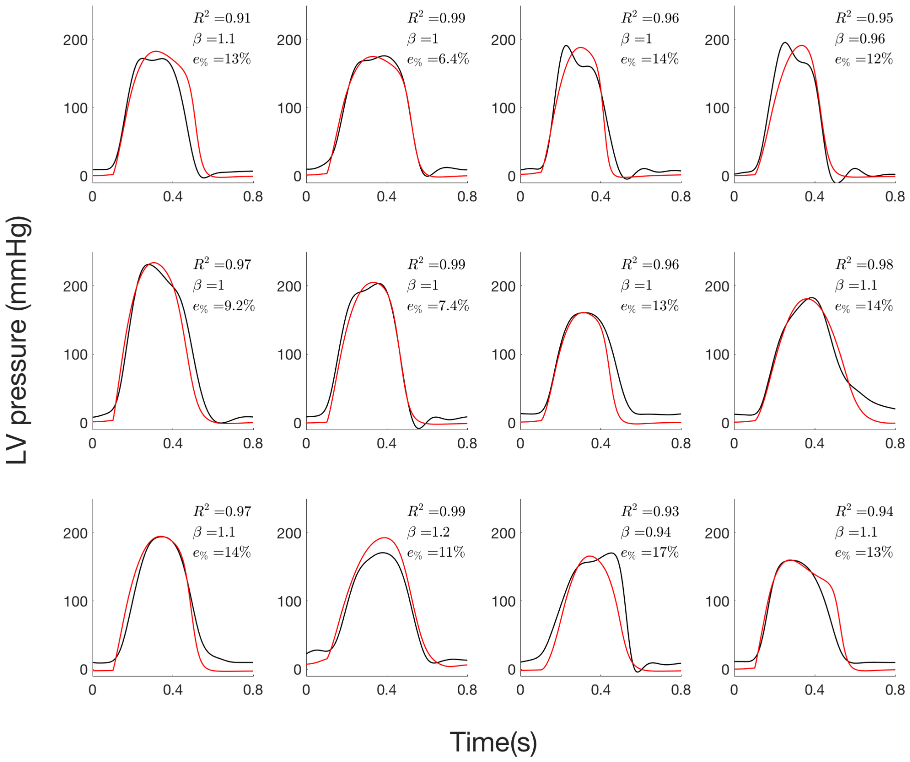

Figure 3.7: Step 1 for *database 1*: LV pressure of the 12 AS patients: i) experimental (black) and ii) simulated (red) curves.

Step 2: Estimation of LV pressure from systolic and diastolic pressure values

Concerning step 2 of the parameter identification, LV pressure waveforms are only estimated from systolic and diastolic pressure values and $A_{eff,max}$ has been fixed to the AVA value measured from TTE specifically to each patient (Fig.3.8) . Slope and intercept of the regression line were 1.03 (0.92, 1.14) and -7.74 (-7.63, -7.85) mmHg respectively, and mean R^2 was 0.91. Total relative error ranged between 5.9% and 17.40% and average value is 12.27%.

3.2.3.2 Database 2

LV pressure waveforms were estimated by a parameter identification procedure, using only systolic and diastolic arterial pressure values and the $A_{eff,max}$ fixed specifically to each patient (Fig 3.9). Slope and intercept of the regression line were 0.91 (0.55,

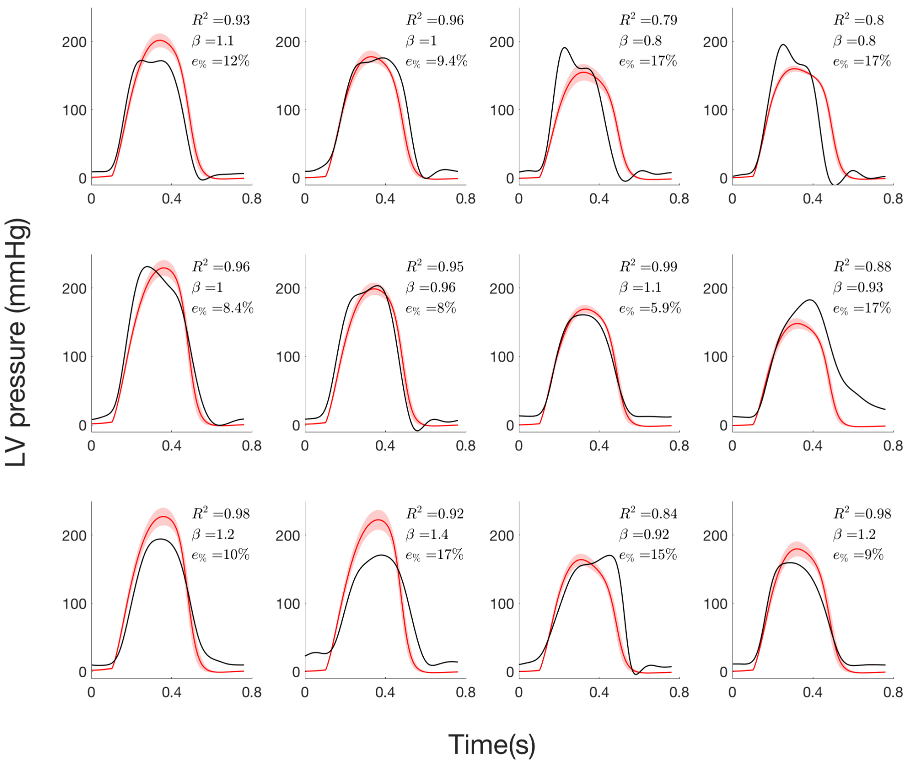

Figure 3.8: Step 2 for *database 1*: LV pressure of the 12 AS patients: i) experimental curve (black), ii) average and standard deviation of simulated curve (red).

1.42) and -13.02 (-29.71, 2.27) mmHg respectively, and mean R^2 was 0.85. Total relative error ranged between 9.93% and 36.97% and average value is 18.42%.

3.2.4 Comparison of global cardiac work indices

3.2.4.1 Database 1

Figure 3.10 presents scatter and BA plots for GCW, GWW and GWE indices. Correlations between measures and model-based estimations were respectively 0.81 ($p < 0.0001$) and 0.62 ($p < 0.003$) for GCW and GWW. When considering both constructive and wasted work indices, global correlation was equal to 0.96 ($p < 0.0001$). In BA analysis, mean bias was -140 mmHg.% and -12 mmHg.% respectively for GCW and GWW, which correspond to relative bias equal to 3.47% and 2.93% with respect to maximum GCW and GWW values. For global work efficiency, correlation was 0.80 ($p < 0.0001$) and mean bias was equal to 0. For GWE, one patient is outside the 95% limits of agreement and corresponds to the third patient of the first row on Fig 3.7 and Fig 3.8. For this patient, the synchronisation, between peaks of simulated and experimental pressures,

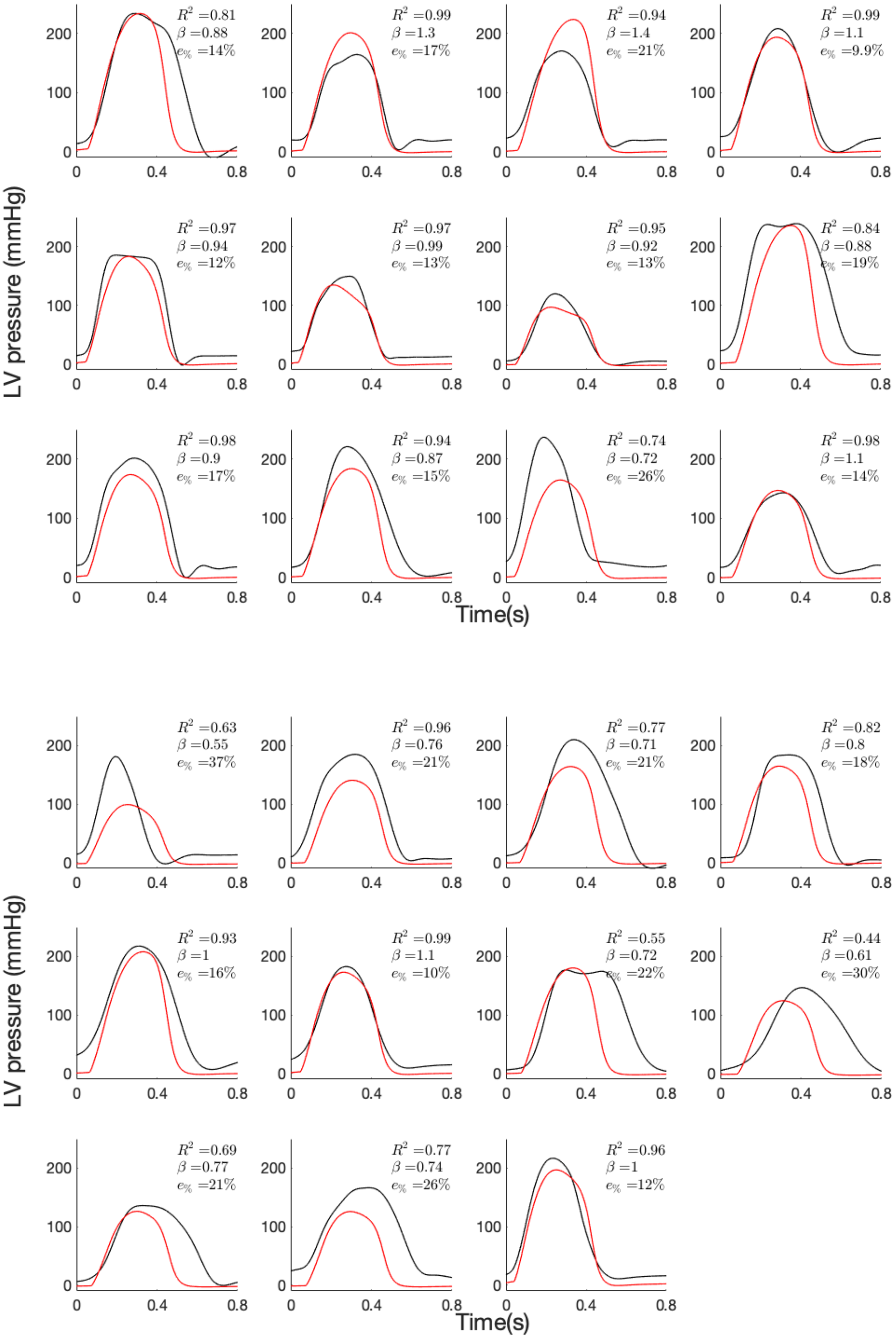

Figure 3.9: Step 2 for *database* 2: LV pressure of the 23 AS patients: i) experimental curve (black) and ii) simulated (red) curves.

is less good, showing the importance of time corresponding to peak pressure for work evaluation.

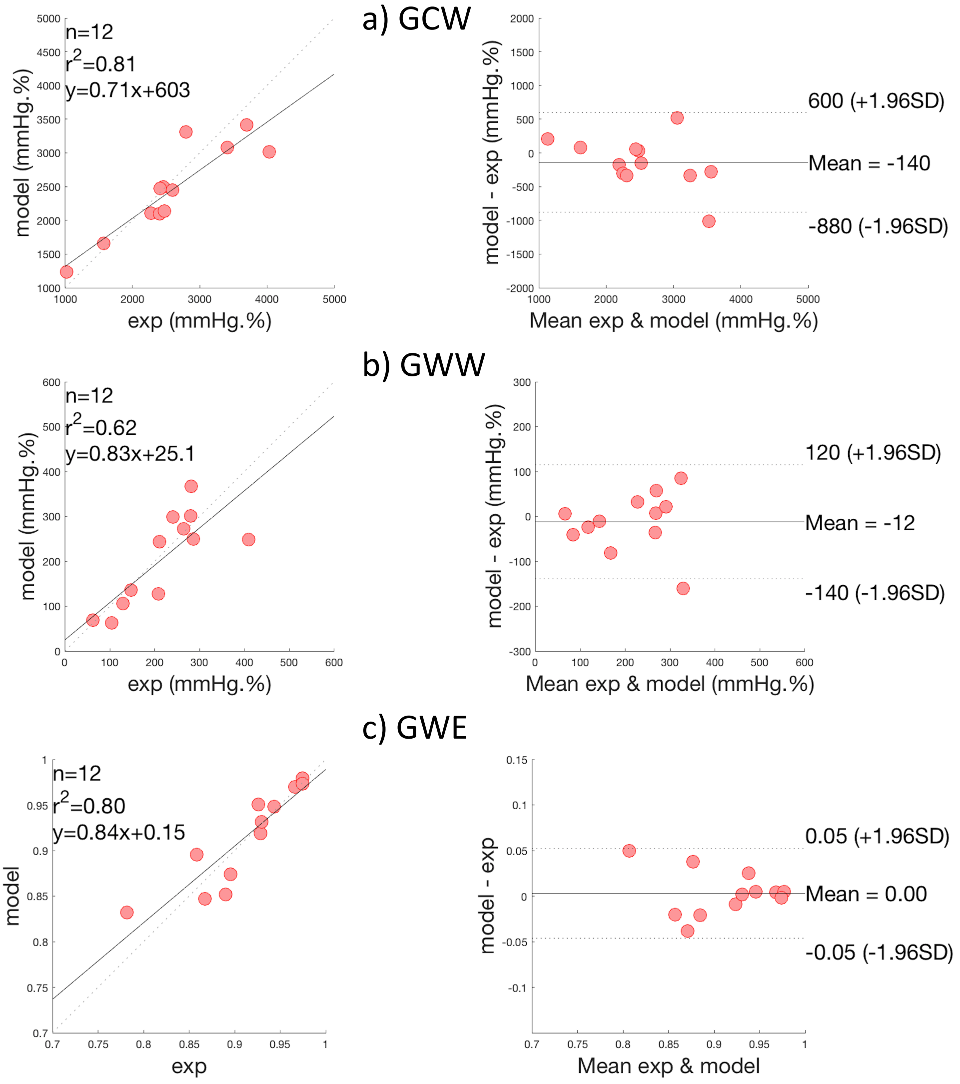

Figure 3.10: *Database 1*: Results of global work indices comparison, on all patients. Scatter plots and Bland–Altman analysis of: a) Global Constructive Work (GCW), b) Global Wasted Work (GWW) and c) Global Work Efficiency (GWE).

3.2.4.2 Database 2

Figure 3.11 presents scatter and BA plots for GCW, GWW and GWE indices obtained from the *database 2* analysis. Correlations between measures and model-based estimations were respectively 0.89 ($p < 0.000004$) and 0.76 ($p < 0.005$) for GCW and GWW. When considering both constructive and wasted work indices, global correlation was equal to 0.93 ($p < 0.0001$). In BA analysis, mean bias was -390 mmHg.%

and -66 mmHg.% respectively for GCW and GWW, which correspond to relative bias equal to 8.30% and 8.86% with respect to maximum GCW and GWW values. For global work efficiency, correlation was 0.89 ($p < 0.0003$) and mean bias was equal to 0.02, corresponding to relative bias equal to 2.02% with respect to maximum GWE value. In GWE diagrams, we noticed an isolated patient. In fact, this patient presents close values of GCW and GWW and consequently a low value of GWE compared with the other patients. However, this result still have a good correlation with the experimental data.

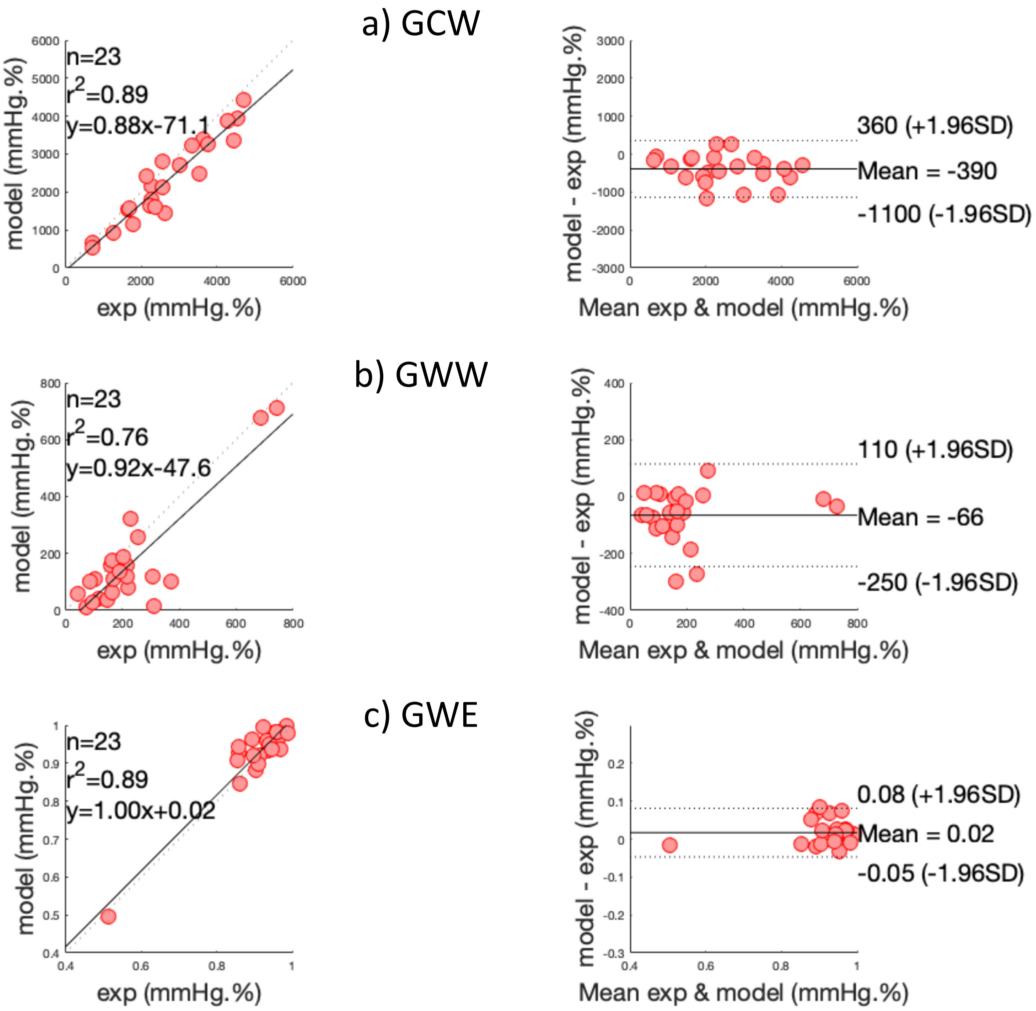

Figure 3.11: *Database 2* analysis: Results of global work indices comparison, on all patients. Scatter plots and Bland–Altman analysis of: a) Global Constructive Work (GCW), b) Global Wasted Work (GWW) and c) Global Work Efficiency (GWE).

3.3 Discussion

In this chapter, a patient-specific model-based estimation method was proposed in order to evaluate constructive, wasted myocardial work and global work efficiency on patients diagnosed with aortic stenosis. The main contributions of this chapter concern: *i)* the proposition of an integrated model of cardiovascular system model, *ii)* the analysis of this cardiovascular model in order to select the most sensitive parameters to be identified in a patient-specific manner, *iii)* a parameter identification approach able to reproduce LV pressure specifically to each patient, *iv)* the experimental validation of the proposed method through a cross-validation technique applied to *database 1* of 12 AS patients, in order to quantitatively evaluate GCW, GWW and GWE indices and *v)* the *database 2* analysis of the proposed model-based approach on a database of 23 AS patients.

The heart valve model, proposed by [22], was coupled to a CVS model that includes representations of cardiac electrical activity, cardiac cavities and the circulation, developed by our group [19, 20, 16, 17, 18, 21]. The integrated model is able to predict the influence of valve motion on hemodynamics in both normal and stenosis cases. The sensitivity analysis, performed on the integrated model, highlights the importance of effective area of the aortic valve and parameters related with LV elastance on the pressure gradient between LV and aorta. In fact, modifications of valve effective area, observed in stenosis, lead to an increased aortic resistance and to an elevated pressure gradient across the valve [13]. When the blood flows through a narrowed aortic valve, the hemodynamic conditions could also lead to modifications of ventricular elastance [29].

The most influential LV and aortic parameters found after sensitivity analysis were then identified for each one of the patients. In order to build the cost function, experimental and simulated pressures were synchronised on QRS peaks of synthesized and experimental ECG.

One of the main originalities of the approach was to apply a Monte-Carlo cross-validation approach for the patient-specific estimations of LV pressures using the *database 1*. In the first step of the identification process, model parameters were identified from invasive measured LV pressures, as well as systolic and diastolic arterial pressure values. Results show a good agreement between estimated and measured pressure waveforms. Concerning the second step of the identification, only systolic, diastolic arterial pressure values and AVA echocardiography estimations were used to identify some model parameters and to estimate LV pressure waveform. Although errors slightly increase compared to step 1, the approach has the advantage of using only non-invasive data for the estimation of LV pressure waveforms.

In the *database 2* analysis, model parameters were identified once in each patient using only non-invasive data as the systolic and diastolic arterial pressure values and AVA echocardiography estimations. The model-based LV pressure waveforms obtained show less precision respect to the experimental curves in some patients compared with the *database 1* analysis. However, in general, a good agreement was observed between experimental and simulated GCW, GWW and specially GWE indices. We believe that the implementation of new methods and strategies can further improve the estimation of the LV curves and consequently the estimation of myocardial work indices.

As shown in previous work of our team [12], although LV pressure is imprecise, the estimation of LV work can provide sufficiently accurate results. In the *database 1* analysis, errors between model-based and measured pressures are around 12%, mean relative bias in BA analysis were 3.47%, 2.93% and 0.0% respectively for GCW, GWW and GWE. In the *database 2* analysis, the mean error between model-based and measured pressures is around 19%, however, 8.30%, 8.86% and 2.02% were found for the mean relative bias in BA in GCW, GWW and GWE respectively.

The consistency of LV work estimation could be explained by: *i)* the temporal integration, which induces a smoothing of the difference between measured and estimated works and *ii)* relative precision of the estimation of the pressure between AVO and AVC. Although the estimation of the LV pressure is imperfect, the non-invasive estimation of global myocardial work indices obtained from modelling approach strongly correlates with invasive measurements and the proposed estimation of LV myocardial work appears as clinically relevant.

Myocardial work indices are novel tools that have been validated in a variety of pathologies, including the response to cardiac resynchronization therapy (CRT) [30]. In particular, Russell et al. have shown that regional differences in myocardial work have a strong correlation with regional myocardial glucose metabolism, as evaluated using PET imaging [9]. However, the assessment of constructive and wasted work, in the case of AS is difficult because the estimation of peak LV pressure is complicated without any invasive measurement. To our knowledge, this study presents the first method for the estimation of myocardial work, based on a physiological model, rather than a template-based estimate, such as in [9]. In this case, the model-based method allows for the integration of physiological knowledge in the evaluation of myocardial work indices. *In silico* assessment of clinical parameters, specifically to each patient, has the advantage of taking into account characteristics associated with the subject and pathology. For instance, by integrating a representation of the pathophysiology of the aortic valves within this physiological model, it becomes adapted to the case of aortic stenosis.

Results show globally a good agreement between work index estimations from LV pressure obtained with patient-specific simulations and with experimental measurements. The evaluation of cardiac work, in the case of AS, is promising because it could be a simple and physiological alternative to more complex and costly investigations (cardiac MRI,..) for the evaluation of myocardial contractility and residual myocardial viability [31]. The assessment of regional myocardial work might be particularly important for the prognosis of patients with severe asymptomatic AS without LV dysfunction. In fact, the timing and indications for surgical intervention in this population remain controversial as the aortic-valve replacement is not recommended despite in the increased risk of cardiovascular mortality [32]. Indeed, as LVEF remains imperfect in asymptomatic AS to determine the optimal delay for the surgery, global longitudinal strain appears to have a better prognostic significance [33] and we can suppose that myocardial work will be robust complementary indices independent of afterload condition. In fact, because afterload data are included in the calculation of myocardial work in the form of LV pressure, the assessment of myocardial work might represent a more robust parameter with respect to the assessment of LV strain or other strain-derived parameters [34]. Although it will be important to confirm these assumptions and to validate the approach in a cohort of AS patients, this study is a first essential step for the proposition of work estimation based on computational modelling. The proposed methodology should be evaluated on a larger prospective clinical database in the future and we believe that model-based work indices, especially GWE, could be promising to improve the assessment of LV mechanical efficiency in AS.

One limitation of this work concerns the number of patients included. Although it appears to be low, it is necessary to recognise that measurement of invasive LV pressure is particularly difficult in AS. In fact, current guidelines discourage catheterization measurement techniques in AS before aortic valve replacement [35]. In this case, catheterization was realised for clinical reasons and all patients were informed. Another limitation is related to the estimation of LV filling pressure, which is not precisely estimated in step 2. In fact, myocardial work is considered in the period from mitral valve closure to mitral valve opening, so inaccuracies before mitral valve closure and after mitral valve opening has no impact on the results [12].

3.4 Conclusion

In this chapter, an original model-based approach to assess constructive and wasted work in AS patients was proposed. The global method is based on a novel approach involving: *i)* a physiological model of the cardiovascular system, including heart valves and *ii)* a 2-step identification procedure, based on a monte-carlo cross-validation method. The proposed model-based approach was evaluated with data from 12 AS patients and subsequently assessed in 23 more patients, for which LV pressure data was acquired invasively. Results show a close match between experimental and simulated LV and aortic pressures. The model-based approach is especially efficient for the evaluation of LV pressure from non-invasive data (systolic, diastolic pressures and aortic valve area). Moreover, estimations of constructive, wasted work and global work efficiency were consistent with indices calculated from measured experimental pressures, showing the model ability to produce realistic LV pressure for the calculation of work indices.

More extensive evaluations including a greater population of patients should be performed in the future. Nevertheless, this thesis presents the first model-based approach towards the evaluation of myocardial work indices in AS patients and, thus, provide a step forward the characterisation of the complex LV mechanics of patients with AS.

Bibliography

[1] K. Rajappan, O. Rimoldi, D. Dutka, B. Ariff, D. Pennell, D. Sheridan, and P. Camici, “Mechanisms of coronary microcirculatory dysfunction in patients with aortic stenosis and angiographically normal coronary arteries,” *Circulation*, vol. 105, pp. 470–476, 2002.

[2] D. Tzivoni, “Effect of transient ischaemia on left ventricular function and prognosis.,” *Eur Heart J.*, vol. 14, pp. Suppl A:2–7, 1993.

[3] T. Taniguchi, T. Morimoto, H. Shiomi, and et al., “Prognostic impact of left ventricular ejection fraction in patients with severe aortic stenosis.,” *ACC Cardiovasc Interv*, vol. 11, pp. 145–157, 2018.

[4] V. Delgado, L. Tops, R. van Bommel, F. van der Kley, N. Marsan, R. Klautz, M. Versteegh, E. Holman, M. Schalij, and J. Bax, “Strain analysis in patients with severe aortic stenosis and preserved left ventricular ejection fraction undergoing surgical valve replacement.,” *Eur Heart J.*, vol. 30, pp. 3037–47, 2009.

[5] L. Kearney, K. Lu, M. Ord, S. Patel, K. Profitis, M. G, and et al., “Global longitudinal strain is a strong independent predictor of all-cause mortality in patients with aortic stenosis.,” *Eur Heart J Cardiovasc Imaging*, vol. 13, pp. 827–33, 2012.

[6] S. Hein, E. Arnon, S. Kostin, M. Schonburg, A. Elsasser, V. Polyakova, and et al., “Progression from compensated hypertrophy to failure in the pressure overloaded human heart: structural deterioration and compensatory mechanisms,” *Circulation*, vol. 107, pp. 984–91, 2003.

[7] B. Villari, G. Vassalli, E. Monrad, M. Chiariello, M. Turina, and O. Hess, “Normalization of diastolic dysfunction in aortic stenosis late after valve replacement,” *Eur Heart J Cardiovasc Imaging*, vol. 91, pp. 2353–8, 1995.

[8] L. Klaeboe, T. Haland, I. Leren, R. Ter Bekke, P. Brekke, H. Rosjo, T. Omland, L. Gullestad, S. Aakhus, K. Haugaa, and T. Edvardsen, “Prognostic value of left ventricular deformation parameters in patients with severe aortic stenosis: A pilot study of the usefulness of strain echocardiography,” *J Am Soc Echocardiogr.*, vol. 30(8), pp. 727–735, 2017.

[9] K. Russell, M. Eriksen, L. Aaberge, N. Wilhelmsen, H. Skulstad, E. W. Remme, K. H. Haugaa, A. Opdahl, J. G. Fjeld, O. Gjesdal, T. Edvardsen, and S. O. A., “Strain analysis in patients with severe aortic stenosis and preserved left ventricular ejection fraction undergoing surgical valve replacement.,” *European Heart Journal*, vol. 33, p. 724?733, 2012.

[10] K. Russell, M. Eriksen, L. Aaberge, N. Wilhelmsen, H. Skulstad, O. Gjesdal, T. Edvardsen, and O. A. Smiseth, “Assessment of wasted myocardial work: a novel method to quantify energy loss due to uncoordinated left ventricular contractions.,” *Am J Physiol Heart Circ Physiol*, vol. 305, pp. H996–H1003,, 2013.

[11] E. Donal, C. Bergerot, H. Thibault, L. Ernande, J. Loufoua, L. Augeul, M. Ovize, and D. G., “Influence of afterload on left ventricular radial and longitudinal systolic functions: a two-dimensional strain imaging study.,” *Eur J Echocardiogr*, vol. 10, p. 914–921, 2009.

[12] A. Hubert, V. Le Rolle, C. Leclercq, E. Galli, E. Samset, C. Casset, P. Mabo, A. Hernandez, and E. Donal, “Estimation of myocardial work from pressure-strain loops analysis: an experimental evaluation.,” *Eur Heart J Cardiovasc Imaging*, 2018.

[13] F. M. Eleid, P. Sorajja, I. H. Michelena, F. J. Malouf, G. C. Scott, and P. A. Pellikka, “Flow-gradient patterns in severe aortic stenosis with preserved ejection fraction: Clinical characteristics and predictors of survival,” *Circulation*, vol. 128, pp. 1781–1789, 2013.

[14] D. Garcia, P. J. Barenbrug, P. Pibarot, A. L. Dekker, F. H. van der Veen, J. G. Maessen, J. G. Dumesnil, and L. G. Durand, “A ventricular-vascular coupling model in presence of aortic stenosis,” *Am. J. Physiol. Heart Circ. Physiol.*, vol. 288, pp. H1874–1884, Apr 2005.

[15] M. Korürek, M. Yıldız, and A. Yuksel, “Simulation of normal cardiovascular system and severe aortic stenosis using equivalent electronic model,” *Anadolu Kardiyol Derg*, vol. 10, pp. 471–478, Dec 2010.

[16] H. M. Romero-Ugalde, D. Ojeda, V. L. Rolle, D. Andreu, D. Guiraud, J.-L. Bonnet, C. Henry, N. Karam, A. Hagege, P. Mabo, G. Carrault, and A. I. Hernandez, “Model-based design and experimental validation of control modules for neuromodulation devices,” *Biomedical Engineering, IEEE Transactions on*, vol. 63, no. 7, pp. 1551–1558, 2015.

[17] M. Calvo, V. Le Rolle, D. Romero, N. Behar, P. Gomis, P. Mabo, and A. I. Hernandez, “Model-based analysis of the autonomic response to head-up tilt testing in Brugada syndrome,” *Comput. Biol. Med.*, vol. 103, pp. 82–92, 2018.

[18] M. Calvo, V. Le Rolle, D. Romero, N. Behar, P. Gomis, P. Mabo, and A. I. Hernandez, “Recursive model identification for the analysis of the autonomic response to exercise testing in Brugada syndrome,” *Artif Intell Med*, vol. 97, pp. 98–104, Jun 2019.

[19] A. I. Hernández, G. Carrault, F. Mora, and A. Bardou, “Model-based interpretation of cardiac beats by evolutionary algorithms: signal and model interaction,” *Artificial Intelligence in Medicine*, vol. 26, no. 3, pp. 211–235, 2002.

[20] V. Le Rolle, A. Hernàndez, P.-Y. Richard, E. Donal, and G. Carrault, “Model-based analysis of myocardial strain data acquired by tissue doppler imaging.,” *Artificial Intelligence in Medicine*, vol. 44, pp. 201–19, 2008.

[21] D. Ojeda, V. Le Rolle, M. Harmouche, A. Drochon, H. Corbineau, J.-P. Verhoye, and A. I. Hernandez, “Sensitivity analysis and parameter estimation of a coronary circulation model for triple-vessel disease,” *IEEE Transactions on Biomedical Engineering*, vol. 61, no. 4, pp. 1208–1219, 2014.

[22] J. P. Mynard, M. R. Davidson, D. J. Penny, and J. J. Smolich, “A simple, versatile valve model for use in lumped parameter and one-dimensional cardiovascular models,” *Int. J. Numer. Meth. Biomed. Engng*, vol. 28, pp. 626–641, 2012.

[23] B. W. Smith, J. G. Chase, R. I. Nokes, G. M. Shaw, and G. Wake, “Minimal haemodynamic system model including ventricular interaction and valve dynamics,” *Medical engineering & physics*, vol. 26, no. 2, pp. 131–139, 2004.

[24] D. Chung, S. Niranjan, J. Clark, A. Bidani, W. Johnston, J. Zwischenberger, and D. Traber, “A dynamic model of ventricular interaction and pericardial influence,” *American Journal of Physiology-Heart and Circulatory Physiology*, vol. 272, no. 6, pp. H2942–H2962, 1997.

[25] N. Stergiopulos, J. Meister, and N. Westerhof, “Determinants of stroke volume and systolic and diastolic aortic pressure,” *Am J. Physiol*, vol. 270, pp. H2050–H2059, 1996.

[26] M. D. Morris, “Factorial sampling plans for preliminary computational experiments,” *Technometrics*, vol. 33, no. 2, pp. 161–174, 1991.

[27] A. L. Goldberger, C.-K. Peng, and L. A. Lipsitz, “What is physiologic complexity and how does it change with aging and disease?,” *Neurobiology of aging*, vol. 23, no. 1, pp. 23–26, 2002.

[28] D. Giavarina, “Understanding Bland Altman analysis,” *Biochemia Medica*, vol. 25, pp. 141–151, June 2015.

[29] Y. Tanoue, T. Maeda, S. Oda, H. Baba, Y. Oishi, S. Tokunaga, A. Nakashima, and R. Tominaga, "Left ventricular performance in aortic valve replacement.," *Interact Cardiovasc Thorac Surg*, vol. 9(2), pp. 255–9, 2009.

[30] E. Galli, C. Leclercq, A. Hubert, A. Bernard, O. Smiseth, P. Mabo, E. Samset, A. Hernandez, and E. Donal, "Role of myocardial constructive work in the identification of responders to crt," *Eur Heart J Cardiovasc Imaging*, vol. 19(9), pp. 1010–1018, 2018.

[31] E. Galli, E. Vitel, F. Schnell, V. Le Rolle, A. Hubert, M. Lederlin, and E. Donal, "Myocardial constructive work is impaired in hypertrophic cardiomyopathy and predicts left ventricular fibrosis," *Echocardiography*, vol. 36(1), pp. 74–82, 2019.

[32] D.-H. Kang, S.-J. Park, S.-A. Lee, S. Lee, D.-H. Kim, H.-K. Kim, S.-C. Yun, G.-R. Hong, J.-M. Song, C.-H. Chung, J.-K. Song, J.-W. Lee, and S.-W. Park, "Early Surgery or Conservative Care for Asymptomatic Aortic Stenosis," *New England Journal of Medicine*, vol. 382, pp. 111–119, Jan. 2020. Publisher: Massachusetts Medical Society _eprint: https://doi.org/10.1056/NEJMoa1912846.

[33] J. Magne, B. Cosyns, B. Popescu, H. Carstensen, J. Dahl, M. Desai, L. Kearney, P. Lancellotti, T. Marwick, K. Sato, M. Takeuchi, C. Zito, A.-C. Casalta, D. Mohty, L. Pierard, G. Habib, and E. Donal, "Distribution and Prognostic Significance of Left Ventricular Global Longitudinal Strain in Asymptomatic Significant Aortic Stenosis: An Individual Participant Data Meta-Analysis.," *JACC Cardiovasc Imaging*, vol. 12, pp. 84–92, 2019.

[34] E. Galli, C. Leclercq, M. Fournet, A. Hubert, A. Bernard, O. A. Smiseth, P. Mabo, E. Samset, A. Hernandez, and E. Donal, "Value of Myocardial Work Estimation in the Prediction of Response to Cardiac Resynchronization Therapy," *Journal of the American Society of Echocardiography: Official Publication of the American Society of Echocardiography*, vol. 31, no. 2, pp. 220–230, 2018.

[35] R. A. Nishimura, C. M. Otto, R. O. Bonow, B. A. Carabello, J. P. Erwin, R. A. Guyton, P. T. O'Gara, C. E. Ruiz, N. J. Skubas, P. Sorajja, T. M. Sundt, J. D. Thomas, J. L. Anderson, J. L. Halperin, N. M. Albert, B. Bozkurt, R. G. Brindis, M. A. Creager, L. H. Curtis, D. DeMets, R. A. Guyton, J. S. Hochman, R. J. Kovacs, E. M. Ohman, S. J. Pressler, F. W. Sellke, W. K. Shen, W. G. Stevenson, C. W. Yancy, J. G. Harold, S. Jacobovitz, W. J. Oetgen, C. L. May, L. Bradfield, E. Cottrell, M. Jessup, N. Brown, R. M. Robertson, G. R. Whitman, M. Di Buono, and J. Hundley, "2014 AHA/ACC guideline for the management of patients with valvular heart disease: a report of the American College of Cardiology/American Heart Association Task Force on Practice Guidelines," *J. Thorac. Cardiovasc. Surg.*, vol. 148, pp. e1–e132, Jul 2014.

4

MODEL-BASED ANALYSIS OF MYOCARDIAL STRAINS IN LEFT BUNDLE BRANCH BLOCK

Left bundle branch block (LBBB) is a common electrocardiographic abnormality that causes intra- and interventricular conduction delay and leads to uncoordinated contraction of the ventricle, alterations in LV mechanical activity and LV dysfunction [1]. Cardiac resynchronization therapy (CRT) usually causes reverse left ventricular (LV) remodeling and has shown a major favorable impact on the care of heart failure patients with LBBB. Despite the great success of randomized clinical trials, 25% to 35% of patients undergoing CRT are non-responders to treatment and can even be harmed by biventricular stimulation [2]. Although, previous studies have suggested that the analysis of strain traces obtained by speckle-tracking echocardiography (STE) might be an alternative for quantifying LV mechanical dyssynchrony and identifying patients suitable for CRT [3, 4, 5], guidelines still neglect the value of the assessment of LV mechanical dyssynchrony for the prediction of CRT-response.

Observational studies of patients with LBBB have shown a relation between strain curve morphologies and responses to CRT [3, 6, 7]. However, the regional distribution patterns of dyssynchrony in LBBB is highly heterogeneous as it involves differently septal and lateral walls [8, 9]. Moreover, strain morphologies could also be affected by mechanical dysfunctions, such as those observed in ischemia [10]. Therefore, the assessment of dyssynchrony patterns in LBBB appears as particularly complex because strain morphologies reflect dynamics associated with both electrical conduction delays and mechanical cardiac activities. Previous studies have shown that only the mechanical dysfunction attributable to an electrical conduction delay can be corrected by CRT [11]. The possibility of using strain-derived data to disclose the complex interplay between electrical conduction delay and the specific mechanical substrate associated with LV dyssynchrony is particularly interesting and might have a pivotal role in the selection of CRT-candidates.

In this context, model-based approaches could be proposed to provide a better understanding of myocardial deformations observed in LBBB curves, as it allows the analysis of underlying physiological mechanisms. Computational modeling appears as efficient tools to integrate knowledge, concerning cardiac electrical activation, mechanical properties and hemodynamic conditions, in the data processing. A variety of cardiac electro-mechanical models have been proposed in the literature, at many different levels of detail, including the cardiac electrical activity [12, 13, 14], the excitation-contraction coupling [15, 16], the mechanical activity [17] and the mechano-hydraulic coupling [18]. Most of proposed human heart models are based on the Finite Element (FE) method [19, 20, 21] for the simulation of cardiac mechanical activity. These models require high computational resources, and they are still difficult to personalize. Moreover, dynamic loading conditions and interventricular interactions are usually not taken into account in these models and their integration is possible only at the expenses of an increasing amount of model complexity. Alternative approaches have been proposed for the analysis of myocardial strains [22, 23, 24, 25], which are associated with lower computational costs, and allows for the haemodynamic incorporation of the heart within the entire circulation. Although, these models have been successfully used to characterize myocardial deformation in function of the underlying physiological mechanisms, efforts are still necessary to develop personalized models specifically to each patient.

In [26], our team has proposed the first model-based approach for the analysis of Tissue Doppler Imaging (TDI). Model parameters for the LV were estimated by minimizing strain signals between the computational model and strain signals obtained with TDI in several myocardial segments. However, this model does not integrate interactions with the right ventricle and the approach was not validated in the case of LV dyssynchrony. The objective of this chapter is to propose a novel model-based approach for the analysis of myocardial strains in LBBB patients. Therefore, a novel approach was developped based on the patient-specific identification of a multi-segment model of left and right ventricles coupled to atria, systemic and pulmonary circulations [27, 28]. Interestingly, this process took into account not only the electrical activation delay of each segment but also the differences in regional contractility, which are known to largely contribute to strain morphology and global cardiac mechanics.

4.1 Materials and Methods

4.1.1 Experimental data

4.1.1.1 Study population

We prospectively included 10 healthy adults and 10 LBBB patients, including ischaemic ($n = 5$) and non-ischaemic ($n = 5$) cardiomyopathies. Table 4.1 summarizes patients' clinical characteristics. The study was carried out in accordance with the principles outlined in the Declaration of Helsinki on research in human subjects and received specific ethical approval from the local Medical Ethical Committee. All patients signed a written informed consent before the participation to the study protocol.

Table 4.1: Patients' clinical characteristics.

	Age *years old*	**Male sex** *n (%)*	**BSA** **(body surface area)**	**NYHA class** **I/II/III**
LBBB ischemia (n=5)	68.8 ± 13.37	5 (100%)	1.91 ± 0.19	1/4/0
LBBB non-ischemia (n=5)	67.8 ± 6.42	4 (80%)	1.68 ± 0.16	0/3/2
Healthy (n=10)	48.8 ± 14.44	7 (70%)	1.88 ± 0.12	—

4.1.1.2 Echocardiography

All patients underwent a standard Trans-Thoracic Echocardiography (TTE) using a Vivid S6, E7 or E9 ultrasound system (General Electric Healthcare, Horten, Norway). Images were recorded on a remote station for off-line analysis by dedicated software (EchoPAC PC, version BT 202, General Electric Healthcare, Horten, Norway). The experimental dataset includes the measured regional myocardial strain curves obtained by STE at transthoracic echocardiography in apical 4-chamber, 2-chamber and 3- chamber views.

4.1.1.3 Magnetic resonance image (MRI)

For the patients with ischemic cardiomyopathy, the location of the scar was performed by cardiac magnetic resonance imaging (MRI) and then confirmed by echocardiography.

Prior to CRT implantation, cardiac magnetic resonance was performed on a 3-T clinical magnetic resonance system (Ingenia, Philips Medical Systems, Best, the Netherlands) with a 32-channel cardiovascular array coil. Late gadolinium enhancement (LGE) images were acquired 10–15 minutes after intravenous administration of 0.2 mmol/kg of gadolinium (Gadoterate meglumine, Dotarem, Guerbet, Aulnay-sous-bois,France), using 2D breath-hold inversion-recovery and phase-sensitive inversion-recovery sequences in short-axis plane (spoiled gradient-echo, slice thickness 8 mm, repetition time 6.1 ms, echo time 2.9 ms, flip angle 25°, inversion time adjusted to null normal myocardium, typical breath-hold 11 seconds). The localization of myocardial scar was performed by a trained radiologist and the regional LGE extent was semiquantitatively assessed on a per-segment basis [29].

4.1.2 Computational model

The model of the cardiovascular system (CVS) integrates four main sub-models : 1) cardiac electrical system, 2) right and left atria, 3) multi-segment representation of the right and the left ventricles and 4) systemic and pulmonary circulations.

Compared to the model proposed in Chapter 3, this model includes a multi-segment sub-model of the right and left ventricles capable of simulating strain-derived data from all the ventricle segments. Moreover, this model contains a much more complex cardiac electrical system that includes differentiated automata for each ventricular segment and not just an automaton representing the entire ventricle, as is the case in the model proposed in Chapter 3. Indeed, for this clinical application we are interested in evaluating the mechanical and electrical dynamic within the myocardium since in LBBB patients different deformation morphologies may occur in all the ventricular regions due to electrical and/or mechanical dysfunction. Therefore, the possibility of having a specific electrical and mechanical parameter values and a strain curve associated with a specific ventricular region could help to interpret the deformation patterns and disclose the interaction between electrical activation delay and cardiac contractility.

4.1.2.1 Cardiac electrical system

The proposed model of the cardiac electrical activity, is based on a set of coupled automata, adapted from [26]. Each automaton represents the electrical activation state of a given myocardial tissue, covering the main electrophysiological activation periods: slow diastolic depolarization (SDD), upstroke depolarization (UDP), absolute refractory (ARP) and relative refractory (RRP). Briefly, the state of the cellular automata cycles through these four stages, sending an output stimulation signal to neighboring cells when a given cell is activated (end of UDP phase).

In order to perform comparisons between simulations and clinical data, the left ventricle wall was divided into 16 segments according to the standardized segmentation of the AHA [32]. The base (Bas) and medium (Mid) layers are separated in six components: anterior (Ant), anteroseptal (AntSep), inferoseptal (InfSep), inferior (Inf), inferolateral (InfLat) and anterolateral (AntLat) walls. The apex (Ap) layer is divided in four components: anterior, septal, inferior, lateral. Right ventricle wall is divided into three layers (base, medium, and apex) (Fig. 4.2). The whole model consists of 26 automata representing: the sinoatrial node (NSA), right and left atria (RA and LA), the atrioventricular node (NAV), upper bundle of His (UH), bundle branches (RBB and LBB), 3 segments of right ventricle (RV) and 16 segments of left ventricle (LV). The distribution of the electrical activation between automata is represented in Fig. 4.1.

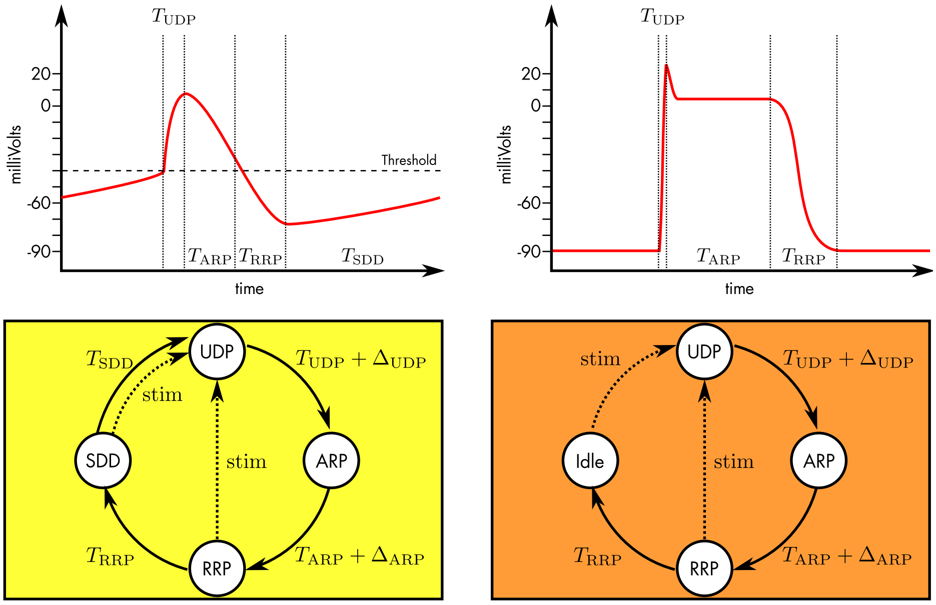

(a) State diagram of the generalized automaton that represents nodal cells (*yellow, left*) and myocardial cells (*orange, right*) and diagrams showing the correspondence of the transition parameters with the myocardial action potential dynamics.

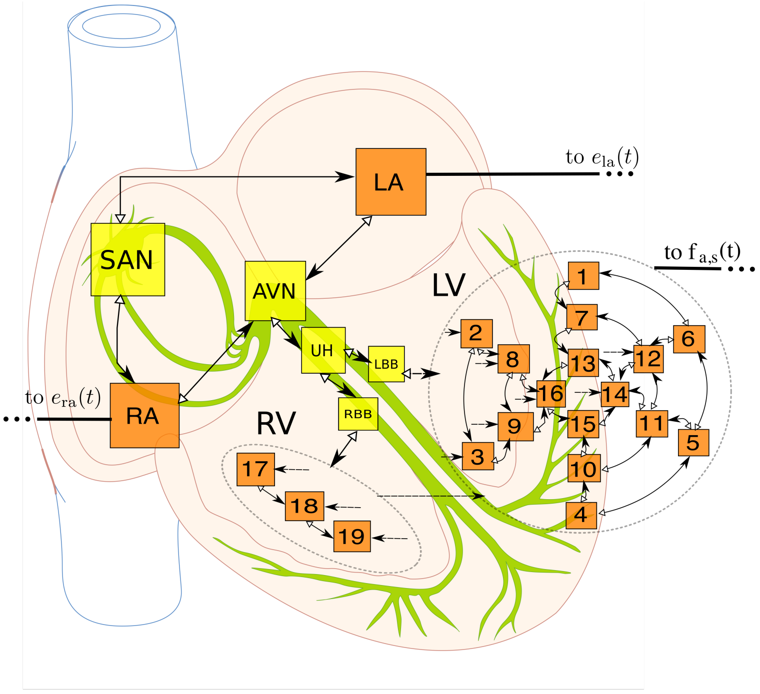

(b) The whole heart represented by 26 cellular automata and their sequence of electrical activation.

Figure 4.1: Cardiac electrical system model

4.1.2.2 Right and left atrium

To account for the mechanical function of the atria, the right and left atrial pressures (P_{ra} and P_{la}) are defined as linear functions of instantaneous volumes (V_{ra} and V_{la}), whose slopes (E_{ra} and E_{la}) represents the elastic properties of the atrial wall:

$$\begin{aligned} P_x(V_x, t_a) &= E_x(V_x(t_a) - V_{x,d}) \\ E_x(t_a) &= e_x(t)\,(E_{x,max} - E_{x,min}) + E_{x,min} \end{aligned} \tag{4.1}$$

where $x \in \{ra,la\}$ and $e_x(t)$ is a Gaussian driving function that cycles between atrial diastole and systole:

$$e_x(t) = A_x \cdot \exp\left(-B_x \cdot (t_a - C_x)^2\right) . \tag{4.2}$$

where t_a is the time elapsed since the atrial activation by the automata corresponding to the right and left atriums. Parameters A_x,B_x and C_x could be used to control the rise and peak of the atrial systole.

4.1.2.3 Right and left ventricles

Each LV and RV automaton triggers an electro-mechanical driving function (EMDF) [33, 34], which represents in a simplified manner, the complex processes involved in the electro-mechanical coupling at the tissue-level:

$$f_{a,s}(t_s) = \left[\frac{\left(\frac{t_s}{\alpha_1 T}\right)^{n_1}}{1+\left(\frac{t_s}{\alpha_1 T}\right)^{n_1}}\right] \cdot \left[\frac{1}{1+\left(\frac{t_s}{\alpha_2 T}\right)^{n_2}}\right] \cdot A_{max}, \tag{4.3}$$

The onset of the cardiac cycle, denoted t_s, is determined by the activation instant of the corresponding segment in the cardiac electrical model presented in the previous section. The first and second terms in Eq. 4.3 represent ventricle segment contraction and relaxation presented after an electrical activation, respectively. T is the heart period, α_1, α_2 are shape parameters, and n_1,n_2 control the steepness of the curve. A_{max} is the maximum EMDF value, and $s \in \{S_{lv}, S_{rv}\}$ with S_{lv} = {BasAnt, BasAntSep, BasInfSep, BasInf, BasInfLat, BasAntLat, MidAnt, MidAntSep, MidInfSep, MidInf, MidInfLat, MidAntLat, ApAnt, ApSep, ApInf, ApLat} and S_{rv} = {BasRV, MidRV, ApRV}.

Concerning each segment s, cardiac mechanical activity can be separated into active and passive components:

$$T_s = T_{s,pass} + T_{s,act}. \tag{4.4}$$

Passive myocardial tension depends on myocardial strain ($\varepsilon_s^{model} = {}^{(l_s - l_{s,ref})}/{}_{l_{s,ref}}$) according to [35]:

$$T_{s,pass} = K_{pass} \cdot (36 \cdot max(0, \varepsilon_s - 0.1)^2 + 0.1(\varepsilon_s - 0.1) + 0.0025e^{10\varepsilon_s}) \tag{4.5}$$

where K_{pass} is a parameter related to passive stiffness that is comprised between 0 and 1, l_s and $l_{s,ref}$ are current and reference fiber lengths. Active myocardial tension is represented by a non-linear law inspired from [36]:

$$T_{s,act} = K_{act} \cdot T_{ref} \cdot (1 + \beta(\varepsilon_s - 1)) \cdot \frac{{f_{a,s}}^2}{f_{a,s}^2 + C_a^2} \tag{4.6}$$

where K_{act} is a parameter related to myofiber contractility, T_{ref} is the reference tension at $\varepsilon_s = 1$, and β, C_a are constants related with the muscle kinetic. The relation between pressure P_s and tension T_s in each segment is approximated by the Laplace law (Eq. 4.7)

$$P_s = e \cdot T_s \left(\frac{\cos(\Theta)}{\varepsilon_s \cdot R_m} + \frac{\sin(\Theta)}{\varepsilon_s \cdot R_p} \right) \tag{4.7}$$

In Eq. 4.7, Θ is the mean angle of the muscular fibers. R_m and R_p are the radii of curvature in the meridian and parallel directions, while e is the mean wall thickness. As the ventricle was assumed to be an ellipsoid of revolution, R_p and R_m could be calculated analytically. Length variation is obtained by a power conservation: $P_s \cdot Q_s = F_s \cdot {}^{dl_s}/{}_{dt}$. Where the force is $F_s = T_s \cdot S_s$, and S_s is the area of each segment. The hydraulic behavior of the blood volume in contact with the wall segment are represented by its inertial (I_s) and resistive (R_s) effects:

$$P_y - P_s = I_s \frac{dQ_s}{dt}, \quad Q_s = \frac{P_y - P_s}{R_s} \tag{4.8}$$

with $y \in$ {lv,rv}. Ventricular flow is calculated taking into account the contribution of the flow of each one of the segments and of the intra-ventricular cavity :

$$Q_y(t) = Q_{c,y}(t) + \sum_{s_y} Q_{s,y}(t) \tag{4.9}$$

where P_y and Q_y are respectively cavity center pressure and flow. Segments, associated with the septum, are treated separately since their pressure depends of the pressure gradient across the septal wall:

$$P_{sept} = P_{lv} - P_{rv} \tag{4.10}$$

4.1.2.4 Systemic and pulmonary circulations

The arteries, veins and capillaries of systemic and pulmonary circulations were included (Fig 4.2). The volume change, $\Delta V(t)$, of each compartment is computed from the integral of their respective net flow: $\Delta V(t) = \int (Q_{\text{in}} - Q_{\text{out}})\, \mathrm{d}t$, while the flow, Q, is defined by the pressure gradient, ΔP, across chambers and a resistance, R: $Q = {}^{\Delta P}/_{R}$. Pressures on venous and arterial vessels are defined as an elastance dependent relationship: $P = E \cdot (V - V_d)$, where E is the elastance and V_d refers the dead volume. The heart valves are modelled as perfect diodes.

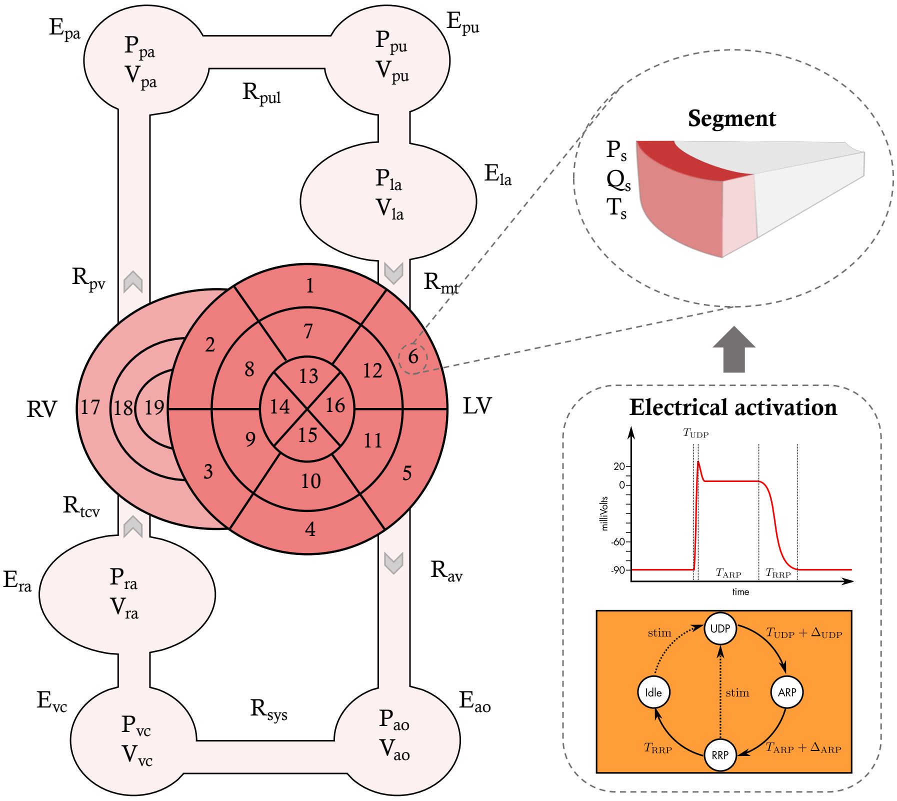

Figure 4.2: Closed-loop model of the cardiovascular system and representation of a myocardial segment. **Vascular network:** ao: aorta, vc: vena cava, pa: pulmonary artery, pu: pulmonary veins. **Heart valves:** mt: mitral, av: aortic, tc: tricuspide, pv: pulmonary. **Left ventricle segmentation:** 1: BasAnt; 2: BasAntSep; 3: BasInfSep; 4: BasInf; 5: BasInfLat; 6: BasAntLat; 7: MidAnt; 8: MidAntSep; 9: MidInfSep; 10: MidInf; 11: MidInfLat; 12: MidAntLat; 13: ApAnt; 14: ApSep; 15: ApInf; 16: ApLat. **Right ventricle segmentation:** 1: BasRV; 2: MidRV; 3: ApRV

4.1.3 Patient-specific adaptation

4.1.3.1 Sensitivity analysis

The first step of patient-specific adaptation corresponds to the sensitivity analysis of the model in order to provide insight into the relation between parameters and outputs and to allow a characterization of the relative significance of each parameter.

Using the Morris elementary effects method described in section 4.5, a set of parameters, with the highest sensitivity to the outputs Y was determined. For each parameter X_j, the range of possible values was defined as ±30% of the initial values, except for the electrical depolarization time parameter that the range was defined between 2 and 150 ms.

Analysis were performed with: $Y = \{\text{mean}(\varepsilon^{model}_{min,s}), \text{mean}(t^{model}_{min,s}), \text{std}(\varepsilon^{model}_{min,s}), \text{std}(t^{model}_{min,s})\}$, where $\varepsilon^{model}_{min,s}$ and $\text{t}^{model}_{min,s}$ correspond respectively to the minimum value of strain and the corresponding time for each segment s. Mean and standard-deviation values were calculated over the 16 strain signals.

4.1.4 Parameter identification

The second step of the patient-specific adaptation is the identification of a set of parameters selected from the sensitivity analysis. For each healthy adult and LBBB patient, an error function J_{error} between simulation outputs and experimental strain curves was minimized in order to find patient-specific parameters:

$$J_{error} = \sum_{s=1}^{16} J_s \tag{4.11}$$

$$J_s = \frac{1}{T_c} \sum_{t_e=0}^{T_c-1} \mid \varepsilon^{exp}_s(t_e) - \varepsilon^{model}_s(t_e) \mid + \mid \varepsilon^{exp}_{s,min} - \varepsilon^{model}_{s,min} \mid \tag{4.12}$$

where ε^{exp}_s and ε^{model}_s are the myocardial strain signals obtained from available clinical data and simulated outputs respectively. t_e corresponds to the time elapsed since the onset of the identification period and T_c is the duration of a cardiac cycle. The error function J_{error} was minimized using evolutionary algorithms (EA). These stochastic search methods are founded on theories of natural evolution, such as selection, crossover and mutation [37]. Robustness of the parameter identification method was assessed by repeating the identification process at least 10 times in healthy subjects and LBBB patients and relative standard deviations of identified parameters were calculated.

4.2 Results

4.2.1 Baseline simulations

Fig. 4.3 illustrates the baseline simulation results from the proposed computational model. Ventricular and arterial pressures as well as ventricular volume are presented at the top of the figure. Myocardial strain signals corresponding to the 16 LV segments are presented at the bottom of the figure. The results are presented for a healthy case. Systolic LV pressure is equal to 120 mmHg and the aortic pressure varies between 50 and 120 mmHg. The LV volume varies between 70 and 120 mL. The strain signals present similar morphologies between all the segments due to the mechanical synchronicity between them. Generally, simulation results agree with the physiological values and behaviors of a healthy subject.

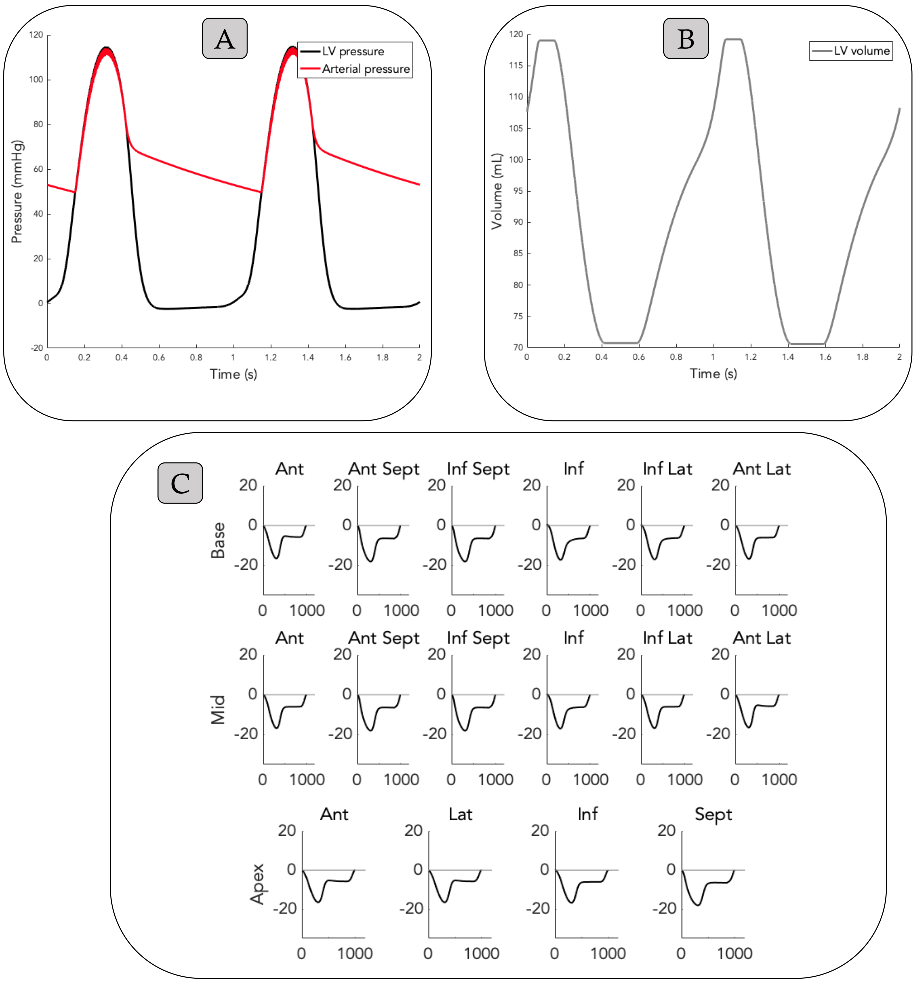

Figure 4.3: Model simulation results in healthy conditions. *A:* Left ventricle pressure (*black*) and arterial pressure (*red*). *B:* Left ventricle volume. *C:* Myocardial strain signals for the 16 LV segments.

In order to reproduce experimental lateral and septal strain traces of representative ischemic and non-ischemic patients with typical LBBB, we varied the value of one model parameter X_j at a time until we obtained simulated curves that resemble the experimental curves. Fig 4.4 illustrates the experimental and model-based strain traces for LBBB patients with non-ischemia, lateral ischemia and anterior ischemia. A typical LBBB patient presents a septal strain pattern characterized by a pre-ejection contraction of the septal wall followed by an immediate re-lengthening (septal rebound stretch) of the wall. As shown in [9], a reduction in the LV lateral wall contractility reduces the septal rebound stretch and increases septal shortening, however, the rebound stretch still present in patients with anterior ischemia. The septal and lateral strain curves obtained from the model are close with the experimental curves. Furthermore, the results agree with the experimental results obtained from [9], which demonstrate that strain morphologies are determined not only by electrical activation delay, but also by mechanical dysfunctions.

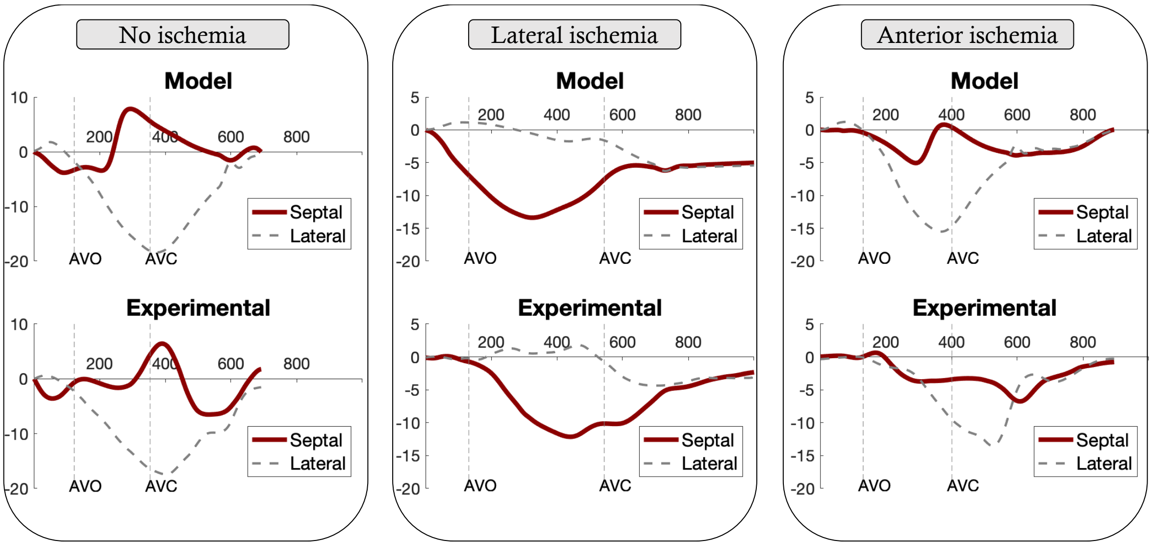

Figure 4.4: Simulated (*top*) and experimental (*bottom*) strain traces from representative LBBB patients with non ischemia (*left*), lateral ischemia (*middle*), and anterior ischemia (*right*).

4.2.2 Sensitivity analysis

Fig. 4.5 shows the 10 parameters with the highest sensitivity evaluated on Y. Sensitivity results are based on the D_j index, calculated from σ_j and μ_j*. Parameters $n1$ and $n2$, which are related with the EMDF, present a greater recurrence on the sensitivity of the evaluated outputs Y. In fact, these parameters affect the electro-mechanical coupling at the tissue-level which cause modifications in mechanical contraction and, consequently, in the deformation of the LV segments. UDP, related with the electrical depolarization time, is also one of the most influential parameters. Indeed, the electrical and mechanical activities are closely related, therefore the deformation of a segment is highly dependent on the occurrence of electrical depolarization. K_{act} and K_{pass}, respectively related with the active and passive components of the cardiac muscle, show also high sensitivity.

Results from the sensitivity analysis were used to select the 7 most significant model parameters to be identified for each segment: parameters related with the EMDF ($n_1, n_2, \alpha_1, \alpha_2$), the active ($K_{act}$) and passive ($K_{pass}$) components of the cardiac muscle and the electrical depolarization time (UDP).

4.2.3 Patient-specific simulations

4.2.3.1 Segmental strain curves

Myocardial strain curves of the 16 LV segments acquired by experimental measurements and patient-specific simulations are presented in one representative healthy subject (Fig. 4.6), an anterior ischemic (Fig. 4.7) and a non-ischemic (Fig. 4.8) LBBB patient. All results are included in supplementary materials. For both healthy and LBBB cases, a good agreement was observed between clinical and simulated strain signals. Concerning healthy cases, the strain curves present similar morphologies in all the segments due to the synchronization in all LV regions when the myocardium contracts. Mean RMSE between estimated and observed strain signals in the healthy adults was equal to 5.04 ± 1.02 (Table 4.2). In LBBB cases, mean RMSE was equal to 3.38 ± 0.91 (Table 4.2). In these cases, the strain curves obtained in LBBB patients present dissimilar morphologies between the different segments. Particularly, the septum and the lateral wall segments of the ventricle present opposite curves, where the shortening of septal segments occurs at the same time as in the lengthening of lateral segments.

By repeatedly applying 10 times the proposed identification method, we obtained for the identified parameters a mean relative standard deviation of 10,87% for healthy subjects and 13,09% for LBBB patients. As a consequence, the identified parameters remain closed for each patient, evidencing the robustness of the method.

4.2.3.2 Bull’s eye representations

From patient-specific simulations, segmental electrical activation delay and the percentage of myofiber contractility (K_{act}) were represented on bull’s-eye plots in Figs. 4.6, 4.7, 4.8, for 3 representative cases : 1) Healthy adult, 2) LBBB patient with LV anterior ischemia and 3) Non-ischemic LBBB patient. For the ischemic patient, a bull’s-eye plot representing the percentage of transmurality, obtained from MRI, was also presented.

In LBBB cases, electrical activation bull’s-eye shows a significant electrical activation delay between the lateral and the septal wall of the LV; while in the healthy case,

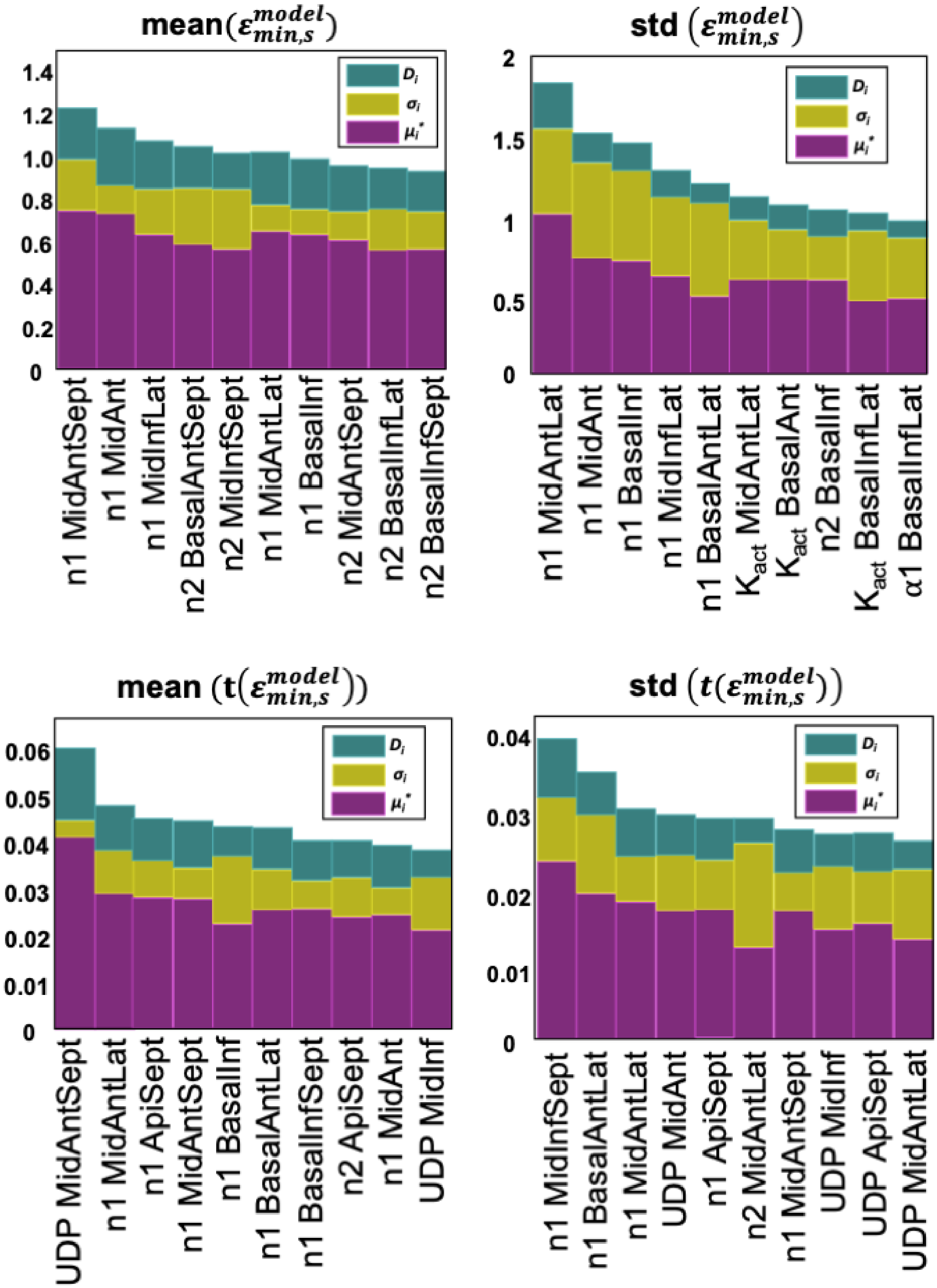

Figure 4.5: Most influential parameters on *i)* the average of the minimum peaks over all segments (*top,left*), *ii)* the standard deviation of the minimum peaks over all segments (*top, right*), *iii)* the average time associated to each minimum peak over all segments (*bottom,left*) and *iv)* the standard deviation of the time associated to each minimum peak over all segments (*bottom,right*); according to Morris sensitivity results. For each parameter, the distance D_j (green bars), the absolute mean μ_i* (purple bars) and the standard deviation σ_j (yellow bars) of the elementary effects are represented.

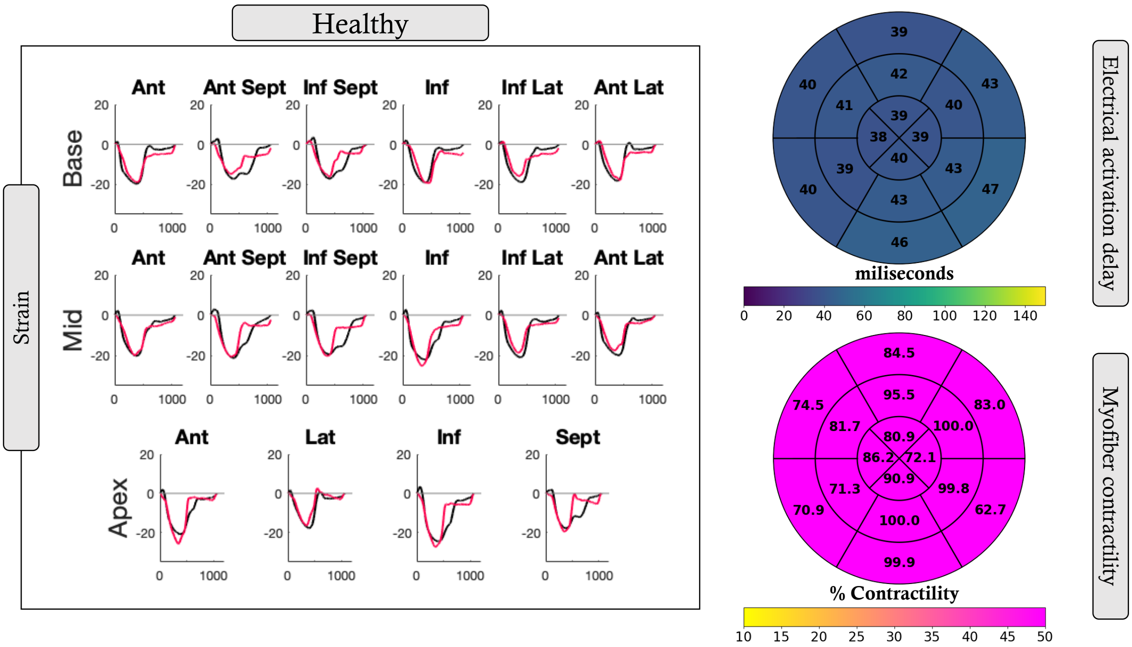

Figure 4.6: Patient-specific simulation results for a healthy subject. Experimental (red) and simulated (black) strain curves corresponding to the 16 LV segments. Bull's-eye representations of segmental electrical activation delay and segmental myofiber contractility. Colour scale at the contractility bull's-eye plot set between 10 and 50% in order to highlight the segments with low contractility.

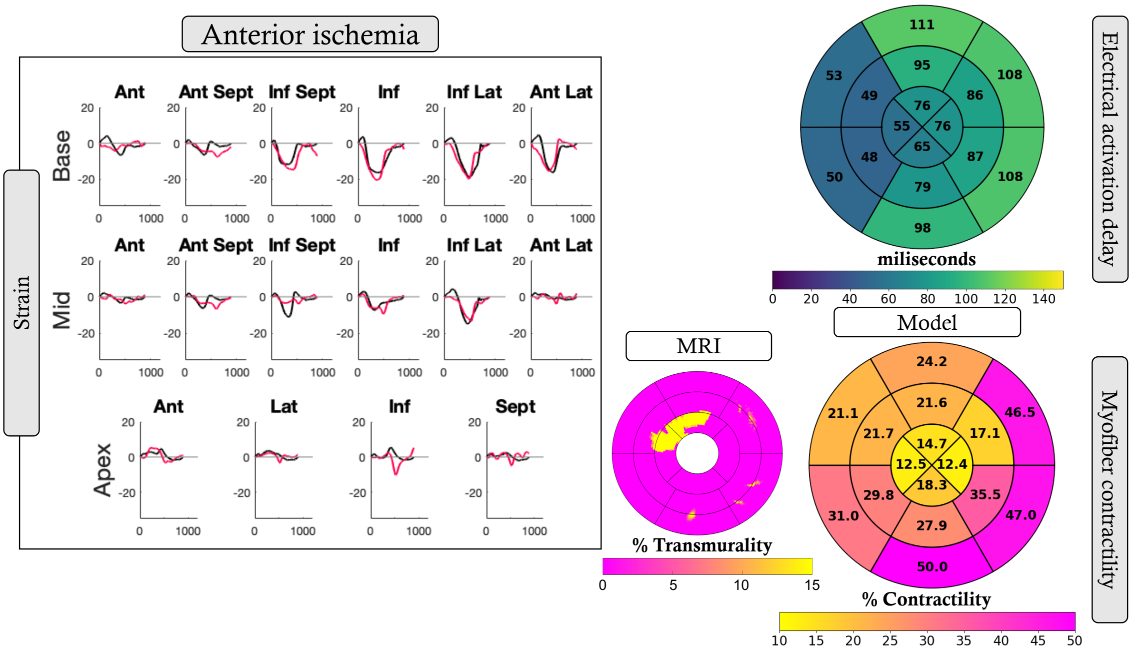

Figure 4.7: Patient-specific simulation results for a LBBB patient with an anterior ischemia. Experimental (red) and simulated (black) strain curves corresponding to the 16 LV segments. Bull's-eye representations of segmental electrical activation delay and segmental myofiber contractility obtained by patient-specific simulations. Bull's eye representation of transmurality obtained by MRI.

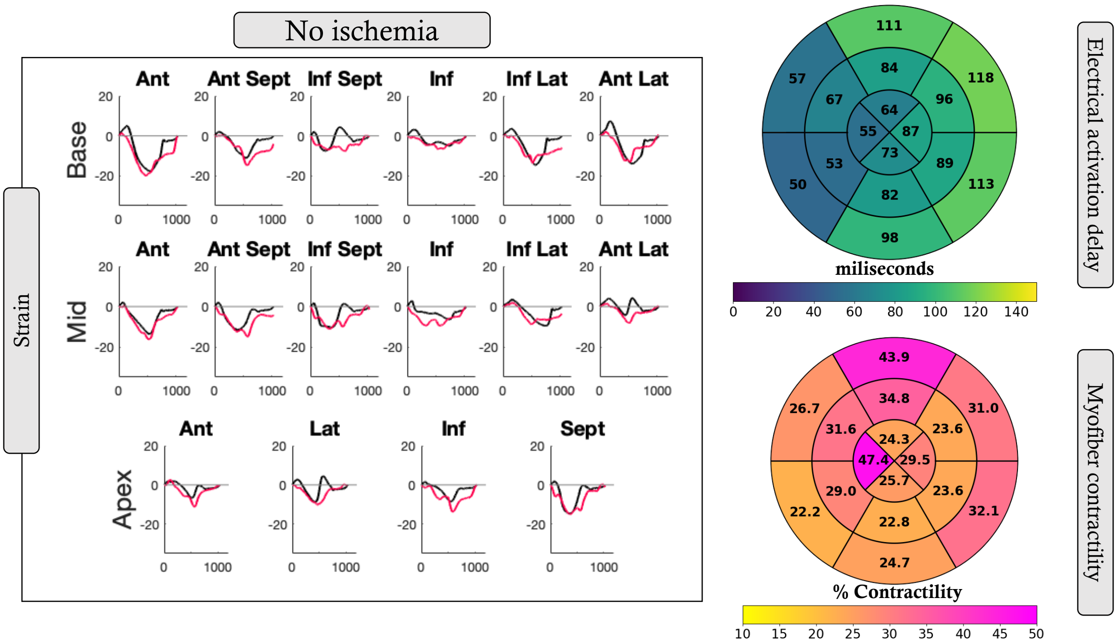

Figure 4.8: Patient-specific simulation results for a non-ischemic LBBB patient. Experimental (red) and simulated (black) strain curves corresponding to the 16 LV segments. Bull's-eye representations of segmental electrical activation delay and segmental myofiber contractility.

Table 4.2: Mean RMSE between the 16 experimental and simulated LV strain curves of the study population.

Healthy	Mean RMSE	LBBB (Ischemia)	Mean RMSE
Patient 1	4.91 ± 2.16	**Patient 1**	2.71 ± 1.13
Patient 2	3.89 ± 1.08	**Patient 2**	2.88 ± 1.0
Patient 3	4.77 ± 1.53	**Patient 3**	2.5 ± 0.56
Patient 4	4.19 ± 1.13	**Patient 4**	1.96 ± 0.69
Patient 5	5.41 ± 1.66	**Patient 5**	3.51 ± 1.1
Healthy	**Mean RMSE**	**LBBB (Non-ischemia)**	**Mean RMSE**
Patient 6	6.23 ± 12.45	**Patient 1**	3.47 ± 1.03
Patient 7	3.43 ± 0.88	**Patient 2**	3.63 ± 0.82
Patient 8	5.45 ± 1.84	**Patient 3**	5.03 ± 1.49
Patient 9	6.72 ± 2.38	**Patient 4**	4.38 ± 2.06
Patient 10	5.4 ± 2.3	**Patient 5**	3.73 ± 1.3

all LV segments are activated almost synchronously. Furthermore, the LBBB patient with LV anterior ischemia presented reduced contractility in anterior segments of the Bull's eye representation, corresponding with the areas of high transmurality reported in MRI (Fig. 4.7). A high percentage of transmurality translates into fibrosis, which is generally associated with low contractility. Therefore, regional contractility results allow ischemic and non-ischemic cases distinction, where reduced contractility could be associated with damaged tissues.

4.3 Discussion

This chapter presented a novel model-based approach that yields simulations of patient-specific strain curves in several LV regions for healthy adults and patients diagnosed with LBBB. The main contributions of this study are: *i)* the proposal of an integrated model of the cardiovascular system coupled to multi-segment representations of ventricles *ii)* the sensitivity analysis of model parameters on myocardial strains, *iii)* the identification of model parameters to reproduce myocardial strain curves specifically to each patient and *iv)* the analysis of patient-specific identified parameters.

It is worth highlighting the incremental added value of the model proposed in this chapter with respect to the model presented in Chapter 3. Both models preserve the same representation of the vascular circulation, however, the electrical and mechanical representations differ since the left and right ventricles were divided into segments to interpret the dynamics in the different LV regions during the cardiac cycle. We propose a model not only capable of simulating the complex mechanisms involved in the generation of ventricular contraction (mechano-hydraulic interactions, electrical activation and propagation, etc.) but also a model capable of overcoming the multidimensionality of the problem with low computational requirements. It is also noteworthy that the model-based approaches proposed in both chapters follow the same methodological framework: the identification of patient-specific model parameters selected from a sensitivity analysis to reproduce simulated data consistent with clinical data.

The CVS model proposed in this chapter is based on a functional integration of interacting physiological systems that takes into account the electro-mechanical coupling, the interventricular interaction and a simplified representation of systemic and pulmonary circulations. The model includes the main cardiac properties required to tackle the problem under study, like the Frank-Starling law and the influence of preload and afterload. Results illustrate the model ability to simulate jointly the hemodynamic variables and myocardial deformations. Strain curves notably reflected typical characteristics associated with each phase of the cardiac cycle. In order to personalize models to patient-specific data, a large number of simulations should be performed. In opposition to FEM representations [19], the proposed model requires limited computational resources, as the simulation of one cardiac cycle (1000 ms of simulation) takes about 0.5 seconds (Processor : 2,2 GHz Intel Core i7). The low computational cost is of primary importance to use cardiac modelling in clinical practice and to adapt models to each patient.

The first step of patient-specific adaptation is the sensitivity analysis of model parameters, which highlights *i)* the close relationship between cardiac electrical and mechanical systems and *ii)* the importance of active and passive properties of the myocardium during cardiac contraction. In fact, a close relationship exists between excitation and contraction since a synchronous ventricular activation is a prerequisite for an adequate LV function, whereas the electrical activation delay between opposite LV walls might lead to dyssynchronous ventricular contraction and LV failure [38]. Nevertheless, it has been shown that typical myocardial strain morphologies in LBBB could be modified by the presence of scar and low regional LV contractility [9]. In this context, the ability of the model to disclose the relationship between electrical activation delay and LV contractility has pivotal importance because it might ease the identification of myocardial substrates that more prone to be associated with CRT-response.

In the second step of patient-specific adaptation, evolutionary algorithms were used to identify the most influential parameters in each patient. Patient-specific simulations have shown satisfactory results since we observed a good agreement between simulated and experimental myocardial strain curves presenting similar morphologies. For healthy cases, morphologies of the myocardial strain curves were similar in all segments due to the synchronous contraction of the entire LV [29]. Associated bull-eyes show normal electrical activation times and elevated contractile levels.

In most patients with non-ischemic LBBB, the early activation of the LV septum, followed by the delayed activations of the LV wall [39, 40], causes a typical myocardial strain pattern. This pattern is characterized by an early marked shortening of the septum in the pre-ejection phase, known as "septal flash" [41] followed by an immediate re-lengthening of the septum, the "septal rebound stretch". Both the septal flash and septal rebound are known to be predictors of CRT response [7, 42].

In ischemic patients, the typical activation pattern induced by LBBB can be disrupted by the association of electrical delay and inhomogeneous LV contractility. In patients with LBBB and lateral scar, hypocontractile regions are localized in the lateral wall. In this case, deformation patterns are highly modified because the local impairment of contractility in the lateral wall caused the loss of the rebound stretch in the septum [9]. On the contrary, the presence of anterior scar was associated with a reduced contractility of the corresponding myocardial segments and had less impact of septal deformation [9]. The strength of our model was therefore to reproduce the "atypical" strain patterns observed in patients with LBBB and ischemic cardiomyopathy thought the correct localization of the hypocontractile segments, which correspond to areas of myocardial scar identified by clinician based on MRI.

There are several important consequences of our findings. First, the result of our model-based approach underscores that septal motion and global strain morphologies are not only explained by electrical conduction delay, but also by the heterogeneity of contractile levels within the myocardium and suggests that the evaluation of LV dyssynchrony should take into account both electrical delay and regional mechanical function. Second, the application of a model-based approach could bring additional information on the regional electrical and mechanical function of the LV from the simple analysis of echocardiography data. This is particularly important because it can help to disclose the intrinsic complexity of LV mechanics in CRT candidates, and represents a step forwards the development of personalized LV modeling in the field of CRT. Third, one of the main strengths of the approach was to perform a parameter identification process for the patient-specific estimations of the segmental strain curves. In order to build the cost function, experimental and simulated strain curves were synchronised on QRS peaks of synthesized and experimental ECG. Model parameters were identified from the myocardial strain curves of the 16 LV segments acquired by STE. For both healthy and LBBB cases, a good agreement was observed between measured and estimated strain signals. Moreover, the identification process was repeatedly applied to evaluate and demonstrate the robustness of the method. This makes our model particularly powerful since the capacity to reproduce clinical measurements provides confidence to analyse the LV function for an individual patient and eventually predict optimal treatments.

Although several studies have successfully used computational models of the CVS to understand myocardial deformation patterns [43, 44, 45], our approach provides interesting advantages and originalities. The multi-segment model of the LV allows not only the analysis of the deformation curves of the septal and lateral walls, but also the strain signals of all the ventricular regions. Therefore, the proposed model resolution was adapted to the standardized segmentation of the AHA, keeping a similar abstraction level as clinicians for the analysis of strain signals. Moreover, our approach applies a parameter identification process, providing customized models specifically for each patient and allowing the recognition of hypocontractile areas that could be associated with the presence of fibrosis.

4.4 Limitations

The proposed model-based approach presents a number of limitations that should be mentioned. Several hypothesis were made in order to propose tissue-level representations of ventricles: *i)* the ventricular torsion was neglected, *ii)* the mechanical continuity between myocardial segments was not always assured because ventricles are represented by a set of sub-pumps controlled by a coordinated electrical activity and coupled in the hydraulic domain, *iii)* only mean myocardial fiber orientation was considered, and *iv)* electro-mechanical coupling was approximated by an analytic expression.

Despite these hypotheses, the model definition is in accordance with the problem under study and appears to be a useful tool to assist the interpretation of strain data. Moreover, in order to reduce computational costs, only a small sample of variables was selected for parameter identification. These parameters may have absorbed changes in other fixed parameters. For instance, septal segment parameters may have been affected by RV variations. Thus, a wider range of parameters could be included in the future. Finally, this study is based on a small population of LBBB patients and further conclusions should be obtained by the extension of our simulations to data obtained from larger clinical series. Nevertheless, this is the first work providing patient-specific simulations of strain curves in the case of LBBB in association with ischemia and the proposed approach is a step forward towards the integration of computational models in patient selection process before CRT procedures. Future work will be dedicated to evaluate the proposed model-based indices, in wider multi-parametric approach [46], for the prediction of CRT response.

4.5 Conclusion

It is important to reiterate the additional value of the model proposed in this chapter with respect to the Chapter 3. Although the model aimed to LBBB patients is much more complex compared to the model proposed for patients with AS, both share a common methodological framework in order to achieve the main objective of this thesis: to propose a set of integrated sub-models of the CVS with low computational requirements, for the analysis of the cardiac function.

In this chapter, a novel model-based approach for the analysis of myocardial strains in LBBB patients is proposed. The global method is based on *i)* a physiological model of the cardiovascular system that integrates the electrical, mechanical and hydraulic processes leading to ventricular contraction and *ii)* a parameter identification procedure for patient-specific simulations. The proposed model-based approach was evaluated with echocardiography data from 10 healthy individuals and 10 LBBB patients. Results show a close match between experimental and simulated strain curves in all the cases. Furthermore, the approach is able to reproduce electrical activation delay and segmental myofiber contractility properly.

More extensive evaluations including a greater population of patients, as well as the analysis on a wider multi-parametric approach should be performed in the future. Nevertheless, this study presents a first work towards the evaluation of myocardial strain signals and the assessment of certain echo-based parameters by patient-specific simulations based on computational models as a useful tool for understanding LV mechanical dyssynchrony and identifying patients suitable for CRT.

Bibliography

[1] A. Sami, M. F. Iftekhar, I. Khan, and R. Jan, “Intraventricular Dyssynchrony among patients with left bundle branch block,” *Pakistan Journal of Medical Sciences*, vol. 34, no. 2, pp. 390–392, 2018.

[2] C. Daubert, S. Cazeau, P. Ritter, and C. Leclercq, “Past, present and future of cardiac resynchronization,” *Archives of Cardiovascular Diseases*, vol. 105, pp. 291–299, May 2012.

[3] N. Risum, B. Tayal, T. F. Hansen, N. E. Bruun, M. T. Jensen, T. K. Lauridsen, S. Saba, J. Kisslo, J. Gorcsan, and P. Sogaard, “Identification of Typical Left Bundle Branch Block Contraction by Strain Echocardiography Is Additive to Electrocardiography in Prediction of Long-Term Outcome After Cardiac Resynchronization Therapy,” *Journal of the American College of Cardiology*, vol. 66, pp. 631–641, Aug. 2015.

[4] A. Gallard, A. Hubert, O. Smiseth, J.-U. Voigt, V. Le Rolle, C. Leclercq, A. Bidaut, E. Galli, E. Donal, and A. I. Hernandez, “Prediction of response to cardiac resynchronization therapy using a multi-feature learning method,” *The International Journal of Cardiovascular Imaging*, Nov. 2020.

[5] A. Hubert, A. Gallard, V. Le Rolle, O. Smiseth, C. Leclercq, J.-U. Voigt, E. Galli, V. Galant, A. I. Hernandez, and E. Donal, “Left ventricular strain for predicting

the response to cardiac resynchronization therapy: Aq1 two methods for one question," *The International Journal of Cardiovascular Imaging*.

[6] B. W. L. De Boeck, A. J. Teske, M. Meine, G. E. Leenders, M. J. Cramer, F. W. Prinzen, and P. A. Doevendans, "Septal rebound stretch reflects the functional substrate to cardiac resynchronization therapy and predicts volumetric and neurohormonal response," *European Journal of Heart Failure*, vol. 11, pp. 863–871, Sept. 2009.

[7] I. Stankovic, C. Prinz, A. Ciarka, A. M. Daraban, M. Kotrc, M. Aarones, M. Szulik, S. Winter, A. Belmans, A. N. Neskovic, T. Kukulski, S. Aakhus, R. Willems, W. Fehske, M. Penicka, L. Faber, and J.-U. Voigt, "Relationship of visually assessed apical rocking and septal flash to response and long-term survival following cardiac resynchronization therapy (PREDICT-CRT)," *European Heart Journal Cardiovascular Imaging*, vol. 17, pp. 262–269, Mar. 2016.

[8] H. B. Rao, R. Krishnaswami, S. Kalavakolanu, and N. Calambur, "Ventricular Dyssynchrony Patterns in Left Bundle Branch Block, With and Without Heart Failure," *Indian Pacing and Electrophysiology Journal*, vol. 10, pp. 115–121, Mar. 2010.

[9] J. M. Aalen, E. W. Remme, C. K. Larsen, O. S. Andersen, M. Krogh, J. Duchenne, E. Hopp, S. Ross, A. S. Beela, E. Kongsgaard, J. Bergsland, H. H. Odland, H. Skulstad, A. Opdahl, J.-U. Voigt, and O. A. Smiseth, "Mechanism of Abnormal Septal Motion in Left Bundle Branch Block: Role of Left Ventricular Wall Interactions and Myocardial Scar," *JACC. Cardiovascular imaging*, vol. 12, no. 12, pp. 2402–2413, 2019.

[10] Hoit Brian D., "Strain and Strain Rate Echocardiography and Coronary Artery Disease," *Circulation: Cardiovascular Imaging*, vol. 4, pp. 179–190, Mar. 2011. Publisher: American Heart Association.

[11] Lumens Joost, Tayal Bhupendar, Walmsley John, Delgado-Montero Antonia, Huntjens Peter R., Schwartzman David, Althouse Andrew D., Delhaas Tammo, Prinzen Frits W., and Gorcsan John, "Differentiating Electromechanical From Non–Electrical Substrates of Mechanical Discoordination to Identify Responders to Cardiac Resynchronization Therapy," *Circulation: Cardiovascular Imaging*, vol. 8, p. e003744, Sept. 2015. Publisher: American Heart Association.

[12] J. P. Ugarte, C. Tobón, J. Saiz, A. M. Lopes, and J. A. Tenreiro Machado, "Spontaneous activation under atrial fibrosis: A model using complex order derivatives," *Communications in Nonlinear Science and Numerical Simulation*, p. 105618, Nov. 2020.

[13] A. Belmiloudi and S. Corre, "Mathematical modeling and analysis of dynamic effects of multiple time-varying delays on electrophysiological wave propagation in the heart," *Nonlinear Analysis: Real World Applications*, vol. 47, pp. 18–44, June 2019. Publisher: Elsevier.

[14] C. Trovato, E. Passini, N. Nagy, A. Varró, N. Abi-Gerges, S. Severi, and B. Rodriguez, "Human Purkinje in silico model enables mechanistic investigations into automaticity and pro-arrhythmic abnormalities," *Journal of Molecular and Cellular Cardiology*, vol. 142, pp. 24–38, May 2020.

[15] S. Cortassa, M. A. Aon, B. O'Rourke, R. Jacques, H.-J. Tseng, E. Marbán, and R. L. Winslow, "A Computational Model Integrating Electrophysiology, Contraction, and Mitochondrial Bioenergetics in the Ventricular Myocyte," *Biophysical Journal*, vol. 91, pp. 1564–1589, Aug. 2006.

[16] L. J. Dupuis, J. Lumens, T. Arts, and T. Delhaas, "Mechano-chemical Interactions in Cardiac Sarcomere Contraction: A Computational Modeling Study," *PLOS Computational Biology*, vol. 12, p. e1005126, Oct. 2016. Publisher: Public Library of Science.

[17] F. Regazzoni, L. Dedè, and A. Quarteroni, "Biophysically detailed mathematical models of multiscale cardiac active mechanics," *PLOS Computational Biology*, vol. 16, p. e1008294, Oct. 2020. Publisher: Public Library of Science.

[18] A. Pironet, T. Desaive, S. Kosta, A. Lucas, S. Paeme, A. Collet, C. G. Pretty, P. Kolh, and P. C. Dauby, "A multi-scale cardiovascular system model can account for the load-dependence of the end-systolic pressure-volume relationship," *BioMedical Engineering OnLine*, vol. 12, p. 8, Jan. 2013.

[19] V. L. Rolle, E. Galli, D. Danan, K. E. Houari, A. Hubert, E. Donal, and A. I. Hernández, "Sensitivity Analysis of a Left Ventricle Model in the Context of Intraventricular Dyssynchrony," *Acta Biotheoretica*, Sept. 2019.

[20] K. L. Sack, Y. Dabiri, T. Franz, S. D. Solomon, D. Burkhoff, and J. M. Guccione, "Investigating the Role of Interventricular Interdependence in Development of Right Heart Dysfunction During LVAD Support: A Patient-Specific Methods-Based Approach," *Frontiers in Physiology*, vol. 9, 2018. Publisher: Frontiers.

[21] J. I. K. Park, A. K. Heikhmakhtiar, C. H. Kim, Y. S. Kim, S. W. Choi, K. S. Song, and K. M. Lim, "The effect of heart failure and left ventricular assist device treatment on right ventricular mechanics: a computational study," *BioMedical Engineering OnLine*, vol. 17, p. 62, May 2018.

[22] J. Lumens, G. E. Leenders, M. J. Cramer, B. W. L. De Boeck, P. A. Doevendans, F. W. Prinzen, and T. Delhaas, "Mechanistic evaluation of echocardiographic dyssynchrony indices: patient data combined with multiscale computer simulations," *Circulation. Cardiovascular Imaging*, vol. 5, pp. 491–499, July 2012.

[23] E. Willemen, R. Schreurs, P. R. Huntjens, M. Strik, G. Plank, E. Vigmond, J. Walmsley, K. Vernooy, T. Delhaas, F. W. Prinzen, and J. Lumens, "The Left and Right Ventricles Respond Differently to Variation of Pacing Delays in Cardiac Resynchronization Therapy: A Combined Experimental- Computational Approach," *Frontiers in Physiology*, vol. 10, p. 17, 2019.

[24] W. M. van Everdingen, J. Walmsley, M. J. Cramer, I. van Hagen, B. W. L. De Boeck, M. Meine, T. Delhaas, P. A. Doevendans, F. W. Prinzen, J. Lumens, and G. E. Leenders, "Echocardiographic Prediction of Cardiac Resynchronization Therapy Response Requires Analysis of Both Mechanical Dyssynchrony and Right Ventricular Function: A Combined Analysis of Patient Data and Computer Simulations," *Journal of the American Society of Echocardiography: Official Publication of the American Society of Echocardiography*, vol. 30, pp. 1012–1020.e2, Oct. 2017.

[25] G. E. Leenders, J. Lumens, M. J. Cramer, B. W. L. De Boeck, P. A. Doevendans, T. Delhaas, and F. W. Prinzen, "Septal deformation patterns delineate mechanical dyssynchrony and regional differences in contractility: analysis of patient data using a computer model," *Circulation. Heart Failure*, vol. 5, pp. 87–96, Jan. 2012.

[26] V. Le Rolle, A. I. Hernández, P.-Y. Richard, E. Donal, and G. Carrault, "Model-based analysis of myocardial strain data acquired by tissue Doppler imaging," *Artificial Intelligence in Medicine*, vol. 44, pp. 201–219, Nov. 2008.

[27] M. Calvo, V. Le Rolle, D. Romero, N. Béhar, P. Gomis, P. Mabo, and A. I. Hernández, "Model-based analysis of the autonomic response to head-up tilt testing in Brugada syndrome," *Computers in Biology and Medicine*, vol. 103, pp. 82–92, Dec. 2018.

[28] K. P. Owashi, A. Hubert, E. Galli, E. Donal, A. I. Hernández, and V. Le Rolle, "Model-based estimation of left ventricular pressure and myocardial work in aortic stenosis," *PloS One*, vol. 15, no. 3, p. e0229609, 2020.

[29] R. M. Lang, L. P. Badano, V. Mor-Avi, J. Afilalo, A. Armstrong, L. Ernande, F. A. Flachskampf, E. Foster, S. A. Goldstein, T. Kuznetsova, P. Lancellotti, D. Muraru, M. H. Picard, E. R. Rietzschel, L. Rudski, K. T. Spencer, W. Tsang, and J.-U. Voigt, "Recommendations for Cardiac Chamber Quantification by Echocardiography in Adults: An Update from the American Society of Echocardiography and the European Association of Cardiovascular Imaging," *Journal of the American Society of Echocardiography*, vol. 28, pp. 1–39.e14, Jan. 2015. Publisher: Elsevier.

[30] N. Kachenoura, A. Redheuil, A. Herment, E. Mousseaux, and F. Frouin, "Robust assessment of the transmural extent of myocardial infarction in late gadolinium-enhanced MRI studies using appropriate angular and circumferential subdivision of the myocardium," *European Radiology*, vol. 18, pp. 2140–2147, Oct. 2008.

[31] N. Baron, N. Kachenoura, P. Cluzel, F. Frouin, A. Herment, P. Grenier, G. Montalescot, and F. Beygui, "Comparison of various methods for quantitative evaluation of myocardial infarct volume from magnetic resonance delayed enhancement data," *International Journal of Cardiology*, vol. 167, p. 739, Aug. 2013.

[32] Cerqueira Manuel D., Weissman Neil J., Dilsizian Vasken, Jacobs Alice K., Kaul Sanjiv, Laskey Warren K., Pennell Dudley J., Rumberger John A., Ryan Thomas, and Verani Mario S., "Standardized Myocardial Segmentation and Nomenclature

for Tomographic Imaging of the Heart," *Circulation*, vol. 105, pp. 539–542, Jan. 2002. Publisher: American Heart Association.

[33] N. Stergiopulos, J. Meister, and N. Westerhof, "Determinants of stroke volume and systolic and diastolic aortic pressure," *Am J. Physiol*, vol. 270, pp. H2050–H2059, 1996;.

[34] V. Le Rolle, G. Carrault, P.-Y. Richard, P. Pibarot, L.-G. Durand, and A. I. Hernández, "A Tissue-Level Electromechanical Model of the Left Ventricle: Application to the Analysis of Intraventricular Pressure," *Acta Biotheoretica*, vol. 57, p. 457, Oct. 2009.

[35] J. Lumens, T. Delhaas, B. Kirn, and T. Arts, "Three-wall segment (TriSeg) model describing mechanics and hemodynamics of ventricular interaction," *Annals of Biomedical Engineering*, vol. 37, pp. 2234–2255, Nov. 2009.

[36] P. J. Hunter, A. D. McCulloch, and H. E. ter Keurs, "Modelling the mechanical properties of cardiac muscle," vol. 69, pp. 289–331.

[37] A. L. Goldberger, C. K. Peng, and L. A. Lipsitz, "What is physiologic complexity and how does it change with aging and disease?," *Neurobiology of Aging*, vol. 23, pp. 23–26, Jan. 2002.

[38] U. C. Nguyên, N. J. Verzaal, F. A. van Nieuwenhoven, K. Vernooy, and F. W. Prinzen, "Pathobiology of cardiac dyssynchrony and resynchronization therapy," *Europace: European Pacing, Arrhythmias, and Cardiac Electrophysiology: Journal of the Working Groups on Cardiac Pacing, Arrhythmias, and Cardiac Cellular Electrophysiology of the European Society of Cardiology*, vol. 20, no. 12, pp. 1898–1909, 2018.

[39] B. W. De Boeck, B. Kirn, A. J. Teske, R. W. Hummeling, P. A. Doevendans, M. J. Cramer, and F. W. Prinzen, "Three-dimensional mapping of mechanical activation patterns, contractile dyssynchrony and dyscoordination by two-dimensional strain echocardiography: Rationale and design of a novel software toolbox," *Cardiovascular Ultrasound*, vol. 6, p. 22, May 2008.

[40] O. Gjesdal, E. W. Remme, A. Opdahl, H. Skulstad, K. Russell, E. Kongsgaard, T. Edvardsen, and O. A. Smiseth, "Mechanisms of abnormal systolic motion of the interventricular septum during left bundle-branch block," *Circulation. Cardiovascular Imaging*, vol. 4, pp. 264–273, May 2011.

[41] C. Parsai, B. Bijnens, G. R. Sutherland, A. Baltabaeva, P. Claus, M. Marciniak, V. Paul, M. Scheffer, E. Donal, G. Derumeaux, and L. Anderson, "Toward understanding response to cardiac resynchronization therapy: left ventricular dyssynchrony is only one of multiple mechanisms," *European Heart Journal*, vol. 30, pp. 940–949, Apr. 2009.

[42] A. Doltra, B. Bijnens, J. M. Tolosana, R. Borràs, M. Khatib, D. Penela, and al, "Mechanical abnormalities detected with conventional echocardiography are associ-

ated with response and midterm survival in CRT," *JACC. Cardiovascular imaging*, vol. 7, pp. 969–979, Oct. 2014.

[43] J. Walmsley, T. Arts, N. Derval, P. Bordachar, H. Cochet, S. Ploux, F. W. Prinzen, T. Delhaas, and J. Lumens, "Fast Simulation of Mechanical Heterogeneity in the Electrically Asynchronous Heart Using the MultiPatch Module," *PLOS Computational Biology*, vol. 11, p. e1004284, July 2015. Publisher: Public Library of Science.

[44] J.-i. Okada, T. Washio, M. Nakagawa, M. Watanabe, Y. Kadooka, T. Kariya, H. Yamashita, Y. Yamada, S.-i. Momomura, R. Nagai, T. Hisada, and S. Sugiura, "Multiscale, tailor-made heart simulation can predict the effect of cardiac resynchronization therapy," *Journal of Molecular and Cellular Cardiology*, vol. 108, pp. 17–23, July 2017.

[45] M. Albatat, H. Arevalo, J. Bergsland, V. Strøm, I. Balasingham, and H. H. Odland, "Optimal pacing sites in cardiac resynchronization by left ventricular activation front analysis," *Computers in Biology and Medicine*, vol. 128, p. 104159, Jan. 2021.

[46] E. Donal, A. Hubert, V. Le Rolle, C. Leclercq, R. Martins, P. Mabo, E. Galli, and A. Hernandez, "New Multiparametric Analysis of Cardiac Dyssynchrony: Machine Learning and Prediction of Response to CRT," *JACC. Cardiovascular imaging*, vol. 12, no. 9, pp. 1887–1888, 2019.

CONCLUSION

Computational modeling has become increasingly popular in biomedical research as it has been shown to be useful for the prediction, diagnosis and risk stratification of diseases, as well as for the assistance to therapy definition. Moreover, this approach allows for a better understanding of the different and complex interactions underlying multifactorial pathologies. Computational modeling appears, therefore, as an efficient tool to integrate physiological knowledge into a data processing chain. The inherent need for computational modeling in cardiology is clear and even more the personalized model-based approaches.

The main contribution of this work was thus **the proposal of a set of integrated sub-models of the cardiovascular system, suited for the analysis of the cardiac function in the case of aortic stenosis (AS) and left bundle branch block (LBBB)**. The proposed approach is based on a methodological framework that combines multi-resolution physiological modelling, parameter sensitivity and identification methods. Integrated models of the cardiovascular systems were proposed and their resolutions were adapted in function of each application These hybrid models, including heterogeneous and dynamic mathematical formalisms, were developed using the modelling and simulation environment proposed by our team (M2SL). One major challenge was to determine patient-specific parameters in order to realize personalized simulations and model-based interpretations. The proposed parameter analysis includes sensitivity analysis, and identification of parameter values. Determination of important parameters with the sensitivity analysis provides key information towards accurate simulations and patient-specific parameters. Evolutionary Algorithms (EA) were applied for the identification of patient-specific parameters of each clinical case. This proposed methodological framework was applied to two clinical applications:

- The first application of this thesis was to propose **a non-invasive model-based estimation of the LV pressure curve in order to obtain reliable myocardial work indices in the case of AS**. An integrated model of the CVS was proposed: i) cardiac electrical activity, ii) elastance-based mechanical activity, iii) systemic and pulmonary circulations and iv) heart valves. Moreover, an identification strategy using a 2-step cross-validation technique was applied on a first database of 12 AS patients, and then a 1-step identification strategy was applied on a second database of 23 AS patients. Results show a good agreement between work index estimations from LV pressure obtained with patient-specific simulations and with experimental measurements. To our knowledge, this is the first method for the estimation of myocardial work, based on a physiological model, rather than a template-based estimation. The results are promising and the proposed model can be a simple and physiological, first-line analyses that could be applied before other more complex and costly investigations (cardiac MRI,..) for the evaluation of myocardial contractility and residual myocardial viability. The assessment of regional myocardial work might be particularly important for the prognosis of patients with severe asymptomatic AS without LV dysfunction, since the timing and indications for surgical intervention in this population remain controversial.

— The second application of the thesis was to propose **a novel model-based approach for the analysis of myocardial strains in LBBB patients**. An integrated model of the CVS was developed based on representations of: i) cardiac electrical system, ii) right and left atrium, iii) multisegments right and left ventricles and iv) systemic and pulmonary circulations. The proposed model is an evolution of the AS model as it integrates a multi-segment representation based on the coupling of multiple, elastance-based elements. After a sensitivity analysis step, model parameters were identified specifically to each patient. The proposed approach was evaluated on data obtained from 10 healthy subjects and 10 LBBB patients, including ischemic (n=5) and non-ischemic (n=5) cardiomyopathy. A close match was observed between estimated and observed strain signals. Results showed that strain morphologies are related to both electrical conduction delay, and heterogeneity of contractile levels within the myocardium. The model-based approach brings additional information on the regional electrical and mechanical function of the LV from the analysis of echocardiography data. Our results can help to disclose the intrinsic complexity of LV mechanics in cardiac resynchronization therapy (CRT) candidates, and represent a step forwards the development of personalized LV modeling in the field of CRT.

The approach adopted in this work, combining multi-resolution physiological modeling, sensitivity analysis and parameter identification appears as particularly promising. In both clinical applications, the model-approach was used to combine physiological knowledge with clinical data, in order to improve the interpretation of echocardiography strain curves. The explainable methods, proposed in this thesis, illustrates how computational models could help to i) access physiological variables to provide clinical indices and ii) maximize the clinical interpretability of markers extracted from data. In fact, these methods are associated with high level of explicability, since most of the parameters provide a direct physiological meaning. For instance, the electro-mechanical parameters, deduced from strain analysis, bring personalized interpretation and additional information compared to classical indices. Moreover, *in silico* assessment of clinical parameters, specifically to each patient, allows for the evaluation of novel clinical indices, while taking into account characteristics associated with the subject and pathology. The proposed approach constitutes a step towards explicit knowledge integration methods for the evaluation of cardiac function, in order to maximize the clinical interpretability of indices extracted from echocardiography data.

Future works will be mainly dedicated to the evaluation of proposed methods to larger clinical databases. Although results presented in this thesis are promising, it is not possible to evaluate the statistical significance because of the low number of patients. Previous works of our team have shown that multi-parametric approaches, using machine-learning algorithms, could improve the prediction of response to CRT [1, 2] and patient outcome [3]. In future works, feature extraction could benefit from the evaluation of electro-mechanical indices extracted from models proposed in this thesis, as illustrated in results obtained from LBBB patients. Moreover, the model-based approach could be used to improve the interpretation of machine-learning results. In fact, feature selections presented in [1] show the importance of some indices associated with septal and lateral wall segments. Similarly, in our model-based approaches, the contractile properties of these segments appeared to be especially influent on strain morphologies. Further works are then required to evaluate septal and lateral electro-mechanical indices, deduced from data analysis and/or modelling methods, as predictors of response to CRT and to improve the interpretation of associated physiological and pathological mechanisms.

Bibliography

[1] A. Gallard, A. Hubert, O. Smiseth, J.-U. Voigt, V. Le Rolle, C. Leclercq, A. Bidaut, E. Galli, E. Donal, and A. I. Hernandez, "Prediction of response to cardiac resynchronization therapy using a multi-feature learning method," *The International Journal of Cardiovascular Imaging*, vol. 37, pp. 989–998, Mar. 2021.

[2] E. Donal, A. Hubert, V. Le Rolle, C. Leclercq, R. Martins, P. Mabo, E. Galli, and A. Hernandez, "New Multiparametric Analysis of Cardiac Dyssynchrony: Machine Learning and Prediction of Response to CRT," *JACC. Cardiovascular imaging*, vol. 12, pp. 1887–1888, Sept. 2019.

[3] E. Galli, V. Le Rolle, O. A. Smiseth, J. Duchenne, J. M. Aalen, C. K. Larsen, E. A. Sade, A. Hubert, S. Anilkumar, M. Penicka, C. Linde, C. Leclercq, A. Hernandez, J.-U. Voigt, and E. Donal, "Importance of Systematic Right Ventricular Assessment in Cardiac Resynchronization Therapy Candidates: A Machine Learning Approach," *Journal of the American Society of Echocardiography*, vol. 34, pp. 494–502, May 2021.

A

LIST OF PUBLICATIONS

A.1 Journal articles

1. **Owashi K.P**, Hubert A, Galli E, Donal E, Hernández A.I, Le Rolle V. Model-based estimation of left ventricular pressure and myocardial work in aortic stenosis. PLoS ONE 15(3): e0229609, 2020. https://doi.org/10.1371/journal.pone.0229609

A.2 International conferences

1. **Owashi K.P**, Hubert A, Galli E, Donal E, Hernández A.I, Le Rolle V. Parameter Identification of a Cardiovascular Model for the Estimation of Ventricular Pressure on Aortic Stenosis. Computing in Cardiology 2019 (CINC 2019). Singapore, September 8-11th, 2019.
2. **Owashi K.P**, Hubert A, Galli E, Donal E, Hernández A.I, Le Rolle V. Estimation of Myocardial Work in Aortic Stenosis through a Modeling Approach. Virtual Physiological Human Conference (VPH 2020). Paris (online), August 24-28th, 2020.
3. **Owashi K.P**, Hubert A, Galli E, Donal E, Hernández A.I, Le Rolle V. Model-based Analysis of myocardial strains in Left Bundle Branch Block Patients. European Society of Cardiology Congress (ESC 2020). Amsterdam (online), August 29th – September 1st, 2020.
4. **Owashi K.P**, Hubert A, Galli E, Donal E, Hernández A.I, Le Rolle V. Non-invasive estimation of myocardial work in aortic stenosis from modelling approach. European Society of Cardiology Congress (ESC 2020). Amsterdam (online), August 29th – September 1st, 2020. **Winner of the best poster award**.
5. **Owashi K.P**, Galli E, Hubert A, Donal E, Hernández A.I, Le Rolle V. Patients-specific analysis of myocardial strains in left bundle branch block based on computational models. Computing in Cardiology 2020 (CINC 2020). Rimini (online), September 13-16th, 2020.

A.3 National conferences

1. **Owashi K.P**, Hubert A, Galli E, Donal E, Hernández A.I, Le Rolle V. Estimation à base de modèle du travail cardiaque dans la sténose aortique. 11ème réunion

annuelle de l'ITS (Institut Thématique Multi-Organismes Technologies pour la Santé). Rennes, October 2nd-3rd, 2019. **Winner of the best poster award**.

A.4 Submitted

1. **Owashi K.P**, Galli E, Hubert A, Donal E, Hernández A.I, Le Rolle V. Model-based analysis of myocardial strains in left bundle branch block. Submitted to Artificial Intelligence In Medicine.

B

Equations

B.1 Aortic stenosis model

B.1.1 Elastance-based cardiac chambers

B.1.1.0.1 Atria:

$$P_a(V_a, t) = E_a(t) \cdot (V_a(t) - V_{d,a}) \tag{B.1}$$

$$E_a(t) = E_{a,max} \left(e_a(t) + \frac{E_{a,min}}{E_{a,max}} \right) \tag{B.2}$$

$$e_a(t) = \exp \left(-B_a \cdot (t - C_a)^2 \right) \tag{B.3}$$

B.1.1.0.2 Ventricles:

$$P_{es,v}(V, t) = E_{es,v}(V(t) - V_{d,v}) \tag{B.4}$$

$$P_{ed,v}(V, t) = P_{0,v} \left(e^{\lambda_v (V(t) - V_{0,v})} - 1 \right) \tag{B.5}$$

$$P_{lv}(V, t) = e_v(t) P_{es,v}(V, t) + (1 - e_v(t)) P_{ed,v}(V, t) \tag{B.6}$$

$$e_v(t) = k \cdot \left[\frac{\left(\frac{t}{\alpha_1 T} \right)^{n_1}}{1 + \left(\frac{t}{\alpha_1 T} \right)^{n_1}} \right] \cdot \left[\frac{1}{1 + \left(\frac{t}{\alpha_2 T} \right)^{n_2}} \right] \tag{B.7}$$

B.1.2 Systemic and pulmonary circulations

$$P_{ao}(V, t) = E_{ao}(V_{ao}(t) - V_{d,ao}) + P_{th} \tag{B.8}$$

$$P_{sa}(V, t) = E_{sa}(V_{sa}(t) - V_{d,sa}) \tag{B.9}$$

$$P_{sv}(V,t) = E_{sv}(V_{sv}(t) - V_{d,sv}) \tag{B.10}$$

$$P_{vc}(V,t) = E_{vc}(V_{vc}(t) - V_{d,vc}) + P_{th} \tag{B.11}$$

$$P_{pa}(V,t) = E_{pa}(V_{pa}(t) - V_{d,pa}) + P_{th} \tag{B.12}$$

$$P_{pv}(V,t) = E_{pv}(V_{pv}(t) - V_{d,pv}) + P_{th} \tag{B.13}$$

$$Q = \frac{\Delta P}{R} \tag{B.14}$$

$$\Delta V(t) = \int (Q_{in} - Q_{out}) \, \mathrm{d}t \tag{B.15}$$

B.1.3 Cardiac valves

$$\Delta P = BQ|Q| + L\frac{dQ}{dt}, \tag{B.16}$$

$$B = \frac{\rho}{2A_{eff}^2} \tag{B.17}$$

$$L = \frac{\rho l_{eff}}{A_{eff}} \tag{B.18}$$

$$A_{eff}(t) = [A_{eff,max}(t) - A_{eff,min}(t)]\,\xi(t) + A_{eff,min}(t) \tag{B.19}$$

$$\frac{d\xi}{dt} = \begin{cases} (1-\xi)K_{vo}\Delta P, & if \Delta P > 0 \\ \xi K_{vc}\Delta P, & if \Delta P \leq 0 \end{cases} \tag{B.20}$$

B.1.4 Myocardial work

$$W_{p,k}^S = \sum_i P_{i,k}^S, \; W_{n,k}^S = \sum_j N_{j,k}^S, \tag{B.21}$$

$$W^{IVR}_{p,k} = \sum_i P^{IVR}_{i,k},\ W^{IVR}_{n,k} = \sum_j N^{IVR}_{j,k} \tag{B.22}$$

$$GCW = \frac{1}{k}\sum_{k=1}^{K}(W^{S}_{p,k} + W^{IVR}_{n,k}) \tag{B.23}$$

$$GWW = \frac{1}{k}\sum_{k=1}^{K}(W^{S}_{n,k} + W^{IVR}_{p,k}) \tag{B.24}$$

$$GWE = \frac{GCW}{GCW + GWW} \tag{B.25}$$

B.2 Left bundle branch block model

B.2.1 Atria

$$P_a(V_a, t_a) = E_a(V_a(t_a) - V_{a,d}) \tag{B.26}$$

$$E_a(t_a) = e_a(t)\,(E_{a,max} - E_{a,min}) + E_{a,min} \tag{B.27}$$

$$e_a(t) = A_a \cdot \exp\left(-B_a \cdot (t_a - C_a)^2\right) \tag{B.28}$$

B.2.2 Multi-segment ventricles

$$T_s = T_{s,pass} + T_{s,act}. \tag{B.29}$$

$$T_{s,pass} = K_{pass} \cdot (36 \cdot max(0, \varepsilon_s - 0.1)^2 + 0.1(\varepsilon_s - 0.1) + 0.0025e^{10\varepsilon_s}) \tag{B.30}$$

$$T_{s,act} = K_{act} \cdot T_{ref} \cdot (1 + \beta(\varepsilon_s - 1)) \cdot \frac{{f_{a,s}}^2}{f_{a,s}^2 + C_a^2} \tag{B.31}$$

$$\varepsilon_s = \frac{l_s}{l_{s,ref}} \tag{B.32}$$

$$f_{a,s}(t_s) = \left[\frac{\left(\frac{t_s}{\alpha_1 T}\right)^{n_1}}{1 + \left(\frac{t_s}{\alpha_1 T}\right)^{n_1}} \right] \cdot \left[\frac{1}{1 + \left(\frac{t_s}{\alpha_2 T}\right)^{n_2}} \right] \cdot A_{max} \tag{B.33}$$

$$P_s = e \cdot T_s \left(\frac{\cos(\Theta)}{\varepsilon_s \cdot R_m} + \frac{\sin(\Theta)}{\varepsilon_s \cdot R_p} \right) \tag{B.34}$$

$$P_s \cdot Q_s = F_s \cdot {}^{dl_s}/_{dt} \tag{B.35}$$

$$F_s = T_s \cdot S_s \tag{B.36}$$

$$P_v - P_s = I_s \frac{dQ_s}{dt} \tag{B.37}$$

$$Q_s = \frac{P_v - P_s}{R_s} \tag{B.38}$$

$$Q_v(t) = Q_{c,v}(t) + \sum_{s_v} Q_{s,v}(t) \tag{B.39}$$

$$P_{sept} = P_{lv} - P_{rv} \tag{B.40}$$

B.2.3 Systemic and pulmonary circulations

$$P(V,t) = E(V(t) - V_d) \tag{B.41}$$

$$\Delta V(t) = \int (Q_{in} - Q_{out})\,\mathrm{d}t \tag{B.42}$$

$$Q = \frac{\Delta P}{R} \tag{B.43}$$

C

List of parameters

C.1 Aortic stenosis model

Symbol	Description	Value	Units
	Time-varying elastances		
$E_{la,max}$	Maximum systolic elastance of left atrium	1.6	$mmHg/ml$
$E_{la,min}$	Diastolic elastance of the left atrium	0.1	$mmHg/ml$
$E_{ra,max}$	Maximum systolic elastance of right atrium	1.6	$mmHg/ml$
$E_{ra,min}$	Diastolic elastance of the right atrium	0.1	$mmHg/ml$
$V_{0,lv}$	Left ventricle volume at zero pressure	10	ml
$V_{0,rv}$	Right ventricle volume at zero pressure	10	ml
λ_{rv}	Curvature	0.013	$1/ml$
$P_{0,rv}$	Gradient	1.2001	$mmHg$
C_{la}	Constant controlling the rise and peak of the atrial systole	0.32	s
B_{la}	Constant controlling the rise and peak of the atrial systole	84.375	$1/s^2$
	Elastances, volumes, resistances and pressures		
E_{rv}	Elastance of the right ventricle	0.6526	$mmHg/ml$
E_{pa}	Elastance of the pulmonary artery	0.3375	$mmHg/ml$
E_{pv}	Elastance of the pulmonary vein	0.0062	$mmHg/ml$
$V_{d,lv}$	Unstressed volume of the left ventricle	10	ml
$V_{d,rv}$	Unstressed volume of the right ventricle	10	ml
$V_{d,la}$	Unstressed volume of the left atrium	3	ml
$V_{d,ra}$	Unstressed volume of the right atrium	3	ml

$V_{d,pa}$	Unstressed volume of the pulmonary artery	160	ml
$V_{d,pv}$	Unstressed volume of the pulmonary vein	200	ml
R_{pul}	Pulmonary resistance	0.1425	$^{mmHgs}/_{ml}$
R_{la}	Left atrium resistance	0.01	$^{mmHgs}/_{ml}$
R_{ra}	Right atrium resistance	0.01	$^{mmHgs}/_{ml}$
P_{th}	Intrathoracic pressure	-4	$mmHg$
Cardiac valves			
ρ	Blood density	1.06	$^{g}/_{cm3}$
$K_{vc,ao}$	Rate coefficient for aortic valve closure	0.15	$^{1}/_{Pa\cdot s}$
$K_{vo,ao}$	Rate coefficient for aortic valve opening	0.12	$^{1}/_{Pa\cdot s}$
$l_{eff,ao}$	Effective length for aortic valve	2.2	cm
$K_{vc,tc}$	Rate coefficient for tricuspid valve closure	0.4	$^{1}/_{Pa\cdot s}$
$K_{vo,tc}$	Rate coefficient for tricuspid valve opening	0.3	$^{1}/_{Pa\cdot s}$
$l_{eff,tc}$	Effective length for tricuspid valve	2	cm
$K_{vc,mt}$	Rate coefficient for mitral valve closure	0.4	$^{1}/_{Pa\cdot s}$
$K_{vo,mt}$	Rate coefficient for mitral valve opening	0.3	$^{1}/_{Pa\cdot s}$
$l_{eff,mt}$	Effective length for mitral valve	1.25	cm
$K_{vc,pu}$	Rate coefficient for pulmonary valve closure	0.2	$^{1}/_{Pa\cdot s}$
$K_{vo,pu}$	Rate coefficient for pulmonary valve opening	0.2	$^{1}/_{Pa\cdot s}$
$l_{eff,pu}$	Effective length for pulmonary valve	0.9	cm
$A_{eff,mt}$	Effective cross-sectional area of mitral valve	5	cm^2
$A_{eff,tc}$	Effective cross-sectional area of tricuspid valve	6	cm^2
$A_{eff,pu}$	Effective cross-sectional area of pulmonary valve	2.8	cm^2
Database 1			

$A_{eff,ao}$	Effective cross-sectional area of aortic valve. **Patient 1**	0.75	cm^2
$A_{eff,ao}$	Effective cross-sectional area of aortic valve. **Patient 2**	0.9	cm^2
$A_{eff,ao}$	Effective cross-sectional area of aortic valve. **Patient 3**	0.9	cm^2
$A_{eff,ao}$	Effective cross-sectional area of aortic valve. **Patient 4**	1.3	cm^2
$A_{eff,ao}$	Effective cross-sectional area of aortic valve. **Patient 5**	0.61	cm^2
$A_{eff,ao}$	Effective cross-sectional area of aortic valve. **Patient 6**	0.75	cm^2
$A_{eff,ao}$	Effective cross-sectional area of aortic valve. **Patient 7**	0.9	cm^2
$A_{eff,ao}$	Effective cross-sectional area of aortic valve. **Patient 8**	0.8	cm^2
$A_{eff,ao}$	Effective cross-sectional area of aortic valve. **Patient 9**	0.6	cm^2
$A_{eff,ao}$	Effective cross-sectional area of aortic valve. **Patient 10**	0.5	cm^2
$A_{eff,ao}$	Effective cross-sectional area of aortic valve. **Patient 11**	0.88	cm^2
$A_{eff,ao}$	Effective cross-sectional area of aortic valve. **Patient 12**	0.86	cm^2
	Database 2		
$A_{eff,ao}$	Effective cross-sectional area of aortic valve. **Patient 1**	0.7	cm^2
$A_{eff,ao}$	Effective cross-sectional area of aortic valve. **Patient 2**	0.59	cm^2
$A_{eff,ao}$	Effective cross-sectional area of aortic valve. **Patient 3**	0.38	cm^2
$A_{eff,ao}$	Effective cross-sectional area of aortic valve. **Patient 4**	0.82	cm^2
$A_{eff,ao}$	Effective cross-sectional area of aortic valve. **Patient 5**	0.7	cm^2
$A_{eff,ao}$	Effective cross-sectional area of aortic valve. **Patient 6**	1.1	cm^2
$A_{eff,ao}$	Effective cross-sectional area of aortic valve. **Patient 7**	0.96	cm^2

$A_{eff,ao}$	Effective cross-sectional area of aortic valve. **Patient 8**	0.72	cm^2
$A_{eff,ao}$	Effective cross-sectional area of aortic valve. **Patient 9**	0.85	cm^2
$A_{eff,ao}$	Effective cross-sectional area of aortic valve. **Patient 10**	0.67	cm^2
$A_{eff,ao}$	Effective cross-sectional area of aortic valve. **Patient 11**	0.54	cm^2
$A_{eff,ao}$	Effective cross-sectional area of aortic valve. **Patient 12**	0.7	cm^2
$A_{eff,ao}$	Effective cross-sectional area of aortic valve. **Patient 13**	0.55	cm^2
$A_{eff,ao}$	Effective cross-sectional area of aortic valve. **Patient 14**	0.71	cm^2
$A_{eff,ao}$	Effective cross-sectional area of aortic valve. **Patient 15**	0.62	cm^2
$A_{eff,ao}$	Effective cross-sectional area of aortic valve. **Patient 16**	0.75	cm^2
$A_{eff,ao}$	Effective cross-sectional area of aortic valve. **Patient 17**	0.6	cm^2
$A_{eff,ao}$	Effective cross-sectional area of aortic valve. **Patient 18**	0.82	cm^2
$A_{eff,ao}$	Effective cross-sectional area of aortic valve. **Patient 19**	0.62	cm^2
$A_{eff,ao}$	Effective cross-sectional area of aortic valve. **Patient 20**	0.95	cm^2
$A_{eff,ao}$	Effective cross-sectional area of aortic valve. **Patient 21**	0.85	cm^2
$A_{eff,ao}$	Effective cross-sectional area of aortic valve. **Patient 22**	0.97	cm^2
$A_{eff,ao}$	Effective cross-sectional area of aortic valve. **Patient 23**	0.74	cm^2

C.1.1 Identified parameters *database 1*

Arterial parameters				
Parameter	**Patient 1**	**Patient 2**	**Patient 3**	**Patient 4**
$R_{sys}({}^{mmHg\cdot s}/_{ml})$	0.76 ± 0.07	0.83 ± 0.07	0.87 ± 0.05	0.83 ± 0.07

$E_{ao}(^{mmHg}/_{ml})$	3.66 ± 0.6	3.5 ± 0.75	2.64 ± 0.63	3.15 ± 0.58
$E_{sa}(^{mmHg}/_{ml})$	0.88 ± 0.23	0.81 ± 0.19	0.84 ± 0.23	0.82 ± 0.22
$E_{vc}(^{mmHg}/_{ml})$	0.017 ± 0.004	0.016 ± 0.004	0.02 ± 0.004	0.02 ± 0.004
$E_{sv}(^{mmHg}/_{ml})$	0.012 ± 0.0015	0.012 ± 0.002	0.01 ± 0.002	0.01 ± 0.002
$V_{d,ao}(ml)$	211.6 ± 39	219.9 ± 40.98	216.7 ± 48.4	221.2 ± 47.3
$V_{d,sa}(ml)$	549.6 ± 133.9	509.1 ± 137.5	565.01 ± 130.8	550.6 ± 134.9
$V_{d,vc}(ml)$	2131.7 ± 367	2317.9 ± 380	2298.3 ± 371.3	2224.5 ± 394
$V_{d,sv}(ml)$	1893.6 ± 321	2025.7 ± 292	1844.5 ± 334	1791.5 ± 339
$R_{ao}(^{mmHg\cdot s}/_{ml})$	0.34 ± 0.05	0.33 ± 0.06	0.32 ± 0.07	0.29 ± 0.06
$R_{vc}(^{mmHg\cdot s}/_{ml})$	0.17 ± 0.04	0.16 ± 0.04	0.15 ± 0.04	0.18 ± 0.05

Parameter	**Patient 5**	**Patient 6**	**Patient 7**	**Patient 8**
$R_{sys}(^{mmHg\cdot s}/_{ml})$	0.8 ± 0.08	0.85 ± 0.07	0.87 ± 0.05	0.66 ± 0.07
$E_{ao}(^{mmHg}/_{ml})$	2.86 ± 0.82	2.67 ± 0.76	2.79 ± 0.62	3.77 ± 0.48
$E_{sa}(^{mmHg}/_{ml})$	0.79 ± 0.25	0.85 ± 0.27	0.82 ±0.23	0.91 ± 0.22
$E_{vc}(^{mmHg}/_{ml})$	0.015 ± 0.003	0.016 ± 0.004	0.016 ± 0.004	0.015 ± 0.003
$E_{sv}(^{mmHg}/_{ml})$	0.01 ± 0.002	0.011 ± 0.002	0.012 ± 0.002	0.011 ± 0.0016
$V_{d,ao}(ml)$	202.7 ± 47.9	217.9 ± 43.9	209.4 ± 55.01	201.3 ± 51.3
$V_{d,sa}(ml)$	526.7 ± 119.1	544.4 ± 137.1	518.5 ± 143.3	519.5 ± 109.2
$V_{d,vc}(ml)$	1995.6 ± 452	2267.8 ± 440	2422.3 ± 351	2124.1 ± 317
$V_{d,sv}(ml)$	1765.1 ± 361	1811.6 ± 374	1963.2 ±283	1789.3 ± 360
$R_{ao}(^{mmHg\cdot s}/_{ml})$	0.29 ± 0.06	0.32 ± 0.07	0.31 ± 0.06	0.33 ± 0.035
$R_{vc}(^{mmHg\cdot s}/_{ml})$	0.19 ± 0.04	0.17 ± 0.05	0.17 ± 0.04	0.17 ± 0.042

Parameter	**Patient 9**	**Patient 10**	**Patient 11**	**Patient 12**
$R_{sys}(^{mmHg\cdot s}/_{ml})$	0.71 ± 0.09	0.78 ± 0.07	0.86 ± 0.07	0.87 ± 0.06
$E_{ao}(^{mmHg}/_{ml})$	3.22 ± 0.67	3.13 ± 0.59	1.94 ± 0.44	2.16 ± 0.71
$E_{sa}(^{mmHg}/_{ml})$	0.88 ± 0.18	0.86 ± 0.20	0.74 ± 0.21	0.80 ± 0.24
$E_{vc}(^{mmHg}/_{ml})$	0.015 ± 0.003	0.02 ± 0.004	0.016 ± 0.004	0.016 ± 0.004
$E_{sv}(^{mmHg}/_{ml})$	0.01 ± 0.003	0.01 ± 0.002	0.012 ± 0.002	0.011 ± 0.002
$V_{d,ao}(ml)$	202.8 ± 44	211.8 ± 46.5	213.4 ± 50.1	185.3 ± 56.03
$V_{d,sa}(ml)$	543.1 ± 117.4	533.9 ± 120.9	529.9 ± 155.1	584.4 ± 129.1
$V_{d,vc}(ml)$	2001.8 ± 390	2156.8 ± 357	2259.6 ± 425	2327.7 ± 421
$V_{d,sv}(ml)$	1533.2 ± 382	1789.6 ± 364	1828.4 ± 333	1904.7 ± 314
$R_{ao}(^{mmHg\cdot s}/_{ml})$	0.29 ± 0.06	0.30 ± 0.05	0.23 ± 0.07	0.26 ± 0.08
$R_{vc}(^{mmHg\cdot s}/_{ml})$	0.19 ± 0.04	0.18 ± 0.05	0.19 ± 0.05	0.17 ± 0.04

Ventricular parameters

Parameter	**Patient 1**	**Patient 2**	**Patient 3**	**Patient 4**	**Patient 5**	**Patient 6**
$E_{lv}(^{mmHg}/_{ml})$	3.4738	2.7828	3.0753	1.8953	3.2923	2.5773
$\lambda_{lv}(^{1}/_{ml})$	0.0149	0.0146	0.0189	0.0105	0.0137	0.0127
$P_{0,lv}(mmHg)$	1.4422	1.3184	0.9674	1.0494	1.5145	0.9559
α_1	0.3077	0.3517	0.3523	0.5141	0.3283	0.3238
α_2	0.4107	0.42	0.3139	0.3257	0.37	0.3646
n_1	1.2798	1.2381	1.3637	1.3934	1.1412	1.2695
n_2	24.2611	21.6158	24.9414	15.6806	13.8802	16.7110
Parameter	**Patient 7**	**Patient 8**	**Patient 9**	**Patient 10**	**Patient 11**	**Patient 12**
$E_{lv}(^{mmHg}/_{ml})$	3.0198	3.2276	3.3745	2.4147	3.1468	3.6446
$\lambda_{lv}(^{1}/_{ml})$	0.0172	0.0133	0.0093	0.0188	0.0152	0.0154
$P_{0,lv}(mmHg)$	1.4185	1.7418	1.13	1.9088	0.7194	1.5269
α_1	0.2420	0.4712	0.5210	0.3781	0.3388	0.3359
α_2	0.3409	0.4416	0.3898	0.4268	0.3919	0.4237
n_1	1.5742	1.5367	1.1278	1.3258	1.8088	1.1276
n_2	19.2338	12.0314	20.9134	12.7301	16.6476	24.4148

C.1.2 Identified parameters *database 2*

Arterial parameters

Parameter	**Patient 1**	**Patient 2**	**Patient 3**	**Patient 4**	**Patient 5**	**Patient 6**
$R_{sys}(^{mmHg\cdot s}/_{ml})$	0.77	0.856	0.819	0.729	0.684	0.821
$E_{ao}(^{mmHg}/_{ml})$	4.55	1.759	1.86	3.183	2.326	4.6003
$E_{sa}(^{mmHg}/_{ml})$	1.22	0.766	0.587	0.864	0.618	0.5812
$E_{vc}(^{mmHg}/_{ml})$	0.0123	0.0152	0.0215	0.0096	0.013	0.01127
$E_{sv}(^{mmHg}/_{ml})$	0.0136	0.0123	0.011	0.012	0.0122	0.0137
$V_{d,ao}(ml)$	131.98	98.281	227.016	256.65	233.924	98.347
$V_{d,sa}(ml)$	556.82	632.332	325.622	512.715	731.248	697.479
$V_{d,vc}(ml)$	2757.92	2502.529	2241.399	2206.903	2235.897	1301.53
$V_{d,sv}(ml)$	2463.56	2020.738	1685.879	1818.504	1849.083	2109.2007
$R_{ao}(^{mmHg\cdot s}/_{ml})$	0.364	0.164	0.173	0.321	0.2797	0.2483
$R_{vc}(^{mmHg\cdot s}/_{ml})$	0.229	0.226	0.223	0.116	0.17095	0.1969
Parameter	**Patient 7**	**Patient 8**	**Patient 9**	**Patient 10**	**Patient 11**	**Patient 12**
$R_{sys}(^{mmHg\cdot s}/_{ml})$	0.889	0.8797	0.7433	0.731	0.872	0.804
$E_{ao}(^{mmHg}/_{ml})$	1.647	3.3618	4.0036	4.072	4.2048	3.4467

$E_{sa}(mmHg/ml)$	0.862	0.7167	1.1308	0.942	0.6236	0.95
$E_{vc}(mmHg/ml)$	0.0085	0.01587	0.0142	0.0181	0.023	0.0155
$E_{sv}(mmHg/ml)$	0.0105	0.0122	0.0122	0.0113	0.0098	0.008
$V_{d,ao}(ml)$	219.896	234.981	222.039	178.43	125.56	149.389
$V_{d,sa}(ml)$	450.057	458.58	654.27	526.17	585.67	426.57
$V_{d,vc}(ml)$	1022.145	2513.01	2106.36	1622.78	1379.65	2667.15
$V_{d,sv}(ml)$	940.671	2204.41	1274.66	2204.087	2219.57	1089.37
$R_{ao}(mmHg \cdot s/ml)$	0.262	0.3491	0.2029	0.3196	0.314	0.186
$R_{vc}(mmHg \cdot s/ml)$	0.1607	0.1872	0.124	0.2043	0.251	0.187

Parameter	**Patient 13**	**Patient 14**	**Patient 15**	**Patient 16**	**Patient 17**	**Patient 18**
$R_{sys}(mmHg \cdot s/ml)$	0.761	0.361	0.637	0.668	0.899	0.8288
$E_{ao}(mmHg/ml)$	2.0498	2.702	2.355	2.0001	2.503	3.0564
$E_{sa}(mmHg/ml)$	0.667	0.9512	1.012	1.233	1.1327	0.5626
$E_{vc}(mmHg/ml)$	0.0224	0.0107	0.0203	0.0189	0.0194	0.0196
$E_{sv}(mmHg/ml)$	0.0086	0.0117	0.0112	0.0106	0.0109	0.01088
$V_{d,ao}(ml)$	194.45	252.66	200.45	285.03	149.85	240.51
$V_{d,sa}(ml)$	485.55	560.082	511.17	542.67	549.57	698.57
$V_{d,vc}(ml)$	1483.12	1701.88	1465.51	2679.97	2453.73	2685.15
$V_{d,sv}(ml)$	945.999	1594.045	1678.46	1777.57	2149.19	1086.66
$R_{ao}(mmHg \cdot s/ml)$	0.222	0.382	0.345	0.371	0.3818	0.3107
$R_{vc}(mmHg \cdot s/ml)$	0.284	0.213	0.196	0.2699	0.2656	0.1828

Parameter	**Patient 19**	**Patient 20**	**Patient 21**	**Patient 22**	**Patient 23**	
$R_{sys}(mmHg \cdot s/ml)$	0.5794	0.634	0.9087	0.6834	0.9139	
$E_{ao}(mmHg/ml)$	1.9779	1.6453	2.1078	2.1293	2.8641	
$E_{sa}(mmHg/ml)$	0.8467	0.6946	0.8451	0.7711	1.02717	
$E_{vc}(mmHg/ml)$	0.0120	0.0156	0.01087	0.0138	0.0164	
$E_{sv}(mmHg/ml)$	0.0102	0.008	0.0072	0.0083	0.014	
$V_{d,ao}(ml)$	249.88	222.603	262.996	230.23	222.45	
$V_{d,sa}(ml)$	703.28	516.82	579.02	663.47	640.5	
$V_{d,vc}(ml)$	1866.68	2411.58	1114.16	1783.33	2177.3	
$V_{d,sv}(ml)$	1858.14	1536.96	1320.40	1801.49	2219.7	
$R_{ao}(mmHg \cdot s/ml)$	0.254	0.2535	0.1458	0.2354	0.3919	
$R_{vc}(mmHg \cdot s/ml)$	0.1692	0.1973	0.1154	0.1953	0.1934	

C.2 Left bundle branch block model

Symbol	**Description**	**Value**	**Units**
	Time-varying elastances		
$E_{la,max}$	Maximum systolic elastance of left atrium	0.5	$^{mmHg}/_{ml}$
$E_{la,min}$	Diastolic elastance of the left atrium	0.01	$^{mmHg}/_{ml}$
$E_{ra,max}$	Maximum systolic elastance of right atrium	0.5	$^{mmHg}/_{ml}$
$E_{ra,min}$	Diastolic elastance of the right atrium	0.01	$^{mmHg}/_{ml}$
A_a	Constant controlling the rise and peak of the atrial systole	1	-
B_a	Constant controlling the rise and peak of the atrial systole	120	$^1/_{s^2}$
C_a	Constant controlling the rise and peak of the atrial systole	0.2	s
	Elastances, volumes, resistances and pressures		
E_{lv}	Elastance of the left ventricle	3.4053	$^{mmHg}/_{ml}$
E_{rv}	Elastance of the right ventricle	0.6526	$^{mmHg}/_{ml}$
E_{pa}	Elastance of the pulmonary artery	0.3375	$^{mmHg}/_{ml}$
E_{pv}	Elastance of the pulmonary vein	0.0062	$^{mmHg}/_{ml}$
E_{ao}	Elastance of the aorta	3.2906	$^{mmHg}/_{ml}$
E_{sa}	Elastance of the systemic arteries	0.7881	$^{mmHg}/_{ml}$
E_{vc}	Elastance of the vena cava	0.0154	$^{mmHg}/_{ml}$
E_{sv}	Elastance of the systemic veins	0.010	$^{mmHg}/_{ml}$
$V_{d,lv}$	Unstressed volume of the left ventricle	5	ml
$V_{d,rv}$	Unstressed volume of the right ventricle	5	ml
$V_{d,la}$	Unstressed volume of the left atrium	3	ml
$V_{d,ra}$	Unstressed volume of the right atrium	3	ml
$V_{d,pa}$	Unstressed volume of the pulmonary artery	160	ml
$V_{d,pv}$	Unstressed volume of the pulmonary vein	200	ml
$V_{d,ao}$	Unstressed volume of the aorta	196.5625	ml
$V_{d,sa}$	Unstressed volume of the systemic arteries	520.6199	ml

$V_{d,vc}$	Unstressed volume of the vena cava	1907.7	ml
$V_{d,sv}$	Unstressed volume of the systemic veins	1648	ml
R_{pul}	Pulmonary resistance	0.1425	$^{mmHgs}/_{ml}$
R_{sys}	Systemic resistance	1.0501	$^{mmHgs}/_{ml}$
R_{la}	Left atrium resistance	0.2	$^{mmHgs}/_{ml}$
R_{ra}	Right atrium resistance	0.8	$^{mmHgs}/_{ml}$
R_{mt}	Mitral valve resistance	0.01	$^{mmHgs}/_{ml}$
R_{ao}	Aortic valve resistance	0.0105	$^{mmHgs}/_{ml}$
R_{tc}	Tricuspid valve resistance	0.01	$^{mmHgs}/_{ml}$
R_{pu}	Pulmonary valve resistance	0.0105	$^{mmHgs}/_{ml}$
R_{art}	Arteries resistance	0.2915	$^{mmHgs}/_{ml}$
R_{veins}	Veins resistance	0.1935	$^{mmHgs}/_{ml}$
P_{th}	Intrathoracic pressure	-4	$mmHg$
Multi-segment ventricles			
β	Constant related with the muscle kinetic	10	$-$
C_a	Constant related with the muscle kinetic	5.33	$-$
T_{ref}	Reference tension	375.0319	$mmHg$
$l_{s,ref}$	Reference fiber lengths	0.95	cm
e	Thickness	0.7	cm
Θ	Mean angle of the muscular fibers	$^{\pi}/_{12}$	rad
R_m	Radii of curvature in the meridian direction	2.1548	cm
R_p	Radii of curvature in the parallel direction	4.5985	cm
S_s	Segmental area	8.8909	cm^2
I_s	Segmental inertia	0.0003	$^{mmHgs}/_{ml}$
R_s	Segmental resistance	0.5	$^{mmHgs}/_{ml}$

C.2.1 Identified parameters for healthy subjects

Parameter	**Patient 1**	**Patient 2**	**Patient 3**	**Patient 4**	**Patient 5**
ApiAnt					
K_{act}	0.579	0.809	0.987	0.723	0.779
K_{pass}	0.08938	0.04078	0.11469	0.04970	0.04954

n_1	1.1180	1.0908	1.1969	1.0000	1.1992
n_2	9.0930	9.9900	13.9885	11.8930	9.4071
α_1	0.4217	0.4013	0.4420	0.4042	0.4500
α_2	0.4390	0.4007	0.4500	0.4206	0.4342
$UDP(ms)$	3.3474	2.4348	4.5367	3.7460	3.6180
			ApiInf		
K_{act}	0.723	0.909	0.585	1	0.756
K_{pass}	0.05336	0.03592	0.09464	0.06731	0.02710
n_1	1.1605	1.0349	1.1546	1.0142	1.1518
n_2	8.0772	14,7496	12.9741	10.8137	10.1274
α_1	0.4499	0.4285	0.4150	0.4245	0.4500
α_2	0.4331	0.4321	0.4423	0.4107	0.4479
$UDP(ms)$	2.7676	1.9024	1.4529	3.1424	1.7577
			ApiLat		
K_{act}	0.856	0.721	0.745	1	0.735
K_{pass}	0.05736	0.02854	0.10234	0.05256	0.07058
n_1	1.1041	1.0000	1.1958	1.0013	1.0552
n_2	9.6071	10.4468	8.7425	9.3507	9.7752
α_1	0.4498	0.4001	0.4499	0.4001	0.4212
α_2	0.4204	0.4000	0.4086	0.4093	0.4183
$UDP(ms)$	3.3655	2.5377	1.6209	3.2898	3.4105
			ApiSept		
K_{act}	0.965	0.862	0.696	1	0.988
K_{pass}	0.05396	0.06067	0.12000	0.03559	0.02468
n_1	1.1999	1.1132	1.2000	1.1211	1.1999
n_2	7.8909	12.8857	12.1747	10.3501	11.4697
α_1	0.4500	0.4000	0.4495	0.4003	0.4500
α_2	0.4265	0.4298	0.4500	0.4223	0.4500
$UDP(ms)$	2.8167	1.5761	1.7722	2.2515	2.2508
			MidAnt		
K_{act}	0.677	0.955	0.833	0.889	0.520
K_{pass}	0.11114	0.05938	0.11941	0.11408	0.01643
n_1	1.0085	1.0031	1.0007	1.0000	1.0000
n_2	9.6887	11.8618	1.0007	11.5388	9.1234
α_1	0.4274	0.4001	0.4001	0.4000	0.4001
α_2	0.4304	0.4124	0.4231	0.4167	0.4250

$UDP(ms)$	3.4711	2.7782	1.8786	4.2174	3.8796
MidAntSept					
K_{act} 0.612	0.817	0.733	0.871	0.940	
K_{pass}	0.06336	0.03426	0.08876	0.02168	0.05016
n_1	1.200	1.1297	1.2000	1.2000	1.1998
n_2	8.8350	11.3399	1.2000	10.6345	8.7238
α_1	0.4498	0.4000	0.4498	0.4497	0.4497
α_2	0.4499	0.4198	0.4374	0.4268	0.4390
$UDP(ms)$	3.3193	4.0754	3.9345	3.6365	3.6775
MidInfSept					
K_{act}	0.550	0.713	0.5	0.820	0.604
K_{pass}	0.07720	0.06859	0.05924	0.09303	0.01049
n_1	1.1692	1.0183	1.1994	1.1014	1.1816
n_2	7.6663	11.8558	1.1994	8.9339	9.8855
α_1	0.4500	0.4251	0.4441	0.4000	0.4491
α_2	0.4500	0.4337	0.4119	0.4248	0.4500
$UDP(ms)$	2.8335	2.7809	3.1684	3.5595	3.3030
MidInf					
K_{act}	0.894	1	0.783	1	0.701
K_{pass}	0.1200	0.07709	0.08559	0.03177	0.03637
n_1	1.1431	1.0005	1.1020	1.0001	1.0072
n_2	10.8518	11.7670	12.3839	10.3622	9.0011
α_1	0.4455	0.4265	0.4470	0.4097	0.4462
α_2	0.4423	0.4160	0.4329	0.4060	0.4278
$UDP(ms)$	3.7659	2.6696	4.7740	3.7573	2.7673
MidInfLat					
K_{act}	0.837	0.998	0.896	0.656	0.866
K_{pass}	0.07671	0.07711	0.11999	0.03184	0.08130
n_1	1.0000	1.0000	1.0539	1.0000	1.0014
n_2	10.1392	14.5488	10.8922	9.9634	11.6274
α_1	0.4232	0.4000	0.4323	0.4004	0.4334
α_2	0.4155	0.4079	0.4093	0.4001	0.4224
$UDP(ms)$	2.6946	3.5069	3.1546	2.5696	4.4477
MidAntLat					
K_{act}	0.683	1	0.911	1	0.849
K_{pass}	0.11972	0.06345	0.07892	0.11981	0.06437

n_1	1.0000	1.0078	1.0053	1.0000	1.0000
n_2	12.4377	11.2565	14.0672	10.9306	11.6215
α_1	0.4000	0.4001	0.4000	0.4001	0.4000
α_2	0.4177	0.4000	0.4201	0.4165	0.4270
$UDP(ms)$	4.3818	3.4532	4.3548	1.6781	4.9408
BasalAnt					
K_{act}	0.788	0.845	0.717	0.863	0.845
K_{pass}	0.1200	0.10882	0.10950	0.05913	0.12000
n_1	1.0013	1.0000	1.0015	1.0088	1.0000
n_2	11.2108	11.9549	10.4007	11.3881	8.0971
α_1	0.4001	0.4015	0.4252	0.4141	0.4141
α_2	0.4388	0.4078	0.4079	0.4067	0.4092
$UDP(ms)$	2.5780	2.1967	2.7356	2.3266	3.2604
BasalAntSept					
K_{act}	0.5	0.745	0.730	0.745	0.890
K_{pass}	0.1200	0.09621	0.11862	0.06457	0.08831
n_1	1.200	1.1345	1.2000	1.1583	1.2000
n_2	7.5109	9.9346	7.9300	9.3298	7.9831
α_1	0.4400	0.4000	0.4494	0.4025	0.4499
α_2	0.4489	0.4238	0.4223	0.4411	0.4344
$UDP(ms)$	2.3051	3.5609	2.1832	2.4667	2.7232
BasalInfSept					
K_{act}	0.502	0.709	0.619	0.564	0.560
K_{pass}	0.1200	0.09008	0.11873	0.10745	0.01949
n_1	1.200	1.0868	1.2000	1.1348	1.2000
n_2	7.5896	10.7703	7.7296	8.6588	7.5040
α_1	0.4438	0.4009	0.4500	0.4006	0.4500
α_2	0.4500	0.4282	0.4173	0.4294	0.4295
$UDP(ms)$	3.0275	3.1553	2.4849	3.4653	1.9404
BasalInf					
K_{act}	0.656	0.999	0.570	1	0.776
K_{pass}	0.11998	0.11919	0.04096	0.05003	0.07767
n_1	1.0005	1.0008	1.0042	1.0001	1.0000
n_2	7.6654	12.1790	8.7544	10.9536	10.0296
α_1	0.4092	0.4098	0.4000	0.4004	0.4000
α_2	0.4044	0.4000	0.4092	0.4289	0.4294

$UDP(ms)$	2.3691	2.8027	1.7552	2.7057	1.9338
BasalInfLat					
K_{act}	0.696	0.627	0.766	0.995	0.784
K_{pass}	0.11986	0.09086	0.07100	0.07819	0.07438
n_1	1.0000	1.0537	1.0495	1.0006	1.0009
n_2	13.3761	12.6828	10.2616	13.0749	9.6903
α_1	0.4000	0.4084	0.4132	0.4166	0.4284
α_2	0.4285	0.4026	0.4071	0.4000	0.4084
$UDP(ms)$	2.4729	3.1814	3.7543	4.0662	3.4830
BasalAntLat					
K_{act}	0.582	0.830	0.910	0.619	0.919
K_{pass}	0.11876	0.07727	0.07900	0.11997	0.07723
n_1	1.0000	1.0000	1.0000	1.0002	1.0000
n_2	10.3239	12.7176	10.3462	11.3290	11.0134
α_1	0.4000	0.4037	0.4010	0.4000	0.4000
α_2	0.4099	0.4000	0.4053	0.4061	0.4132
$UDP(ms)$	2.4654	3.2321	2.7506	3.1054	2.5898
$LBBUDP(ms)$	4.4518	2.2276	4.3329	2.5755	1.9389

Parameter	**Patient 6**	**Patient 7**	**Patient 8**	**Patient 9**	**Patient 10**
ApiAnt					
K_{act}	0.511	0.893	0.907	0.516	0.587
K_{pass}	0.02819	0.07370	0.05708	0.07850	0.07666
n_1	1.2000	1.0984	1.1309	1.1877	1.2000
n_2	7.5000	9.9463	12.2575	7.9492	10.1337
α_1	0.4451	0.4226	0.4455	0.4500	0.4497
α_2	0.4500	0.4006	0.4442	0.4310	0.4481
$UDP(ms)$	2.5533	2.0582	2.9576	4.3085	2.2065
ApiInf					
K_{act}	0.5	0.878	0.832	0.693	0.521
K_{pass}	0.01002	0.03317	0.06258	0.06511	0.04185
n_1	1.2000	1.1055	1.1996	1.1936	1.2000
n_2	7.5000	11.0996	10.6434	15.0000	10.4033
α_1	0.4490	0.4500	0.4500	0.4500	0.4500
α_2	0.4500	0.4132	0.4333	0.4500	0.4500
$UDP(ms)$	2.9950	3.0363	5.0000	1.5701	1.9387

ApiLat

K_{act}	0.596	0.675	0.980	0.971	0.798
K_{pass}	0.03760	0.10181	0.06857	0.5069	0.3422
n_1	1.1242	1.0001	1.0573	1.2000	1.0928
n_2	7.5000	12.0185	12.1703	9.5481	8.2054
α_1	0.4500	0.4002	0.4407	0.4500	0.4463
α_2	0.4304	0.4072	0.4455	0.4357	0.4001
$UDP(ms)$	3.7781	2.2283	1.3579	2.4872	2.8611

ApiSept

K_{act}	1	0.697	0.654	0.790	0.726
K_{pass}	0.01590	0.11549	0.01076	0.01462	0.01000
n_1	1.2000	1.2000	1.2000	1.2000	1.1996
n_2	7.5000	8.9988	8.7709	13.4272	9.9844
α_1	0.4500	0.4500	0.4494	0.4500	0.4409
α_2	0.4500	0.4064	0.4243	0.4448	0.4386
$UDP(ms)$	3.1384	3.3103	2.1572	2.8295	2.3607

MidAnt

K_{act}	0.710	0.731	0.935	0.861	0.701
K_{pass}	0.11913	0.05976	0.06219	0.04065	0.04388
n_1	1.1277	1.0000	1.0651	1.1144	1.0363
n_2	7.5000	9.9020	11.1838	12.6331	9.6016
α_1	0.4500	0.4216	0.4438	0.4069	0.4024
α_2	0.4438	0.4000	0.4295	0.4500	0.4347
$UDP(ms)$	1.5034	2.1768	3.7657	3.0716	1.7663

MidAntSept

K_{act}	1	0.620	0.752	0.632	0.690
K_{pass}	0.01000	0.03683	0.05002	0.03802	0.04312
n_1	1.2000	1.1686	1.2000	1.2000	1.2000
n_2	7.5000	10.7349	9.8572	8.6211	8.8146
α_1	0.4500	0.4102	0.4500	0.4458	0.4500
α_2	0.4500	0.4206	0.4496	0.4500	0.4476
$UDP(ms)$	1.4946	4.0929	2.2421	3.2874	4.0426

MidInfSept

K_{act}	0.870	0.708	0.964	0.642	0.531
K_{pass}	0.05857	0.07185	0.09576	0.02639	0.03281
n_1	1.2000	1.1951	1.1917	1.2000	1.2000

n_2	7.5000	10.0440	8.6264	8.0050	9.4109
α_1	0.4500	0.4419	0.4500	0.4500	0.4428
α_2	0.4500	0.4211	0.4286	0.4371	0.4500
$UDP(ms)$	3.0999	2.5789	2.1961	2.5433	1.7639
MidInf					
K_{act}	0.573	0.859	0.978	1	0.870
K_{pass}	0.05359	0.05179	0.07551	0.05499	0.11996
n_1	1.1104	1.0031	1.1081	1.2000	1.1734
n_2	7.5877	9.6427	11.2030	12.5747	8.5890
α_1	0.4380	0.4008	0.4500	0.4457	0.4376
α_2	0.4500	0.4002	0.4336	0.4500	0.4249
$UDP(ms)$	2.9198	3.2310	3.3166	2.0656	3.1702
MidInfLat					
K_{act}	0.982	0.777	0.878	0.761	1
K_{pass}	0.12000	0.05662	0.08793	0.10476	0.06450
n_1	1.0000	1.0000	1.0671	1.0060	1.0000
n_2	10.9208	11.3896	10.5262	10.7905	13.0905
α_1	0.4251	0.4007	0.4500	0.4366	0.4000
α_2	0.4500	0.4001	0.4153	0.4386	0.4371
$UDP(ms)$	2.5705	2.5505	3.6765	5.0000	3.1793
MidAntLat					
K_{act}	0.758	1	0.896	0.692	0.841
K_{pass}	0.12000	0.11982	0.10323	0.12000	0.08118
n_1	1.0625	1.0023	1.0000	1.0411	1.0093
n_2	7.5000	13.3793	12.1532	8.3022	11.2307
α_1	0.4000	0.4266	0.4434	0.4303	0.4063
α_2	0.4261	0.4145	0.4261	0.4203	0.4262
$UDP(ms)$	1.3167	3.4063	3.3975	1.0927	3.5529
BasalAnt					
K_{act}	1	0.929	1	0.917	0.738
K_{pass}	0.06185	0.10636	0.10784	0.12000	0.05115
n_1	1.0607	1.0001	1.0000	1.0000	1.0000
n_2	7.5000	11.4794	9.7867	10.1259	9.7803
α_1	0.4500	0.4000	0.4401	0.4000	0.4116
α_2	0.4500	0.4000	0.4183	0.4408	0.4206
$UDP(ms)$	4.3150	4.5049	3.7393	4.2820	2.4385

BasalAntSept

K_{act}	0.568	0.641	0.5	0.570	0.668
K_{pass}	0.05567	0.12000	0.10911	0.04218	0.11687
n_1	1.2000	1.1807	1.2000	1.2000	1.1996
n_2	8.1483	9.8105	7.5374	8.0941	7.9926
α_1	0.4500	0.4488	0.4500	0.4499	0.4500
α_2	0.4500	0.4250	0.4307	0.4466	0.4444
$UDP(ms)$	4.2100	1.9469	1.8435	2.7486	2.8662

BasalInfSept

K_{act}	0.731	0.628	0.5	0.5	0.5
K_{pass}	0.09347	0.11755	0.05980	0.01719	0.11996
n_1	1.2000	1.1956	1.2000	1.2000	1.2000
n_2	7.5000	10.6760	13.0172	7.5000	8.3141
α_1	0.4380	0.4256	0.4000	0.4500	0.4500
α_2	0.4500	0.4274	0.4500	0.4500	0.4487
$UDP(ms)$	2.2489	1.6259	2.9608	4.5755	2.1797

BasalInf

K_{act}	0.553	0.750	0.789	1	0.585
K_{pass}	0.12000	0.08693	0.06967	0.07407	0.06041
n_1	1.0000	1.0000	1.0000	1.0833	1.0000
n_2	7.5000	11.6910	11.7870	8.6041	8.5110
α_1	0.4169	0.4187	0.4000	0.4500	0.4087
α_2	0.4232	0.4000	0.4399	0.4183	0.4141
$UDP(ms)$	2.8488	2.6474	2.4895	4.3778	1.6436

BasalInfLat

K_{act}	0.807	0.851	0.584	0.737	1
K_{pass}	0.12000	0.11952	0.12000	0.04240	0.04127
n_1	1.0507	1.0009	1.0001	1.0577	1.0000
n_2	7.5000	11.9306	10.5879	9.9400	9.5219
α_1	0.4057	0.4161	0.4002	0.4094	0.4000
α_2	0.4107	0.4076	0.4040	0.4256	0.4131
$UDP(ms)$	2.3123	2.4533	3.5748	2.9708	3.7447

BasalAntLat

K_{act}	0.936	0.781	1	1	1
K_{pass}	0.03260	0.11982	0.07944	0.06743	0.11937
n_1	1.0000	1.0006	1.0000	1.0089	1.0000

n_2	13.1600	11.9351	13.3274	10.7793	12.1036
α_1	0.4171	0.4012	0.4053	0.4198	0.4000
α_2	0.4426	0.4004	0.4197	0.4213	0.4146
$UDP(ms)$	2.6985	3.6879	3.2351	1.7301	2.5652
$LBBUDP(ms)$	3.6182	4.2567	4.7633	1.0321	4.4247

C.2.2 Identified parameters for ischemic LBBB patients

Parameter	**Patient 1**	**Patient 2**	**Patient 3**	**Patient 4**	**Patient 5**
			ApiAnt		
K_{act}	0.422	0.147	0.249	0.110	0.173
K_{pass}	0.46500	0.99832	0.92692	0.57291	0.99999
n_1	1.0736	1.0622	1.4221	1.4688	1.4142
n_2	9.6817	12.3276	11.4785	11.6664	11.9211
α_1	0.5181	0.5675	0.3459	0.4217	0.2000
α_2	0.4458	0.3760	0.3384	0.3943	0.3180
$UDP(ms)$	8.5938	20.8217	18.4741	11.1734	4.3110
			ApiInf		
K_{act}	0.393	0.183	0.348	0.189	0.458
K_{pass}	0.55983	1	0.99954	0.72017	0.84556
n_1	1.0493	1.1467	1.0603	1.2834	1.5871
n_2	10.1396	8.5159	8.1182	9.0422	7.3124
α_1	0.3173	0.2382	0.3429	0.2004	0.3722
α_2	0.4344	0.3421	0.3502	0.4617	0.4656
$UDP(ms)$	12.3646	9.5120	11.0313	15.6765	22.5000
			ApiLat		
K_{act}	0.302	0.124	0.214	0.148	0.189
K_{pass}	0.34956	0.92167	1	0.88810	0.66251
n_1	1.1271	0.7255	1.3100	1.6636	1.1890
n_2	7.9002	10.6977	9.1039	11.8263	5.7918
α_1	0.3977	0.4116	0.3297	0.3319	0.2817
α_2	0.4365	0.4178	0.3686	0.4221	0.4244
$UDP(ms)$	19.1731	10.3669	18.3341	14.0303	19.3398
			ApiSept		
K_{act}	0.334	0.125	0.202	0.200	0.243
K_{pass}	0.52116	0.93998	0.47853	0.69365	0.84347

n_1	1.0932	1.5575	1.2746	1.7888	1.0349
n_2	11.3788	5.8235	11.7197	8.7152	11.6222
α_1	0.3049	0.2504	0.2000	0.3981	0.4240
α_2	0.4861	0.3991	0.3842	0.4180	0.4763
$UDP(ms)$	15.1226	19.2286	15.7248	15.1451	16.1101
MidAnt					
K_{act}	0.260	0.216	0.249	0.205	0.198
K_{pass}	0.59528	0.99630	0.57858	0.98968	0.98059
n_1	0.8194	0.9017	1.2818	0.7541	0.8590
n_2	9.0846	9.3443	9.3293	9.2899	12.1482
α_1	0.3945	0.4171	0.2003	0.5333	0.4657
α_2	0.4693	0.4092	0.3878	0.4095	0.3704
$UDP(ms)$	7.9211	18.0790	9.6734	19.5805	8.6678
MidAntSept					
K_{act}	0.369	0.217	0.241	0.189	0.436
K_{pass}	0.68076	0.99712	0.54112	0.91467	0.78075
n_1	1.1164	1.3530	1.0228	1.2787	1.6247
n_2	7.6949	7.9806	8.8143	10.8452	7.3438
α_1	0.5571	0.5051	0.4363	0.3482	0.2000
α_2	0.4414	0.4068	0.3781	0.4513	0.4929
$UDP(ms)$	14.0627	13.6677	20.4416	16.1215	15.5048
MidInfSept					
K_{act}	0.303	0.298	0.207	0.265	0.227
K_{pass}	0.63557	0.99500	0.99079	0.42414	0.62385
n_1	1.5503	1.5085	0.9987	1.4348	1.0466
n_2	6.4747	11.0513	9.7881	8.2682	7.0339
α_1	0.5665	0.4116	0.2007	0.4379	0.4999
α_2	0.4012	0.3964	0.3758	0.4326	0.5173
$UDP(ms)$	19.9045	12.8543	20.9283	11.4880	14.0138
MidInf					
K_{act}	0.247	0.279	0.339	0.297	0.438
K_{pass}	0.37212	0.68858	0.99082	0.36360	0.85608
n_1	0.7970	1.4656	1.0210	1.3012	0.9150
n_2	6.5660	5.4055	9.2144	7.8733	8.3112
α_1	0.2061	0.3383	0.2518	0.4869	0.5569
α_2	0.4459	0.3669	0.3633	0.4121	0.4948

$UDP(ms)$	18.9951	13.3941	10.0505	11.3981	24.9548
MidInfLat					
K_{act}	0.236	0.355	0.155	0.262	0.327
K_{pass}	0.99748	0.99417	0.50367	0.35807	0.87654
n_1	1.9831	1.5373	1.1486	0.9820	1.0706
n_2	5.0000	11.5750	9.5768	8.2651	5.8352
α_1	0.5366	0.4809	0.2727	0.3336	0.3010
α_2	0.3549	0.4365	0.3539	0.4184	0.4470
$UDP(ms)$	21.9631	10.1356	16.4152	12.2780	26.1445
MidAntLat					
K_{act}	0.166	0.171	0.247	0.29	0.324
K_{pass}	1	0.93780	0.64845	0.99815	0.86730
n_1	0.5484	0.8235	1.1256	1.3104	1.1721
n_2	10.7936	8.8525	9.8886	10.9400	5.0036
α_1	0.5474	0.3140	0.3806	0.2152	0.5386
α_2	0.4708	0.4206	0.3791	0.4000	0.4009
$UDP(ms)$	12.7706	9.6498	14.7461	21.9183	15.6703
BasalAnt					
K_{act}	0.277	0.242	0.277	0.333	0.299
K_{pass}	0. 71804	0.64059	0.40773	0.45686	0.51997
n_1	1.2573	1.1935	1.0524	1.3141	1.7459
n_2	11.9454	8.3235	8.6388	6.0768	5.0120
α_1	0.2258	0.2802	0.4672	0.5158	0.5731
α_2	0.4415	0.3846	0.3760	0.3597	0.2973
$UDP(ms)$	14.7852	15.4969	16.9921	12.4219	26.2211
BasalAntSept					
K_{act}	0.285	0.211	0.160	0.138	0.351
K_{pass}	0.58576	0.80631	0.84812	0.92094	0.71004
n_1	1.6560	1.1975	1.2208	1.9770	1.2033
n_2	7.7412	9.9320	14.1271	5.0000	8.0959
α_1	0.4732	0.4409	0.3989	0.3746	0.3774
α_2	0.3933	0.4285	0.4106	0.3220	0.5131
$UDP(ms)$	23.4235	17.4530	17.1110	12.2390	7.5513
BasalInfSept					
K_{act}	0.205	0.310	0.145	0.256	0.274
K_{pass}	0.98351	0.84819	0.57491	0.62300	0.28321

n_1	1.1920	1.1906	0.9901	1.1832	1.2903
n_2	7.8760	8.2109	6.5232	10.0552	5.0553
α_1	0.2871	0.3123	0.2232	0.5990	0.3690
α_2	0.4585	0.4195	0.3506	0.4470	0.4552
$UDP(ms)$	13.6256	14.2649	18.1208	16.0770	22.5825
			BasalInf		
K_{act}	0.184	0.5	0.183	0.384	0.457
K_{pass}	0.49627	0.40479	0.56396	0.74475	0.50401
n_1	1.6816	1.1515	1.5164	1.0592	1.1418
n_2	6.9446	8.3151	9.3201	13.2578	10.8307
α_1	0.3741	0.2414	0.2647	0.2301	0.4686
α_2	0.4185	0.3993	0.3443	0.4450	0.4975
$UDP(ms)$	12.2610	18.7295	18.8316	14.0557	7.4394
			BasalInfLat		
K_{act}	0.420	0.470	0.203	0.262	0.497
K_{pass}	0.99662	0.96055	0.90867	0.60565	0.70504
n_1	1.8575	1.1460	1.4084	0.9099	1.0694
n_2	7.3810	15.0000	12.2643	9.4703	8.7358
α_1	0.4562	0.4826	0.4716	0.2014	0.2001
α_2	0.4375	0.4701	0.3896	0.4292	0.4665
$UDP(ms)$	17.0677	20.1018	15.5268	15.7470	15.6691
			BasalAntLat		
K_{act}	0.462	0.465	0.270	0.498	0.351
K_{pass}	0.58402	0.57477	0.80507	0.49892	0.76991
n_1	1.9891	1.5858	1.8315	0.9576	0.5010
n_2	8.5605	12.6353	7.4866	10.0581	8.6082
α_1	0.3677	0.2786	0.4653	0.3557	0.6000
α_2	0.4909	0.4052	0.3397	0.3976	0.4779
$UDP(ms)$	23.3650	21.0890	19.3492	25.5648	18.4712
$LBBUDP(ms)$	157.2588	76.9279	106.9720	112.5649	144.0385

C.2.3 Identified parameters for non-ischemic LBBB patients

Parameter	**Patient 1**	**Patient 2**	**Patient 3**	**Patient 4**	**Patient 5**
			ApiAnt		
K_{act}	0.234	0.243	0.344	0.279	0.211

K_{pass}	1	0.77836	0.46059	0.64842	0.88830
n_1	1.3286	1.0189	0.8918	0.8734	1.2441
n_2	7.0179	11.0306	11.6417	7.9574	10.4452
α_1	0.3854	0.3792	0.6000	0.3558	0.2693
α_2	0.4097	0.4728	0.4856	0.3994	0.3887
$UDP(ms)$	11.2255	8.6203	16.8675	13.6385	14.3058
ApiInf					
K_{act}	0.295	0.257	0.490	0.307	0.328
K_{pass}	0.62966	0.91245	0.68277	0.59100	0.79861
n_1	1.0178	1.0709	1.4679	0.8184	1.4138
n_2	5.9921	10.0690	10.9087	10.2640	5.3737
α_1	0.3944	0.2006	0.4145	0.3881	0.3349
α_2	0.4055	0.4906	0.4721	0.4452	0.3584
$UDP(ms)$	2.8755	17.0702	12.1846	18.6732	23.0527
ApiLat					
K_{act}	0.303	0.295	0.447	0.414	0.199
K_{pass}	0.59393	0.45855	0.52352	0.83455	0.35211
n_1	0.8083	1.2424	1.4852	1.1447	1.1093
n_2	9.8309	11.9649	10.3279	11.9967	10.8024
α_1	0.5986	0.2000	0.3046	0.4147	0.4675
α_2	0.4690	0.4128	0.4097	0.4279	0.4293
$UDP(ms)$	29.1348	22.3668	13.8962	12.6276	20.3639
ApiSept					
K_{act}	0.223	0.474	0.345	0.168	0.339
K_{pass}	0.55213	1	0.99990	0.55126	0.99976
n_1	0.6339	1.3393	1.4969	1.3641	1.2587
n_2	5.0000	7.0785	9.4781	13.3680	11.4716
α_1	0.4062	0.6000	0.3774	0.3164	0.3715
α_2	0.4374	0.4013	0.4291	0.3407	0.4053
$UDP(ms)$	22.0428	11.5736	8.4838	9.8203	16.2277
MidAnt					
K_{act}	0.264	0.348	0.5	0.312	0.203
K_{pass}	0.62668	0.63578	0.38070	1	0.60593
n_1	1.1666	0.8668	0.7153	0.9776	1.0250
n_2	9.2530	11.4351	10.7664	5.0047	10.7099
α_1	0.3940	0.3165	0.3419	0.3703	0.4001
α_2	0.4313	0.4812	0.4690	0.4569	0.4038

$UDP(ms)$	20.1837	19.9733	14.9720	8.7270	19.0571
MidAntSept					
K_{act}	0.216	0.316	0.356	0.128	0.291
K_{pass}	0.97686	0.61556	0.54065	0.22851	0.54595
n_1	0.9069	1.1484	1.1353	0.7213	1.2912
n_2	5.0000	9.2304	10.2273	7.5270	7.8979
α_1	0.4929	0.2895	0.2141	0.2660	0.3943
α_2	0.3957	0.4698	0.3833	0.4062	0.3519
$UDP(ms)$	25.5342	23.3318	21.9096	17.6623	12.4399
MidInfSept					
K_{act}	0.145	0.290	0.322	0.085	0.269
K_{pass}	0.39992	0.68190	0.71855	0.16751	0.75807
n_1	0.7182	1.0613	0.6446	0.7606	1.2761
n_2	8.4446	8.1803	9.0548	5.4258	9.1910
α_1	0.2199	0.2000	0.3140	0.3882	0.4296
α_2	0.4122	0.4380	0.4424	0.3502	0.3600
$UDP(ms)$	14.6551	9.3519	25.1486	11.1056	15.2825
MidInf					
K_{act}	0.265	0.228	0.359	0.245	0.317
K_{pass}	0.99660	0.42263	0.85489	0.50348	0.36966
n_1	0.9572	0.6960	0.6528	0.9668	1.4480
n_2	7.5274	5.3399	9.5187	9.0416	9.6051
α_1	0.2000	0.3876	0.2899	0.2484	0.4146
α_2	0.4086	0.4404	0.4596	0.4503	0.3690
$UDP(ms)$	8.8139	8.8335	13.1994	13.1266	17.6963
MidInfLat					
K_{act}	0.238	0.236	0.5	0.314	0.181
K_{pass}	0.54952	0.99349	0.99962	0.59237	0.99877
n_1	1.1738	1.1716	1.1082	0.8771	1.4745
n_2	10.1933	6.2917	11.6265	10.6309	6.5131
α_1	0.4540	0.3059	0.2000	0.4589	0.2001
α_2	0.4383	0.4529	0.4959	0.5248	0.4418
$UDP(ms)$	5.5427	6.5093	5.7505	20.0289	15.5443
MidAntLat					
K_{act}	0.242	0.236	0.499	0.314	0.137
K_{pass}	0.93012	0.60460	1	0.18500	1

n_1	1.2273	1.0899	1.3528	0.9769	1.0159
n_2	8.8363	12.3144	9.8488	9.3540	10.1635
α_1	0.4204	0.3044	0.2184	0.4167	0.4142
α_2	0.4520	0.3999	0.4576	0.4560	0.4525
$UDP(ms)$	4.5894	11.7797	14.7691	21.5134	12.8569
BasalAnt					
K_{act}	0.317	0.439	0.5	0.298	0.280
K_{pass}	0.85683	0.32017	0.74675	0.64253	0.61082
n_1	1.1219	1.1449	1.4378	1.0595	1.7512
n_2	8.2842	9.9701	6.6798	10.4311	5.0098
α_1	0.4906	0.4005	0.2000	0.4674	0.3764
α_2	0.5037	0.4624	0.4476	0.4337	0.4622
$UDP(ms)$	27.1332	26.9613	30.0000	14.4901	7.0681
BasalAntSept					
K_{act}	0.184	0.267	0.5	0.138	0.150
K_{pass}	0.66400	0.69331	0.59515	0.51332	0.70204
n_1	1.1892	1.2041	0.9083	1.2639	1.2406
n_2	9.2956	11.7314	13.5912	6.6589	7.6256
α_1	0.3649	0.3906	0.2868	0.3989	0.2353
α_2	0.3413	0.5043	0.3972	0.3315	0.3489
$UDP(ms)$	4.4761	13.6640	21.3711	8.8365	10.4224
BasalInfSept					
K_{act}	0.285	0.222	0.344	0.182	0.230
K_{pass}	1	0.64564	0.4.4720	1	0.42383
n_1	1.2465	1.2093	0.9036	1.2537	1.3842
n_2	9.3015	5.0000	5.4289	5.0000	9.7320
α_1	0.2140	0.2518	0.3267	0.2000	0.4768
α_2	0.4342	0.3648	0.3983	0.3469	0.3617
$UDP(ms)$	14.6647	6.6760	16.8010	12.0451	22.3750
BasalInf					
K_{act}	0.226	0.247	0.358	0.236	0.233
K_{pass}	0.49744	0.52095	0.42762	0.34817	0.86110
n_1	1.1475	0.9623	0.5616	1.1805	1.1534
n_2	11.4395	5.0544	5.0308	7.8154	10.2866
α_1	0.2146	0.5383	0.4899	0.2027	0.2000
α_2	0.4528	0.3974	0.3889	0.4715	0.4074

$UDP(ms)$	18.7211	15.3442	17.6598	15.0357	21.3351
BasalInfLat					
K_{act}	0.242	0.321	0.5	0.371	0.240
K_{pass}	0.44589	0.67592	0.49909	0.63081	0.50483
n_1	1.0664	1.0106	0.9404	1.1232	1.2515
n_2	11.0246	10.9480	9.1593	9.0059	5.0043
α_1	0.5544	0.3597	0.3535	0.4382	0.3541
α_2	0.4961	0.4749	0.4401	0.5061	0.3650
$UDP(ms)$	2.8828	23.0425	11.7026	13.9645	15.0578
BasalAntLat					
K_{act}	0.301	0.310	0.4	0.319	0.158
K_{pass}	0.33578	0.46114	0.21690	0.19736	0.57613
n_1	1.3246	1.5132	0.9264	1.0358	1.9932
n_2	9.8050	8.4362	7.0887	8.8630	5.1330
α_1	0.4574	0.2812	0.5087	0.3702	0.3930
α_2	0.4610	0.4521	0.4891	0.4763	0.3875
$UDP(ms)$	21.7876	21.2621	20.7890	10.7620	20.4348
$LBBUDP(ms)$	85.5068	131.8916	168.6731	132.8939	132.3611

D

Complementary Results

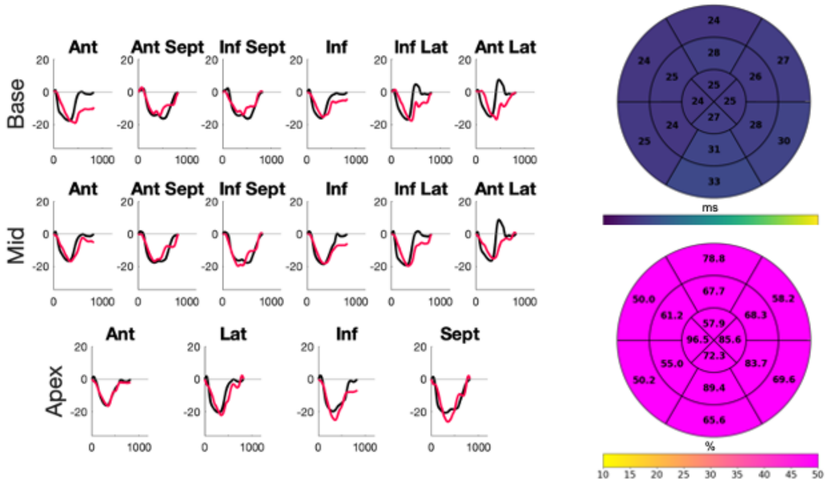

Figure D.1: Healthy Patient 1. Experimental (red) and simulated (black) strain curves corresponding to the 16 LV segments (*left*). Bull-eye representations of segmental electrical activation delay (*top*) and segmental myofiber contractility (*bottom*).

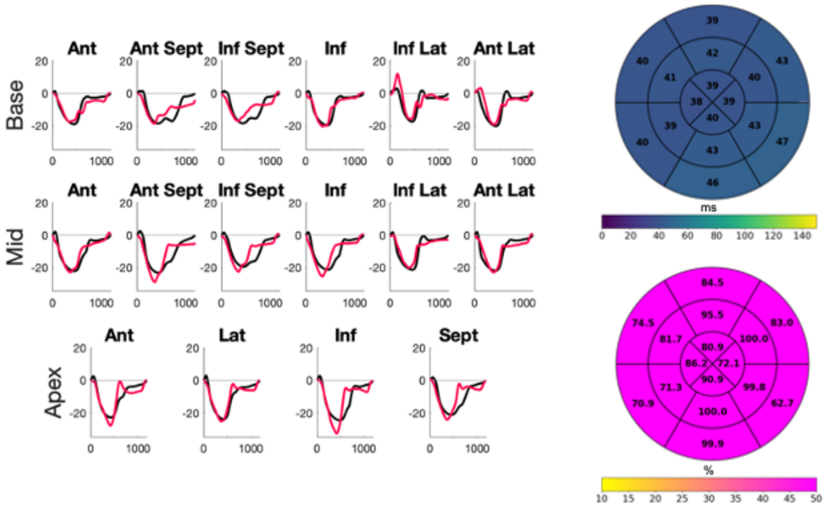

Figure D.2: Healthy Patient 2. Experimental (red) and simulated (black) strain curves corresponding to the 16 LV segments (*left*). Bull-eye representations of segmental electrical activation delay (*top*) and segmental myofiber contractility (*bottom*).

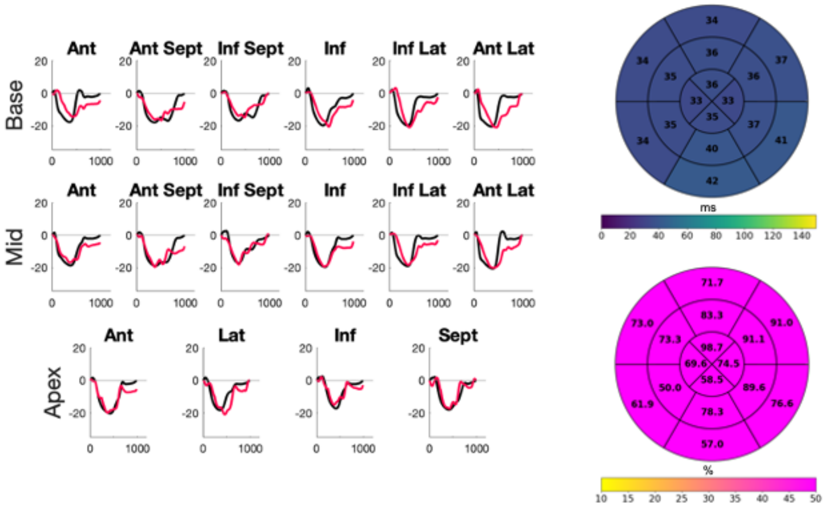

Figure D.3: Healthy Patient 3. Experimental (red) and simulated (black) strain curves corresponding to the 16 LV segments (*left*). Bull-eye representations of segmental electrical activation delay (*top*) and segmental myofiber contractility (*bottom*).

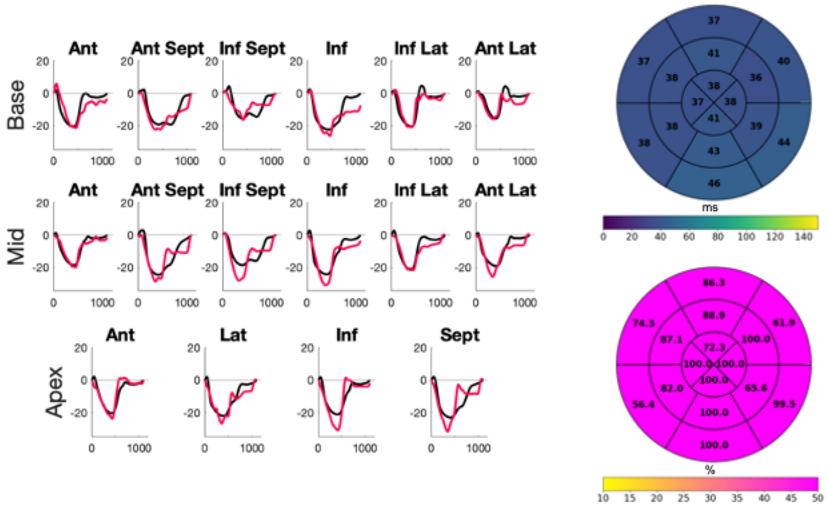

Figure D.4: Healthy Patient 4. Experimental (red) and simulated (black) strain curves corresponding to the 16 LV segments (*left*). Bull-eye representations of segmental electrical activation delay (*top*) and segmental myofiber contractility (*bottom*).

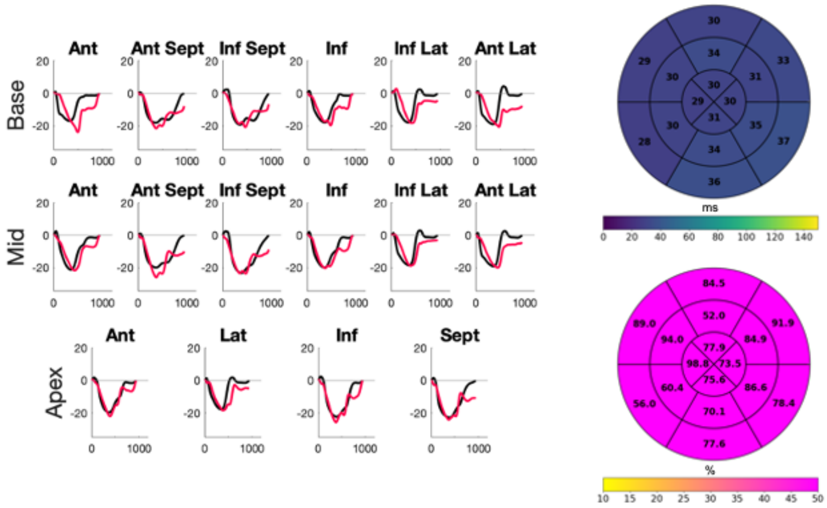

Figure D.5: Healthy Patient 5. Experimental (red) and simulated (black) strain curves corresponding to the 16 LV segments (*left*). Bull-eye representations of segmental electrical activation delay (*top*) and segmental myofiber contractility (*bottom*).

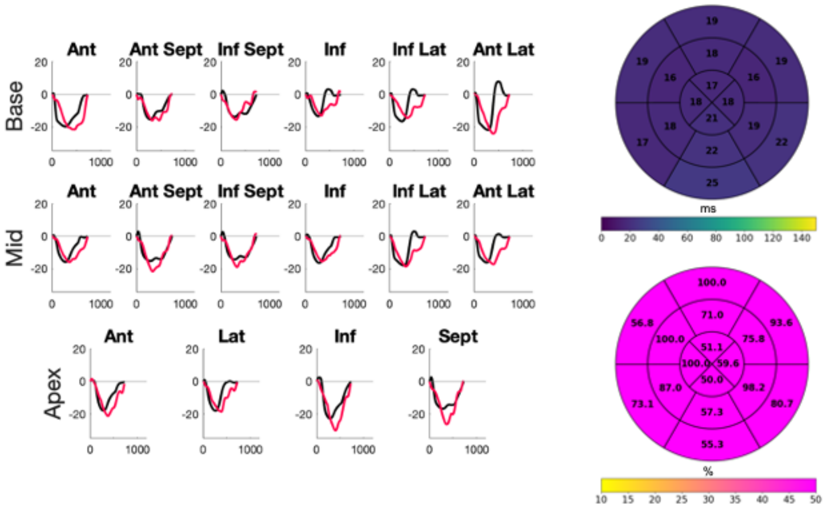

Figure D.6: Healthy Patient 6. Experimental (red) and simulated (black) strain curves corresponding to the 16 LV segments (*left*). Bull-eye representations of segmental electrical activation delay (*top*) and segmental myofiber contractility (*bottom*).

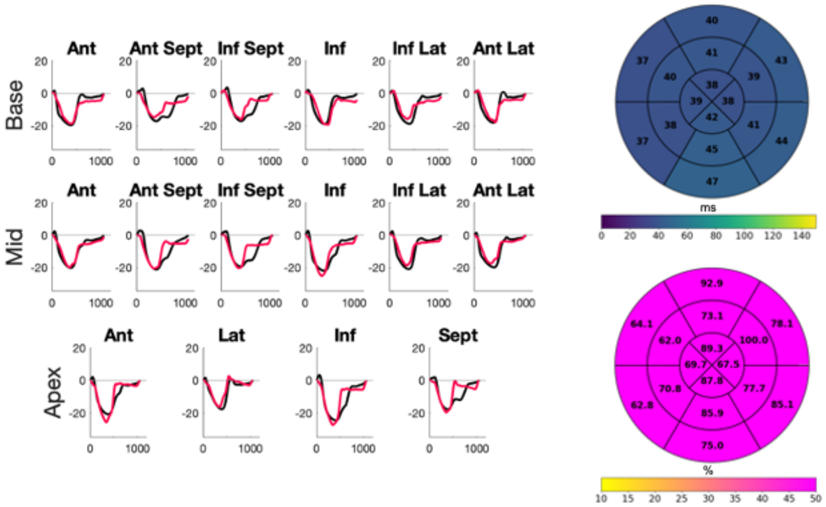

Figure D.7: Healthy Patient 7. Experimental (red) and simulated (black) strain curves corresponding to the 16 LV segments (*left*). Bull-eye representations of segmental electrical activation delay (*top*) and segmental myofiber contractility (*bottom*).

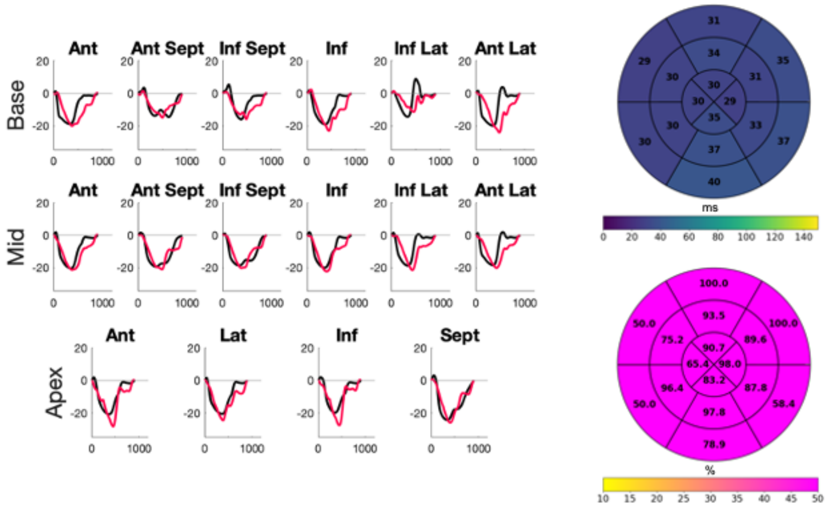

Figure D.8: Healthy Patient 8. Experimental (red) and simulated (black) strain curves corresponding to the 16 LV segments (*left*). Bull-eye representations of segmental electrical activation delay (*top*) and segmental myofiber contractility (*bottom*).

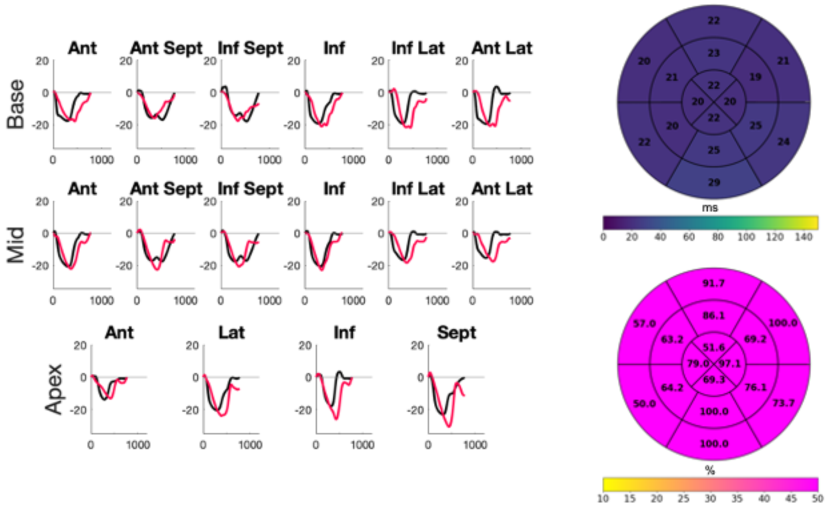

Figure D.9: Healthy Patient 9. Experimental (red) and simulated (black) strain curves corresponding to the 16 LV segments (*left*). Bull-eye representations of segmental electrical activation delay (*top*) and segmental myofiber contractility (*bottom*).

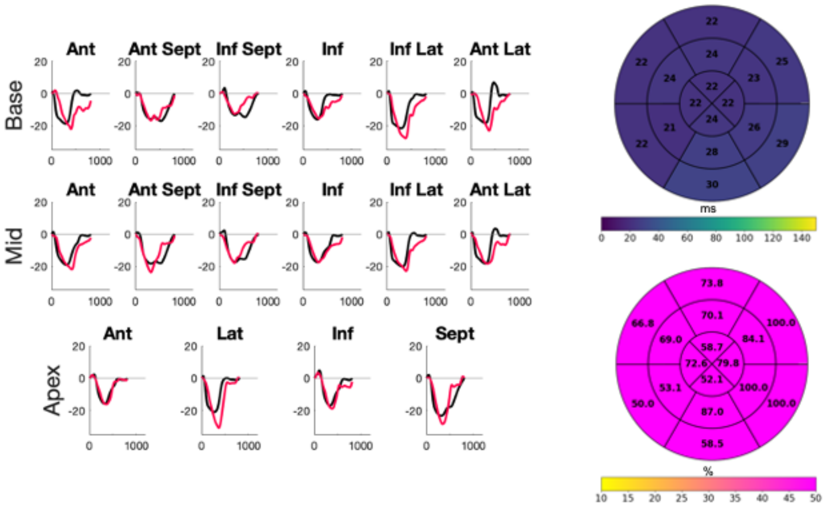

Figure D.10: Healthy Patient 10. Experimental (red) and simulated (black) strain curves corresponding to the 16 LV segments (*left*). Bull-eye representations of segmental electrical activation delay (*top*) and segmental myofiber contractility (*bottom*).

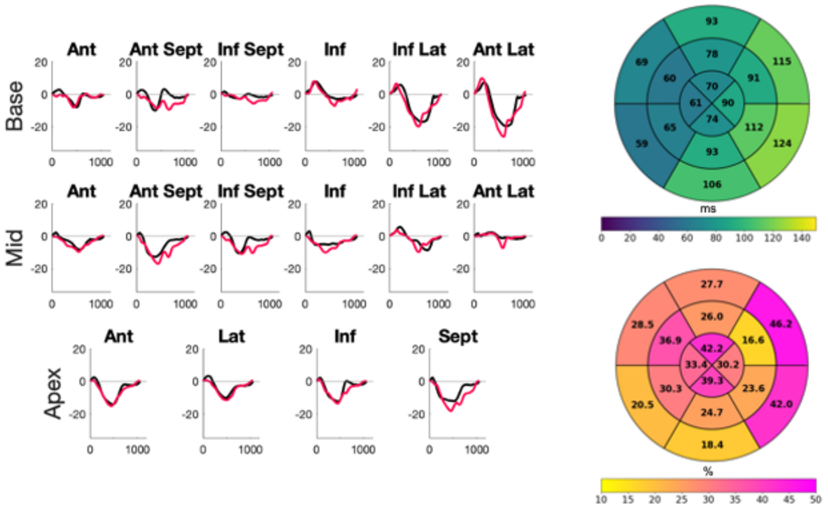

Figure D.11: Ischemic LBBB Patient 1. Experimental (red) and simulated (black) strain curves corresponding to the 16 LV segments (*left*). Bull-eye representations of segmental electrical activation delay (*top*) and segmental myofiber contractility (*bottom*).

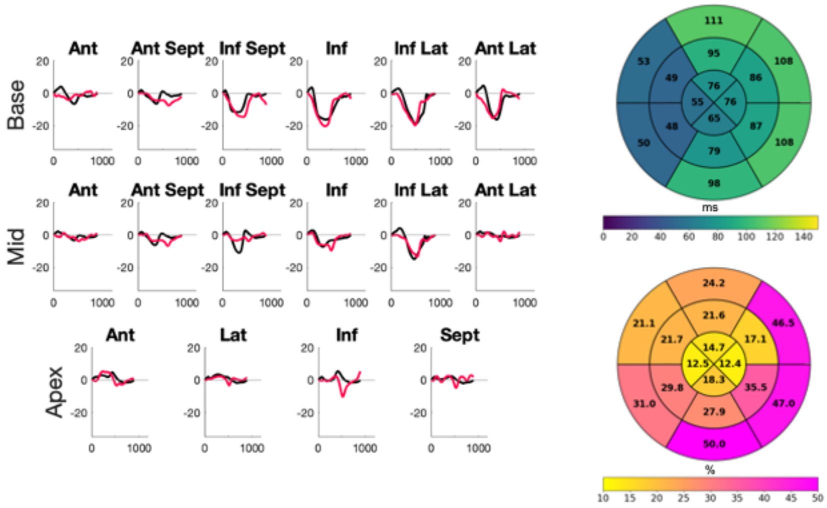

Figure D.12: Ischemic LBBB Patient 2. Experimental (red) and simulated (black) strain curves corresponding to the 16 LV segments (*left*). Bull-eye representations of segmental electrical activation delay (*top*) and segmental myofiber contractility (*bottom*).

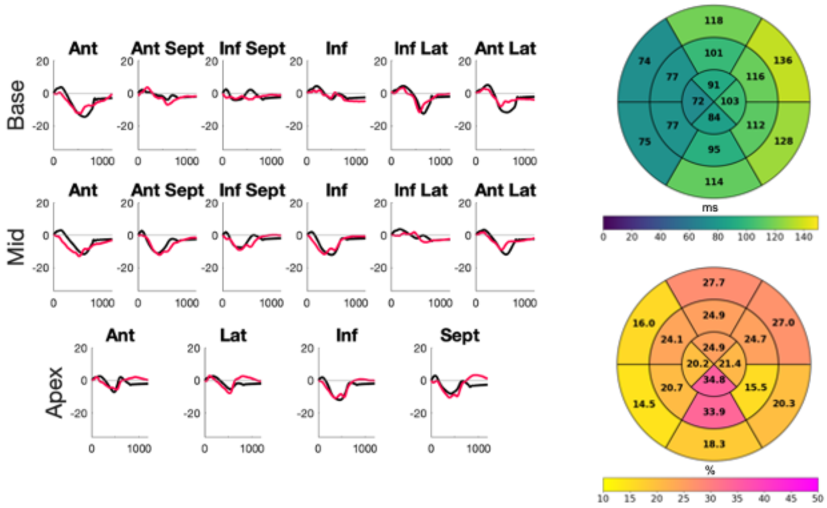

Figure D.13: Ischemic LBBB Patient 3. Experimental (red) and simulated (black) strain curves corresponding to the 16 LV segments (*left*). Bull-eye representations of segmental electrical activation delay (*top*) and segmental myofiber contractility (*bottom*).

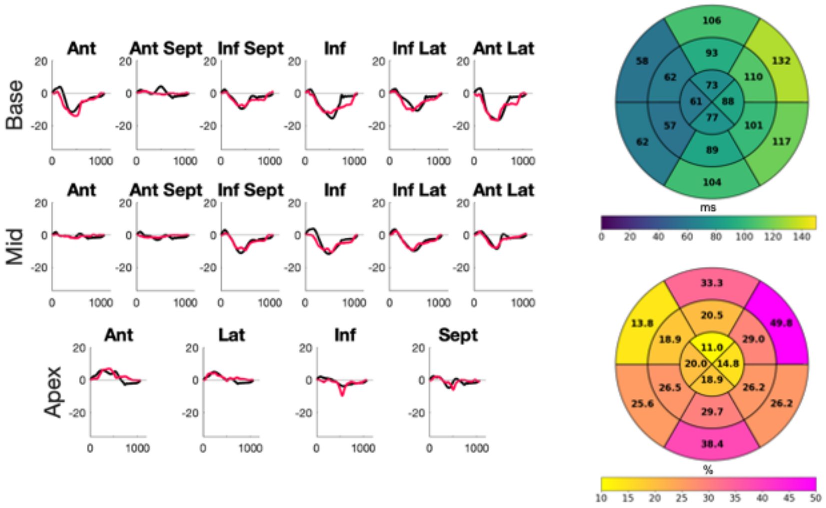

Figure D.14: Ischemic LBBB Patient 4. Experimental (red) and simulated (black) strain curves corresponding to the 16 LV segments (*left*). Bull-eye representations of segmental electrical activation delay (*top*) and segmental myofiber contractility (*bottom*).

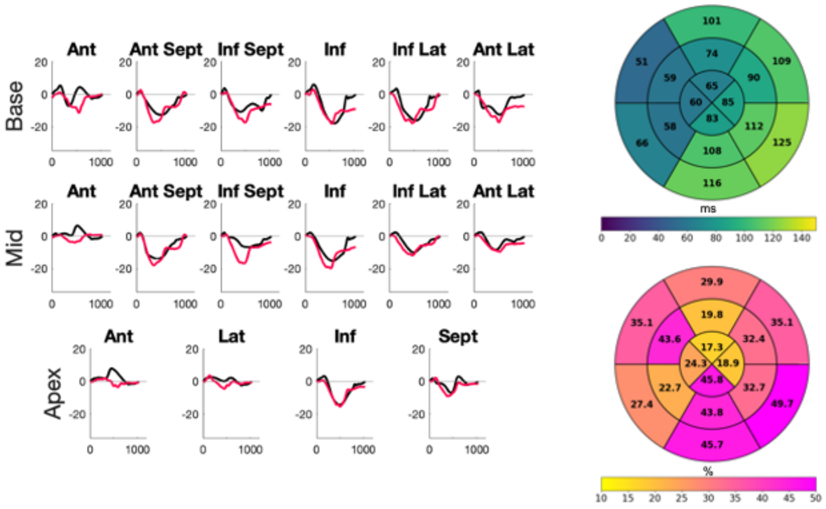

Figure D.15: Ischemic LBBB Patient 5. Experimental (red) and simulated (black) strain curves corresponding to the 16 LV segments (*left*). Bull-eye representations of segmental electrical activation delay (*top*) and segmental myofiber contractility (*bottom*).

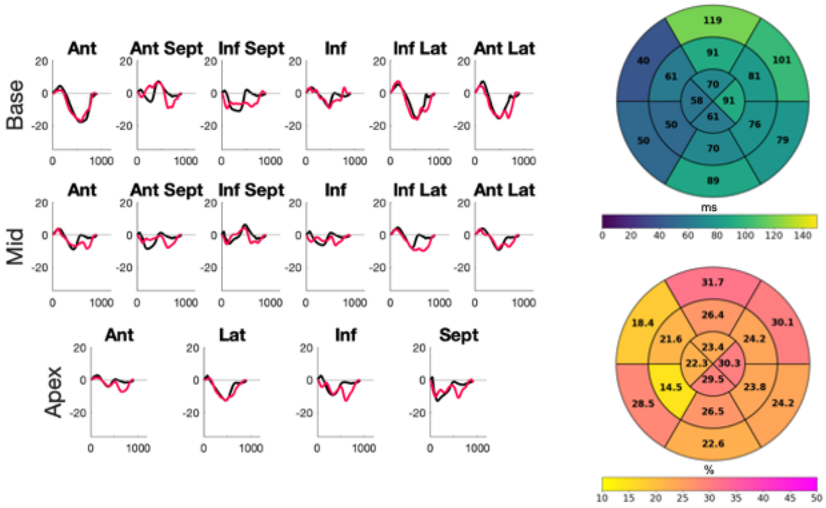

Figure D.16: Non-ischemic LBBB Patient 1. Experimental (red) and simulated (black) strain curves corresponding to the 16 LV segments (*left*). Bull-eye representations of segmental electrical activation delay (*top*) and segmental myofiber contractility (*bottom*).

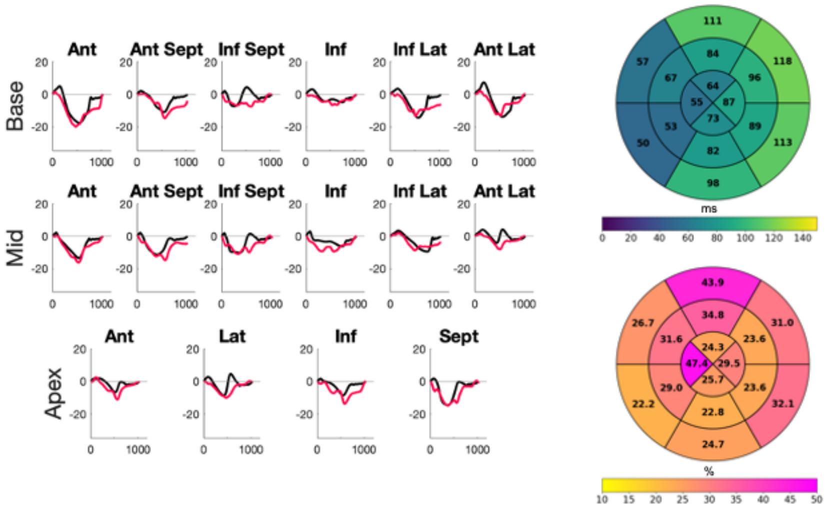

Figure D.17: Non-ischemic LBBB Patient 2. Experimental (red) and simulated (black) strain curves corresponding to the 16 LV segments (*left*). Bull-eye representations of segmental electrical activation delay (*top*) and segmental myofiber contractility (*bottom*).

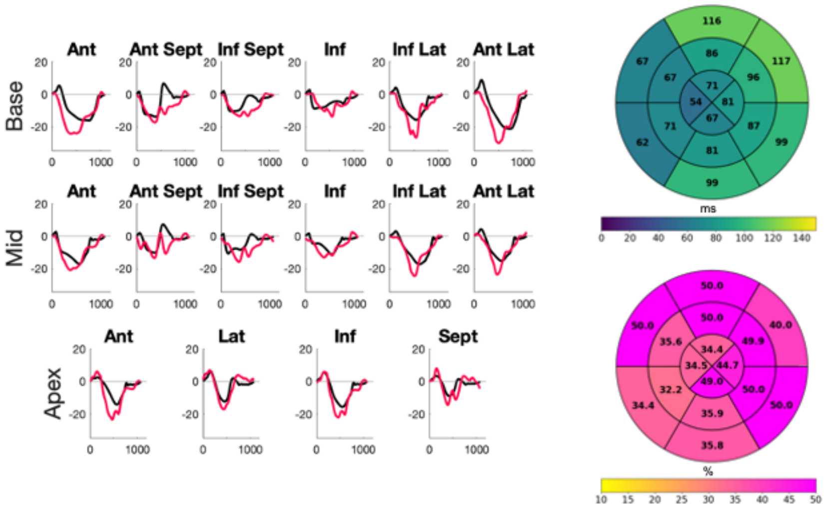

Figure D.18: Non-ischemic LBBB Patient 3. Experimental (red) and simulated (black) strain curves corresponding to the 16 LV segments (*left*). Bull-eye representations of segmental electrical activation delay (*top*) and segmental myofiber contractility (*bottom*).

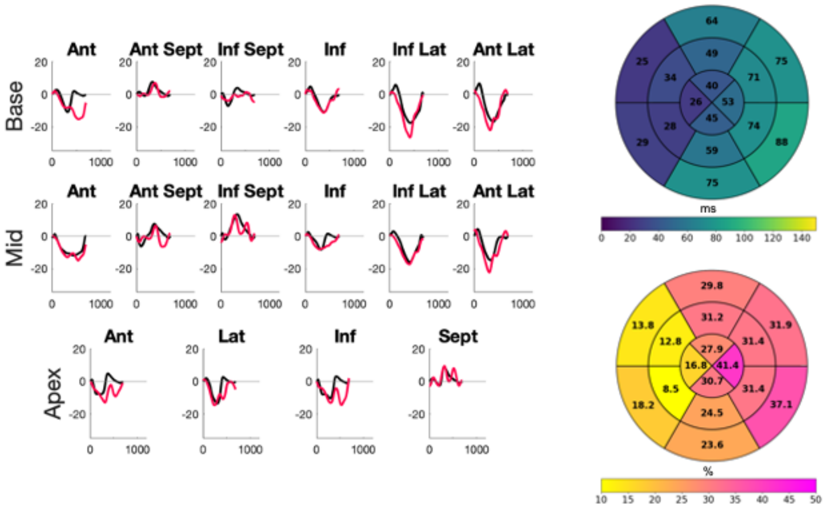

Figure D.19: Non-ischemic LBBB Patient 4. Experimental (red) and simulated (black) strain curves corresponding to the 16 LV segments (*left*). Bull-eye representations of segmental electrical activation delay (*top*) and segmental myofiber contractility (*bottom*).

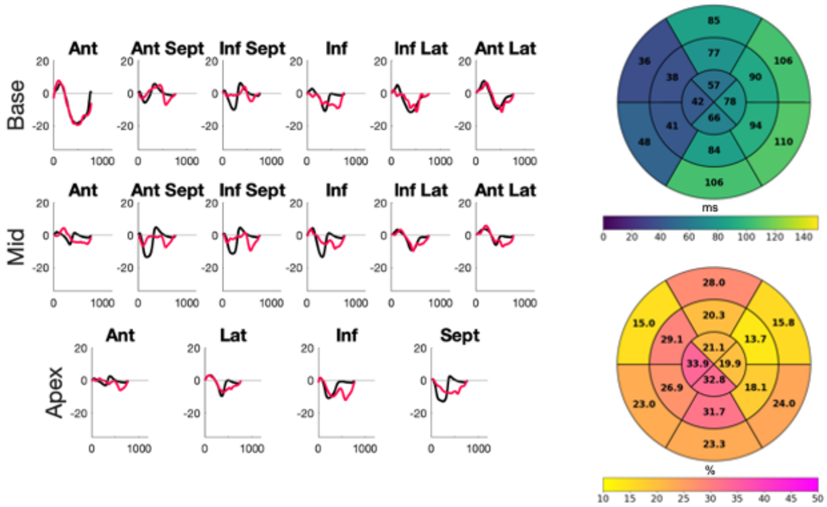

Figure D.20: Non-ischemic LBBB Patient 5. Experimental (red) and simulated (black) strain curves corresponding to the 16 LV segments (*left*). Bull-eye representations of segmental electrical activation delay (*top*) and segmental myofiber contractility (*bottom*).

List of Figures

List of Tables

UNIVERSITÉ DE
RENNES 1

Titre : Approche à base de modèles pour l’analyse du *strain* myocardique obtenu en échocradiographie.

Mot clés : Modélisation, analyse de sensibilité, identification spécifique au patient, fonction cardiaque, *strain* myocardique, sténose aortique, bloc de branche gauche.

Résumé : Le *«speckle-tracking echocardiography»* (STE) permet la quantification de l’asynchronisme ventriculaire en produisant des signaux de ‘strain’ associés à la déformation. Cependant, la majorité des méthodes existantes d’analyse du ‘strain’ négligent la morphologie des signaux. De nouvelles méthodes sont donc nécessaires pour analyser conjointement la morphologie des signaux de ‘strain’ acquis simultanément dans différentes régions du myocarde. L’objectif du travail de thèse est de proposer une approche à base de modèles afin d’améliorer l’analyse des signaux de ‘strain’ issus de l’échocardiographie. Deux applications cliniques sont visées par nos travaux : la sténose aortique et la thérapie de resynchronisation cardiaque. Une première application de cette thèse consiste à proposer une nouvelle approche à base de modèle pour 1) estimer la courbe de pression ventriculaire de manière non-invasive et 2) évaluer les indices de travail cardiaque à partir des signaux de strain obtenus par échocardiographie. La seconde application de cette thèse consiste à proposer une nouvelle approche à base de modèles afin d’améliorer l’analyse des signaux de *strain*. Les résultats montrent globalement un bon accord entre les données obtenues à partir des simulations spécifiques au patient et des mesures expérimentales. Les approches proposées dans cette thèse sont prometteuses, non seulement pour l’optimisation du traitement clinique et du développement, mais aussi pour comprendre les origines de la maladie.

Title: Model-based analysis of myocardial strains for the evaluation of cardiovascular function.

Keywords: Computational modeling, sensitivity analysis, patient-specific identification, cardiac function, myocardial strain, aortic stenosis, left bundle branch block.

Abstract: Strain imaging by speckle-tracking echocardiography (STE) has been introduced as a complementary tool for the assessment of myocardial function. Compared to other measures of cardiac function, such as left ventricle (LV) ejection fraction (LVEF), the pathophysiological value of STE is still neglected in several clinical conditions. As a consequence, new methods are needed to improve the analysis of echocardiography strain curves for the evaluation of myocardial function. In this context, model-based methods appear as promising alternatives to provide a better understanding of the physiological mechanisms related to the cardiovascular system, as well as to improve diagnosis and therapy support. The main objective of this thesis is to propose a new model-based method for the analysis of cardiac regional strain data, obtained from cardiac echocardiography, particularly in two clinical applications: aortic stenosis (AS) and left bundle branch block (LBBB). The first application of this thesis was to propose a non-invasive model-based estimation of the LV pressure curve in order to obtain reliable myocardial work indices in the case of AS. The second application of the thesis was to propose a novel model-based approach for the analysis of myocardial strains in LBBB patients. Results show a good agreement between data obtained with patient-specific simulations and with experimental measurements. The approaches proposed in this thesis are promising, not only for the optimization of clinical treatment and development but also for understanding the origins of disease.